Breathing motion detection in computed tomography using data consistency conditions

Mélanie Mouchet

N°d'ordre NNT : 2022ISAL0108

THESE de DOCTORAT DE L'INSA LYON,
membre de l'Université de Lyon

Ecole Doctorale N° 160
Electronique, Electrochimique, Automatique

Spécialité/ discipline de doctorat :
Traitement du Signal et de l'Image

Soutenue publiquement le 06/12/2022, par :
Mélanie Mouchet

Breathing motion detection in computed tomography using data consistency conditions

---

Devant le jury composé de :

Defrise, Michel	Professeur émérite, Vrije Universiteit Brussel	Rapporteur
Maier, Andreas	Professeur, Friedrich-Alexander-Universität, Erlangen-Nürnberg	Rapporteur
Etxebeste, Ane	Maîtresse de conférences, INSA-LYON	Examinatrice
Desbat, Laurent	Professeur, Université Grenoble Alpes	Examinateur
Létang, Jean	Maître de conférences, INSA- LYON	Directeur de thèse
Rit, Simon	Chargé de recherche, CNRS, Lyon	Co-directeur de thèse
Lesaint, Jérôme	Chercheur post doctorat, CNRS, Lyon	Invité
Lepetit Coiffe, Matthieu	Responsable Partenariat, Siemens Healthcare, Saint Denis	Invité

Département FEDORA – INSA Lyon - Ecoles Doctorales

SIGLE	ECOLE DOCTORALE	NOM ET COORDONNEES DU RESPONSABLE
CHIMIE	**CHIMIE DE LYON** **https://www.edchimie-lyon.fr** Sec. : Renée EL MELHEM Bât. Blaise PASCAL, 3e étage secretariat@edchimie-lyon.fr	**M. Stéphane DANIELE** C2P2-CPE LYON-UMR 5265 Bâtiment F308, BP 2077 43 Boulevard du 11 novembre 1918 69616 Villeurbanne **directeur@edchimie-lyon.fr**
E.E.A.	**ÉLECTRONIQUE, ÉLECTROTECHNIQUE, AUTOMATIQUE** **https://edeea.universite-lyon.fr** Sec. : Stéphanie CAUVIN Bâtiment Direction INSA Lyon Tél : 04.72.43.71.70 secretariat.edeea@insa-lyon.fr	**M. Philippe DELACHARTRE** INSA LYON Laboratoire CREATIS Bâtiment Blaise Pascal, 7 avenue Jean Capelle 69621 Villeurbanne CEDEX Tél : 04.72.43.88.63 **philippe.delachartre@insa-lyon.fr**
E2M2	**ÉVOLUTION, ÉCOSYSTÈME, MICROBIOLOGIE, MODÉLISATION** **http://e2m2.universite-lyon.fr** Sec. : Bénédicte LANZA Bât. Atrium, UCB Lyon 1 Tél : 04.72.44.83.62 secretariat.e2m2@univ-lyon1.fr	**Mme Sandrine CHARLES** Université Claude Bernard Lyon 1 UFR Biosciences Bâtiment Mendel 43, boulevard du 11 Novembre 1918 69622 Villeurbanne CEDEX **sandrine.charles@univ-lyon1.fr**
EDISS	**INTERDISCIPLINAIRE SCIENCES-SANTÉ** **http://ediss.universite-lyon.fr** Sec. : Bénédicte LANZA Bât. Atrium, UCB Lyon 1 Tél : 04.72.44.83.62 secretariat.ediss@univ-lyon1.fr	**Mme Sylvie RICARD-BLUM** Institut de Chimie et Biochimie Moléculaires et Supramoléculaires (ICBMS) - UMR 5246 CNRS - Université Lyon 1 Bâtiment Raulin - 2ème étage Nord 43 Boulevard du 11 novembre 1918 69622 Villeurbanne Cedex Tél : +33(0)4 72 44 82 32 **sylvie.ricard-blum@univ-lyon1.fr**
INFOMATHS	**INFORMATIQUE ET MATHÉMATIQUES** **http://edinfomaths.universite-lyon.fr** Sec. : Renée EL MELHEM Bât. Blaise PASCAL, 3e étage Tél : 04.72.43.80.46 infomaths@univ-lyon1.fr	**M. Hamamache KHEDDOUCI** Université Claude Bernard Lyon 1 Bât. Nautibus 43, Boulevard du 11 novembre 1918 69 622 Villeurbanne Cedex France Tél : 04.72.44.83.69 **hamamache.kheddouci@univ-lyon1.fr**
Matériaux	**MATÉRIAUX DE LYON** **http://ed34.universite-lyon.fr** Sec. : Yann DE ORDENANA Tél : 04.72.18.62.44 yann.de-ordenana@ec-lyon.fr	**M. Stéphane BENAYOUN** Ecole Centrale de Lyon Laboratoire LTDS 36 avenue Guy de Collongue 69134 Ecully CEDEX Tél : 04.72.18.64.37 **stephane.benayoun@ec-lyon.fr**
MEGA	**MÉCANIQUE, ÉNERGÉTIQUE, GÉNIE CIVIL, ACOUSTIQUE** **http://edmega.universite-lyon.fr** Sec. : Stéphanie CAUVIN Tél : 04.72.43.71.70 Bâtiment Direction INSA Lyon mega@insa-lyon.fr	**M. Jocelyn BONJOUR** INSA Lyon Laboratoire CETHIL Bâtiment Sadi-Carnot 9, rue de la Physique 69621 Villeurbanne CEDEX **jocelyn.bonjour@insa-lyon.fr**
ScSo	**ScSo*** **https://edsciencessociales.universite-lyon.fr** Sec. : Mélina FAVETON INSA : J.Y. TOUSSAINT Tél : 04.78.69.77.79 melina.faveton@univ-lyon2.fr	**M. Bruno MILLY** Université Lumière Lyon 2 86 Rue Pasteur 69365 Lyon CEDEX 07 **bruno.milly@univ-lyon2.fr**

*ScSo : Histoire, Géographie, Aménagement, Urbanisme, Archéologie, Science politique, Sociologie, Anthropologie

Abstract

Four-dimensional (4D) computed tomography (CT) images are used for the radiotherapy planning of thoracic and upper-abdominal tumors to account for breathing motion. It assumes that the breathing cycle is periodic which is often not the case, especially for patients suffering from respiratory diseases, resulting in artifacts in tomographic images which may impact the radiotherapy. The aim of this thesis is to detect motion in helical CT using data consistency conditions (DCCs). DCCs are mathematical equations characterizing the redundancy in the projection data. They have been developed for several source and detector configurations but the literature is scarce on helical CT with a cylindrical detector which is the most used geometry in 4D CT. The first contribution of this thesis is the development of two approaches to apply DCCs to pairs of cone-beam projections. The first approach resamples two projections onto a virtual detector which rows are parallel to the line connecting the source positions to apply a fan-beam DCC along each row. The second approach computes DCCs in the cylindrical detector coordinates to increase the number of DCCs in a helical acquisition. The second contribution studies the ability of DCCs to locally detect motion. A consistency metric is introduced to account for the effect of the acquisition noise in the DCCs by computing the variance of the DCCs. Lastly, two methods are proposed to detect motion during an acquisition. The first constructs a graph in which the vertices are the projections and two vertices are connected if a DCC can be computed between the projections. The second extracts the respiratory signal from the projections using the consistency metric. All contributions were evaluated using simulated and real data. DCCs allowed the detection of motion for most pairs, but not directly for those whose DCC was heavily impacted by noise where a low-pass filter was applied to enable motion detection.

Resumé

Les images de tomodensitométrie (TDM) quadridimensionnelles (4D) sont utilisées pour la planification de la radiothérapie des tumeurs thoraciques et abdominales supérieures afin de tenir compte des mouvements respiratoires. Cette modalité repose sur l'hypothèse que le cycle respiratoire est périodique, ce qui n'est pas toujours le cas, en particulier pour les patients souffrant de maladies respiratoires, entraînant des artefacts sur les images tomographiques qui peuvent avoir un impact sur la radiothérapie. Le but de cette thèse est de détecter le mouvement en TDM hélicoïdale en utilisant des conditions de cohérence des données (CCD). Les CCD sont des équations mathématiques caractérisant la redondance dans les données de projections. Elles ont été développées pour plusieurs configurations de source et de détecteur, mais la littérature est rare sur la TDM hélicoïdale avec un détecteur cylindrique qui est la géométrie la plus utilisée en TDM 4D. La première contribution de cette thèse propose deux approches pour appliquer les CCD à des paires de projections à faisceau conique. La première approche rééchantillonne deux projections sur un détecteur virtuel dont les lignes sont parallèles à la ligne reliant les positions de source pour appliquer des CCD de faisceau en éventail le long de chaque ligne. La seconde approche calcule les CCD dans les coordonnées du détecteur cylindrique pour augmenter le nombre de CCD dans une acquisition hélicoïdale. La deuxième contribution étudie la capacité des CCD à détecter localement le mouvement. Une mesure de cohérence est introduite pour tenir compte du bruit d'acquisition dans les CCD en calculant la variance des CCD. Enfin, deux méthodes sont proposées pour détecter le mouvement lors d'une acquisition. La première construit un graphe dans lequel les sommets sont les projections et deux sommets sont connectés s'il existe des CCD entre les projections. La seconde extrait le signal respiratoire des projections en utilisant la mesure de cohérence. Toutes les contributions sont évaluées à l'aide de données simulées et réelles. Les CCD permettent la détection de mouvement pour la plupart des paires, mais pas directement pour celles dont les CCD sont fortement impactées par le bruit et pour lesquelles un filtre passe-bas a été appliqué afin de rendre la détection possible.

Contents

Abstract **v**

Résumé **vii**

Content **xi**

List of figures **xvii**

List of tables **xix**

List of Acronyms **xxi**

Introduction **1**

I State of the art **3**

1 X-ray Computed Tomography **5**
1.1 X-ray physics . . . 5
1.1.1 X-ray source . . . 5
1.1.2 X-ray/matter interactions . . . 7
1.1.3 Attenuation law . . . 8
1.1.4 X-ray detection . . . 8
1.2 X-ray Computed Tomography . . . 9
1.2.1 Parallel beam . . . 9
1.2.2 Divergent beam . . . 10
1.2.3 An example: 2D fan-beam with a circular source trajectory . . . 10
1.3 Helical CT . . . 10
1.3.1 Generalities . . . 10
1.3.2 Geometry and line integrals . . . 12
1.3.3 Basics of reconstruction in helical CT . . . 13
1.4 Conclusion . . . 17

2 Breathing motion in Computed Tomography **19**
2.1 Motion and radiotherapy planning . . . 19
2.1.1 Respiratory motion . . . 19
2.1.2 Impact of motion on conventional radiotherapy planning . . . 20
2.1.3 Motion encompassing for treatment planning in 4D radiotherapy . . . 21
2.2 4D helical CT . . . 23
2.2.1 Principle and Data sufficiency condition . . . 23
2.2.2 Reconstruction algorithm in 4D helical CT . . . 23
2.2.3 Limitations . . . 25
2.2.4 Possible improvements . . . 26

2.3 Conclusion . . . 26

3 Data consistency conditions **27**
3.1 Data consistency conditions with the 2D parallel geometry . . . 27
3.1.1 A first intuition . . . 27
3.1.2 Helgason-Ludwig consistency conditions . . . 28
3.2 Fan-beam data consistency conditions . . . 28
3.2.1 Complete fan-beam consistency conditions for sources on a line . . . 29
3.2.2 The zeroth order case . . . 29
3.3 Cone-beam consistency conditions . . . 30
3.3.1 From fan-beam to cone-beam consistency conditions . . . 30
3.3.2 Cone-beam consistency conditions for sources on a plane . . . 32
3.3.3 Cone-beam consistency conditions for sources on a circular trajectory 32
3.3.4 Grangeat-based consistency conditions . . . 33
3.4 Review of DCC applications . . . 34
3.4.1 Correction of physics- and system- based artifacts in CT . . . 35
3.4.2 Application to motion detection and correction in CT . . . 35
3.5 Conclusion . . . 37

II Contributions **39**

4 Data Consistency conditions in helical CT **41**
4.1 Pair-wise geometry in helical CT . . . 41
4.2 Pair-wise cone-beam DCCs using rebinning . . . 41
4.2.1 Rebinning from cylindrical to virtual flat detector . . . 42
4.2.2 Expression of the DCC . . . 47
4.2.3 Discretization of the moment . . . 47
4.2.4 Applicability conditions . . . 47
4.2.5 Consistency metric . . . 49
4.3 Pair-wise cone-beam DCCs on cylindrical detectors . . . 49
4.3.1 Definition of the DCC planes . . . 49
4.3.2 Expression of the DCC . . . 51
4.3.3 Discretization of the moment . . . 54
4.3.4 Applicability conditions . . . 57
4.3.5 Consistency metric . . . 58
4.4 Numerical validation of DCCs . . . 58
4.4.1 Datasets . . . 58
4.4.2 Experiment . . . 59
4.4.3 Results . . . 59
4.4.4 Discussion . . . 67
4.5 Conclusion . . . 71

5 Local motion detection in helical CT using data consistency conditions **73**
5.1 Cone-beam pair wise DCCs in helical CT . . . 73
5.2 Noise-aware consistency metric . . . 74
5.2.1 Noise model . . . 74
5.2.2 The consistency metric . . . 76
5.3 Datasets . . . 79
5.3.1 Numerical phantom . . . 79
5.3.2 Mechanical phantom . . . 79
5.3.3 Patient data . . . 80
5.4 Results . . . 81

5.4.1 Numerical phantom . . . 81
5.4.2 Phantom data . . . 83
5.4.3 Patient data . . . 85
5.5 Discussion . . . 87
5.6 Conclusion . . . 88

6 Global motion detection in helical CT using data consistency conditions 89
6.1 Cone-beam pair-wise DCCs in helical CT . . . 89
6.2 Motion detection in helical CT using a graph approach . . . 89
6.2.1 Theory . . . 89
6.2.2 Datasets . . . 91
6.2.3 Results . . . 92
6.2.4 Discussion . . . 99
6.3 Extraction of the respiratory signal using DCCs . . . 100
6.3.1 Experimental observations . . . 100
6.3.2 Extraction of the respiratory signal . . . 102
6.3.3 Results . . . 102
6.3.4 Discussion . . . 105
6.4 Conclusion . . . 106

Conclusions and prospects 107

Résumé étendu 111

Appendix A: Scientific contributions 131

Bibliography 133

List of Figures

1.1 Illustration of the generation of x-rays. 5
1.2 X-ray spectrum generated from an x-ray tube with a tungsten target and a tube voltage of 90 kV. Image from [Bushberg et al., 2011] 6
1.3 Illustration of the effect of the bow-tie on the dose distribution in the patient. Image adapted from [Bushberg et al., 2011]. 7
1.4 Illustration of x-ray/matter interactions. 8
1.5 Illustration of the 2D parallel geometry for the definition of parallel projections. 9
1.6 Illustration of the divergent beam transform Equation 1.6 of a 2D object with sources on a circular trajectory. 11
1.7 Picture of the SOMATOM go.Sim Siemens CT scanner at the anti-cancer center Léon Bérard in Lyon. 11
1.8 Illustration of the helical acquisition mode. 12
1.9 Illustration of the cone-beam geometry with helical source trajectory. 13
1.10 Illustration of the CG algorithm and Tikhonov regularization. 16

2.1 Example of incorrect volume reconstruction because of motion during a conventional CT scan. 20
2.2 Illustration of slow and 4D CT. 22
2.3 Illustration of the RCCT algorithm using phase-based sorting. 24
2.4 Respiratory monitoring devices. 24
2.5 Illustration of phase-based (a) and amplitude-based (b) sorting. 25
2.6 Example of 4D CT artifacts from 3 different patients acquired with the somatom go.Sim Siemens CT scan. 25

3.1 Illustration of two parallel beams. 28
3.2 Illustration of the fan-beam geometry for sources on a line. 29
3.3 Illustration of the rebinning process of a pair of cone-beam projections with planar detector. 31
3.4 Illustration of the cone-beam geometry with sources on a plane for the description of the complete cone-beam DCCs. 32
3.5 3D illustration of the cone-beam geometry for planar detector and circular trajectory for the description of the cone-beam DCCs with sources on a circular trajectory. 33
3.6 Illustration of a Grangeat-based DCCs for cone-beam projections with linear trajectory. 34

4.1 3D illustration of the pair-wise geometry in helical CT. 42
4.2 Illustration of the virtual detector frame and the backprojection plane for a pair of projections. 43
4.3 Illustration of the definition of the intersection $\mathcal{L}_\lambda(\gamma, v)$ with the backprojection plane Π_{BP}. 44
4.4 Illustration of the definition of the virtual detector boundaries. 44

4.5 Illustration of the final computation of the virtual detector for a pair of projections. 46
4.6 Illustration of the mapping of a point $\boldsymbol{a} = (x_a, y_a, z_a)$ on the backprojection plane Π_{BP} to the corresponding cylindrical detector pixel $\boldsymbol{p}_\lambda(\gamma_a, v_a)$. 46
4.7 Illustration of the FOV intersection condition for the application of the rebinning approach. The source positions are $\boldsymbol{s}_\lambda$ and $\boldsymbol{s}_{\lambda'}$. R_{Fov} and R are respectively the FOV radius and the helical trajectory radius. 48
4.8 Illustration of an insufficient overlap between two backprojections. 48
4.9 Illustration of the definition of $\bar{\lambda}$ from two source positions $\boldsymbol{s}_\lambda$ and $\boldsymbol{s}_{\lambda'}$. . . . 50
4.10 3D illustration of the cone-beam pair-wise geometry. The baseline $\mathcal{B}_{\lambda,\lambda'}$ is defined by the source positions $\boldsymbol{s}_\lambda$ and $\boldsymbol{s}_{\lambda'}$ (with $\lambda < \lambda'$ in this case). The intersection of the reference plane $\Pi_{\lambda,\lambda'}$ with the two detectors defines the two curves $\mathcal{C}_{\lambda,\lambda'}$ and $\mathcal{C}_{\lambda',\lambda}$ (thick dotted lines). The intersection of a plane $\Pi_{\boldsymbol{\tau}}$ with the two detectors defines the two curves $\mathcal{C}_{\boldsymbol{\tau}}$ and $\mathcal{C}_{\boldsymbol{\tau}'}$ with $\boldsymbol{\tau} = (\lambda, \lambda', \beta)$ and $\boldsymbol{\tau}' = (\lambda', \lambda, \beta)$ (thick continuous lines). The dotted limits of the detectors are below the reference plane $\Pi_{\lambda,\lambda'}$ and the dashed ones are below the plane $\Pi_{\boldsymbol{\tau}}$. 51
4.11 Geometric illustration in the plane $\Pi_{\boldsymbol{\tau}}$ of the angle ϕ between $\boldsymbol{c}_{\boldsymbol{\tau}}$ and the line defined by $\boldsymbol{s}_\lambda$ and $\boldsymbol{p}_\lambda(\gamma, v_{\boldsymbol{\tau}})$. 52
4.12 Illustration of the first order approximation with the function $1/\sin(\gamma^s_{\lambda,\lambda'} - \gamma)$. 55
4.13 Presentation of the phantoms used for the validation of the DCC. 58
4.14 FBDCCs computed with the rebinning approach applied to a pair of projections largely satisfying the FOV condition. 60
4.15 2D view of a pair geometry that largely satisfies the FOV condition. The two fans are plotted in yellow and purple and the virtual detector is plotted in red. 60
4.16 Illustration of the backprojection for a pair largely satisfying the FOV condition. The backprojections are the dotted colored lines and the virtual detector is the continuous red line. 60
4.17 FBDCCs computed with the rebinning approach applied to a pair of projections whose baseline is tangent to the FOV. 61
4.18 2D view of a pair geometry whose baseline is tangent to the FOV. The two fans are plotted in yellow and purple and the virtual detector in red. 61
4.19 Illustration of the backprojection for a pair whose baseline is tangent to the FOV. The backprojections are the dotted colored lines and the virtual detector is the continuous red line. 61
4.20 FBDCCs computed with the direct approach applied to a pair of simulated projections whose baseline does not intersect the FOV. 62
4.21 FBDCCs computed with the direct approach applied to a pair of simulated projections whose baseline intersects the FOV. The singular point is located in a spatially smooth region of the two cone-beam projections. 62
4.22 FBDCCs computed with the direct approach applied to a pair of simulated projections whose baseline intersects the FOV. The singular point is located close to steep spatial gradients of the two cone-beam projections. 63
4.23 FBDCCs computed with the rebinning approach applied to a pair of noisy projections largely satisfying the FOV condition. 63
4.24 FBDCCs computed with the rebinning approach applied to a pair of noisy projections whose baseline is tangent to the FOV. 64
4.25 FBDCCs computed with the direct approach applied to a pair of noisy projections whose baseline does not intersect the FOV. 64

4.26 FBDCCs computed with the direct approach applied to a pair of noisy projections whose baseline intersects the FOV. The singular point is located in a spatially smooth region of the two cone-beam projections. 65
4.27 FBDCCs computed with the direct approach applied to a pair of noisy projections whose baseline intersects the FOV. The singular point is located close to steep spatial gradients of the two cone-beam projections. 65
4.28 FBDCCs computed with the rebinning approach applied to a pair of projections of the mechanical phantom (real data) largely satisfying the FOV condition. 66
4.29 FBDCCs computed with the rebinning approach applied to a pair of projections of the mechanical phantom (real data) whose baseline is tangent to the FOV. 66
4.30 FBDCCs computed with the direct approach applied to a pair of projections of the mechanical phantom (real data) whose baseline does not intersect the FOV. 67
4.31 FBDCCs computed with the direct approach applied to a pair of projections of the mechanical phantom (real data) whose baseline intersects the FOV. . 68
4.32 Plot of the three kernels used in the numerical integration of the FBDCC with the direct approach for the pair in Figure 4.21. 69
4.33 Computation of the FBDCC for a pair of simulated projection with a ten times thinner sampling than Figure 4.22. The singular point is close to the spatial gradients of both projections. 69
4.34 FBDCC of the pair Figure 4.22 computed with the direct approach and the Hilbert kernel $h_{0.2}^{\mathrm{Rect}}$. 70

5.1 Computation of the different variables for the estimation of the proportionality coefficient m_Z. 75
5.2 Coronal (top) and axial (bottom) slices of the three CT images reconstructed from the projections used in this study: Forbild phantom (simulated, left), CIRS phantom (real data, center) and clinical data (real data, right). The two extreme positions are superimposed in green (end-exhale) and purple (end-inhale). 79
5.3 Workflow for the correction of truncated sinogram. 80
5.4 Validation of the noise approximation. Theoretical (black line) and experimental (dotted light-gray line) standard deviations of the mean moments difference, experimental standard deviation of the mean moments absolute difference (dash-dotted gray line) for all eligible pairs $(\boldsymbol{s}_\lambda, \boldsymbol{s}_{\lambda'})$ computed from the fixed reference projection $\lambda = 0$. 81
5.5 Validation of the noise approximation. Theoretical (black line) and batch (dotted light-gray line) standard deviations of the mean moments difference, batch standard deviation of the mean moments absolute difference (dash-dotted gray line) for all eligible pairs $(\boldsymbol{s}_\lambda, \boldsymbol{s}_{\lambda'})$ computed from the fixed reference projection $\lambda = 90°$. 82
5.6 Consistency metric $E_{\lambda,\lambda'}$ (top row) and its parts (bottom row) for all pairs (λ, λ') with noisy projections. 83
5.7 Consistency metric $E_{\lambda,\lambda'}$ computed from a reference projection at $\lambda = 36 \times 360° + 0.14°$ acquired when the tumor was at an extreme position of the breathing cycle. 84
5.8 Consistency metric $E_{\lambda,\lambda'}$ computed from a reference projection at $\lambda = 51 \times 360° + 169.83°$ acquired when the tumor was at an intermediate position of the breathing cycle. 84

5.9 Consistency metric (top) and moving average (bottom) for patient 1 set of projections using a reference projection at $\lambda = 154 \times 360° + 0.14°$ at end-inhale. 85
5.10 Consistency metric (top) and moving average (bottom) for patient 1 set of projections using a reference projection at $\lambda = 159 \times 360° + 0.14°$ at end-exhale. 86
5.11 Consistency metric (top) and moving average (bottom) for patient 1 set of projections using a reference projection at $\lambda = 171 \times 360° + 180°$ at an intermediate position of the respiratory cycle. 86
5.12 Consistency metric (top) and moving average (bottom) for patient 2 set of projections using a reference projection at $\lambda = 131 \times 360° + 322.56°$ at an intermediate position of the respiratory cycle. 87

6.1 Pairs used in the graph approach computed for six source positions. 90
6.2 Motion of the phantom lungs during the acquisition. The motion model is taken from [Bergner and Kachelriess, 2009]. 91
6.3 3D frames of the 4D CT image of patient 2. The ten images (0% to 90%) correspond to the ten phases of the respiratory cycle. A tumor is located at the axial displacement $z = -75$ mm and a strong artifact is visible around $z = -50$ mm. 92
6.4 3D frames of the 4D CT image of patient 2. The ten images (0% to 90%) correspond to the ten phases of the respiratory cycle. A tumor is located at the axial displacement $z = -75$ mm and a no artifact is visible around $z = -50$ mm. 93
6.5 Graph approach applied to a simulated conventional CT. From left to right: sum of the DCCs along the shortest path from the projection at $t_0 = 0$ s (red circle); length of the shortest path; sum of the DCC along the shortest path normalized by the shortest path length. 93
6.6 Graph approach applied to a simulated conventional CT. From left to right: sum of the DCCs along the shortest path from the projection at $t_4 = 8$ s (red circle); length of the shortest path; sum of the DCC along the shortest path normalized by the shortest path length. 94
6.7 Graph approach applied to a simulated 4D CT. 95
6.8 Graph approach applied to the first 4D CT acquisition of patient 2 from the reference projections at $z = -100$ mm. 96
6.9 Graph approach applied to the second 4D CT acquisition of patient 2 from the reference projections at z=−100 mm. 97
6.10 Graph approach applied to the second 4D CT acquisition of patient 2 from the reference projections at $z = 50$ mm. 98
6.11 Signed consistency metric (top) and its moving average (bottom) the projections of patient 1 using a reference projection $\lambda = 154 \times 360° + 0.14°$ at end-inhale. 100
6.12 Signed consistency metric (top) and its moving average (bottom) for the projections of patient 1 using a reference projection $\lambda = 159 \times 360° + 360° + 0.14°$ at end-exhale. 101
6.13 Signed consistency metric (top) and its moving average (bottom) for patient 1's set of projections using a reference projection $\lambda = 171 \times 360° + 180.14°$ at an intermediate position of the respiratory cycle. 101
6.14 Adjustment of the three moving average from the Figures 6.11 (blue line), 6.12 (orange line), and 6.11 (green line) computed with all pairs. 102
6.15 Extraction of the respiratory signal from acquisition 1 of the patient with algorithm 1 using the mean M_λ of the metrics (continuous red line). The visually estimated phase corresponds to the dashed black line. 103

6.16 Extraction of the respiratory signal from acquisition 2 of the patient with algorithm 1 using the mean M_λ of the metrics (continuous red line). The visually estimated phase corresponds to the dashed black line. 104
6.17 Extraction of the respiratory signal from acquisition 1 of the patient with algorithm 1 using the centered moving average. The visually estimated phase corresponds to the dashed black line. 104
6.18 Extraction of the respiratory signal from acquisition 2 of the patient with algorithm 1 using the centered moving average. The visually estimated phase corresponds to the dashed black line. 105

List of Tables

2.1 4D acquisition protocols proposed by Siemens for the go.Sim CT scan. . . . 23

4.1 Errors $E^{Virt}_{\lambda,\lambda'}$ (Table 4.1a) and $E^{Real}_{\lambda,\lambda'}$ (Table 4.1b) (stated as percentage) computed with the rebinning approach or the direct approach for various pairs of cone-beam projections from simulated and real data. 59

List of Acronyms

2D	two-dimensional
4D	four-dimensional
CT	computed Tomography
DCC	data consistency condition
CG	conjugated gradient
RCCT	respiratory-correlated computed tomography
3D	three-dimensional
FOV	field-of-view
FBDCC	zeroth order of the fan-beam data consistency conditions
RHS	right-hand side
1D	one-dimensional
FDK	Feldkamp,David and Kress
MR	magnetic Resonance
SI	superior-inferior
AP	antero-posterior
GTV	gross tumor volume
DSC	data sufficiency condition
LHS	left-hand side
SPECT	single photon emission computed tomography

Introduction

Lung cancer is one of the most common cancer in the world and was the deadliest cancer in 2020 with 1.8 million deaths [World Health Organization, 2022]. The first choice of treatment is surgery, during which the cancerous cells are removed from the body, but it is not always possible. Alternatively, radiation therapy, or radiotherapy, can be used to kill cancerous cells by irradiating them with high energy x-rays. One major difficulty in the radiotherapy of lung cancers is the breathing of patients. It induces lung and tumor motion which are not accounted for in conventional radiotherapy. Four-dimensional (4D) radiotherapy has emerged to estimate tumor motion and deal with it during radiation delivery. It is mostly based on 4D computed tomography (CT) images.

X-ray projections correspond to the images of x-ray attenuation by the body. During a CT scan, several projections of the patient are acquired under different angles. The projections are processed to obtain a CT image of the patient, which is called tomographic reconstruction. During an acquisition, the patient is assumed to remain still. If the patient breathes freely, it creates artifacts on CT images because the breathing motion is not accounted for in the conventional reconstruction algorithms. 4D CT accounts for breathing motion by synchronizing the projections with a breathing signal acquired simultaneously. The breathing signal is divided into phases and subsets of projections are formed accordingly. Each subset, corresponding to a phase of the respiratory cycle, is reconstructed separately with conventional reconstruction algorithms, and the corresponding 3D CT images are grouped to obtain a 4D CT image of the patient at the different phases of the respiratory cycle. This algorithm, called respiratory-correlated CT (RCCT), assumes that the breathing motion is cyclic, which is not always the case, especially for patients suffering from respiratory diseases. Therefore, motion artifacts may degrade the quality of 4D CT images. Moreover, the acquired breathing signal refers to the external motion of the patient and may differ from the internal motion of the tumor, leading to an incorrect reconstruction of the tumor.

It is necessary to clearly identify if two or more projections belong to the same respiratory phase to limit artifacts on the tomographic images, i.e. to assess the consistency between two projections. Data consistency conditions (DCCs) are a mathematical tool that characterize the redundancy in x-ray projections and evaluates the consistency between two projections. DCCs have been proposed for various acquisition systems, but not for helical CT which is the geometry of most 4D CT scanners.

The objective of this thesis is to detect motion in helical CT using DCCs with an application to the detection of unexpected or irregular motion in 4D CT images used for the radiotherapy planning of lung cancers. In the first chapter, the basics of x-ray physics and x-ray CT are introduced with a particular focus on helical CT. In the second chapter, the impact of breathing motion on conventional radiotherapy and CT is developed and the basics of 4D CT along with its current limitations are presented. In the third chapter, DCCs are first illustrated with an example in parallel geometry before introducing DCCs for various acquisition geometries. An extensive review of the DCCs applications is made with a focus on motion detection and correction.

The contributions of this thesis are presented in Chapters 4 to 6. In Chapter 4, we

propose two approaches to apply DCCs to helical CT and state the applicability conditions of those DCCs. In Chapter 5, a local motion detection method based on consistency conditions, taking into account the impact of noise on the DCCs, is presented. In chapter 6, two global motion detection methods are introduced: the first assesses the consistency of one projection with the other projections in the acquisition; the second method extracts the respiratory signal directly from the projections. The DCCs implementations and the motion detection methods are both evaluated on simulated and real data acquired on the CT scanner of the radiotherapy department of the anti-cancer center Leon Bérard in Lyon.

Part I

State of the art

Chapter 1

X-ray Computed Tomography

In this chapter, we explain the fundamentals of x-ray CT imaging. CT images are obtained from the attenuation of x-rays by a specific object. We introduce x-ray production and their interactions with matter. Then, we present the link between the attenuation of x-rays and CT. Finally, we describe helical CT, a widely used acquisition technique and explain how CT images are reconstructed from helical acquisitions.

1.1 X-ray physics

X-rays are electromagnetic waves discovered in 1895 by the German scientist Wilhem Röntgen (1845-1923). Their characteristics and properties are explained by the wave-particle duality. As waves, they are characterized by a wavelength (from 10^{-8} to 10^{-12} m), and as particles, called photons, they are characterized by an energy, expressed in keV.

In this section, we give a brief overview of the physics of x-rays. The presented elements are mostly from [Bushberg et al., 2011] and [Beutel et al., 2000] which the reader can refer to for more details.

1.1.1 X-ray source

1.1.1.1 X-ray production

X-rays result from the interaction between electrons and matter. They are produced with an x-ray tube: electrons, contained in a filament (cathode), are accelerated towards a target (anode) using very high voltage (between 40 kV and 150 kV for diagnostic imaging). The most common material for the filament and the target is tungsten. At their impact with the target, electrons interact with matter, creating two types of radiation: Bremsstrahlung radiation and characteristic x-rays, illustrated in Figure 1.1.

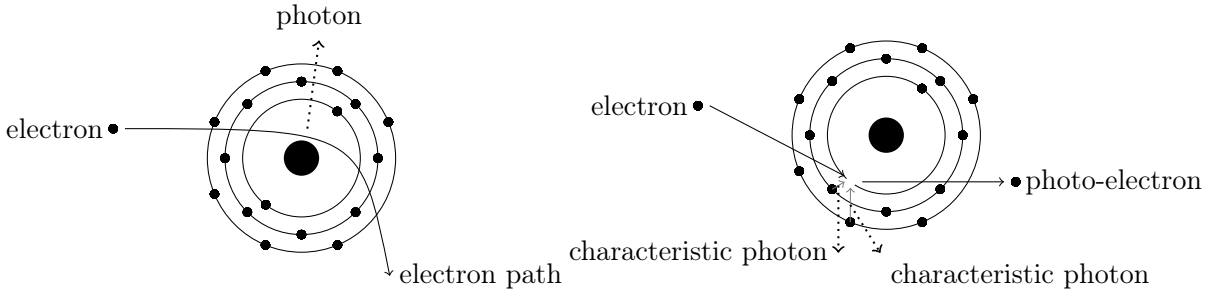

(a) Bremsstrahlung x-ray (b) Characteristic x-ray

Figure 1.1: Illustration of the generation of x-rays.

Bremsstrahlung x-rays
When an electron interacts with the Coulomb field of the target atom's nucleus, it is decelerated. The Bremsstrahlung radiation is created from that deceleration. The closer the electron gets to the nucleus, the higher the deceleration and the higher the energy of the resulting radiation. This interaction is illustrated in Figure 1.1a.

Characteristic x-rays
An accelerated electron can also eject an atomic electron from the electronic shell of the target atoms. To stabilize the atom, an electron from an outer shell fills the vacant position of the inner shell generating in some cases a characteristic radiation, also called fluorescence. This interaction is illustrated in Figure 1.1b.

All electrons are not decelerated identically and photons exiting the x-ray tube do not have identical energies. In other words, the energy distribution of the x-ray beam exiting an x-ray tube is poly-energetic. It is composed of a continuous component from the Bremsstrahlung radiations and a discrete component from fluorescence. This phenomenon can be visualized with the x-ray spectrum of an x-ray tube as shown in Figure 1.2.

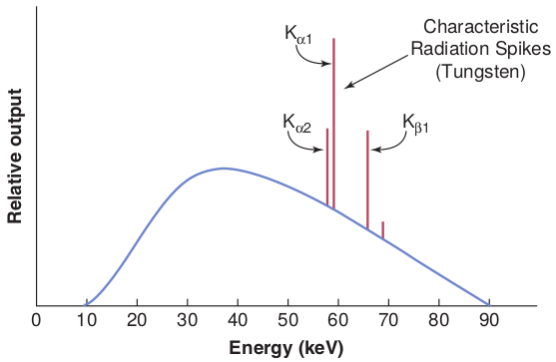

Figure 1.2: X-ray spectrum generated from an x-ray tube with a tungsten target and a tube voltage of 90 kV. The Bremsstrahlung component is plotted in blue. The characteristic x-rays, denoted $K_{\alpha 1}$, $K_{\alpha 2}$, $K_{\beta 1}$, are plotted in red. Image from [Bushberg et al., 2011].

1.1.1.2 X-ray modulation

The many choices of material target, voltage for the acceleration of the electrons and tube current make x-rays an important technology for medical imaging. The link between the initial x-ray energy fluence I_0, the tube current i and the tube voltage U is

$$I_0 = miZU^2 \tag{1.1}$$

where Z is the atomic number of the target and m is a proportionality constant characterizing the probability of x-ray production. The beam exiting the x-ray tube is usually modulated by a filter to remove low energy photons. A common filter is the *bow-tie* filter which is placed at the exit of the tube. The objective of this filter is two-fold: first, it reduces the beam energy fluence on the borders of the detector as those photons are generally less attenuated because they pass through thinner thicknesses of the patient than the photons hitting the center of the detector; secondly, it homogenizes the dose (quantity of received radiation) distribution in the patient.

In practice, the voltage and the filters are pre-determined to conform the radiation quality of the beam to medical imaging standards. The tube current can be modulated depending on the position of the x-ray tube with respect to the patient. For instance, large patients require a higher tube current to compensate for the strong attenuation.

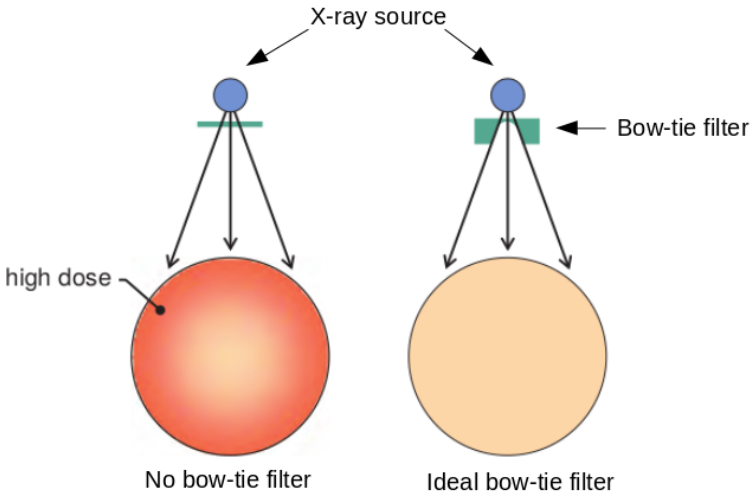

Figure 1.3: Illustration of the effect of the bow-tie on the dose distribution in the patient. Image adapted from [Bushberg et al., 2011]. Without a bow-tie filter, the dose received by the patient is higher at the edges of the body than in its center (left plot). Adding a bow-tie filter attenuates the rays at the borders of the beam and homogenizes the dose distribution in the patient (right plot).

1.1.2 X-ray/matter interactions

Passing through an object, x-rays may or may not interact with matter. There are four major interactions: the photoelectric absorption, Compton scattering, Rayleigh scattering, pair and triplet production, illustrated in Figure 1.4.

Photoelectric absorption
The photoelectric absorption corresponds to a total absorption of the incident photon by an atom. The entire energy of the photon is used to eject an electron from the inner electronic shell of an atom. This ejected electron, called photo-electron, can then ionize surrounding atoms. As previously described, an electronic re-arrangement of the shells occurs to stabilize the atom which may lead to the emission of characteristic x-rays. The secondary radiations having low energies, they are rapidly attenuated.

Compton scattering
In Compton scattering, the incident photon interacts with an electron from the outer shell of an atom or a free electron in the medium, one part of its energy is transferred to the atom and ejects the electron. The other part creates a scattered photon of lower energy than the incident photon. Photons with low energy are mostly back-scattered while photons with high energy are more likely forward-scattered.

Rayleigh scattering
Rayleigh scattering occurs when the incident photon interacts with the magnetic field of an electron from the electronic shells of an atom and is deviated. The photon retains its energy and the atom is not ionized.

Pair and triplet production
Pair production corresponds to the formation of an ionic pair (one electron and one positron) resulting from the interaction between an incident photon (which is totally absorbed) and the electric field of an atom's nucleus. Triplet production occurs when the

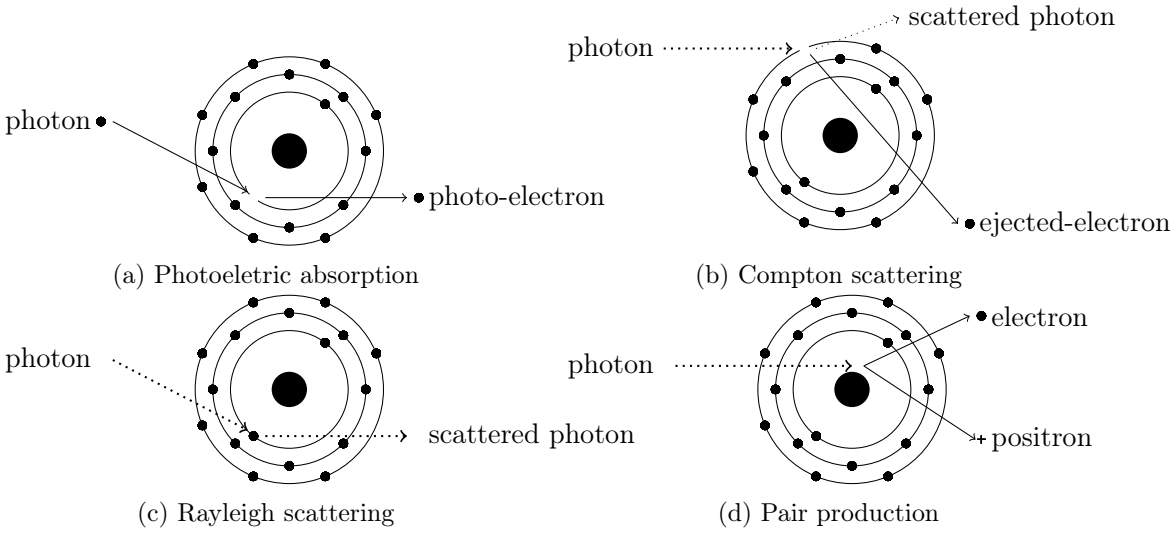

Figure 1.4: Illustration of x-ray/matter interactions.

incident photon interacts with the electric field of an electron from the inner electronic shell of an atom. The electron is ejected from the atom and an ionic pair emerges. Those two interactions only take place for high energy photons (over 1 MeV i.e. the sum of the mass at rest of the electron and the positron) and do not arise in medical imaging. In both interactions, the resulting positron rapidly loses its kinetic energy and merges with any free electron. From this merge, two photons (511 keV each) arise in opposite directions. This phenomenon is called annihilation radiation.

In transmission imaging, the photons are mainly absorbed (photoelectric effect) or scattered (Rayleigh and Compton scatterings) when going through and interacting with the human body or scanned object.

1.1.3 Attenuation law

Attenuation can be qualified as the quantity of interactions that photons encounter when crossing a material. The attenuation power of a material is given by its attenuation coefficient, expressed in cm^{-1}. In medical imaging for example, the body of the patient is made of different materials (water, bones, muscles...), each with its own attenuation coefficient.

Let $\boldsymbol{x}$ be a point in space. The attenuation coefficient at this point is noted $f(\boldsymbol{x})$. The final energy fluence I of a mono-energetic photon beam with initial energy fluence I_0 after traveling along the line $\mathcal{L}$ and going through the patient, characterized by its attenuation function f, is given by the *Beer-Lambert* law:

$$I = I_0 \exp\left(-\int_{\mathcal{L}} f(\boldsymbol{x})\mathrm{d}\boldsymbol{x}\right). \tag{1.2}$$

The hypothesis of mono-energetic photons is kept throughout the entire thesis.

1.1.4 X-ray detection

The final energy fluence of the beam is measured with x-ray detectors. In conventional CT, the detector, called energy-integrating, measures the total energy received by a detector pixel. Recently, a novel type of detector, called photon-counting, counting each photon and discriminating it depending on its energy, emerged. Using the various energy

bins of the detected beam, images highlighting the materials composing the object can be reconstructed from a single acquisition. For example, it is possible to obtain separate reconstructions of water-like materials (soft tissues) and bones in photon-counting CT.

The measurements of the received energy can be done directly or indirectly. Direct detectors measure the electrical charge resulting from the ionization of the detector's atoms by x-rays. Indirect detectors first convert x-rays to visible light with a scintillator. The distribution of the generated visible light is then measured with a photodetector to obtain an image.

In the rest of the thesis, the detector is assumed perfect, i.e. there is no dark current or electronic noise.

1.2 X-ray Computed Tomography

The aim of CT is to recover $f(\boldsymbol{x})$ from the detected intensities. To do so, Equation 1.2 is re-written as

$$-\ln\left(\frac{I}{I_0}\right) = \int_{\mathcal{L}} f(\boldsymbol{x})\mathrm{d}\boldsymbol{x}. \tag{1.3}$$

The right-hand side (RHS) of Equation 1.3 is called a line integral and is the starting point of CT. The definition of line integrals depends on the acquisition geometry of the scanner, i.e. the x-ray source trajectory (which can be linear, circular, helical, etc.) and the shape of the x-ray beam (which can be parallel or divergent).

We present in this section the expression of line integrals for parallel and divergent beams independently of the source trajectory. We note $\mathbb{R}^n$ and S^{n-1} the n-dimensional real vector space and its corresponding set of unit-vectors, with $n \in \{2, 3\}$.

1.2.1 Parallel beam

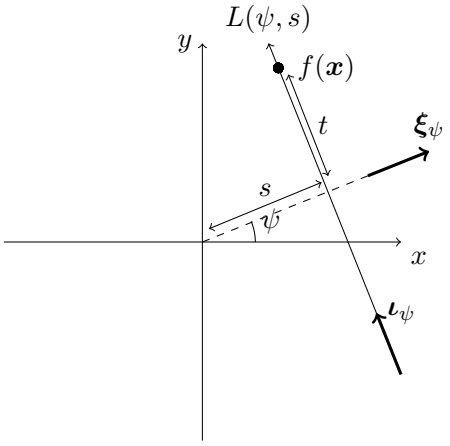

Figure 1.5: Illustration of the 2D parallel geometry for the definition of parallel projections.

In this part, we consider the 2D space $\mathbb{R}^2$ with the coordinate system $(\boldsymbol{e}_x, \boldsymbol{e}_y)$, thus we have $f(\boldsymbol{x}) = f(x, y)$. The source sends a beam where the rays are parallel to each other. Each ray of the beam defines a line $\mathcal{L}(\psi, s)$ where $\psi \in [0, \pi)$ is the angle between the line's perpendicular and the x-axis and $s \in \mathbb{R}$ is the distance between $\mathcal{L}$ and the origin of the system as shown in Figure 1.5. The direction of $\mathcal{L}(\psi, s)$ and its perpendicular are respectively given by $\boldsymbol{\iota}_\psi = (-\sin\psi, \cos\psi)$ and $\boldsymbol{\xi}_\psi = (\cos\psi, \sin\psi)$. The corresponding line integral is written as

$$\int_{\mathcal{L}(\psi,s)} f(\boldsymbol{x})\mathrm{d}\boldsymbol{x} = \int_{-\infty}^{\infty} f(s\boldsymbol{\xi}_\psi + t\boldsymbol{\iota}_\psi)\mathrm{d}t = p(\psi, s). \tag{1.4}$$

For a given ψ, the set of line integrals $p(\psi, .)$ is called a *projection*. From a mathematical point of view, p is called the *Radon transform* of f

$$\mathcal{R}f(\psi, s) = p(\psi, s). \tag{1.5}$$

1.2.2 Divergent beam

In this part, both $\mathbb{R}^2$ and $\mathbb{R}^3$ are considered. We denote $\boldsymbol{s}_\lambda \in \mathbb{R}^n$, with $n \in \{2, 3\}$, the source position where λ is a parameter characterizing the position of the source along its trajectory. We consider an x-ray, emitted from the source position $\boldsymbol{s}_\lambda$, in the direction $\boldsymbol{\theta} \in S^{n-1}$, with $n \in \{2, 3\}$. The corresponding line integral is

$$\mathcal{D}f(\lambda, \boldsymbol{\theta}) = \int_0^\infty f\left(\boldsymbol{s}_\lambda + t\boldsymbol{\theta}\right) \mathrm{d}t \tag{1.6}$$

where $\mathcal{D}$ is the divergent beam operator that associates f to its set of line integrals.

In general, the expression of $\boldsymbol{s}_\lambda$ depends on the source trajectory. Typically, if the source moves along a linear trajectory, λ is taken along an axis of reference and is defined in $\mathbb{R}$. If the source follows a circular trajectory, λ is an angle defined in $[0, 2\pi)$. When the trajectory is an helix, λ is also an angle defined in $n_{rot} \times [0, 2\pi)$, with n_{rot} the number of rotations in the acquisition, and the axial displacement of the source is proportional to λ. The expression of $\boldsymbol{\theta}$ depends on the source trajectory and the detector type. In the 2D case, called *fan-beam*, $\boldsymbol{\theta}$ is defined as the angle between a ray and a specified reference axis (see Figure 1.6a). In the 3D case, called *cone-beam*, $\boldsymbol{\theta}$ is defined with two parameters, e.g., one angular and one axial parameter (see Figure 1.9).

1.2.3 An example: 2D fan-beam with a circular source trajectory

To illustrate the divergent beam transform, let us consider the 2D object shown in Figure 1.6b. The coordinate system is $(\boldsymbol{e}_x, \boldsymbol{e}_y)$ and we have $f(\boldsymbol{x}) = f(x, y)$. In order to perform the acquisition of this object, the x-ray source follows a circular trajectory, such that $\boldsymbol{s}_\lambda = (R\cos\lambda, R\sin\lambda)$ where λ is an angle defined between 0 and 2π, and R is the trajectory radius as drawn in Figure 1.6a. The vector $\boldsymbol{\theta} = (-\cos(\theta - \lambda), \sin(\theta - \lambda)) \in S^1$ characterizes the direction of one ray within the fan beam as shown in Figure 1.6a. The sinogram, shown in Figure 1.6c, is obtained by plotting the projection values as a function of the acquisition angle λ and the fan-angle θ. The 1D fan-beam projection of the object acquired at angle $\lambda = 45°$ is plotted in Figure 1.6d.

1.3 Helical CT

In this section, we introduce the helical geometry, the main geometry considered in this thesis, and briefly describe the main categories of reconstruction algorithms for helical CT.

1.3.1 Generalities

Throughout this thesis, we apply our methodology to real data acquired with a daily used CT scanner in the radiotherapy department of the anti-cancer center Léon Bérard in Lyon: the SOMATOM go.Sim CT scan from Siemens Healthcare. This scanner is made of a rotation system, called gantry, including the x-ray source and the detector. The patient is placed on a table between the source and the detector. The gantry rotates around the patient's table which is simultaneously moving axially through the gantry. From the patient's point of view, the x-ray source follows a helical trajectory as illustrated in Figure 1.8. This acquisition mode is called helical or spiral CT and was introduced

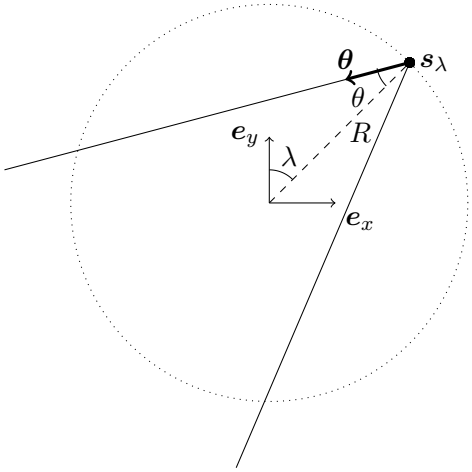

(a) Illustration of the 2D circular geometry.

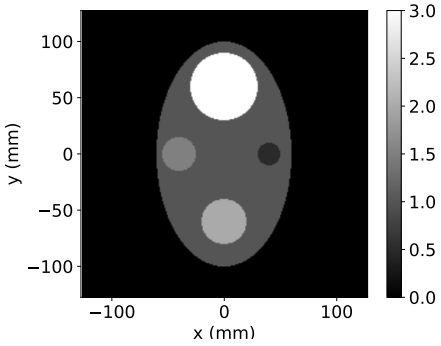

(b) 2D object made of water with various attenuation coefficients (from 0.5 to 3 cm^{-1}).

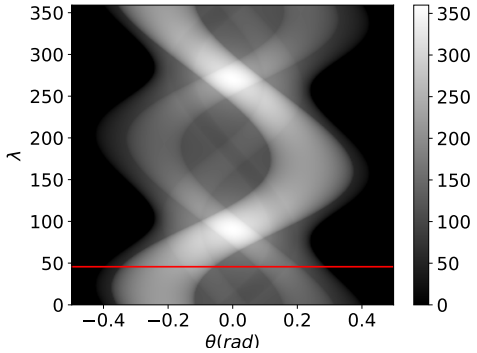

(c) Sinogram of the 2D object shown in Figure 1.6b.

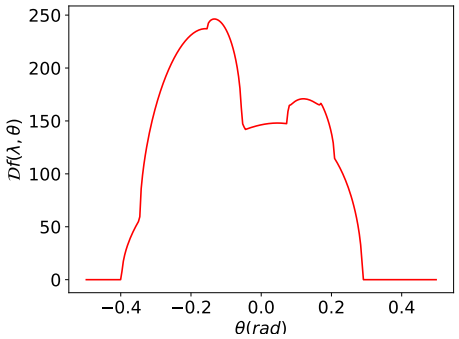

(d) Projection of the 2D object shown in Figure 1.6b at $\lambda = 45°$.

Figure 1.6: Illustration of the divergent beam transform Equation 1.6 of a 2D object with sources on a circular trajectory.

Figure 1.7: Picture of the SOMATOM go.Sim Siemens CT scanner at the anti-cancer center Léon Bérard in Lyon.

in 1989 by Willi A. Kalender (1949-) during the Radiological Society of North America annual meeting [Kalender et al., 1990b, Vock et al., 1989].

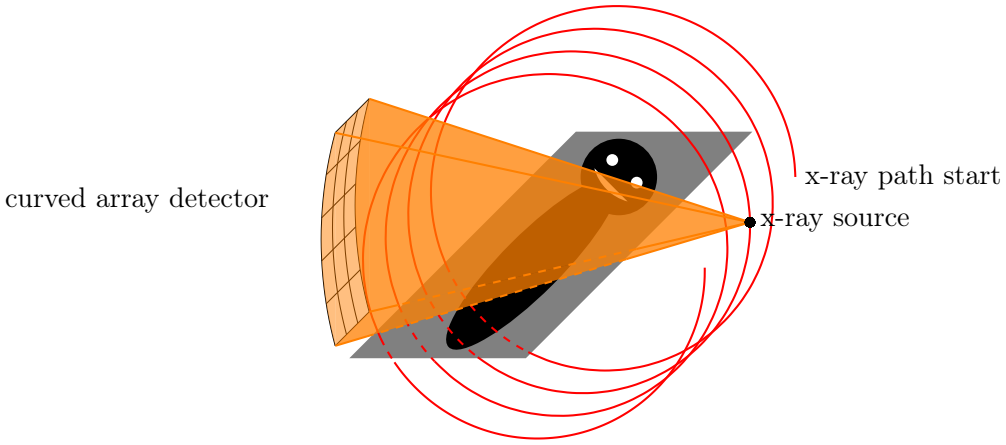

Figure 1.8: Illustration of the helical acquisition mode.

Helical CT was first developed with 1D array detectors (fan-beam) [Kalender et al., 1990a, Vock et al., 1990, Kalender, 1994]. The continuous rotation of helical CT offered the possibility to perform whole body scans in shorter times than the translation-rotation systems that scanned the body slice by slice. In the late nineties, considerable progress was made with regards to x-ray technology. The introduction of 2D array detectors (cone-beam) increased a lot the speed of an acquisition. Nowadays, most commercialized helical scanners feature 2D array detectors with an adaptive number of rows (from 16-slices to 64-slices). For an acquisition time of about 10 s, the acquired axial range reaches about 30 cm with good image quality for medical applications. Due to those advantages, helical CT has become a widely used acquisition mode in diagnostic CT.

1.3.2 Geometry and line integrals

Throughout this thesis, we consider the 3D patient coordinates (x, y, z) defined in the ortho-normal basis $(\boldsymbol{e}_x, \boldsymbol{e}_y, \boldsymbol{e}_z)$. The point source $\boldsymbol{s}_\lambda$ moves along the helix $(R\cos\lambda, R\sin\lambda, \frac{d\lambda}{2\pi})$, where R is the radius of the helix, $\lambda \in n_{rot} \times [0, 2\pi)$ is the gantry angle, taken between $\boldsymbol{e}_x$ and the projection of $\boldsymbol{s}_\lambda$ on the $(\boldsymbol{e}_x, \boldsymbol{e}_y)$ plane (measured positively in the clockwise direction when viewed in the direction $\boldsymbol{e}_z$), n_{rot} the number of rotations, and d is the table feed per rotation, i.e. the distance traveled by the source along the z-axis in one rotation.

The detector is a curved detector corresponding to a portion of a cylinder of radius D which axis is defined by the source $\boldsymbol{s}_\lambda$ and the axis of rotation $\boldsymbol{e}_z$. At a given source position $\boldsymbol{s}_\lambda$, the coordinates of a detector point $\boldsymbol{p}_\lambda$ with coordinates (γ, v) are

$$\boldsymbol{p}_\lambda(\gamma, v) = \boldsymbol{s}_\lambda + \begin{pmatrix} -D\cos(\gamma - \lambda) \\ D\sin(\gamma - \lambda) \\ v \end{pmatrix}. \tag{1.7}$$

The angle γ is taken between the rays $\boldsymbol{p}_\lambda(0, 0)$ and $\boldsymbol{p}_\lambda(\gamma, 0)$, and is measured positively in the counterclockwise direction when viewed in the direction $\boldsymbol{e}_z$. The detector limits are $\gamma \in [-\gamma_{\max}, \gamma_{\max}]$ and $v \in [-v_{\max}, v_{\max}]$.

The direction $\boldsymbol{\theta}$ of the ray exiting from $\boldsymbol{s}_\lambda$ and hitting the curved detector of radius D at the point $\boldsymbol{p}_\lambda(\gamma, v)$ after going through an object with attenuation function f is

$$\boldsymbol{\theta}(\lambda, \gamma, v) = \frac{\boldsymbol{p}_\lambda(\gamma, v) - \boldsymbol{s}_\lambda}{\sqrt{D^2 + v^2}}. \tag{1.8}$$

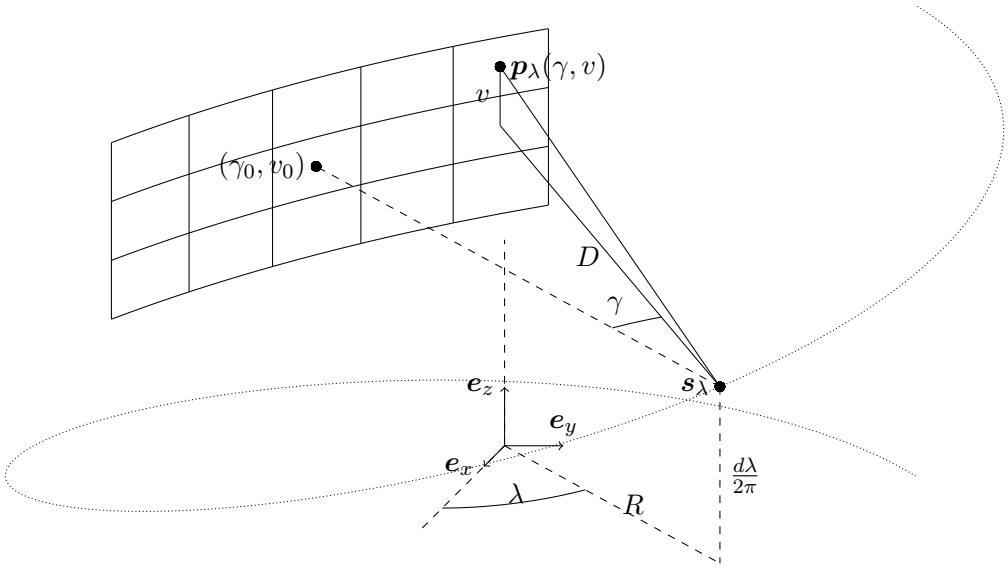

Figure 1.9: Illustration of the cone-beam geometry with helical source trajectory.

The corresponding line integral is

$$g(\lambda, \gamma, v) = \int_0^\infty f\left(\boldsymbol{s}_\lambda + t\,\frac{\boldsymbol{p}_\lambda(\gamma, v) - \boldsymbol{s}_\lambda}{\sqrt{D^2 + v^2}}\right) \mathrm{d}t. \tag{1.9}$$

To simplify the notations, we note $g_\lambda(\gamma, v) = g(\lambda, \gamma, v)$ and g_λ is the cone-beam projection from the source position $\boldsymbol{s}_\lambda$.

Throughout the thesis, we make the following hypothesis: the patient is entirely contained in the region called field of view (FOV). The FOV is the region defined by $\sqrt{x^2 + y^2} \leq R_{\mathrm{FOV}}$, with $R > R_{\mathrm{FOV}} \overset{\mathrm{def}}{=} R \sin \gamma_{\max}$. Consequently, f is zero outside the FOV and the above-defined line integrals are not truncated in the direction of γ. However, due to the limited height of the detector that does not entirely cover the patient, projections are most of the time axially truncated in helical CT. This issue is known as the long object problem.

1.3.3 Basics of reconstruction in helical CT

In CT, there are two classes of algorithms used to recover the attenuation coefficients f from the projections. The first category, called analytic reconstruction, consists of the mathematical inversion of the integral operator, e.g. $\mathcal{R}$ (Equation 1.5) or $\mathcal{D}$ (Equation 1.6), to obtain an analytic expression of f from its projections. The second category, called iterative reconstruction, discretizes the function f, as a grid of pixels (in 2D) or voxels (in 3D). The reconstruction problem then comes down to solving a set of linear equations. This system is solved using iterative methods. In this part, we give a brief summary of available reconstruction algorithms in helical CT.

1.3.3.1 Analytic reconstruction

Analytic reconstruction algorithms are developed for specific geometries as line integrals depend on the geometrical parameters of the acquisitions (source trajectory, detector shape). Their development for 1D array detectors are not detailed in this section, but the reader can refer to the third edition of [Kallender, 2011] for more information. We focus on the last generation CT scanners with multi-slice detectors which we refer to as cone-beam helical CT. For this type of detectors, the cone shape of the beam cannot be

neglected as it was the case for single-slice detectors or multi-slice detectors with less than 4 rows. There are four main categories of analytic reconstruction algorithms for helical CT: slice-rebinning, Feldkamp-type, quasi-exact and exact algorithms.

Slice-rebinning algorithms
Slice-rebinning algorithms consist of the rebinning of the cone-beam data to parallel or fan-beam data, a 2D filtered-backprojection of the rebinned data and finally the resampling of the reconstructed volume onto the correct grid. They have been improved over the years and the reader may find mathematical development and more information in the original papers [Noo et al., 1999, Schaller et al., 2001, Stierstorfer et al., 2002]. They give good image quality while being approximate algorithms. Those algorithms are clinically used.

Feldkamp-type algorithms
Feldkamp-type algorithms [Kudo and Saito, 1991a, Yan and Leahy, 1992] extend the well-known Feldkamp, David and Kress (FDK) algorithm [Feldkamp et al., 1984] to the helical trajectory of the source. The FDK algorithm is performed in three steps: projection weighting, 1D row filtering, and backprojection. Later, other FDK-type algorithms were derived by first rebinning the divergent data into parallel beams in order to increase reconstruction speed, minimize cone-beam artifacts and increase noise uniformity [Turbell and Danielsson, 1999, Kachelrieß et al., 2004, Stierstorfer et al., 2004, Kudo et al., 2004, Tang et al., 2006]. [Stierstorfer et al., 2004] formulate a 3D version of [Stierstorfer et al., 2002] and make the link between slice-rebinning algorithms and Feldkamp-type algorithms for spiral CT.

Quasi-exact algorithms
Quasi-exact algorithms are based on the link between cone-beam projections and the Radon transform of the object [Kudo et al., 1998, Tam, 2000]. Their derivation is performed using local operators so that they can deal with truncated cone-beam data by only using the data in the region of the detector defined by the projections of the upper and lower spiral turns on the detector. This region is called the Tam-Danielson window [Tam et al., 1998]. The main drawback of quasi-exact algorithms is that they are computationally more demanding than the other approximate algorithms.

Exact algorithms
Mathematically exact inversion formulas for cone-beam projections acquired on a spiral path have been obtained by various authors. In [Grangeat, 1991, Schaller et al., 2000], a formula is derived using the link between the cone-beam projections and the Radon transform of the scanned object. The first theoretically exact filtered-backprojection type formula for helical CT was derived in [Katsevich, 2002]. Some improvements and developments followed in [Noo et al., 2004, Katsevich, 2004].

1.3.3.2 Iterative reconstruction

Iterative algorithms are adapted to various types of detectors (1D or 2D, flat or curved) and general source trajectories as the acquisition geometry is intrinsic to the model of the reconstruction problem. Iterative reconstruction is based on the discretization of the image space and projection space. What follows is a non-exhaustive summary of [Grangeat, 2002, chapter 4].

Discrete model
We assume that the attenuation function $f(\boldsymbol{x})$ is divided into N voxels $V_j, j \in \{0, ..., N-1\}$.

The value of f in the voxel V_j is f_j and we can write

$$f(\boldsymbol{x}) = \sum_{j=0}^{N-1} f_j \chi_j(\boldsymbol{x}) \tag{1.10}$$

where χ_j is the indicator function of the voxel V_j

$$\chi_j(\boldsymbol{x}) = \begin{cases} 1 & \text{if } \boldsymbol{x} \in V_j \\ 0 & \text{otherwise.} \end{cases} \tag{1.11}$$

Using the line integral model, the projection g_i measured along the line L_i is

$$g_i = \int_{L_i} f(\boldsymbol{x}) \mathrm{d}\boldsymbol{x}. \tag{1.12}$$

Developing f with Equation 1.10 gives

$$g_i = \sum_{j=0}^{N-1} \left[\int_{L_i} \chi_j(\boldsymbol{x}) \mathrm{d}\boldsymbol{x} \right] f_j, \ i \in \{0, ..., M-1\} \tag{1.13}$$

with M the number of line integrals. All the measurements can be written following Equation 1.13 and are gathered in a projection vector $\boldsymbol{g}$. Thus, the tomographic reconstruction comes down to solving the following system of linear equations:

$$\boldsymbol{g} = \boldsymbol{A}\boldsymbol{f}, \tag{1.14}$$

where $\boldsymbol{A}$ is an $M \times N$ matrix representing the projection operator and $\boldsymbol{f}$ contains the values f_j. Geometrically, the scalar $A_{i,j}$ represents the length of intersection between the line L_i and the voxel V_j. In our case, $\boldsymbol{A}$ can be understood as the discrete version of the divergent beam operator $\mathcal{D}$ presented in Equation 1.6.

Approximation of the solution

Due to the large size of the matrix $\boldsymbol{A}$ and the potentially small number of measurements M, the system given in Equation 1.14 is not directly solvable. Moreover, the matrix $\boldsymbol{A}$ is often not invertible. Thus, an estimation of the solution for Equation 1.14 is obtained by minimizing the cost function

$$C(\boldsymbol{f}) = ||\boldsymbol{g} - \boldsymbol{A}\boldsymbol{f}||_2^2 . \tag{1.15}$$

Taking the derivative of this cost function and making it equal to zero gives a new linear system which is

$$\boldsymbol{A}^T\boldsymbol{A}\boldsymbol{f} = \boldsymbol{A}^T\boldsymbol{g} \tag{1.16}$$

where $\boldsymbol{A}^T$ is the transpose of $\boldsymbol{A}$.

Regularization

The noise present in real life acquisition makes the model presented above unstable. To compensate for those instabilities, the cost function of Equation 1.15 can be combined with a Tikhonov regularization [Tikhonov, 1963]. The cost function becomes

$$C(\boldsymbol{f}) = ||\boldsymbol{g} - \boldsymbol{A}\boldsymbol{f}||_2^2 + \Gamma \, ||\nabla \boldsymbol{f}||_2^2 \tag{1.17}$$

where we used the differential operator ∇. This regularization penalizes the solutions with a high spatial gradient norm. Therefore, the reconstruction is smoother with higher Γ. This leads to a slightly different new system of equations:

$$\left(\boldsymbol{A}^T\boldsymbol{A} + \Gamma\nabla^T\nabla\right)\boldsymbol{f} = \boldsymbol{A}^T\boldsymbol{g}. \tag{1.18}$$

A possible algorithm: the Conjugate gradient

The resolution of the systems Equation 1.16 and Equation 1.18 is possible because the matrices to inverse $\boldsymbol{A}^T\boldsymbol{A}$ and $\boldsymbol{A}^T\boldsymbol{A} + \Gamma\nabla^T\nabla$ are now symmetric and positive. However, the matrices have high dimensions making their inversion computationally demanding. An alternative is to use iterative algorithms to estimate the solutions. Here, we present the *conjugate gradient* (CG) algorithm which is a basic iterative algorithm. For other iterative algorithms, the reader can refer to [Kak and Slaney, 1988, Grangeat, 2002].

We present here the resolution of Equation 1.16 with the CG algorithm. We begin with the initialization of the solution $f^{(0)}$. If an estimate of the reconstruction is available, then $\boldsymbol{f}^{(0)}$ is initialized with this estimate, which can accelerate the algorithm convergence. Otherwise, $\boldsymbol{f}^{(0)}$ is usually set to 0. The corresponding residue is $\boldsymbol{r}^{(0)} = \boldsymbol{A}^T(\boldsymbol{g} - \boldsymbol{A}\boldsymbol{f}^{(0)})$ and the initial direction of the gradient descent is $\boldsymbol{d}^{(0)} = \boldsymbol{r}^{(0)}$. The iterative scheme at iteration $k+1$ is given by

$$\begin{aligned} \boldsymbol{f}^{(k+1)} &= \boldsymbol{f}^{(k)} + \alpha^{(k)}\boldsymbol{d}^{(k)}, \\ \boldsymbol{r}^{(k+1)} &= \boldsymbol{r}^{(k)} - \alpha^{(k)}\boldsymbol{A}^T\boldsymbol{A}\boldsymbol{d}^{(k)}, \\ \boldsymbol{d}^{(k+1)} &= \boldsymbol{r}^{(k+1)} + \beta^{(k)}\boldsymbol{d}^{(k)} \end{aligned} \tag{1.19}$$

where

$$\begin{aligned} \alpha^{(k)} &= \frac{{\boldsymbol{r}^{(k)}}^T\boldsymbol{r}^{(k)}}{{\boldsymbol{d}^{(k)}}^T\boldsymbol{A}^T\boldsymbol{A}\boldsymbol{d}^{(k)}}, \\ \beta^{(k)} &= \frac{{\boldsymbol{r}^{(k+1)}}^T\boldsymbol{r}^{(k+1)}}{{\boldsymbol{r}^{(k)}}^T\boldsymbol{r}^{(k)}}. \end{aligned} \tag{1.20}$$

The convergence of this algorithm is theoretically obtained after N iterations, which is the number of unknown variables in the linear system. In practice, a number $n \ll N$ of iterations is taken because the convergence time would be too high. Typically, a value of n between 50 and 100 iterations gives a good approximation of the solution and the final estimation is $\boldsymbol{f}^{(n)} \approx \boldsymbol{f}$.

As an example, the reconstruction of the object presented in Figure 1.6b from its sinogram in Figure 1.6c is shown in Figure 1.10a. The reconstruction was performed with $n = 50$ iterations. The impact of noise on the CG algorithm is shown in Figure 1.10b where the object is reconstructed from a noisy sinogram. The use of regularization stabilizes the solution as shown in Figure 1.10c where streaks resulting from the noisy data are reduced with the regularization.

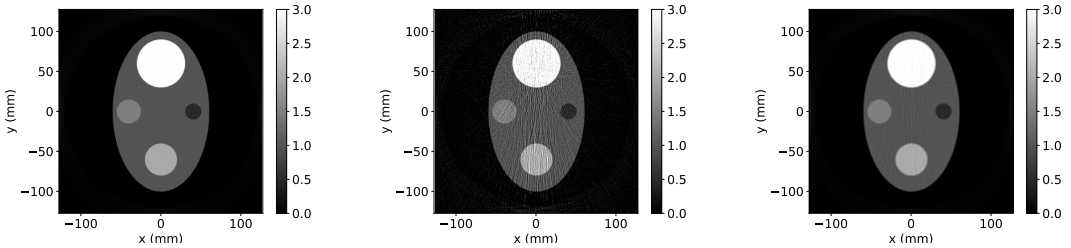

(a) Reconstruction from the ideal sinogram shown Figure 1.6c.

(b) Reconstruction from a noisy sinogram.

(c) Reconstruction from a noisy sinogram with regularization $\Gamma = 100$.

Figure 1.10: Illustration of the CG algorithm and Tikhonov regularization. Reconstruction of the object in Figure 1.6b from ideal and noisy projections with and without regularization. The number of iterations is $n = 50$.

We choose to work with this algorithm because of its simplicity, the small number of hyper-parameters to tune and its quite good efficiency. In the rest of the thesis, the

number of iterations n and the regularization parameter Γ will be stated for each image reconstructed with this algorithm.

1.4 Conclusion

In this chapter, the basics of CT were presented. We described how x-rays are generated, their main interactions with matter, specifically in the context of medical imaging, and their detection. The line integral model was presented and illustrated with a simple example. Helical CT, which is the main CT acquisition geometry considered in this thesis, was introduced, and a review of reconstruction algorithms for this geometry was laid out. Finally, we illustrated the CG algorithm with a simple example and how regularization can be used to account for the presence of noise in the measurements.

Chapter 2

Breathing motion in Computed Tomography

Radiotherapy is the treatment during which cancerous cells are irradiated in order to stop their ability to propagate. The first stage of the treatment corresponds to the acquisition of anatomical images of the patient to identify the localization of the tumor and to define the treatment plan. During treatment planning, the volume to irradiate is defined and the parameters of the irradiation beams are chosen by the physicist. The second stage is the delivery of the treatment. CT imaging is used at almost every stage of the treatment. In the first stage, CT images can be coupled with Magnetic Resonance (MR) or emission tomography images for treatment planning. Although MR-only treatment planning has been developed, CT is still the main modality for the treatment plan. In the second stage, cone-beam CT is the most used imaging modality during treatment delivery to check that the patient is correctly positioned according to the treatment plan and that the correct volume is irradiated.

In the context of thoracic and upper abdominal cancers, the tumor is not static because of the breathing motion of the patient. Motion creates artifacts on tomographic images used for treatment planning, which can lead to an incorrect definition of the volumes. Therefore, tumors can be insufficiently irradiated and surrounding healthy cells too much irradiated. Various CT imaging techniques have been proposed to take into account motion during imaging for treatment planning and predict as precisely as possible tumors' motion during treatment.

In this chapter, we first detail some characteristics of the breathing motion, its impact on thoracic and upper abdominal tumor motion and its repercussions on conventional treatment planning. Then, we briefly present 4D radiotherapy and the commonly used imaging techniques to account for motion during the acquisition of images for treatment planning. Finally, we describe 4D helical CT, one of the most used modality for treatment planning of thoracic cancers and the modality considered in this thesis.

2.1 Motion and radiotherapy planning

2.1.1 Respiratory motion

Breathing is the biological mechanism consisting of the inhalation of oxygen and the exhalation of carbon dioxide. During inhalation, the diaphragm, the main respiratory muscle, tightens itself which extends the lungs towards the abdomen and the thorax. The inhaled oxygen is transmitted to the blood via a thin membrane separating the lung's alveoli from the bloodstream. Exhalation is a passive mechanism corresponding to the relaxation of the lungs and the respiratory muscles.

Breathing motion can be characterized by two variables: its frequency and its resulting motion amplitude and direction. The number of respiratory cycles for an adult varies between 12 to 20 per minute [George et al., 2005].

During breathing, the contraction of the diaphragm leads to the deformation of the lungs and to the motion of upper abdominal organs. In [Keall et al., 2006], a correlation between motion amplitude and direction for the upper abdominal organs and the diaphragm is reported. The trajectory of the motion is mostly in the superior-inferior (SI) direction with an amplitude between 10 to 30 mm for shallow breathing and can be up to 95 mm for a deep inspiration. The motion amplitude in the other directions (anterior-posterior (AP) and lateral) is no more than 2 mm. Regarding lung tumor motion, the report points out that the motion of tumors in the lower lobes is larger than in mid and upper lobes. This is due to the proximity of the tumors to the diaphragm whose movement causes SI motion. However, the authors [Keall et al., 2006] also report some studies in which, for some patients, lung tumors moved more in the AP and lateral directions than in the SI direction. Moreover, it was observed that the lung tumor does not follow the same trajectory during inhalation and exhalation.

All those characteristics introduce high variability for the treatment of thoracic cancers and have an impact on radiotherapy planning and radiation therapy.

2.1.2 Impact of motion on conventional radiotherapy planning

The physicists define the Gross Tumor Volume (GTV) on CT images as the volume of the tumor visible on the CT image. From it, well-established margins are used to define other volumes that characterize the extent of the tumor motion and the uncertainty due to targeting uncertainties during treatment delivery.

During a conventional CT acquisition, the patient is assumed static throughout the entire process. The reconstruction algorithms are not designed to account for the breathing motion of the patient which results in blur and deformed structures on the reconstructed images on which the treatment plan is based. If the tumor is inaccurately reconstructed, the GTV is incorrectly defined leading to an escalation of errors for the other volumes [Keall et al., 2006, Clements et al., 2013]. If the reconstructed volume is smaller than the actual size of the tumor, the GTV will be too small and only a part of the tumor will be irradiated (see Figure 2.1). On the other hand, if the reconstructed volume is bigger than the actual size of the tumor, the GTV will be larger than necessary meaning that the tumor and surrounding healthy tissues will be irradiated during the treatment which can aggravate treatment complications.

(a) Correct volume (b) Incorrect volume

Figure 2.1: Example of incorrect volume reconstruction because of motion during a conventional CT scan. The phantom is static but the tumor in the left lung is moving during the acquisition. The correct volume of the tumor is shown in (a), and the reconstructed volume is shown in (b).

To limit those artifacts and avoid errors in volume delineation, 4D radiotherapy has emerged and many techniques have been developed to account for motion during treatment planning.

2.1.3 Motion encompassing for treatment planning in 4D radiotherapy

4D radiotherapy deals with motion during treatment planning and treatment delivery by adding the time dimension to the conventional (i.e 3D) techniques. The aim of treatment planning in 4D radiotherapy is to obtain as much and as precise information as possible regarding the motion of the tumor to predict its behavior during radiation delivery. Consequently, motion encompassing techniques must transcribe as faithfully as possible the tumor motion. The main CT techniques of motion encompassing are listed below. For motion encompassing techniques in other modalities, the reader can refer to [Ehrhardt and Lorenz, 2013].

Slow CT
Slow CT corresponds to the acquisition and reconstruction of the full range of tumor motion. To this end, the duration of a full gantry rotation is increased. For conventional CT, the duration of a full gantry rotation is between 0.5 s to 1 s. For a slow CT, it can be up to 4 s. This acquisition is useful to accurately define the volume characterizing the extent of the tumor motion. However, it is not accurate enough for the delineation of the GTV and surroundings organs [Dieterich et al., 2016]. Indeed, as shown in Figure 2.2, the limits of the tumor and the lungs are hardly visible because of the blurry traces resulting from the motion.

Multiple conventional CT
Multiple conventional CT corresponds to the acquisition of at least three conventional CT scans: one during which the patient holds its breath at end-inhale, one during which the patient holds its breath at end-exhale and one during which the patient breathes freely. The addition of the breath-holds scans to the single conventional CT allows for a more precise identification of the GTV and the tumor motion range than a single conventional CT scanner [Shih et al., 2004]. Two issues have been reported with this protocol: first, many patients, especially those suffering from lung cancer, cannot hold their breath correctly which results in artifacts on the tomographic images [Dieterich et al., 2016]; secondly, the extreme positions of the tumor at end-inhale and end-exhale may differ from those obtained with a free-breathing scan and induce errors in the definition of the tumor motion extent [Hunjan et al., 2008].

4D CT
4D CT corresponds to a set of 3D CT reconstructed at different phases of the respiratory cycle (see Figure 2.2). It allows the visualization of the tumor trajectory during a respiratory cycle. It assumes a cyclic motion of the tumor due to the respiration and reconstructs a few phases along the cycle [Ford et al., 2003]. Usually, the respiratory cycle is divided in 10 phases as shown in Figure 2.2. It is the preferred protocol in clinical practice to acquire images for the treatment plan in body parts affected by motion. To perform a 4D CT acquisition, a high number of projections (oversampled acquisition) is acquired. The projections are sorted according to their position in the respiratory cycle and each subset is reconstructed. There are two protocols to obtain 4D CT images: 4D Ciné-CT and 4D helical CT. In 4D Ciné-CT, the patient table is stationary, while the acquisition of one axial position is performed throughout an entire respiratory cycle. Once the acquisition of an axial position is done, the table is moved to the next axial position and the acquisition starts again, and so on until the entire volume of interest is covered. In 4D helical CT,

the table moves continuously during the acquisition, but the table feed is very small so that each axial position is acquired for every state of the respiratory cycle. 4D acquisitions allow for better delineation of the GTV but the images are more noisy than those obtained with a slow CT [Dieterich et al., 2016]. A slow CT image can be recovered from a 4D acquisition using all acquired projections without any sorting (see Figure 2.2).

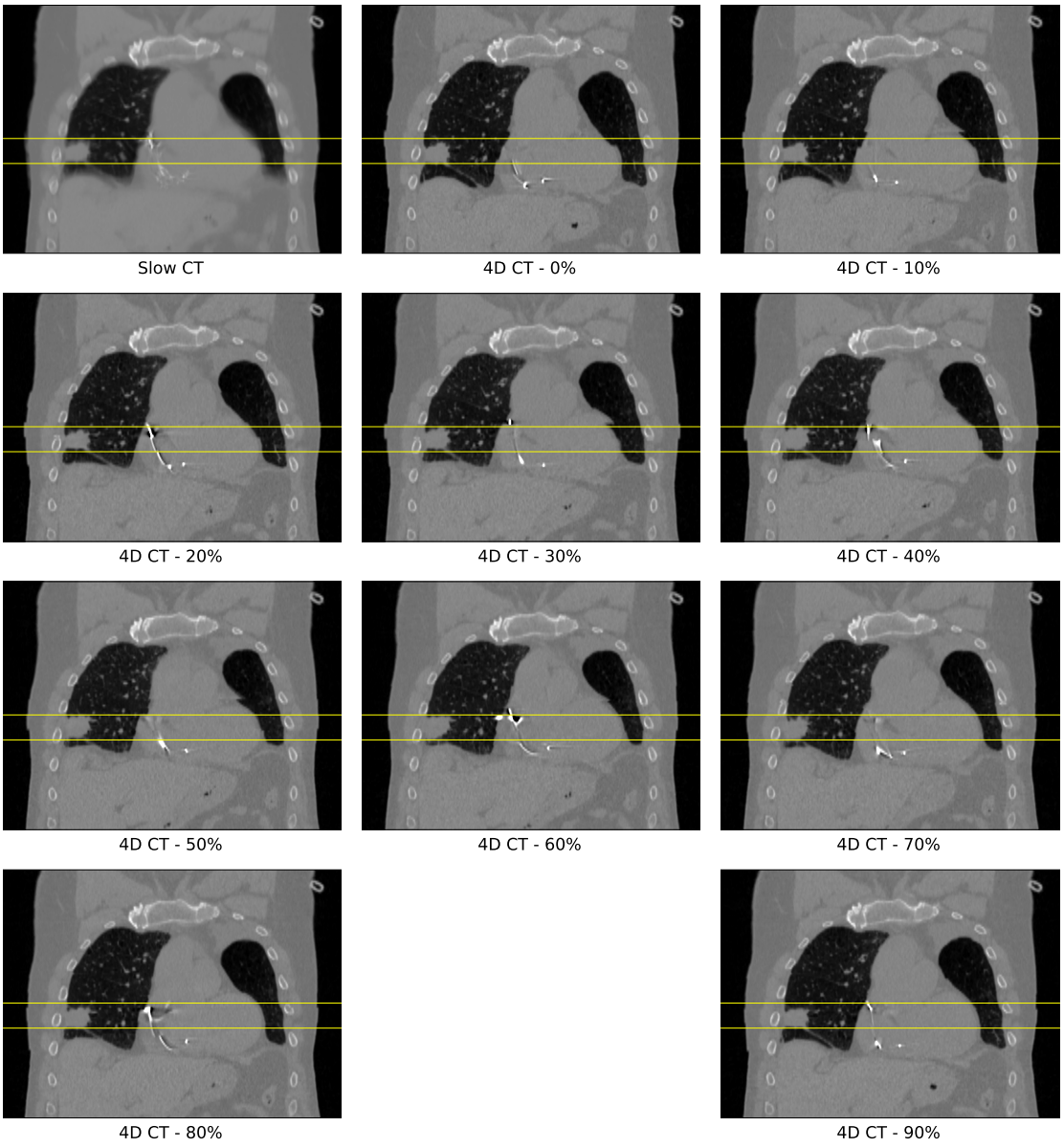

Figure 2.2: Illustration of slow and 4D CT. The ten images (0% to 90%) correspond to the ten phases of the respiratory cycle. The breath-hold CT would correspond to the 4D CT reconstructions at 0% (end-inhale) and 50% (end-exhale). The yellow lines show the axial range of the tumor motion.

4D helical CT is the main acquisition technique considered in this thesis. We present its technical aspects in the next section.

2.2 4D helical CT

This section gathers the basics of 4D helical CT, its limitations, possible solutions as well as recent improvements in the field.

2.2.1 Principle and Data sufficiency condition

4D helical CT requires that each point of the scanned volume is acquired for every stage of the respiratory cycle and that there are enough projections to reconstruct each point at each stage. This requirement is defined by [Pan, 2005] as the data sufficiency condition (DSC) and is written as

$$P \leq \frac{T_{rot}}{T_{resp} + T_{rot}} \tag{2.1}$$

where T_{rot} is the duration of a full gantry rotation, T_{resp} is an estimation of the patient respiratory period and P is the pitch corresponding to the portion of detector covered in one rotation expressed as

$$P = \frac{d}{W}, \tag{2.2}$$

with d the table feed introduced in Section 1.3.2 and W the detector height at the isocenter.

To meet this requirement, manufacturers define several acquisition protocols depending on the patient respiratory period. The main 4D acquisition protocols for the go.Sim Siemens CT scan are listed below in Table 2.1.

T_{resp} (s)	P	T_{rot} (s)
< 5	0.07	0.35
< 6.67	0.07	0.5
< 10	0.05	0.5

Table 2.1: 4D acquisition protocols proposed by Siemens for the go.Sim CT scan. The height of the detector W is fixed and P varies because the table feed per rotation d varies.

2.2.2 Reconstruction algorithm in 4D helical CT

The ground work for 4D helical CT reconstruction was proposed by [Ford et al., 2003]. This algorithm, called respiratory-correlated CT (RCCT), sorts the projections according to an external breathing signal acquired simultaneously. The breathing signal is divided into phases, and the projections sorted accordingly as illustrated in Figure 2.3. Then each subset of projections is reconstructed independently of the others using appropriate 3D reconstruction algorithms. Finally, the set of 3D reconstructed volumes throughout the respiratory cycle is stacked to obtain a 4D reconstruction.

The most common tools, shown in Figure 2.4, to acquire the breathing signal are:

(a) Real-time Position Management (RPM) systems (Varian Medical Systems) made of an infrared diode placed on the patient abdomen and an infrared camera that tracks the motion of the diode.

(b) Pressure belt systems (Anzai Medical Corporation) that include a belt placed around the patient chest. The abdomen motion makes the pressure detected by the sensor vary resulting in a breathing signal.

(c) Air bellow systems (Philips) which is a belt placed around the patient chest that contracts and expands as the patient breathes. The resulting pressure on the belt is then converted into a breathing signal.

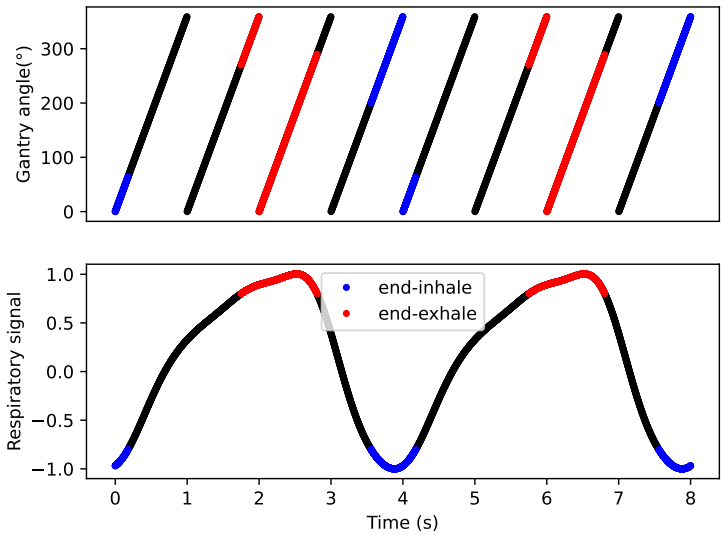

Figure 2.3: Illustration of the RCCT algorithm using phase-based sorting. The red parts correspond to end-exhalation and the blue part to end-inhalation.

These three systems give similar results in image quality [Li et al., 2006, Glide-Hurst et al., 2013].

(d) More recently, a new system that measures the pressure change on the back of the patient has been developed, and gave results similar as the RPM system [Zhang et al., 2020].

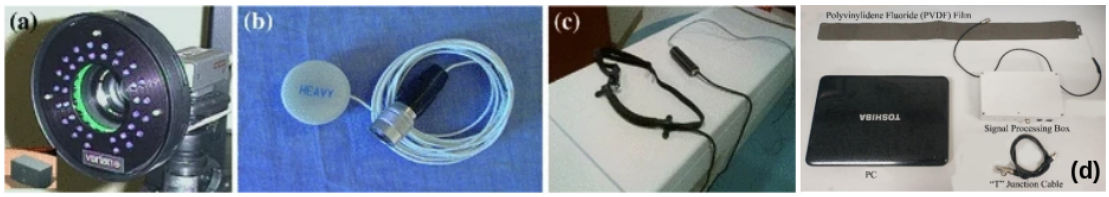

Figure 2.4: Respiratory monitoring devices. (a) RPM device (Varian Medical Systems). (b) Pressure sensor (Anzai Medical Corporation). (c) Air bellow and pressure belt (Philips). (d) Back pressure sensor. Images (a), (b) and (c) are from [Ehrhardt and Lorenz, 2013] and (d) is from [Zhang et al., 2020].

The sorting of projections is either phase-based or amplitude-based.

For phase-based sorting, one phase is chosen to be the beginning of a respiratory cycle (typically end-inhalation). The time separating the same phase from two successive respiratory cycles is supposed to be equal to the breathing period. The respiratory cycle is divided into several phases and projections are selected accordingly as illustrated in Figure 2.3.

One way of doing amplitude-based sorting is to define a respiratory cycle between two peaks of the same amplitude from the extracted breathing signal. The maximum and minimum amplitude (usually corresponding to end-inhalation and end-exhalation) measured on the extracted breathing signal are averaged to define the motion range. Similarly to the phase-based method, a respiratory cycle is divided into phases according to a certain amplitude to form subsets of projections. It was established that the amplitude-based algorithm was more likely to compensate for irregular breathing (varying period or varying amplitude) than the phase-based algorithm [Lu et al., 2006, Li et al., 2012, Abdelnour

et al., 2007]. However, the described amplitude-based sorting method might not cover the entire motion range of the tumor, especially for large motion amplitude [Li et al., 2012]. Both sorting methods are illustrated in Figure 2.5.

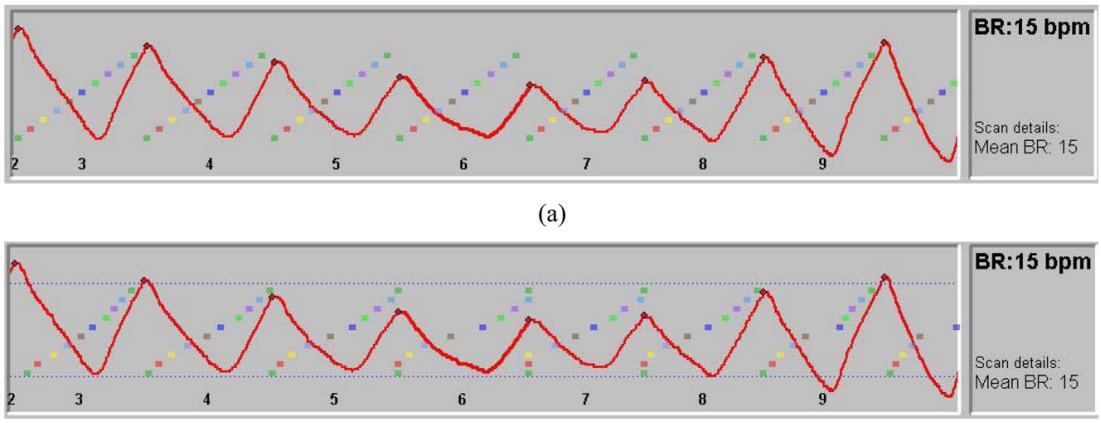

Figure 2.5: Illustration of phase-based (a) and amplitude-based (b) sorting. Image from [Li et al., 2012]. The 10 colored dots are the 10 phases of the respiratory cycle. For phase-based sorting, projections are sorted according to their acquisition time. For amplitude-based sorting, projections are sorted according to the amplitude of the acquired breathing signal at the time of their acquisition.

2.2.3 Limitations

While 4D CT takes into account breathing and lung tumor motion during treatment planning, it has significant limitations. The majority of sorting methods are based on the hypothesis that breathing motion is regular, which is not always the case, especially for patients suffering from respiratory diseases. It has been shown that irregular breathing causes artifacts on 4D CT images [Yamamoto et al., 2008]. Other 4D CT artifacts are also visible around the cardiac region as the heart motion is not accounted for. The last type of artifact is caused by missing data at an axial location for which the breathing cycle duration is underestimated [Han et al., 2011]. Figure 2.6 shows an example of each type of artifact from 3D frames of 4D CT images obtained with the go.Sim CT scanner. Moreover, the signal acquired with the tracking methods refers to the external motion of the body and is often different from the internal motion of the organs and the tumor.

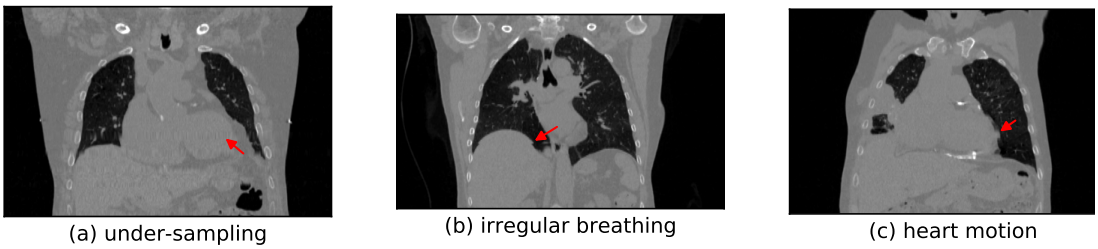

Figure 2.6: Example of 4D CT artifacts from 3 different patients acquired with the somatom go.Sim Siemens CT scan.

Those artifacts - and particularly those resulting from irregular breathing - lead to inaccurate volume delineations, especially at the end-inhale and end-exhale positions of

the respiratory cycle [Clements et al., 2013]. Hence, improving the quality of 4D CT images is necessary for treatment planning.

2.2.4 Possible improvements

Among the techniques that compensate for irregular breathing, one may find breathing coaching where the patient is trained to breath more regularly by following audio and visual respiratory instructions [George et al., 2006, Neicu et al., 2006, Venkat et al., 2008]. Some cancer centers may use a compression plate pressing against the patient abdomen to reduce SI motion [Negoro et al., 2001]. Post-processing techniques are also available to remove motion artifacts [Ehrhardt et al., 2007, Schreibmann et al., 2006, Zhang et al., 2013]. Another possibility is to improve the sorting of the projections [Fitzpatrick et al., 2006, Rietzel and Chen, 2006] or combine optimized sorting with artifacts removal techniques during reconstruction [Werner et al., 2017].

Alternative methods to generate 4D CT images were also published. [Thomas et al., 2014] proposed a new acquisition protocol to generate artifact-free 4D CT images from a set of fast helical CT scans.

2.3 Conclusion

In this chapter, we have highlighted the limitations of conventional radiotherapy planning regarding lung tumors. We introduced 4D radiotherapy and 4D CT and presented the fundamentals and practical considerations of this modality. Finally, we explained the limitations of 4D helical CT, especially the fact that it relies on the hypothesis of regular breathing which is not always verified, resulting in artifacts on tomographic images. Possible improvements to correct those artifacts have been presented, notably the development of projection sorting algorithms that may better handle irregular breathing. However, more accurate algorithms are still needed to cope with irregular breathing to further improve the quality of 4D CT images for radiotherapy planning.

Chapter 3

Data consistency conditions

From a mathematical point of view, *Data Consistency Conditions* (DCCs), or *range conditions*, are mathematical equations characterizing the range of a linear operator. This means that all elements belonging to the range of this operator should satisfy the DCCs. In CT, the acquisition is modeled as a linear operator, such as the Radon transform for the 2D parallel geometry and the divergent beam transform for divergent geometries, from an object space to a projection space. Hence, DCCs should be verified by the projections. In other words, DCCs characterize the redundancies in x-ray projections. Any external effect not considered in the model will likely yield inconsistencies in the projections that will not verify the DCCs anymore. Among those, one may find motion, noise, beam hardening, scatter, etc... DCCs apply directly to the projections, prior to any reconstruction. This makes them a very interesting and convenient tool to correct or use information in the projections to reconstruct artifacts-free CT images.

In this chapter, we first introduce consistency conditions with the parallel beam geometry. Then, we present DCCs in the divergent geometry. We conclude this chapter with an overview of DCC-based artifacts reduction methods and particularly focus on their use for motion detection and correction in CT.

3.1 Data consistency conditions with the 2D parallel geometry

DCCs depend on the geometry of the CT scanner as they depend on the projections given by the line integral model which are specific to the x-ray acquisition system. To better understand consistency conditions, we first focus on the 2D parallel case.

3.1.1 A first intuition

The object $f(\boldsymbol{x}) = f(x, y)$ is entirely contained in the FOV, defined by the black circle in Figure 3.1. We consider the two projections acquired at angles ψ_a and ψ_b. The resulting parallel projections are written $p(\psi_a, \cdot)$ and $p(\psi_b, \cdot)$. Let us define the function

$$J_0(\psi) = \int_{\mathbb{R}} p(\psi, s)\mathrm{d}s \tag{3.1}$$

which is the sum of all the measured line integrals within the projection at angle ψ. Calculating this integral for our two projections, we obtain

$$J_0(\psi_a) = \int_{\mathbb{R}} p(\psi_a, s)\mathrm{d}s = \int_{\mathbb{R}}\int_{\mathbb{R}} f(s\boldsymbol{\xi}_{\psi_a} + t\boldsymbol{\iota}_{\psi_a})\mathrm{d}t\mathrm{d}s = \int_{\mathbb{R}^2} f(\boldsymbol{x})\mathrm{d}\boldsymbol{x} \tag{3.2}$$

and

$$J_0(\psi_b) = \int_{\mathbb{R}} p(\psi_b, s)\mathrm{d}s = \int_{\mathbb{R}}\int_{\mathbb{R}} f(s\boldsymbol{\xi}_{\psi_b} + t\boldsymbol{\iota}_{\psi_b})\mathrm{d}t\mathrm{d}s = \int_{\mathbb{R}^2} f(\boldsymbol{x})\mathrm{d}\boldsymbol{x}. \tag{3.3}$$

We observe that $J_0(\psi_a) = J_0(\psi_b) = \int_{\mathbb{R}^2} f(\boldsymbol{x})\mathrm{d}\boldsymbol{x}$ is a constant corresponding to the integral of f over the FOV (f is entirely contained in the FOV and equals zero outside of it). The

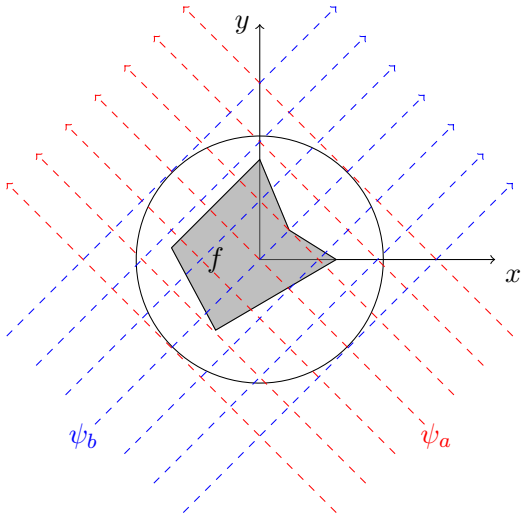

Figure 3.1: Illustration of two parallel beams.

following necessary consistency conditions is deduced from the previous example:

If a function p is the Radon transform of some attenuation function f, i.e. $p = \mathcal{R}f$, then the intermediate function J_0, from Equation 3.1, is a constant $\forall\psi \in [0, \pi)$.

Equivalently, if $\exists\psi \in [0, \pi)$ such that J_0 is not constant, then $p(\psi, \cdot)$ is not the Radon transform of the object f at angle ψ. This second proposition is what is used to detect inconsistencies with the DCCs.

3.1.2 Helgason-Ludwig consistency conditions

The previous DCC is a particular case, referred to as the *zeroth order* DCC, of a set of complete (i.e necessary and sufficient) consistency conditions for the 2D parallel geometry called Helgason-Ludwig consistency conditions [Helgason, 1965, Ludwig, 1966]. The DCCs state that a function p is the Radon transform of some density function f, i.e. $p = \mathcal{R}f$, if and only if:

- $p(\psi, s) = p(\psi + \pi, -s), \forall\psi \in [0, \pi), \forall s \in \mathbb{R}$,
- The intermediate function

$$J_n(\psi) = \int_{\mathbb{R}} s^n p(\psi, s)\mathrm{d}s, n \in \mathbb{N} \tag{3.4}$$

  is a homogeneous polynomial in $\cos\psi$ and $\sin\psi$ of degree n.

The function J_n is referred to as the moment of order n of the projection $p(\psi, \cdot)$.

3.2 Fan-beam data consistency conditions

The derivation of DCCs in divergent geometries is more complex than in the parallel case. As mentioned above, DCCs are derived for a specific x-ray trajectory. Complete DCCs may exist for uncommon trajectories and only necessary DCCs may exist for commonly used trajectories. In this section, we give a brief mathematical description of some consistency conditions for the 2D divergent geometry.

3.2.1 Complete fan-beam consistency conditions for sources on a line

The fan-beam DCCs have been proposed in [Clackdoyle, 2013]. The coordinate system is $(\boldsymbol{e}_x, \boldsymbol{e}_y)$. The source $\boldsymbol{s}_\lambda$ with $\lambda \in \mathbb{R}$ follows a linear trajectory on the y axis, as illustrated in Figure 3.2. The fan angle is noted ϕ. It is assumed that the object lies entirely in the space $x > 0$.

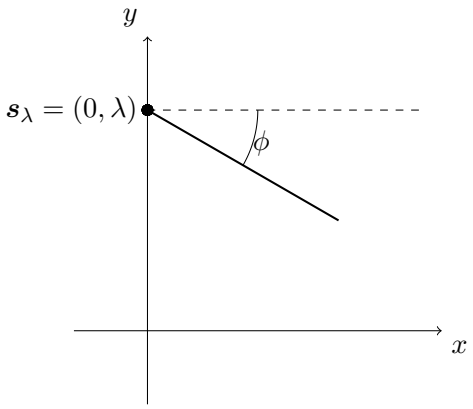

Figure 3.2: Illustration of the fan-beam geometry for sources on a line.

In this case, the direction $\boldsymbol{\theta}$ of a ray is given by $\boldsymbol{\theta} = \cos\phi \boldsymbol{e}_x + \sin\phi \boldsymbol{e}_y$. Consequently, line integrals are written

$$g_F(\lambda, \phi) = \int_0^\infty f\left(\boldsymbol{s}_\lambda + t(\cos\phi \boldsymbol{e}_x + \sin\phi \boldsymbol{e}_y)\right) \mathrm{d}t. \tag{3.5}$$

and $g_F(\lambda, \cdot)$ is the fan-beam projection from the source position λ.

Let M_n be an intermediate function defined as

$$M_n(\lambda) = \int_{-\pi/2}^{\pi/2} \frac{g_F(\lambda, \phi)}{\cos\phi} \tan^n\phi \ \mathrm{d}\phi. \tag{3.6}$$

We refer to M_n as the moment of order n of the 1D fan-beam projection $g_F(\lambda, \cdot)$.

The fan-beam DCCs for linear trajectory state that $M_n(\lambda)$ is a polynomial in λ of degree n, $\forall n \in \mathbb{N}$, if and only if g_F is the divergent beam transform along a linear trajectory of some attenuation function f.

3.2.2 The zeroth order case

Similarly to the Helgason-Ludwig DCCs, the zeroth order moment of the fan-beam projections is equal for all projections acquired along the linear trajectory. The moment M_0 is a constant that does not depend on λ. Let us demonstrate the zeroth order fan-beam DCC for sources on a line. From Equation 3.6, we have with $n = 0$

$$M_0 = \int_{-\pi/2}^{\pi/2} \frac{g_F(\lambda, \phi)}{\cos\phi} \ \mathrm{d}\phi \tag{3.7}$$

$$= \int_{-\pi/2}^{\pi/2} \int_0^\infty \frac{1}{\cos\phi} f\left(\boldsymbol{s}_\lambda + t(\cos\phi \boldsymbol{e}_x + \sin\phi \boldsymbol{e}_y)\right) \mathrm{d}t\mathrm{d}\phi \tag{3.8}$$

$$= \int_{-\pi/2}^{\pi/2} \int_0^\infty \frac{1}{\cos\phi} f\left(t\cos\phi, \lambda + t\sin\phi\right)\right) \mathrm{d}t\mathrm{d}\phi. \tag{3.9}$$

With the change of variable $(x, y) = (t\cos\phi, \lambda + t\sin\phi)$, we have $t\mathrm{d}t\mathrm{d}\phi = \mathrm{d}x\mathrm{d}y$. Thus,

$$M_0 = \int_{-\pi/2}^{\pi/2}\int_0^{\infty} f(x,y)\frac{t}{x}\frac{\mathrm{d}x\mathrm{d}y}{t} \tag{3.10}$$

$$= \int_{-\pi/2}^{\pi/2}\int_0^{\infty} \frac{f(x,y)}{x}\mathrm{d}x\mathrm{d}y \tag{3.11}$$

which is independent of λ. It is important to note that while the DCCs presented in the previous section are necessary and sufficient conditions, the zeroth order DCC is only a necessary condition. In the rest of the thesis, we will refer to this particular case as FBDCC.

The FBDCC belongs to the family of consistency conditions called *integral invariants*. They have been derived in many ways [Chen and Leng, 2005, Wei et al., 2006, Levine et al., 2010, Tang et al., 2012] and proven equivalent in [Tang et al., 2012]. Although some of them only compare pairs of fan-beam projections [Wei et al., 2006, Levine et al., 2010], others link one fan-beam projection to more than one other projection [Chen and Leng, 2005, Tang et al., 2012].

3.3 Cone-beam consistency conditions

In this section, we give a brief mathematical description of some consistency conditions for the 3D divergent geometry.

3.3.1 From fan-beam to cone-beam consistency conditions

Many papers [Leng et al., 2007, Berger et al., 2017] have generalized fan-beam DCCs to the cone-beam geometry by applying the DCCs along each row of the cone-beam detector. Such a process was mostly used for a circular trajectory of the x-ray source.

Another possibility is to apply the FBDCC to pairs of cone-beam projections using rebinning. Such a process can be applied to any x-ray source trajectory and was described in [Levine et al., 2010, Lesaint et al., 2017]. Let us consider two source positions $\boldsymbol{s}_\lambda$ and $\boldsymbol{s}_{\lambda'}$, with $\lambda, \lambda' \in [0, 2\pi)$, on the circular trajectory as illustrated in Figure 3.3. The two corresponding cone-beam projections, noted $\hat{g}_\lambda$ and $\hat{g}_{\lambda'}$, are acquired on flat detectors with coordinate system (u, v). To apply the FBDCC, the two projections are rebinned onto a virtual detector (in red in Figure 3.3), with coordinates (q, r), whose rows are parallel to the line connecting the two source positions. The rebinned projections are noted g^*_λ and $g^*_{\lambda'}$.

The intersection of the plane Π_r, defined by the two source positions $(\boldsymbol{s}_\lambda, \boldsymbol{s}_{\lambda'})$ and the row r of the virtual detector, with the rebinned projection g^*_λ represents a fan-beam projection noted $g_F(\lambda, \phi_r) = g^*_\lambda(q, r)$, where ϕ_r is the angle between a ray emitted from $\boldsymbol{s}_\lambda$ hitting the virtual detector pixel (q, r) and the line orthogonal to the row r (in the plane Π_r). The zeroth order moment of the fan-beam projection $g_F(\lambda, \phi_r)$ is written

$$M_0(\lambda) = \int_{-\pi/2}^{\pi/2} \frac{g_F(\lambda, \phi_r)}{\cos\phi_r}\,\mathrm{d}\phi_r. \tag{3.12}$$

To express $M_0(\lambda)$ in terms of the virtual detector coordinates (q, r), we make the following geometrical observations:

- the orthogonal distance between the line connecting the source positions and a virtual detector row r is $\sqrt{r^2 + D^2_{virt}}$,

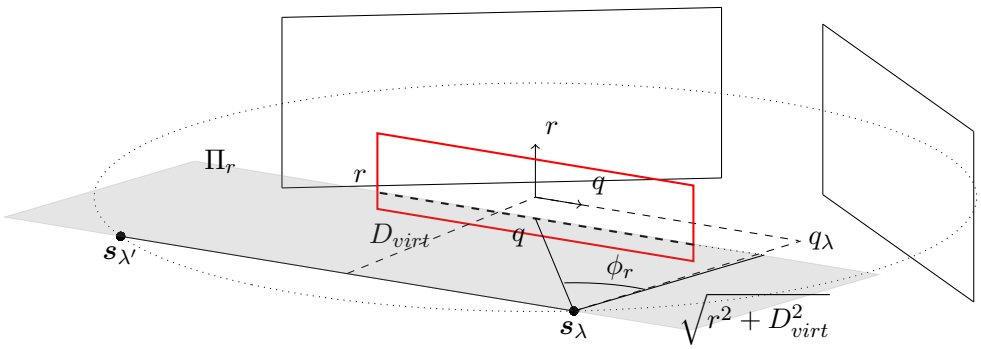

Figure 3.3: Illustration of the rebinning process of a pair of cone-beam projections with a planar detector. The virtual detector is drawn in red and is parallel to the virtual trajectory line defined by the two source positions $(\boldsymbol{s}_\lambda, \boldsymbol{s}_{\lambda'})$.

- the distance between the source $\boldsymbol{s}_\lambda$ and the pixel (q, r) of the virtual detector is $\sqrt{(q - q_\lambda)^2 + r^2 + D_{virt}^2}$, with q_λ the coordinate (in the virtual detector frame) of the ray orthogonal to the baseline.

The expression of $\cos\phi_r$ is therefore given by

$$\cos\phi_r = \frac{\sqrt{r^2 + D_{virt}^2}}{\sqrt{(q - q_\lambda)^2 + r^2 + D_{virt}^2}}. \tag{3.13}$$

To determine $\mathrm{d}\phi_r$ as a function of $\mathrm{d}q$, we use the relation $\tan\phi_r = \dfrac{q - q_\lambda}{\sqrt{r^2 + D_{virt}^2}}$. Differentiating each side of this equation with respect to q leads to

$$\frac{1}{\cos^2\phi_r}\frac{\mathrm{d}\phi_r}{\mathrm{d}q} = \frac{1}{\sqrt{r^2 + D_{virt}^2}} \tag{3.14}$$

Inserting Equation 3.13 and Equation 3.14 into Equation 3.12 and changing the integration interval from $\phi_r \in [-\pi/2, \pi/2]$ to $q \in \mathbb{R}$, $M_0(\lambda)$ is re-written as

$$I_0(\lambda) = \int_{\mathbb{R}} \frac{g_\lambda^*(q, r)}{\sqrt{(q - q_\lambda)^2 + r^2 + D_{virt}^2}}\mathrm{d}q \tag{3.15}$$

and the zeroth order DCC becomes

$$\int_{\mathbb{R}} \frac{g_\lambda^*(q, r)}{\sqrt{(q - q_\lambda)^2 + r^2 + D_{virt}^2}}\mathrm{d}q = \int_{\mathbb{R}} \frac{g_{\lambda'}^*(q, r)}{\sqrt{(q - q_{\lambda'})^2 + r^2 + D_{virt}^2}}\mathrm{d}q. \tag{3.16}$$

The benefit of applying extended fan-beam DCCs to cone-beam data is that they are able to deal with axially truncated projections as only an axial part of the projections can be selected to apply the DCCs, whereas existing cone-beam DCCs (presented in the following Section 3.3.2, Section 3.3.3) require non-truncated projections to be computed. This observation makes the FBDCC relevant to the helical trajectory where axial truncation is always present when scanning patients.

3.3.2 Cone-beam consistency conditions for sources on a plane

The complete cone-beam DCCs have been proposed in [Clackdoyle and Desbat, 2013]. It is assumed here that the trajectory plane and the detector plane do not intersect. The coordinate system is $(\boldsymbol{e}_x, \boldsymbol{e}_y, \boldsymbol{e}_z)$. The source $\boldsymbol{s} = (x_s, y_s, 0)$ only moves in the plane $z = 0$. The detector plane is the plane $z = D$. The cone-beam projections are characterized by the angular coordinates (θ, ϕ) such that the direction of a ray $\boldsymbol{\theta}$ is written

$$\boldsymbol{\theta} = \cos\phi \sin\theta \boldsymbol{e}_x + \sin\phi \sin\theta \boldsymbol{e}_y + \cos\theta \boldsymbol{e}_z. \tag{3.17}$$

All parameters are illustrated in Figure 3.4. The cone-beam projections are written

$$g_P(\boldsymbol{s}, \theta, \phi) = \int_0^\infty f\left(\boldsymbol{s} + t(\cos\phi \sin\theta \boldsymbol{e}_x + \sin\phi \sin\theta \boldsymbol{e}_y + \cos\theta \boldsymbol{e}_z)\right) \mathrm{d}t. \tag{3.18}$$

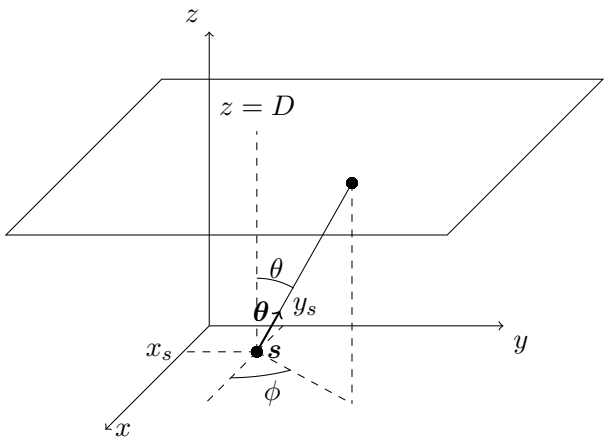

Figure 3.4: Illustration of the cone-beam geometry with sources on a plane for the description of the complete cone-beam DCCs.

The object f is entirely contained in the space $z > 0$ so that the trajectory plane and the object do not intersect. Let G_n^P be an intermediate function of order n defined as

$$G_n^P(\boldsymbol{s}, X, Y) = \int_0^{\pi/2} \int_0^{2\pi} g_P(\boldsymbol{s}, \theta, \phi)(X\cos\phi + Y\sin\phi)^n \frac{\tan^{n+1}\theta}{\cos\theta} \mathrm{d}\phi \mathrm{d}\theta. \tag{3.19}$$

For non-truncated cone-beam projections g_P, the cone-beam DCCs for sources on the plane $z = 0$ state that

$$G_n^P(\boldsymbol{s}, X, Y) = K_n(X, Y, -x_s X - y_s Y) \tag{3.20}$$

for some homogeneous polynomial $K_n(X, Y, Z)$ of degree $n \in \mathbb{N}$, if and only if g_P is the divergent beam transform, from sources on the plane $z = 0$, of some attenuation function f.

In practice (see [Clackdoyle and Desbat, 2013]), the two variables X, Y are expressed in terms of source position coordinates x_s, y_s, and the DCCs take the form of a polynomial of degree n in the source coordinates (similarly to the Helgason-Ludwig DCCs or the complete fan-beam DCCs for sources on a line).

3.3.3 Cone-beam consistency conditions for sources on a circular trajectory

In the previous section, we presented complete DCCs for sources on a plane that does not intersect the detector plane. In this section, we present only necessary cone-beam DCCs for a circular trajectory where the detector plane and the object may intersect the trajectory plane [Clackdoyle et al., 2016]. Let us consider the source position

$\boldsymbol{s}_\lambda = (R\cos\lambda, R\sin\lambda, 0)$ with $\lambda \in [0, 2\pi)$ the angle between $\boldsymbol{s}_\lambda$ and $\boldsymbol{e}_x$, and R the radius trajectory. The cone-beam projections $\hat{g}_\lambda$ are acquired on a planar detector, with coordinates (u, v), perpendicular to the trajectory plane and placed at a distance D from the source as illustrated in Figure 3.5.

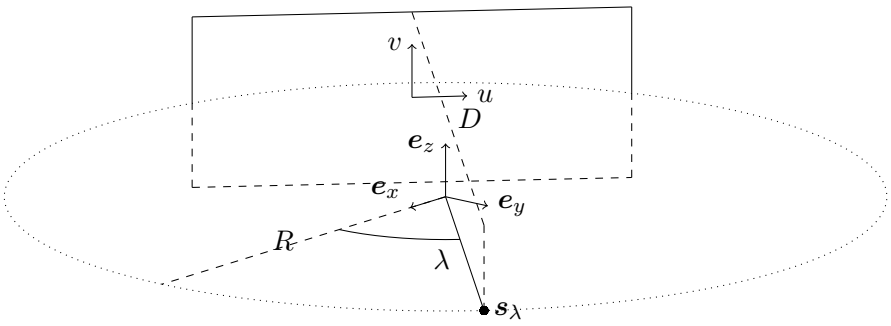

Figure 3.5: 3D illustration of the cone-beam geometry for planar detector and circular trajectory for the description of the cone-beam DCCs with sources on a circular trajectory.

The necessary cone-beam DCCs for circular trajectory state that, if all the projections $\hat{g}_\lambda, \lambda \in [0, 2\pi)$ are consistent, then the function

$$G_n^C(\lambda) = \int_{-\infty}^{\infty}\int_{-\infty}^{\infty} \frac{D}{\sqrt{u^2+v^2+D^2}} u^n \rho_n(v)\hat{g}_\lambda(u,v)\mathrm{d}u\mathrm{d}v, \tag{3.21}$$

with

$$\rho_n(v) = \int_{\mathbb{R}} \frac{(-2i\pi)^n + 2}{2(n+2)!}|\omega|\omega^n e^{2i\pi\omega v}\mathrm{d}\omega, \tag{3.22}$$

is a homogeneous polynomial of degree n in the source coordinates $\cos\lambda$ and $\sin\lambda$.

Both cone-beam DCCs ([Clackdoyle and Desbat, 2013] and [Clackdoyle et al., 2016]) were extensively studied in [Nguyen, 2021]. The author developed other polynomial cone-beam DCCs for various configurations of trajectory plane and detector plane by studying the link between [Clackdoyle and Desbat, 2013] and [Clackdoyle et al., 2016].

The major drawback with polynomial cone-beam DCCs is that they cannot handle truncated projections. Thus, they are not good candidates for the helical trajectory.

3.3.4 Grangeat-based consistency conditions

Grangeat-based DCCs are derived from Grangeat's relation [Grangeat, 1991] and apply to pairs of cone-beam projections. Grangeat relation provides a link between a cone-beam projection and the derivative of the 3D Radon transform of an attenuation function f. Some Grangeat-based DCCs were derived in the flat panel detector coordinates for pairs of cone beam projections with sources on a circular trajectory using the 2D Radon transform of the projections [Debbeler et al., 2013, Aichert et al., 2015].

In this section, we illustrate a Grangeat-based DCC for sources on a linear trajectory [Lesaint et al., 2018]. We consider two source positions $\boldsymbol{s}_\lambda = (x_0, \lambda, 0)$ and $\boldsymbol{s}_{\lambda'} = (x_0, \lambda', 0)$, with $\lambda, \lambda' \in \mathbb{R}$ along this trajectory as illustrated in Figure 3.6. Their cone-beam projections, respectively noted $\hat{g}_\lambda$ and $\hat{g}_{\lambda'}$, are acquired on a flat detector with coordinates (u, v) placed at a distance D from the linear trajectory. The detector is large enough such that the projections are not truncated in the u-direction. We note β the angle between the reference plane $(\boldsymbol{e}_x, \boldsymbol{e}_y)$ and the plane Π_β defined by the two source positions $\boldsymbol{s}_\lambda$, $\boldsymbol{s}_{\lambda'}$ and

the row v of the detector. Its normal vector is noted $\boldsymbol{n}_\beta$ and we have $v = D\tan\beta$. For the plane Π_β, Grangeat relation [Grangeat, 1991] is

$$\frac{\partial}{\partial s}\mathcal{R}f(\Pi_\beta)\bigg|_{s=\boldsymbol{s}_\lambda\cdot\boldsymbol{n}_\beta} = \frac{1}{\cos^2\beta}\frac{\partial}{\partial v}\int_{\mathbb{R}}\hat{g}_\lambda(u,v)\frac{D}{\sqrt{(u-\lambda)^2+v^2+D^2}}\mathrm{d}u \tag{3.23}$$

where the LHS of Equation 3.23 is the derivative in the direction of $\boldsymbol{n}_\beta$ of the 3D Radon transform of the object f over the plane Π_β. For this particular geometry, this derivative is constant over the entire trajectory as all source positions verify $s = \boldsymbol{s}_\lambda \cdot \boldsymbol{n}_\beta$. Hence, the RHS of Equation 3.23 is also constant over the trajectory and we have the following Grangeat-based DCC: for any plane Π_β containing two source positions $\boldsymbol{s}_\lambda$ and $\boldsymbol{s}_{\lambda'}$ and intersecting the detector row $v = D\tan\beta$, the cone-beam projections $\hat{g}_\lambda$ and $\hat{g}_{\lambda'}$ should verify

$$\frac{\partial}{\partial v}\int_{\mathbb{R}}\hat{g}_\lambda(u,v)\frac{D}{\sqrt{(u-\lambda)^2+v^2+D^2}}\mathrm{d}u = \frac{\partial}{\partial v}\int_{\mathbb{R}}\hat{g}_{\lambda'}(u,v)\frac{D}{\sqrt{(u-\lambda')^2+v^2+D^2}}\mathrm{d}u \tag{3.24}$$

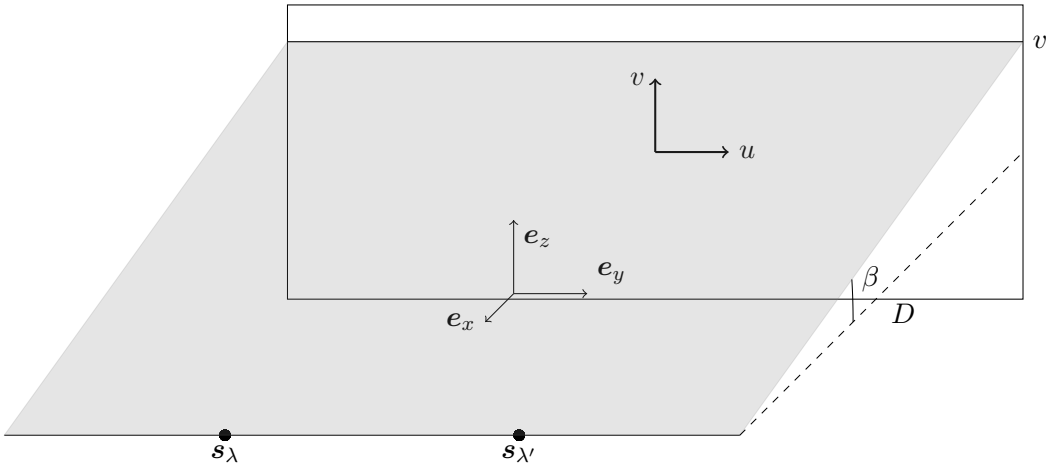

Figure 3.6: Illustration of a Grangeat-based DCCs for cone-beam projections with linear trajectory.

In the case of a linear trajectory, the Grangeat DCC implies that if all the projections $\hat{g}_\lambda,\ \lambda \in \mathbb{R}$ are consistent, then the function $\frac{\partial}{\partial v}\int_{\mathbb{R}}\hat{g}_\lambda(u,v)\frac{D}{\sqrt{(u-\lambda)^2+v^2+D^2}}\mathrm{d}u$ is a constant along the linear trajectory.

Grangeat-based DCCs can also deal with axially truncated projections because the derivative in the v direction is local (supposing that the projections are not truncated in the direction of the integration), so it is possible to select an axial part of the projections. Therefore, they may be relevant DCCs for the helical trajectory. However, they necessitate at least two planes to perform the differentiation step.

3.4 Review of DCC applications

In CT, numerous DCC-based artifacts correction algorithms were proposed. Generally, all DCC-based artifacts reduction algorithms are built on the minimization of a cost function derived from the DCCs. In this section, a short review of those methods is presented, starting with the correction of physics- and system- based artifacts. In a second part, we focus on the application of the DCCs to motion detection and correction.

3.4.1 Correction of physics- and system- based artifacts in CT

A few papers explored the use of DCCs for beam-hardening correction. Helgason-Ludwig DCCs were applied to fan-beam data by rebinning them into parallel data for the optimization of the bone-correction scaling factor [Tang et al., 2011] and the estimation of the polynomial coefficients of the projection linearization [Mou et al., 2008]. More recent publications have focused on the cone-beam geometry using Grangeat-based DCCs: in [Abdurahman et al., 2016], DCCs are used to find the optimal polynomial coefficients of the projection linearization for mono-material beam-hardening correction. The computation speed of the method was increased in [Wurfl et al., 2017] and it was generalized to bi-material beam-hardening correction in [Abdurahman et al., 2018].

On-line calibration algorithms for C-arm cone-beam CT were proposed to estimate the missing geometrical parameters such as the detector offsets, the source-to-detector distance and the source-to-isocenter distance using Grangeat-based DCCs in [Debbeler et al., 2013, Aichert et al., 2015] and the zeroth order of fan-beam DCCs in [Lesaint et al., 2017].

In recent works, DCCs were studied for scatter correction. Notably, DCCs were coupled to scatter deconvolution methods to optimize the scatter kernel parameters [Kim et al., 2015, Debbeler et al., 2019] or used to estimate the coefficients of empirical scatter models [Hoffmann et al., 2018] for cone-beam CT.

In the parallel beam geometry, Helgason-Ludwig DCCs were used to complete sinograms for limited angle tomography [Kudo and Saito, 1991b, Huang, 2020] but also in the context of truncated projections [Van Gompel et al., 2006] where a part of the object lies outside the FOV. This algorithm is similar to the one proposed in [Welch et al., 1998] for SPECT data. For the fan-beam geometry, integral invariants were used to restore projections deteriorated by some detector defaults [Chen and Leng, 2005, Tang et al., 2012]. In the latter papers, DCCs provide a link between a pixel value of the projections and the other projections in the acquisition, making it is possible to estimate the missing data.

3.4.2 Application to motion detection and correction in CT

One of the main application of DCCs is the detection and correction of motion. We present here some relevant papers that dealt with this topic depending on the type of motion, rigid or non-rigid.

3.4.2.1 Rigid motion

In 2D fan-beam CT, various integral invariants were presented in [Wei et al., 2006] and their use was illustrated with a motion detection problem. For a pair of projections, a consistency measurement is defined as the ratio of the two corresponding integral invariants. If the measurement is 1, then the projections were assumed consistent, otherwise, the projections were corrupted by motion.

In [Yu et al., 2006] and [Yu and Wang, 2007], Helgason-Ludwig DCCs were expressed in the fan-beam geometry using the parallel to fan-beam rebinning. DCCs were then extended to the case of a translating object [Yu et al., 2006] and a general in-plane moving object [Yu and Wang, 2007] in the fan-beam geometry. The motion is modeled with a smooth function whose parameters are estimated by minimizing a least squared error based on the extended Helgason-Ludwig DCCs.

The complete DCC for fan-beam projections with sources on a line were applied to a motion detection problem [Clackdoyle et al., 2014]. Knowing the CT image of the dynamic elements of the phantom, sinograms of the dynamic elements were simulated for various motion parameters. Their moments of order n were computed and subtracted from the moments of the original sinogram. This operation is equivalent to subtracting the simulated

sinograms from the original sinogram because the moments Equation 3.6 are linear. The moments difference was fitted with a polynomial of degree n in the source coordinates and a cost function is defined as the ratio of the fit residual over the moments difference. The motion parameters were estimated by minimizing the cost function. The estimated parameters were far from the ground truth using only the zeroth order of the DCCs but could be correctly approximated with higher orders. The FBDCC was applied to a circular trajectory using pairs of projections. It was shown that motion parallel to the trajectory line could not be detected with the DCC.

More recent work employed Grangeat-based consistency conditions for the compensation of rigid motion in C-arm CT. In [Frysch and Rose, 2015], rigid motion was modeled with 6 parameters (3 in plane and 3 out of plane motion parameters). The consistency of a pair of projections was defined as the mean, over all available rows, of a smoothed absolute difference between the corresponding intermediate functions (as Equation 3.24). A global cost function was then defined as the sum of the consistency measurements for all possible pair combinations and minimized to estimate the parameters. The use of redundant pairs made this cost function quite robust with respect to noise. This article stated that the pairs with the most redundant data are the pairs of projections acquired with opposite gantry angles. In [Bier et al., 2017], motion was modeled with a global rigid motion matrix including detector shifts, patient translation and rotation. The consistency measurement was the sum over all possible combinations of the mean squared difference between two intermediate functions. The minimization of this cost function gave an estimation of motion parameters. The results were satisfying using only the shift detector and 3D patient translation but inconclusive with the addition of rotational parameters. In [Preuhs et al., 2019], the consistency measurement was defined as a function of the motion parameters. By differentiating the measurement with respect to the motion parameters, motion gradients in the axial direction were estimated.

3.4.2.2 Non-rigid motion

The non-rigid motion applications mostly focus on cardiac and respiratory motion. All the following papers deal with cone-beam CT with a circular source trajectory.

In [Leng et al., 2007], the integral invariants extended to the cone-beam geometry were used to replace motion corrupted projections by corrected projections obtained from projections acquired when the object was static. DCCs expressed a projection pixel value as a function of the integral of other projections from the acquisition, similarly as in [Chen and Leng, 2005, Tang et al., 2012]. The drawback of this algorithm is that it requires prior information regarding the time interval of the acquisition during which the object is moving or static.

[Unberath et al., 2017] proposed a respiratory motion compensation algorithm using Grangeat-based DCCs. The algorithm assumed that the heart motion results from the cranio-caudal displacement of the diaphragm which is parallel to the vertical axis of the detectors. For each projection, the diaphragm motion was associated to a vertical shift of the detector. Grangeat-DCCs were applied to pairs of cone-beam projections along specific set of planes containing the corresponding source positions. A global consistency metric was defined as the sum over all pair combinations of the mean squared difference of two intermediate functions over all planes. The metric was minimized to estimate the corresponding vertical shift for each projection. The low frequency components of the estimated detector shift corresponded to the breathing motion and were used in a reconstruction algorithm to compensate for respiratory motion. The high frequency components corresponded to the cardiac motion and were used as a cardiac surrogate for 4D reconstruction. A similar work was proposed in [Berger et al., 2017] with other fan-beam DCCs generalized to cone-beam projections by applying the DCCs along each row of the detectors.

Lastly, more recent work employed Grangeat-based DCCs to extract the respiratory signal [Luo and Luo, 2018] and used it as a surrogate for gating [Lian et al., 2020] in small animal cone-beam CT. In the two papers, DCCs applied to pairs of projections and the consistency metric of a pair was the mean squared absolute difference of the intermediate functions over all available planes. A global consistency measure for each projection was then defined by summing the consistency metric computed for all possible pairs with this reference projection. Plotted as a function of the projections' index, this consistency measure allowed the recovery of the respiratory signal.

3.5 Conclusion

In this chapter, we presented some well-known DCCs and their numerous applications in CT, particularly those regarding motion detection and correction. While some of the presented papers briefly mentioned the helical trajectory, they mostly studied the circular or linear trajectories of the x-ray source. Moreover, cylindrical detectors, which is the common shape of detectors for helical CT, are rarely mentioned in the context of cone-beam DCC.

In the next chapters of this thesis, we present our contributions regarding the application of DCCs to the helical trajectory with a cylindrical detector and how they can be used to detect unexpected and/or irregular respiratory motion in helical acquisitions, with a particular focus on those performed for the radiotherapy planning of thoracic and upper-abdominal cancers.

Part II

Contributions

Chapter 4

Data Consistency conditions in helical CT

The previous chapter presented existing DCCs along with their applications. Most of DCCs applied to linear or circular x-ray source trajectories, but none directly to a helical trajectory.

The objective of this chapter is to develop methods to apply DCCs to helical CT. The cone-beam DCCs for sources on a plane cannot be applied to the helical geometry because they require non-truncated projections. In helical CT, projections are generally axially truncated because of the limited size of the detector that does not cover the entire object. Due to this particularity of helical CT, known as the long object problem, we can only use DCCs that are able to handle axial truncation. Grangeat-based DCCs and FBDCC can apply to axially truncated projections because they only require a part of the cone-beam projections. In this thesis, we choose to work with the FBDCC because it has been shown to be more robust than the Grangeat-based DCCs with respect to the detection of inconsistencies [Lesaint et al., 2018]. This choice is discussed at the end of this chapter.

We propose here two approaches to apply the FBDCC to helical CT. We begin by introducing the pair-wise geometry of a pair of cone-beam projections in helical CT. Then, the two methods to apply the FBDCC to a helical trajectory are detailed. Firstly, we apply the FBDCC using rebinning. Secondly, the FBDCC is directly expressed in the cylindrical detector coordinates. Implementation details are given and both methods are validated with numerical simulations and mechanical phantom data acquired on a clinical CT scanner.

4.1 Pair-wise geometry in helical CT

The object coordinate system is noted $(\boldsymbol{e}_x, \boldsymbol{e}_y, \boldsymbol{e}_z)$. Let us consider two source positions $\boldsymbol{s}_\lambda$ and $\boldsymbol{s}_{\lambda'}$ on a helical trajectory and their corresponding cone-beam projections g_λ and $g_{\lambda'}$. The expression of the cone-beam projections is given in Section 1.3.2. The line connecting the two source positions, noted $\mathcal{B}_{\lambda,\lambda'}$, is called the *baseline*. This configuration is illustrated in Figure 4.1. This pair-wise geometry is the starting point for applying FBDCC to helical CT.

4.2 Pair-wise cone-beam DCCs using rebinning

In this section, we adapt the rebinning approach, described in Section 3.3.1, to the helical trajectory.

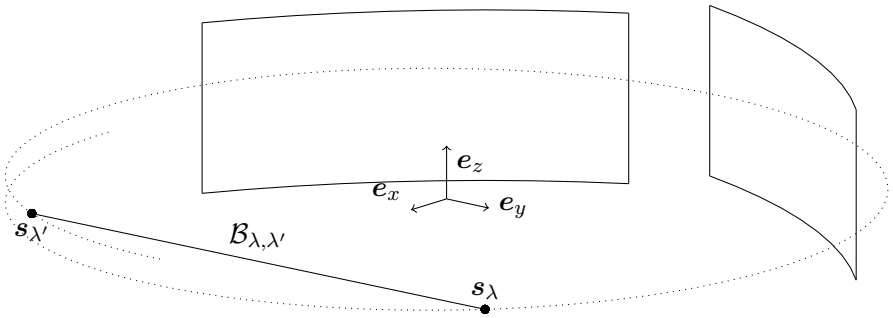

Figure 4.1: 3D illustration of the pair-wise geometry in helical CT. The two source positions $\boldsymbol{s}_\lambda$ and $\boldsymbol{s}_{\lambda'}$ are connected by the baseline $\mathcal{B}_{\lambda,\lambda'}$.

For a helical trajectory, projections are acquired on cylindrical detectors. The only pairs for which the detectors are parallel to the baseline are those in the direction of the helix axis. However, such pairs cannot be considered because the rebinning of their projections, which are axially truncated, would lead to truncated data on the virtual detector (the axial truncation becomes a lateral truncation at the rebinning). Consequently, such pairs, as well as other pairs (see Section 4.2.4), are not eligible for the use of FBDCC.

The rebinning process was mentioned in [Levine et al., 2010] and applied to a circular trajectory with flat detectors in [Lesaint et al., 2017]. We adapted it to the helical trajectory with cylindrical detectors.

4.2.1 Rebinning from cylindrical to virtual flat detector

We start from the pair-wise situation described in Section 4.1. The baseline $\mathcal{B}_{\lambda,\lambda'}$ is assimilated to a virtual linear trajectory with two source positions on it, $\boldsymbol{s}_\lambda$ and $\boldsymbol{s}_{\lambda'}$. To apply the FBDCC, projections are resampled onto a virtual detector whose rows are parallel to the baseline. It is assumed that the baseline $\mathcal{B}_{\lambda,\lambda'}$ and the FOV do not intersect. If they do, the rebinning process cannot be performed because the virtual detector cannot be defined (see Section 4.2.1.2). The first part of this rebinning process is the computation of the virtual detector which is performed as follows:

1. define the virtual detector orientation,
2. define the virtual detector boundaries,
3. backproject the projections g_λ and $g_{\lambda'}$ onto the virtual detector.

4.2.1.1 Virtual detector orientation

The virtual detector orientation is given by a frame, called *virtual detector frame*, which is defined such that

- the first axis is parallel to the baseline and is oriented by the unit vector $\boldsymbol{q}_{\lambda,\lambda'} = \operatorname{sign}(\sin(\lambda' - \lambda))\dfrac{\boldsymbol{s}_{\lambda'} - \boldsymbol{s}_\lambda}{\|\boldsymbol{s}_{\lambda'} - \boldsymbol{s}_\lambda\|}$.
- the third axis is oriented by the normalized mean $\boldsymbol{l}_{\lambda,\lambda'} = \dfrac{\boldsymbol{l}_\lambda + \boldsymbol{l}_{\lambda'}}{\|\boldsymbol{l}_\lambda + \boldsymbol{l}_{\lambda'}\|}$ of the two detectors' normals $\boldsymbol{l}_\lambda$ and $\boldsymbol{l}_{\lambda'}$. The normal of a cylindrical detector is orthogonal to the vertical axis of the detector, and points from the detector origin $(0, 0)$ to the source.

- the second axis, which is $\boldsymbol{l}_{\lambda,\lambda'} \times \boldsymbol{q}_{\lambda,\lambda'} = \boldsymbol{r}_{\lambda,\lambda'}$ such that $(\boldsymbol{q}_{\lambda,\lambda'}, \boldsymbol{r}_{\lambda,\lambda'}, \boldsymbol{l}_{\lambda,\lambda'})$ is an orthonormal basis, forms an acute angle with the helix axis $\boldsymbol{e}_z$ ($\boldsymbol{r}_{\lambda,\lambda'} \cdot \boldsymbol{e}_z > 0$). For a circular trajectory, the table feed is $d = 0$ and the third axis $\boldsymbol{r}_{\lambda,\lambda'} = \boldsymbol{e}_z$.

The rotation matrix from the virtual detector coordinate system to the object coordinate system, illustrated in Figure 4.2, is

$$R_{\text{BP}} = \begin{pmatrix} | & | & | \\ \boldsymbol{q}_{\lambda,\lambda'} & \boldsymbol{r}_{\lambda,\lambda'} & \boldsymbol{l}_{\lambda,\lambda'} \\ | & | & | \end{pmatrix}. \tag{4.1}$$

We call backprojection plane Π_{BP} the plane defined with $(\boldsymbol{q}_{\lambda,\lambda'}, \boldsymbol{r}_{\lambda,\lambda'})$, orthogonal to $\boldsymbol{l}_{\lambda,\lambda'}$, and passing through the origin $\boldsymbol{o} = (0, 0, 0)$. Π_{BP} contains the helix axis $\boldsymbol{e}_z$ since $\boldsymbol{l}_{\lambda,\lambda'}$ is orthogonal to $\boldsymbol{e}_z$.

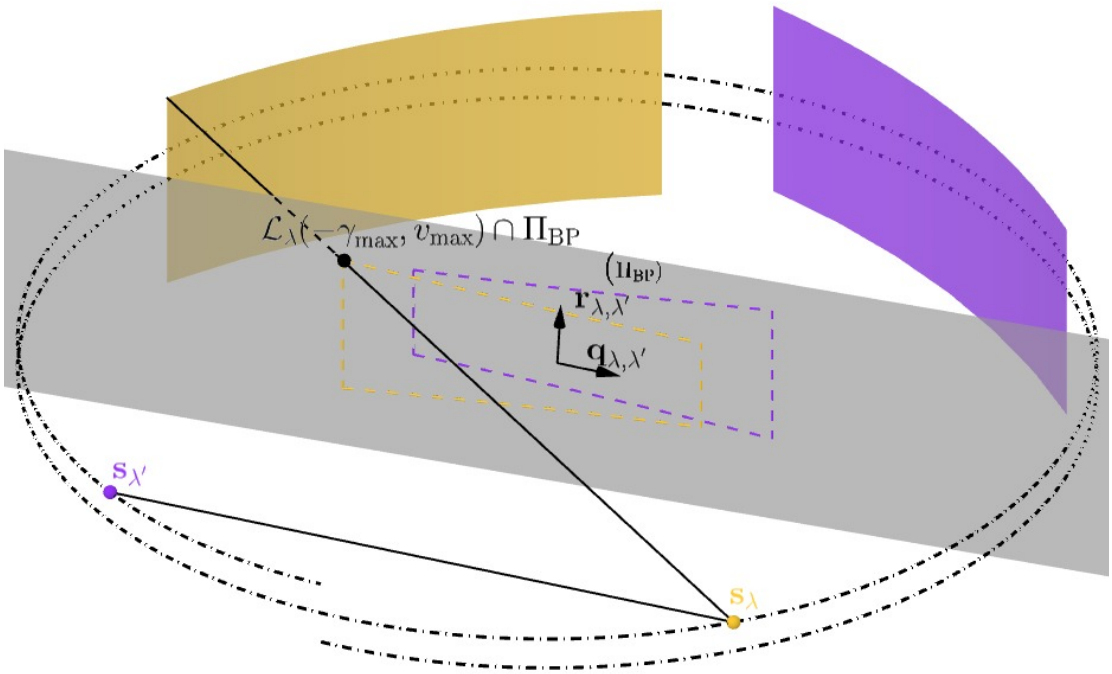

Figure 4.2: Illustration of the virtual detector frame and the backprojection plane for a pair of projections. The cylindrical detectors are shown in yellow and purple. The intersection $\mathcal{L}_\lambda(-\gamma_{\max}, v_{\max}) \cap \Pi_{\text{BP}}$ between the ray $(-\gamma_{\max}, v_{\max})$ emanating from $\boldsymbol{s}_\lambda$ and the backprojection plane Π_{BP} is drawn in gray. The limits of the two backprojections are drawn in yellow and purple on the backprojection plane (dotted colored lines) Π_{BP}.

4.2.1.2 Virtual detector boundaries

The virtual detector boundaries should account for the fact that the resampled projections should not be truncated laterally and that the FBDCC applies to the data acquired with both detectors. Therefore, the virtual detector should be defined as a function of the overlap between the two projections at their intersection with the backprojection plane Π_{BP}.

Let $\mathcal{L}_\lambda(\gamma, v)$ be the line from the source position $\boldsymbol{s}_\lambda$, to a detector pixel $\boldsymbol{p}_\lambda(\gamma, v)$, given by Equation 1.7. Its direction is $\boldsymbol{p}_\lambda(\gamma, v) - \boldsymbol{s}_\lambda$. With Figure 4.3, we see that the intersection

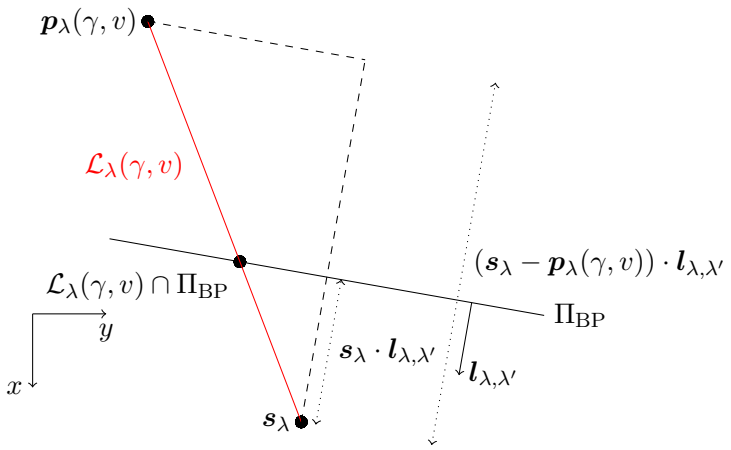

Figure 4.3: Illustration for the definition of the intersection $\mathcal{L}_\lambda(\gamma, v)$ with the backprojection plane Π_{BP}. The source position is $\boldsymbol{s}_\lambda$ and the cylindrical detector pixel is $\boldsymbol{p}_\lambda(\gamma, v)$.

of $\mathcal{L}_\lambda(\gamma, v)$ with the backprojection plane Π_{BP} is written as

$$\mathcal{L}_\lambda(\gamma, v) \cap \Pi_{\mathrm{BP}} = \boldsymbol{s}_\lambda + \frac{\boldsymbol{s}_\lambda \cdot \boldsymbol{l}_{\lambda,\lambda'}}{(\boldsymbol{s}_\lambda - \boldsymbol{p}_\lambda(\gamma, v)) \cdot \boldsymbol{l}_{\lambda,\lambda'}} (\boldsymbol{p}_\lambda(\gamma, v) - \boldsymbol{s}_\lambda) \,. \tag{4.2}$$

The limits of the backprojections are obtained by calculating this intersection for both projections and for all (γ, v) in $[-\gamma_{\max}, \gamma_{\max}] \times \{-v_{\max}, v_{\max}\}$, as illustrated in Figure 4.2 (dotted lines).

To define the detector boundaries, the coordinates $(q_\lambda(\gamma, v), r_\lambda(\gamma, v), l_\lambda(\gamma, v))^T$ of each intersection point with the backprojection plane $\mathcal{L}_\lambda(\gamma, v) \cap \Pi_{\mathrm{BP}}$ are computed in the virtual detector coordinate system $(\boldsymbol{q}_{\lambda,\lambda'}, \boldsymbol{r}_{\lambda,\lambda'}, \boldsymbol{l}_{\lambda,\lambda'})$ with

$$R_{\mathrm{BP}}^{\mathrm{T}} \left[\mathcal{L}_\lambda(\gamma, v) \cap \Pi_{\mathrm{BP}}\right] = \begin{pmatrix} q_\lambda(\gamma, v) \\ r_\lambda(\gamma, v) \\ l_\lambda(\gamma, v) \end{pmatrix} . \tag{4.3}$$

The coordinate $l_\lambda(\gamma, v)$ of the intersection along $\boldsymbol{l}_{\lambda,\lambda'}$ is in fact 0 as the calculations are now performed in the virtual detector coordinate system. The change of frame is illustrated in Figure 4.4.

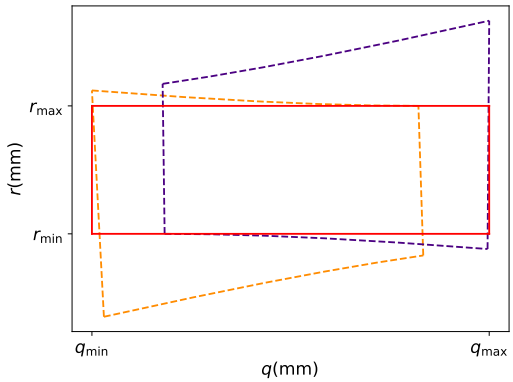

Figure 4.4: Illustration of the definition of the virtual detector boundaries. The frame considered here is the virtual detector frame. The two backprojections are the yellow and purple dotted lines and the resulting virtual detector is drawn in red.

To avoid any lateral truncation of the resampled projections, the limits of the virtual detector are defined as the ascribed range of the two backprojections in the direction of $\boldsymbol{q}_{\lambda,\lambda'}$ and the inscribed range in the direction of $\boldsymbol{r}_{\lambda,\lambda'}$.

• The backprojections ranges along the axis $\boldsymbol{q}_{\lambda,\lambda'}$ are given by

$$(q_\lambda^{\min}, q_\lambda^{\max}) = \left(\min_{\substack{\gamma\in\{-\gamma_{\max},\gamma_{\max}\}\\ v\in\{-v_{\max},v_{\max}\}}} (q_\lambda(\gamma, v)) \,, \max_{\substack{\gamma\in\{-\gamma_{\max},\gamma_{\max}\}\\ v\in\{-v_{\max},v_{\max}\}}} (q_\lambda(\gamma, v)) \right) \tag{4.4}$$

for the source position $\boldsymbol{s}_\lambda$ and

$$(q_{\lambda'}^{\min}, q_{\lambda'}^{\max}) = \left(\min_{\substack{\gamma\in\{-\gamma_{\max},\gamma_{\max}\}\\ v\in\{-v_{\max},v_{\max}\}}} (q_{\lambda'}(\gamma, v)) \,, \max_{\substack{\gamma\in\{-\gamma_{\max},\gamma_{\max}\}\\ v\in\{-v_{\max},v_{\max}\}}} (q_{\lambda'}(\gamma, v)) \right) \tag{4.5}$$

for the source position $\boldsymbol{s}_{\lambda'}$. Hence, to avoid any truncation, as shown in Figures 4.15 and 4.4, the largest range of overlap of the two backprojections, or ascribed range $[q_{\min}, q_{\max}]$, is taken in the direction of $\boldsymbol{q}_{\lambda,\lambda'}$, where

$$q_{\min} = \min\left(q_\lambda^{\min}, q_{\lambda'}^{\min}\right), \tag{4.6}$$

$$q_{\max} = \max\left(q_\lambda^{\max}, q_{\lambda'}^{\max}\right). \tag{4.7}$$

• With the objective of avoiding lateral truncation, the axial limits of the detector correspond to the smallest overlap of the two backprojections in the direction of $\boldsymbol{r}_{\lambda,\lambda'}$. Hence, the inscribed range in the direction of $\boldsymbol{r}_{\lambda,\lambda'}$ is written $[r_{\min}, r_{\max}]$, where

$$r_{\min} = \max\left(\max_{\gamma\in[-\gamma_{\max},\gamma_{\max}]} (r_\lambda(\gamma, -v_{\max})) \,, \max_{\gamma\in[-\gamma_{\max},\gamma_{\max}]} (r_{\lambda'}(\gamma, -v_{\max})) \right), \tag{4.8}$$

$$r_{\max} = \min\left(\min_{\gamma\in[-\gamma_{\max},\gamma_{\max}]} (r_\lambda(\gamma, v_{\max})) \,, \min_{\gamma\in[-\gamma_{\max},\gamma_{\max}]} (r_{\lambda'}(\gamma, v_{\max})) \right). \tag{4.9}$$

Finally, the virtual detector is defined with the coordinates of two opposite corners in the virtual detector coordinate system, $(q_{\min}, r_{\min}, 0)$ and $(q_{\max}, r_{\max}, 0)$, as illustrated in Figure 4.4.

If we allowed pairs whose baseline intersects with the FOV, the two rays matching the direction of the baseline (one from $\boldsymbol{s}_\lambda$ and one from $\boldsymbol{s}_{\lambda'}$) would be parallel to the backprojection plane, and would never intersect. For such rays we would have $(\boldsymbol{s}_\lambda - \boldsymbol{p}_\lambda(\gamma, v)) \cdot \boldsymbol{l}_{\lambda,\lambda'} = 0$. Equation 4.2 is not defined, hence, Equation 4.3 and the virtual detector cannot be defined.

4.2.1.3 Backprojection onto the virtual detector

To perform the backprojection, the virtual detector coordinates $(q_\lambda, r_\lambda, 0)$ of a pixel from the virtual detector can be converted into (x, y, z) coordinates of the object coordinate system $(\boldsymbol{e}_x, \boldsymbol{e}_y, \boldsymbol{e}_z)$ (Figure 4.5) with

$$(x, y, z)^T = R_{\mathrm{BP}}(q_\lambda, r_\lambda, 0)^T. \tag{4.10}$$

Using Figure 4.6, any point $\boldsymbol{a}$ with coordinates (x_a, y_a, z_a) on the backprojection plane Π_{BP} can be mapped to a cylindrical detector pixel with

$$\gamma_a = \tan^{-1}\left(\frac{(\boldsymbol{a} - \boldsymbol{s}_\lambda) \cdot \boldsymbol{l}_\lambda^\perp}{(\boldsymbol{a} - \boldsymbol{s}_\lambda) \cdot \boldsymbol{l}_\lambda}\right) \tag{4.11}$$

$$v_a = \boldsymbol{e}_z \cdot \left[(\boldsymbol{a} - \boldsymbol{s}_\lambda)\frac{D\cos\gamma_a}{(\boldsymbol{s}_\lambda - \boldsymbol{a}) \cdot \boldsymbol{l}_\lambda}\right] \tag{4.12}$$

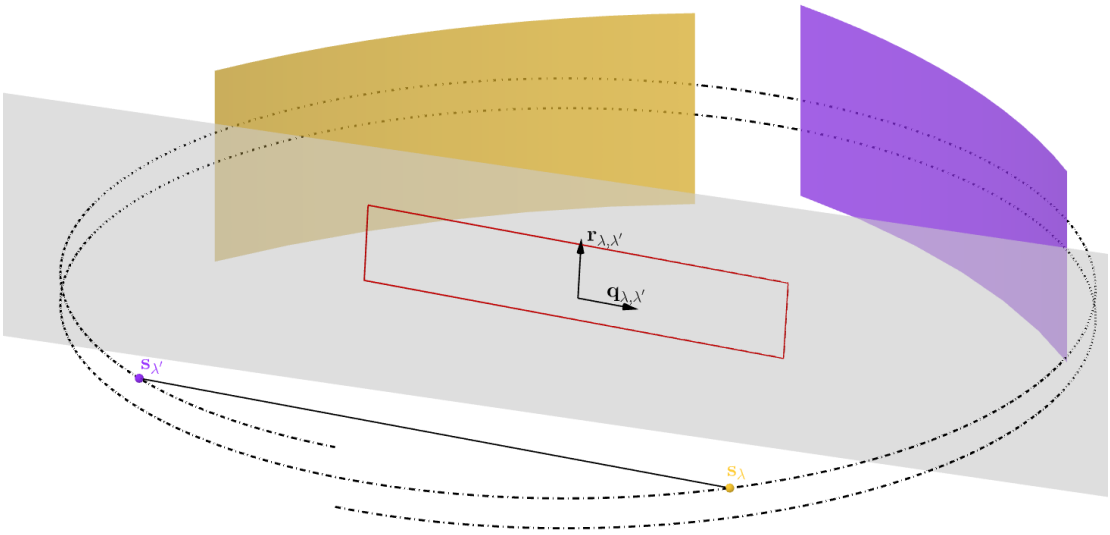

Figure 4.5: Illustration of the final computation of the virtual detector (continuous red line) for a pair of projections.

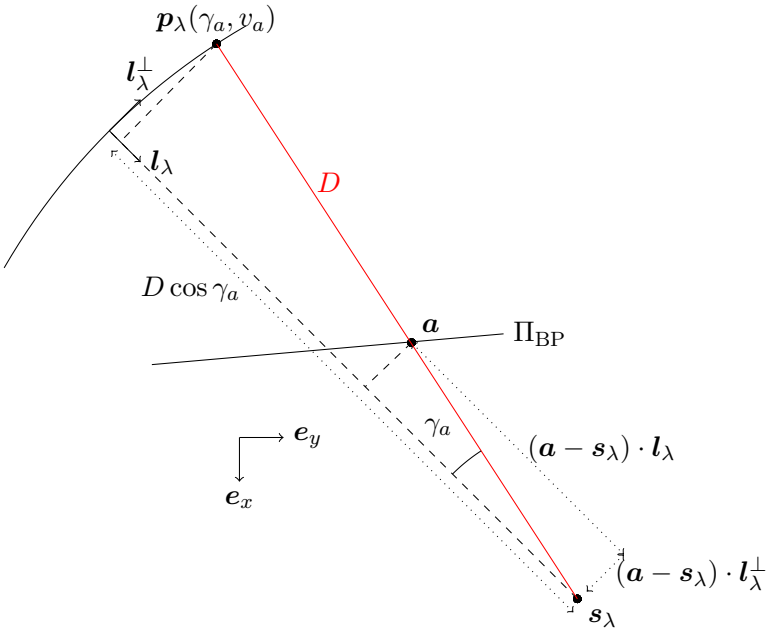

Figure 4.6: Illustration of the mapping of a point $\boldsymbol{a} = (x_a, y_a, z_a)$ on the backprojection plane Π_{BP} to the corresponding cylindrical detector pixel $\boldsymbol{p}_\lambda(\gamma_a, v_a)$.

where D is the source-detector distance, $\boldsymbol{l}_\lambda$ is the normal of the cylindrical detector and $\boldsymbol{l}_\lambda^\perp = \boldsymbol{e}_z \times \boldsymbol{l}_\lambda$ is the orthogonal to $\boldsymbol{l}_\lambda$ and $\boldsymbol{e}_z$. The values of the backprojected images g^*_λ and $g^*_{\lambda'}$ are estimated with the mapping Equation 4.11 for each pixel of the virtual detector.

4.2.2 Expression of the DCC

After the rebinning process, the FBDCC is applied along each row of the virtual detector as described in Section 3.3.1. For a pair of rebinned projections $(g^*_\lambda(q,r), g^*_{\lambda'}(q,r))$, the FBDCC in the virtual detector coordinate system is (see Figure 4.2)

$$\int_{q_{\min}}^{q_{\max}} \frac{g^*_\lambda(q,r)}{\sqrt{(q-q_\lambda)^2 + r^2 + D^2_{virt}}} \mathrm{d}q = \int_{q_{\min}}^{q_{\max}} \frac{g^*_{\lambda'}(q,r)}{\sqrt{(q-q_{\lambda'})^2 + r^2 + D^2_{virt}}} \mathrm{d}q. \tag{4.13}$$

with $R^{\mathrm{T}}_{\mathrm{BP}} \boldsymbol{s}_\lambda = (q_\lambda, 0, l_\lambda)^{\mathrm{T}}$ and $R^{\mathrm{T}}_{\mathrm{BP}} \boldsymbol{s}_{\lambda'} = (q_{\lambda'}, 0, l_{\lambda'})^{\mathrm{T}}$, the coordinates of the source positions $\boldsymbol{s}_\lambda$ and $\boldsymbol{s}_{\lambda'}$ in the virtual coordinate system and $l_\lambda = l_{\lambda'} = D_{virt}$, the orthogonal distance between the baseline and the virtual detector.

4.2.3 Discretization of the moment

To discretize the FBDCC, we first define the discretization of the virtual detector. The virtual detector is discretized in $N^*_{\mathrm{cols}} \times N^*_{\mathrm{rows}}$ such that

$$N^*_{\mathrm{cols}} = \lfloor \frac{q_{\max} - q_{\min}}{\Delta_q} \rfloor \tag{4.14}$$

$$N^*_{\mathrm{rows}} = \lfloor \frac{r_{\max} - r_{\min}}{\Delta_r} \rfloor \tag{4.15}$$

with $\Delta_q = m_{BP}\Delta_\gamma$, $\Delta_r = m_{BP}\Delta_v$ and m_{BP} is the magnitude corresponding to the mean normalized inverse distance between both source positions and their backprojections. The two backprojections being symmetrical with respect to the plane $(\boldsymbol{l}_{\lambda,\lambda'}, \boldsymbol{r}_{\lambda,\lambda'})$, the magnitude can be defined from one source position only, and we have

$$m_{BP} = \frac{1}{2N_{cols}} \sum_{\substack{\gamma \in [-\gamma_{\max}, \gamma_{\max}] \\ v \in \{-v_{\max}, v_{\max}\}}} \frac{\boldsymbol{s}_\lambda \cdot \boldsymbol{l}_{\lambda,\lambda'}}{(\boldsymbol{s}_\lambda - \boldsymbol{p}_\lambda(\gamma, v)) \cdot \boldsymbol{l}_{\lambda,\lambda'}}. \tag{4.16}$$

where N_{cols} is the number of samples of γ (see Section 4.3.3).

Therefore, the virtual detector coordinates q and r are sampled as $q_{i^*} = q_{\min} + i^*\Delta_q$ with $i^* \in \{1, ..., N^*_{\mathrm{cols}}\}$, and $r_{j^*} = r_{\min} + j^*\Delta_r$ with $j^* \in \{1, ..., N^*_{\mathrm{rows}}\}$.

The discretization of the left side of Equation 4.13 yields

$$M_{j^*} \simeq \sum_{i^*=1}^{N^*_{\mathrm{cols}}} \frac{g^*_\lambda(q_{i^*}, r_{j^*})}{\sqrt{(q_{i^*} - q_\lambda)^2 + r^2_{j^*} + D^2_{virt}}} \Delta_q \tag{4.17}$$

and the same for the RHS of Equation 4.13 with λ' instead of λ.

4.2.4 Applicability conditions

To ensure that the FBDCC computed along each row are correct and valid, not all pairs of projections can be considered. In this part, we describe the necessary requirements to apply the rebinning approach to a pair of projections. They can be summarized in the two following geometrical considerations.

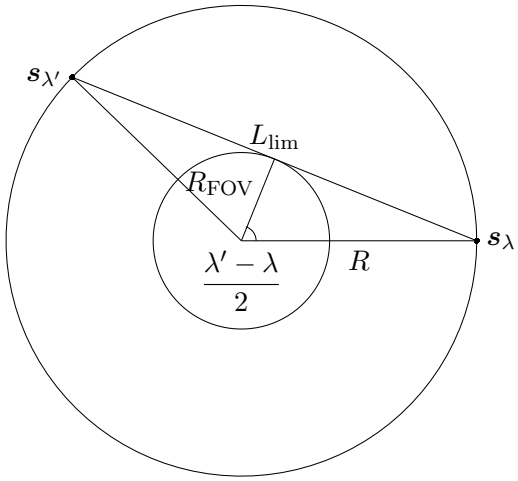

Figure 4.7: Illustration of the FOV intersection condition for the application of the rebinning approach. The source positions are $\boldsymbol{s}_\lambda$ and $\boldsymbol{s}_{\lambda'}$. R_{Fov} and R are respectively the FOV radius and the helical trajectory radius.

4.2.4.1 Field-of-view intersection

To allow for the computation of the virtual detector, the compact support of the object f and the baseline $\mathcal{B}_{\lambda,\lambda'}$ must not intersect. In practice, as we do not assume prior knowledge regarding the aspect of f, we impose that the FOV of the scanner and the baseline do not intersect. Visualizing the trajectory from an axial point of view, as in Figure 4.7, we see that the maximal length of the segment L_{lim} connecting two source positions $\boldsymbol{s}_\lambda$ and $\boldsymbol{s}_{\lambda'}$ must be such that $\sqrt{(x_{\lambda'} - x_\lambda)^2 + (y_{\lambda'} - y_\lambda)^2} < L_{lim} = 2\sqrt{R^2 - R_{\text{FOV}}^2}$ where (x_λ, y_λ) and $(x_{\lambda'}, y_{\lambda'})$ are the x-coordinate and y-coordinate of $\boldsymbol{s}_\lambda$ and $\boldsymbol{s}_{\lambda'}$ respectively. With the geometrical observations from Figure 4.7, we deduce

$$\cos\left(\frac{\lambda - \lambda'}{2}\right) > \frac{R_{\text{FOV}}}{R} \tag{4.18}$$

4.2.4.2 Overlapping and truncation

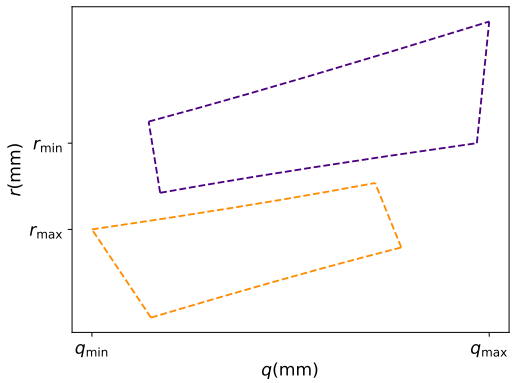

Figure 4.8: Illustration of an insufficient overlap between two backprojections. The frame considered here is the virtual detector frame. The two backprojections are the yellow and purple dotted lines. No virtual detector is computed because the overlap condition is not respected. Here we have $r_{\max} < r_{\min}$. A sufficient overlap is illustrated in Figure 4.4.

One major benefit of the FBDCC is that they can deal with axial truncation because the moments (Equation 4.13) are calculated along the virtual detector rows. The computation of the FBDCC on the virtual detector requires a sufficient overlap of the two projections in the region of the backprojection plane to avoid any lateral truncation and apply the DCCs to the common data of both projections. This requirement is met if the inscribed zone formed by the backprojections of a pair of projections is at least one line. Mathematically we have

$$r_{\max} - r_{\min} > 0. \tag{4.19}$$

Figure 4.8 illustrates the lack of overlapping between two backprojections: FBDCC cannot be applied to this pair.

4.2.5 Consistency metric

For a given pair of projections $(g_\lambda, g_{\lambda'})$, moments are computed following Equation 4.17 for all N^*_{rows} rows of the virtual detector. The pair-wise cone-beam consistency metric is defined as

$$E^{Virt}_{\lambda,\lambda'} = 2 \times \frac{1}{N^*_{\text{rows}}} \sum_{j^*=1}^{N^*_{\text{rows}}} \frac{\left| M_{j^*} - M'_{j^*} \right|}{M_{j^*} + M'_{j^*}}. \tag{4.20}$$

If the two projections g_λ and $g_{\lambda'}$ are consistent, then $E^{Virt}_{\lambda,\lambda'} = 0$.

4.3 Pair-wise cone-beam DCCs on cylindrical detectors

The content of this section is based on the contribution [Mouchet et al., 2022b] that was submitted to the journal IEEE Transactions on Medical Imaging.

In this part, DCCs are applied to helical CT by computing the zeroth order moments directly in the cylindrical detector coordinates. By doing so, we avoid the computation of the virtual detector which enables the computation of the FBDCC for pairs whose baseline intersects the FOV and increase the number of pairs with a DCC in a helical CT.

We consider a pair of source positions $(\boldsymbol{s}_\lambda, \boldsymbol{s}_{\lambda'})$ as in Section 4.1. FBDCC can be computed on any plane containing the two source positions. As the FBDCC applies to untruncated projections, the plane must also intersect the two lateral borders of the projections to avoid lateral truncation (the cone-beam projections are initially not laterally truncated). We begin by defining such planes and then give the expression of the zeroth order moments using the cylindrical detector coordinates.

4.3.1 Definition of the DCC planes

We start from the pair-wise situation described in Section 4.1 and by the definition of the direction of the baseline. Its definition differs from the one in the previous section as we now allow pairs with a baseline intersecting with the FOV. If $\lambda = 0$ and $\lambda' = \pi$, we have $\boldsymbol{q}_{\lambda,\lambda'} = 0$ because of $\text{sign}(\sin(\lambda - \lambda'))$, and the direction of the baseline is not correctly defined. Therefore, the baseline $\mathcal{B}_{\lambda,\lambda'}$ is oriented here with the unit vector

$$\boldsymbol{b}_{\lambda,\lambda'} = \text{sign}(\lambda' - \lambda) \frac{\boldsymbol{s}_{\lambda'} - \boldsymbol{s}_\lambda}{\|\boldsymbol{s}_{\lambda'} - \boldsymbol{s}_\lambda\|} \tag{4.21}$$

illustrated in Figure 4.10 (which is now the one forming an acute angle with the helix axis $\boldsymbol{e}_z$, $\boldsymbol{b}_{\lambda,\lambda'} \cdot \boldsymbol{e}_z > 0$). We define a reference plane $\Pi_{\lambda,\lambda'}$ with its orthogonal $\boldsymbol{n}_{\lambda,\lambda'}$ that is

$$\boldsymbol{n}_{\lambda,\lambda'} = \boldsymbol{c}_{\lambda,\lambda'} \times \boldsymbol{b}_{\lambda,\lambda'} \tag{4.22}$$

where

$$\boldsymbol{c}_{\lambda,\lambda'} = \cos\bar{\lambda}\,\boldsymbol{e}_x + \sin\bar{\lambda}\,\boldsymbol{e}_y \tag{4.23}$$

is the unit vector orthogonal to the baseline $\mathcal{B}_{\lambda,\lambda'}$ and the rotation axis $\boldsymbol{e}_z$. The vector $\boldsymbol{c}_{\lambda,\lambda'}$ points from the midpoint between $\boldsymbol{s}_\lambda$ and $\boldsymbol{s}_{\lambda'}$ (which is on the baseline $\mathcal{B}_{\lambda,\lambda'}$) towards the helix axis, with

$$\bar{\lambda} \;=\; \begin{cases} \dfrac{\lambda+\lambda'}{2} & \text{if } \dfrac{\lambda'-\lambda}{2} \pmod{2\pi} \in \left[\dfrac{\pi}{2}, \dfrac{3\pi}{2}\right], \\ \dfrac{\lambda+\lambda'}{2} + \pi & \text{otherwise.} \end{cases} \tag{4.24}$$

The two cases are illustrated in Figure 4.9.

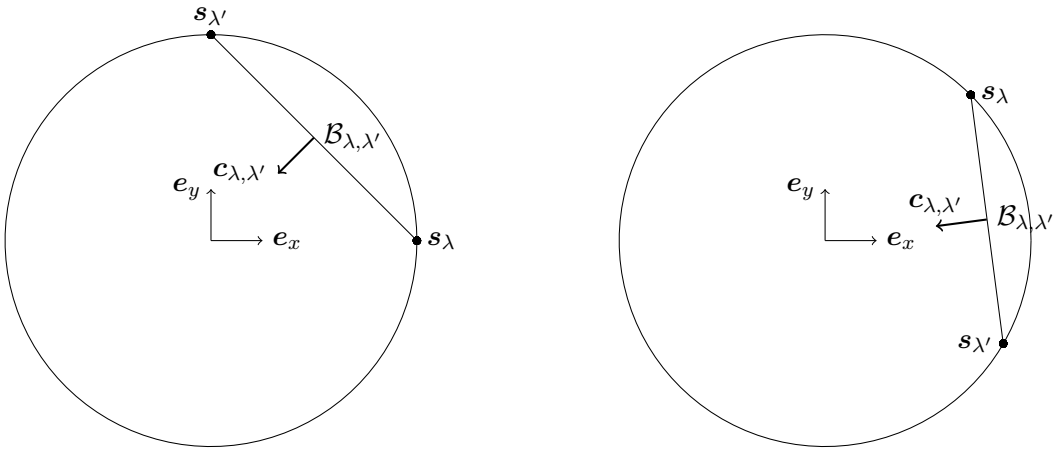

(a) $\bar{\lambda} = \dfrac{\lambda+\lambda'}{2} + \pi$. (b) $\bar{\lambda} = \dfrac{\lambda+\lambda'}{2}$.

Figure 4.9: Illustration of the definition of $\bar{\lambda}$ from two source positions $\boldsymbol{s}_\lambda$ and $\boldsymbol{s}_{\lambda'}$.

The other planes $\Pi_{\boldsymbol{\tau}}$ with $\boldsymbol{\tau} = (\lambda, \lambda', \beta)$ are defined by their angle β with the reference plane $\Pi_{\lambda,\lambda'}$ (Figure 4.10). Their orthogonal is

$$\boldsymbol{n}_\tau = \cos\beta\,\boldsymbol{n}_{\lambda,\lambda'} - \sin\beta\,\boldsymbol{c}_{\lambda,\lambda'}. \tag{4.25}$$

The angle β is measured positively in the counter-clockwise direction when viewed in the direction $\boldsymbol{b}_{\lambda,\lambda'}$. With the third vector $\boldsymbol{c}_{\boldsymbol{\tau}} = \boldsymbol{b}_{\lambda,\lambda'} \times \boldsymbol{n}_{\boldsymbol{\tau}}$, the triplet $(\boldsymbol{c}_{\boldsymbol{\tau}}, \boldsymbol{b}_{\lambda,\lambda'}, \boldsymbol{n}_{\boldsymbol{\tau}})$ is an orthonormal basis which is used in Section 4.3.2 to derive cone-beam DCCs from the FBDCC. If we let $\boldsymbol{c}_{\boldsymbol{\tau}} = (c_1, c_2, c_3)$, $\boldsymbol{b}_{\lambda,\lambda'} = (b_1, b_2, b_3)$ and $\boldsymbol{n}_{\boldsymbol{\tau}} = (n_1, n_2, n_3)$ be the coordinates of these vectors, they can be derived by three successive rotations

$$\begin{pmatrix} c_1 & b_1 & n_1 \\ c_2 & b_2 & n_2 \\ c_3 & b_3 & n_3 \end{pmatrix} = \begin{pmatrix} \cos\bar{\lambda} & -\sin\bar{\lambda} & 0 \\ \sin\bar{\lambda} & \cos\bar{\lambda} & 0 \\ 0 & 0 & 1 \end{pmatrix} \begin{pmatrix} 1 & 0 & 0 \\ 0 & \cos\alpha & -\sin\alpha \\ 0 & \sin\alpha & \cos\alpha \end{pmatrix} \begin{pmatrix} \cos\beta & 0 & -\sin\beta \\ 0 & 1 & 0 \\ \sin\beta & 0 & \cos\beta \end{pmatrix} \tag{4.26}$$

with $\alpha = \arccos(\boldsymbol{b}_{\lambda,\lambda'} \cdot (\boldsymbol{e}_z \times \boldsymbol{c}_{\lambda,\lambda'}))$ the angle between the axial planes (defined by $z = \text{const}$)

and $\mathcal{B}_{\lambda,\lambda'}$. We obtain

$$\begin{cases} c_1 = \cos\bar{\lambda}\cos\beta + \sin\bar{\lambda}\sin\alpha\sin\beta, \\ c_2 = \sin\bar{\lambda}\cos\beta - \cos\bar{\lambda}\sin\alpha\sin\beta, \\ c_3 = \cos\alpha\sin\beta, \\ b_1 = -\sin\bar{\lambda}\cos\alpha, \\ b_2 = \cos\bar{\lambda}\cos\alpha, \\ b_3 = \sin\alpha, \\ n_1 = -\cos\bar{\lambda}\sin\beta + \sin\bar{\lambda}\sin\alpha\cos\beta, \\ n_2 = -\sin\bar{\lambda}\sin\beta - \cos\bar{\lambda}\sin\alpha\cos\beta, \\ n_3 = \cos\alpha\cos\beta. \end{cases} \tag{4.27}$$

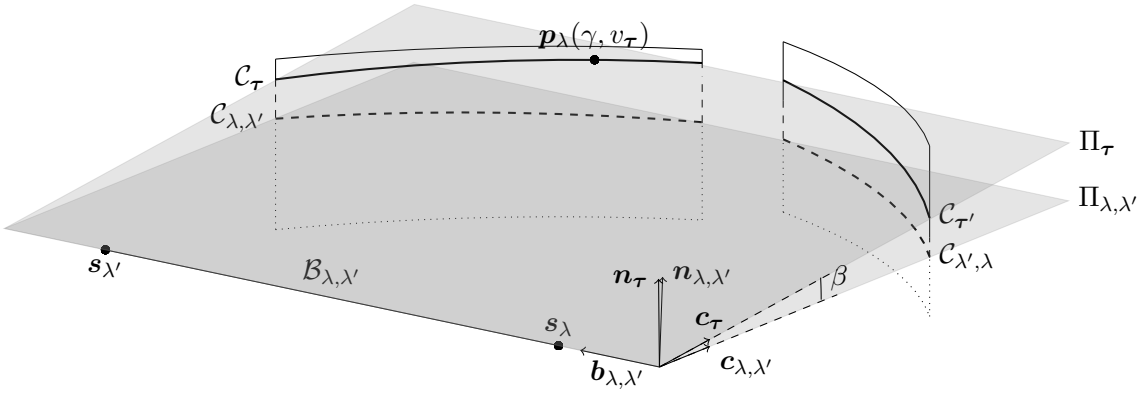

Figure 4.10: 3D illustration of the cone-beam pair-wise geometry. The baseline $\mathcal{B}_{\lambda,\lambda'}$ is defined by the source positions $\boldsymbol{s}_\lambda$ and $\boldsymbol{s}_{\lambda'}$ (with $\lambda < \lambda'$ in this case). The intersection of the reference plane $\Pi_{\lambda,\lambda'}$ with the two detectors defines the two curves $\mathcal{C}_{\lambda,\lambda'}$ and $\mathcal{C}_{\lambda',\lambda}$ (thick dotted lines). The intersection of a plane $\Pi_{\boldsymbol{\tau}}$ with the two detectors defines the two curves $\mathcal{C}_{\boldsymbol{\tau}}$ and $\mathcal{C}_{\boldsymbol{\tau}'}$ with $\boldsymbol{\tau} = (\lambda, \lambda', \beta)$ and $\boldsymbol{\tau}' = (\lambda', \lambda, \beta)$ (thick continuous lines). The dotted limits of the detectors are below the reference plane $\Pi_{\lambda,\lambda'}$ and the dashed ones are below the plane $\Pi_{\boldsymbol{\tau}}$.

4.3.2 Expression of the DCC

We now derive the expression of the FBDCC in the cylindrical detector coordinates. The intersection of the plane $\Pi_{\boldsymbol{\tau}}$ and the cone-beam from the source position $\boldsymbol{s}_\lambda$ defines a fan-beam which may be parameterized by the angle ϕ between $\boldsymbol{c}_{\boldsymbol{\tau}}$ and each ray (see Figure 4.11). We note

$$g_{\boldsymbol{\tau}}(\phi) = \int_0^\infty f\left(\boldsymbol{s}_\lambda + t(\cos\phi\,\boldsymbol{c}_{\boldsymbol{\tau}} + \sin\phi\,\boldsymbol{b}_{\lambda,\lambda'})\right)\mathrm{d}t \tag{4.28}$$

the line integral at angle ϕ in the fan-beam. We define the intermediate function $M_{\boldsymbol{\tau}}$ in terms of the projection $g_{\boldsymbol{\tau}}(\phi)$ as

$$M_{\boldsymbol{\tau}} = \int_{-\pi}^{\pi} \frac{g_{\boldsymbol{\tau}}(\phi)}{\cos\phi}\mathrm{d}\phi \tag{4.29}$$

and refer to it as the moment of the projection $g_{\boldsymbol{\tau}}(\phi)$. This integral, which presents two singularities at $-\pi/2$ and $\pi/2$, must be understood in the sense of the Cauchy principal value.

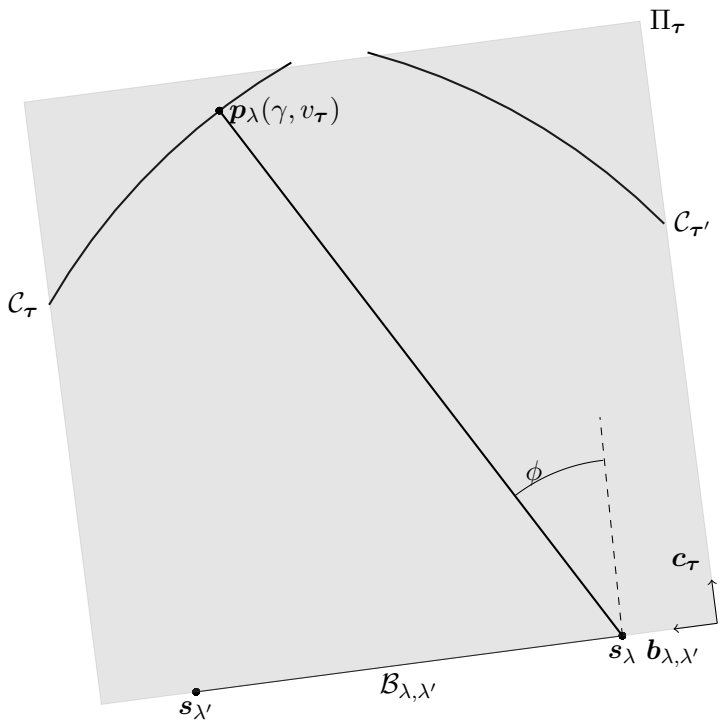

Figure 4.11: Geometric illustration in the plane $\Pi_{\boldsymbol{\tau}}$ of the angle ϕ between $\boldsymbol{c}_{\boldsymbol{\tau}}$ and the line defined by $\boldsymbol{s}_\lambda$ and $\boldsymbol{p}_\lambda(\gamma, v_{\boldsymbol{\tau}})$.

The computation of the moment $M_{\boldsymbol{\tau}}$ requires untruncated fan-beam projections. Since the cone-beam projections are generally truncated in the v direction, we exclude projection pairs which define a baseline in the direction $\boldsymbol{e}_z$, and planes with a normal $\boldsymbol{n}_{\boldsymbol{\tau}}$ orthogonal to $\boldsymbol{e}_z$, as in the previous section, by setting $\lambda' - \lambda \neq 0 \,(\mathrm{mod}\, 2\pi)$, $\alpha \in [0, \pi) \setminus \{\frac{\pi}{2}\}$ and $\beta \in (-\pi/2, \pi/2)$. Consequently, the two source positions $\boldsymbol{s}_\lambda$ and $\boldsymbol{s}_{\lambda'}$ are the only ones along $\mathcal{B}_{\lambda,\lambda'}$ to which the FBDCC can be applied in the plane $\Pi_{\boldsymbol{\tau}}$ and we have from Equation 4.29 the DCC

$$M_{\boldsymbol{\tau}} = M_{\boldsymbol{\tau}'} \tag{4.30}$$

where $M_{\boldsymbol{\tau}'}$ is the moment of the projection $g_{\boldsymbol{\tau}'}$ with $\boldsymbol{\tau}' = (\lambda', \lambda, \beta)$. We demonstrated this DCC in Section 3.2.2 when no singularity arises in Equation 4.29 (or Equation 3.11 from Section 3.2.2). [Clackdoyle, 2013, Equation (21)] shows that this DCC is also valid in the presence of a singularity by making the link between Equation 3.11 and [Chen and Leng, 2005, Equation (20)] that was derived for general fan-beam trajectories where the baseline may intersect the object.

To express $M_{\boldsymbol{\tau}}$ in terms of the cylindrical detector coordinates (γ, v), we start by defining the intersection curve $\mathcal{C}_{\boldsymbol{\tau}}$ between the plane $\Pi_{\boldsymbol{\tau}}$ and the cylindrical detector of the source position $\boldsymbol{s}_\lambda$. The curve $\mathcal{C}_{\boldsymbol{\tau}}$ is defined by $(\boldsymbol{p}_\lambda(\gamma, v_{\boldsymbol{\tau}}) - \boldsymbol{s}_\lambda) \cdot \boldsymbol{n}_{\boldsymbol{\tau}} = 0$, which is written as

$$\mathcal{C}_{\boldsymbol{\tau}} : v_{\boldsymbol{\tau}}(\gamma) = \frac{D}{n_3}(n_1 \cos(\gamma - \lambda) - n_2 \sin(\gamma - \lambda)) \tag{4.31}$$

where $n_3 = \cos\alpha \cos\beta \neq 0$ since $\alpha \in [0, \pi) \setminus \{\frac{\pi}{2}\}$ and $\beta \in (-\pi/2, \pi/2)$. The ray direction $\boldsymbol{p}_\lambda(\gamma, v_{\boldsymbol{\tau}}(\gamma)) - \boldsymbol{s}_\lambda$ now depends on γ only. We have a one-to-one mapping between the angles ϕ and γ and we can change variable from ϕ to γ in the integral defined by Equation 4.29. Given the definition of $\boldsymbol{c}_{\boldsymbol{\tau}}$, which points from the baseline $\mathcal{B}_{\lambda,\lambda'}$ towards the object, and that we assume no lateral truncation of the projections, the range of γ is limited to $[-\gamma_{\max}, \gamma_{\max}]$. By definition, we have $g_{\boldsymbol{\tau}}(\phi) = g_\lambda(\gamma, v_{\boldsymbol{\tau}}(\gamma))$. The denominator

of the integrand in Equation 4.29 is

$$\cos\phi = \frac{(\boldsymbol{p}_\lambda(\gamma, v_{\boldsymbol{\tau}}) - \boldsymbol{s}_\lambda)}{\sqrt{D^2 + v_{\boldsymbol{\tau}}^2(\gamma)}} \cdot \boldsymbol{c}_{\boldsymbol{\tau}} \tag{4.32}$$

$$= \frac{D}{\sqrt{D^2 + v_{\boldsymbol{\tau}}^2(\gamma)}} \left(-c_1 \cos(\gamma - \lambda) + c_2 \sin(\gamma - \lambda) + c_3 \frac{v_{\boldsymbol{\tau}}(\gamma)}{D} \right) \tag{4.33}$$

$$= \frac{D}{\sqrt{D^2 + v_{\boldsymbol{\tau}}^2(\gamma)}} \frac{[(-n_3 c_1 + n_1 c_3)\cos(\gamma - \lambda) + (n_3 c_2 - n_2 c_3)\sin(\gamma - \lambda)]}{n_3} \tag{4.34}$$

$$= \frac{-D}{\sqrt{D^2 + v_{\boldsymbol{\tau}}^2(\gamma)}} \frac{b_2 \cos(\gamma - \lambda) + b_1 \sin(\gamma - \lambda)}{n_3}. \tag{4.35}$$

The last line is obtained using the relation

$$\boldsymbol{b}_{\lambda,\lambda'} = -\boldsymbol{c}_{\boldsymbol{\tau}} \times \boldsymbol{n}_{\boldsymbol{\tau}} \tag{4.36}$$

$$\begin{pmatrix} b_1 \\ b_2 \\ b_3 \end{pmatrix} = - \begin{pmatrix} c_2 n_3 - c_3 n_2 \\ c_3 n_1 - c_1 n_3 \\ c_1 n_2 - c_2 n_1 \end{pmatrix}. \tag{4.37}$$

The derivative of ϕ with respect to γ can be calculated by differentiating the expression of $\cos\phi$ with respect to γ using the chain rule

$$\frac{\mathrm{d}\cos\phi}{\mathrm{d}\gamma} = \frac{\mathrm{d}\cos\phi}{\mathrm{d}\phi}\frac{\mathrm{d}\phi}{\mathrm{d}\gamma} = -\sin\phi \frac{\mathrm{d}\phi}{\mathrm{d}\gamma}. \tag{4.38}$$

The expression for $\sin\phi$ can be obtained in the same way as $\cos\phi$:

$$\sin\phi = \frac{(\boldsymbol{p}_\lambda(\gamma, v_{\boldsymbol{\tau}}) - \boldsymbol{s}_\lambda)}{\sqrt{D^2 + v_{\boldsymbol{\tau}}^2(\gamma)}} \cdot \boldsymbol{b}_{\lambda,\lambda'} \tag{4.39}$$

$$= \frac{D}{\sqrt{D^2 + v_{\boldsymbol{\tau}}^2(\gamma)}} \left(-b_1 \cos(\gamma - \lambda) + b_2 \sin(\gamma - \lambda) + b_3 \frac{v_{\boldsymbol{\tau}}(\gamma)}{D} \right) \tag{4.40}$$

$$= \frac{D}{\sqrt{D^2 + v_{\boldsymbol{\tau}}^2(\gamma)}} \frac{[(-n_3 b_1 + n_1 b_3)\cos(\gamma - \lambda) + (n_3 b_2 - n_2 b_3)\sin(\gamma - \lambda)]}{n_3} \tag{4.41}$$

$$= \frac{D}{\sqrt{D^2 + v_{\boldsymbol{\tau}}^2(\gamma)}} \frac{c_2 \cos(\gamma - \lambda) + c_1 \sin(\gamma - \lambda)}{n_3}. \tag{4.42}$$

this time using

$$\boldsymbol{c}_{\boldsymbol{\tau}} = \boldsymbol{b}_{\lambda,\lambda'} \times \boldsymbol{n}_{\boldsymbol{\tau}} \tag{4.43}$$

$$\begin{pmatrix} c_1 \\ c_2 \\ c_3 \end{pmatrix} = \begin{pmatrix} b_2 n_3 - b_3 n_2 \\ b_3 n_1 - b_1 n_3 \\ b_1 n_2 - b_2 n_1 \end{pmatrix}. \tag{4.44}$$

The differentiation of $\cos\phi$ (Equation 4.35) with respect to γ is tedious but straighforward using the relations $\boldsymbol{c}_{\boldsymbol{\tau}} = \boldsymbol{b}_{\lambda,\lambda'} \times \boldsymbol{n}_{\boldsymbol{\tau}}$ and $\boldsymbol{b}_{\lambda,\lambda'} \cdot \boldsymbol{n}_{\boldsymbol{\tau}} = 0$, resulting in

$$\frac{\mathrm{d}\cos\phi}{\mathrm{d}\gamma} = \frac{D^3(c_2 \cos(\gamma - \lambda) + c_1 \sin(\gamma - \lambda)}{n_3^2 \left(D^2 + v_{\boldsymbol{\tau}}^2(\gamma)\right)^{3/2}}. \tag{4.45}$$

Finally, assembling Equations (4.38), (4.42) and (4.45) yields

$$\left|\frac{\mathrm{d}\phi}{\mathrm{d}\gamma}\right| = \frac{D^2}{|n_3|(D^2 + v_{\boldsymbol{\tau}}^2(\gamma))}. \tag{4.46}$$

The absolute value accounts for the potential change of order of the limits of the integral. The expression of $M_{\boldsymbol{\tau}}$ in the detector coordinates is

$$M_{\boldsymbol{\tau}} = \int_{-\gamma_{\max}}^{\gamma_{\max}} \frac{-D \operatorname{sign} n_3}{\sqrt{D^2 + v_{\boldsymbol{\tau}}^2(\gamma)}} \frac{g_\lambda(\gamma, v_{\boldsymbol{\tau}}(\gamma))}{b_2 \cos(\gamma - \lambda) + b_1 \sin(\gamma - \lambda)} \mathrm{d}\gamma \tag{4.47}$$

$$= \int_{-\gamma_{\max}}^{\gamma_{\max}} \frac{-D}{\sqrt{D^2 + v_{\boldsymbol{\tau}}^2(\gamma)}} \frac{g_\lambda(\gamma, v_{\boldsymbol{\tau}}(\gamma))}{|\cos\alpha| \cos(\gamma + \bar{\lambda} - \lambda)} \mathrm{d}\gamma \tag{4.48}$$

where we have injected into the second line the expressions of n_3, b_1 and b_2 from Equation 4.27 and simplified the resulting expression. Similarly to Equation 4.29, Equation 4.48 might have a singularity if the denominator is null, i.e. if $\gamma = \gamma^s_{\lambda,\lambda'}$ with

$$\gamma^s_{\lambda,\lambda'} = \left(\lambda - \bar{\lambda}\right) \pmod{\pi} - \frac{\pi}{2} \tag{4.49}$$

$$= \frac{\lambda - \lambda'}{2} \pmod{\pi} - \frac{\pi}{2}. \tag{4.50}$$

These two derivations of $\gamma^s_{\lambda,\lambda'}$ (Equation 4.49 and Equation 4.50) account for the domain of $|\gamma| < \gamma_{\max} < \pi/2$. Geometrically, $\gamma^s_{\lambda,\lambda'}$ is the angular coordinate of the detector at which the baseline may intersect the detector. Injecting Equation 4.49 into the denominator of Equation 4.48, we obtain

$$\cos(\gamma + \bar{\lambda} - \lambda) = \begin{cases} \sin(\gamma - \gamma^s_{\lambda,\lambda'}) \text{ if} (\lambda - \bar{\lambda}) \pmod{2\pi} < \pi \\ -\sin(\gamma - \gamma^s_{\lambda,\lambda'}) \text{ otherwise} \end{cases} \tag{4.51}$$

$$= -\operatorname{sign}\gamma^s_{\lambda,\lambda'} \sin(\gamma^s_{\lambda,\lambda'} - \gamma). \tag{4.52}$$

The condition on $(\lambda - \bar{\lambda}) \pmod{2\pi}$ has been translated into $\operatorname{sign}\gamma^s_{\lambda,\lambda'}$. Indeed, from the definition of $\bar{\lambda}$ (see Equation 4.24), the condition on $(\lambda - \bar{\lambda}) \pmod{2\pi}$ is converted into a condition on $(\lambda' - \lambda)/2$ that is directly linked to $\operatorname{sign}\gamma^s_{\lambda,\lambda'}$ with Equation 4.50. The resulting expression of the moment Equation 4.48 is

$$M_{\boldsymbol{\tau}} = \int_{-\gamma_{\max}}^{\gamma_{\max}} \frac{D \operatorname{sign}(\gamma^s_{\lambda,\lambda'})}{\sqrt{D^2 + v_{\boldsymbol{\tau}}^2(\gamma)}} \frac{g_\lambda(\gamma, v_{\boldsymbol{\tau}}(\gamma))}{|\cos\alpha| \sin(\gamma^s_{\lambda,\lambda'} - \gamma)} \mathrm{d}\gamma \tag{4.53}$$

4.3.3 Discretization of the moment

For this approach, the discretization of the moment is not as straightforward as for the rebinning approach because of the singularity $\gamma^s_{\lambda,\lambda'}$ present in the moment expression (Equation 4.53). We propose two numerical integration methods that can deal with the singularity $\gamma^s_{\lambda,\lambda'}$. The numerical integrations are based on the discretization of the cylindrical detector made of $N_{\text{cols}} \times N_{\text{rows}}$ pixels of size $\Delta_\gamma \times \Delta_v$. Their coordinates γ and v are $\gamma_i = -\gamma_{\max} + (i-1)\Delta_\gamma, i \in \{1, ..., N_{\text{cols}}\}$ and $v_j = -v_{\max} + (j-1)\Delta_v, j \in \{1, ..., N_{\text{rows}}\}$.

4.3.3.1 Integration with a first order approximation

We wish to evaluate the integral from Equation 4.53, that we re-write

$$M_{\boldsymbol{\tau}} = \int_{-\gamma_{\max}}^{\gamma_{\max}} \frac{\tilde{g}_\lambda(\gamma, v_{\boldsymbol{\tau}}(\gamma))}{\sin(\gamma^s_{\lambda,\lambda'} - \gamma)} \mathrm{d}\gamma \tag{4.54}$$

where

$$\tilde{g}_\lambda(\gamma, v_{\boldsymbol{\tau}}(\gamma)) = \frac{D \operatorname{sign}(\gamma^s_{\lambda,\lambda'})}{\sqrt{D^2 + v_{\boldsymbol{\tau}}^2(\gamma)}} \frac{g_\lambda(\gamma, v_{\boldsymbol{\tau}}(\gamma))}{|\cos\alpha|} \tag{4.55}$$

to ease the notations. Equation 4.54 may or may not have a singularity depending on $\gamma^s_{\lambda,\lambda'}$.

• If $\gamma^s_{\lambda,\lambda'} \notin [-\gamma_{\max}, \gamma_{\max}]$, the discretization of Equation 4.54 is straightforward. Using the trapezoidal rule, $M_{\boldsymbol{\tau}}$ is estimated by

$$M_{\boldsymbol{\tau}} \simeq \sum_{i=1}^{N_{cols}} \frac{\tilde{g}_\lambda(\gamma_i, v_{\boldsymbol{\tau}}(\gamma_i))}{\sin(\gamma^s_{\lambda,\lambda'} - \gamma_i)} \Delta_\gamma \tag{4.56}$$

where $v_{\boldsymbol{\tau}}(\gamma_i) \in [v_j, v_{j+1})$ is the v-coordinate of the point on the curve $\mathcal{C}_{\boldsymbol{\tau}}$ at angle $\gamma = \gamma_i$ such that $j = \lfloor (v_{\boldsymbol{\tau}}(\gamma_i) + v_{\max})/\Delta_v \rfloor$ depends on i. The projection value is obtained with linear interpolation along the i-th column

$$g_\lambda(\gamma_i, v_{\boldsymbol{\tau}}(\gamma_i)) = (1 - w_{i,j}) g_\lambda(\gamma_i, v_j) + w_{i,j} g_\lambda(\gamma_i, v_{j+1}) \tag{4.57}$$

with $w_{i,j} = (v_{\boldsymbol{\tau}}(\gamma_i) - v_j)/\Delta_v$ the linear interpolation weight.

• If $\gamma^s_{\lambda,\lambda'} \in [-\gamma_{\max}, \gamma_{\max}]$, the singularity needs to be carefully dealt with. To approximate the integral around the singularity, we chose to add a sample, noted $\gamma^*_{\lambda,\lambda'} = \gamma^s_{\lambda,\lambda'} + (\gamma^s_{\lambda,\lambda'} - \lfloor \gamma^s_{\lambda,\lambda'} \rceil)$ where $\lfloor \gamma^s_{\lambda,\lambda'} \rceil$ is the nearest sample to $\gamma^s_{\lambda,\lambda'}$, to form a symmetrical interval around the singularity and evaluate the contribution of the singularity in this symmetrical interval according to [King, 2009, chapter 14]. With $\Delta^s_\gamma = |\gamma^s_{\lambda,\lambda'} - \gamma^*_{\lambda,\lambda'}|$, the two other intervals $[\gamma_1, \gamma_s - \Delta^s_\gamma]$ and $[\gamma_s + \Delta^s_\gamma, \gamma_{N_{cols}}]$, do not contain any singularity and the corresponding integrals are approximated with the trapezoidal rule. The integration process is illustrated on Figure 4.12 with the function $\tilde{g}_\lambda = 1$. The contribution around

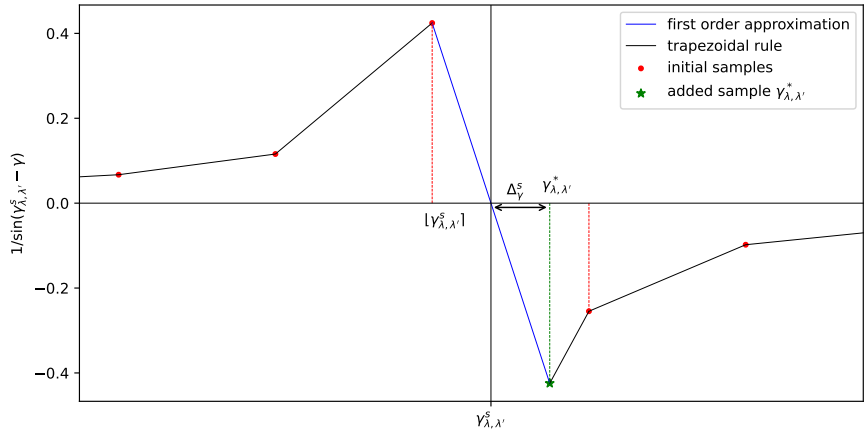

Figure 4.12: Illustration of the first order approximation with the function $1/\sin(\gamma^s_{\lambda,\lambda'} - \gamma)$. The samples $\gamma_i, i \in \{1, ..., N_{cols}\}$ are drawn as the red bullet points. The nearest sample to $\gamma^s_{\lambda,\lambda'}$ is $\lfloor \gamma^s_{\lambda,\lambda'} \rceil$. The symmetrical sample at $\gamma^*_{\lambda,\lambda'} = \gamma^s_{\lambda,\lambda'} + (\gamma^s_{\lambda,\lambda'} - \lfloor \gamma^s_{\lambda,\lambda'} \rceil)$ (green star point) was added to form a symmetrical interval with $\lfloor \gamma^s_{\lambda,\lambda'} \rceil$ around the singularity γ_s. The value of $\tilde{g}(\gamma^*_{\lambda,\lambda'}, v_{\boldsymbol{\tau}}(\gamma^*_{\lambda,\lambda'}))$ was interpolated according to Equation 4.57. The trapezoidal rule is applied along the black lines. The first order approximation is applied along the blue line.

the singularity is written as

$$\int_{\gamma^s_{\lambda,\lambda'} - \Delta^s_\gamma}^{\gamma^s_{\lambda,\lambda'} + \Delta^s_\gamma} \frac{\tilde{g}_\lambda(\gamma, v_{\boldsymbol{\tau}}(\gamma))}{\sin(\gamma^s_{\lambda,\lambda'} - \gamma)} \mathrm{d}\gamma \approx \int_{\gamma^s_{\lambda,\lambda'} - \Delta^s_\gamma}^{\gamma^s_{\lambda,\lambda'} + \Delta^s_\gamma} \frac{\tilde{g}_\lambda(\gamma, v_{\boldsymbol{\tau}}(\gamma))}{\gamma^s_{\lambda,\lambda'} - \gamma} \mathrm{d}\gamma \tag{4.58}$$

because we can assume that in the interval $[\gamma^s_{\lambda,\lambda'} - \Delta^s_\gamma, \gamma^s_{\lambda,\lambda'} + \Delta^s_\gamma]$, $\gamma \approx \gamma^s_{\lambda,\lambda'}$, thus $\sin(\gamma^s_{\lambda,\lambda'} - \gamma) \approx \gamma^s_{\lambda,\lambda'} - \gamma$. According to [King, 2009, Chapter 14, equation (14.23)], the LHS of Equation 4.58 can be approximated with

$$\int_{\gamma^s_{\lambda,\lambda'} - \Delta^s_\gamma}^{\gamma^s_{\lambda,\lambda'} + \Delta^s_\gamma} \frac{\tilde{g}_\lambda(\gamma, v_{\boldsymbol{\tau}}(\gamma))}{\gamma^s_{\lambda,\lambda'} - \gamma} \mathrm{d}\gamma \simeq -2\Delta^s_\gamma \tilde{g}'_\lambda(\gamma^s_{\lambda,\lambda'}, v_{\boldsymbol{\tau}}(\gamma^s_{\lambda,\lambda'})) \tag{4.59}$$

where

$$\tilde{g}'_\lambda(\gamma_i, v_{\boldsymbol{\tau}}(\gamma^s_{\lambda,\lambda'})) = \frac{\tilde{g}_\lambda(\gamma^s_{\lambda,\lambda'} + \Delta^s_\gamma, v_{\boldsymbol{\tau}}(\gamma^s_{\lambda,\lambda'} + \Delta^s_\gamma)) - \tilde{g}_\lambda(\gamma_s - \Delta^s_\gamma, v_{\boldsymbol{\tau}}(\gamma_s - \Delta^s_\gamma))}{2\Delta^s_\gamma}. \quad (4.60)$$

The values of $v_{\boldsymbol{\tau}}(\gamma^s_{\lambda,\lambda'})$ and $v_{\boldsymbol{\tau}}(\gamma^s_{\lambda,\lambda'} + \Delta^s_\gamma)$ or $v_{\boldsymbol{\tau}}(\gamma^s_{\lambda,\lambda'} - \Delta^s_\gamma)$ are given by Equation 4.31 and the value of $g_\lambda(\gamma^s_{\lambda,\lambda'} + \Delta^s_\gamma, v_{\boldsymbol{\tau}}(\gamma^s_{\lambda,\lambda'} + \Delta^s_\gamma))$ or $g_\lambda(\gamma^s_{\lambda,\lambda'} - \Delta^s_\gamma, v_{\boldsymbol{\tau}}(\gamma^s_{\lambda,\lambda'} - \Delta^s_\gamma))$ are linearly interpolated with Equation 4.57. We only need to interpolate the values of $v_{\boldsymbol{\tau}}$ and $\tilde{g}$ for one of the two coordinate $\gamma^s_{\lambda,\lambda'} + \Delta^s_\gamma$ or $\gamma^s_{\lambda,\lambda'} - \Delta^s_\gamma$ as one of them corresponds to one sampled value of γ.

If $\Delta^s_\gamma = 0$, then the singularity γ_s coincides with one sample of γ. The contribution around the singularity is zero, and the integral in Equation 4.54 is estimated by applying the trapezoidal rule on all the samples except the one corresponding to γ_s. This formula corresponds to the one given in [King, 2009, Chapter 14, equation (14.21)] for the estimation of a Hilbert transform in a singular point that matches one of the samples.

4.3.3.2 Integration with the Hilbert Transform

In this part, we present an alternative integration method. We slightly modify the moment's expression in Equation 4.53 by defining $h(x) = (\pi x)^{-1}$ as the kernel of the Hilbert transform and writing

$$\frac{1}{\sin(\gamma^s_{\lambda,\lambda'} - \gamma)} = \pi h(\sin(\gamma^s_{\lambda,\lambda'} - \gamma)) = \frac{\pi h(\gamma^s_{\lambda,\lambda'} - \gamma)}{\operatorname{sinc}(\gamma^s_{\lambda,\lambda'} - \gamma)} \quad (4.61)$$

where the right hand side is obtained because h is homogeneous of degree -1. Combining Equations 4.53, and 4.61 leads to

$$M_{\boldsymbol{\tau}} = \int_{-\gamma_{\max}}^{\gamma_{\max}} \frac{D \operatorname{sign}(\gamma^s_{\lambda,\lambda'})}{\sqrt{D^2 + v^2_{\boldsymbol{\tau}}(\gamma)}|\cos\alpha|} \frac{\pi h(\gamma^s_{\lambda,\lambda'} - \gamma)}{\operatorname{sinc}(\gamma^s_{\lambda,\lambda'} - \gamma)} g_\lambda(\gamma, v_{\boldsymbol{\tau}}(\gamma))\mathrm{d}\gamma. \quad (4.62)$$

In Equation 4.62, the singularity is now present in the Hilbert kernel which has been previously implemented in several reconstruction algorithms. It can be dealt with using a band-limited version of the Hilbert kernel. The integral in Equation 4.62 is discretized as follows:

$$M_{\boldsymbol{\tau}} \simeq \sum_{i=1}^{N_{\text{cols}}} \frac{D \operatorname{sign}(\gamma^s_{\lambda,\lambda'})}{\sqrt{D^2 + v^2_{\boldsymbol{\tau}}(\gamma_i)}|\cos\alpha|} \frac{\pi h_\nu(\gamma^s_{\lambda,\lambda'} - \gamma_i)}{\operatorname{sinc}(\gamma^s_{\lambda,\lambda'} - \gamma_i)} g_\lambda(\gamma_i, v_{\boldsymbol{\tau}}(\gamma_i))\Delta_\gamma \quad (4.63)$$

where $v_{\boldsymbol{\tau}}(\gamma_i) \in [v_j, v_{j+1})$ is the v-coordinate of the point on the curve $\mathcal{C}_{\boldsymbol{\tau}}$ at angle $\gamma = \gamma_i$ such that $j = \lfloor (v_{\boldsymbol{\tau}}(\gamma_i) + v_{\max})/\Delta_v \rfloor$ depends on i. The kernel $h_\nu(\gamma)$ is a band-limited version of $h(\gamma)$ with ν a parameter controlling the bandwidth. The projection value is obtained with the linear interpolation described in Equation 4.57.

We explore two band-limited versions of $h(\gamma)$ obtained by taking the inverse Fourier transform of the product between the Fourier transform of the Hilbert kernel and either a rectangular window or a Hann window. The resulting expressions are

$$h^{\text{Rect}}_\nu(\gamma) = \frac{1 - \cos\left(\nu \frac{\pi\gamma}{\Delta_\gamma}\right)}{\pi\gamma} \quad (4.64)$$

and

$$h^{\text{Hann}}_\nu(\gamma) = \frac{h^{\text{Rect}}_\nu(\gamma)}{2} + \frac{\gamma\left(1 + \cos\left(\nu \frac{\pi\gamma}{\Delta_\gamma}\right)\right)}{2\pi\left(\gamma^2 - \frac{\Delta^2_\gamma}{\nu^2}\right)} \quad (4.65)$$

where $\nu \in (0, 1]$ characterizes a fraction of Nyquist's frequency and controls the bandwidth of the kernel.

4.3.4 Applicability conditions

By dealing with the singularity, the computation of the FBDCC in the physical detector alleviates the FOV condition of the rebinning approach. The main benefit of this approach is to consider pairs whose baseline can intersect the FOV. Consequently, the validity of the FBDCC only depends on having untruncated fan-beam projections $g_{\boldsymbol{\tau}}(\phi)$ (Equation 4.28). Since the projections may be truncated in the axial direction, DCCs are only applicable for some pairs of source positions (i.e. some $\lambda - \lambda'$) and some planes (i.e. some β) for which the detector curves $\mathcal{C}_{\boldsymbol{\tau}}$ and $\mathcal{C}_{\boldsymbol{\tau}'}$ (Figure 4.10) are between the inferior and superior limits of the detector:

$$|v_{\boldsymbol{\tau}}(\gamma)| \leq v_{\max}. \tag{4.66}$$

Replacing (n_1, n_2, n_3) of $v_{\boldsymbol{\tau}}(\gamma)$ from Equation 4.31 by their expression from Equation 4.27 and $\bar{\lambda}-\lambda$ by $\gamma^s_{\lambda,\lambda'}$ from Equation 4.49, we have, similarly to Equation 4.52, $\sin(\gamma+\bar{\lambda}-\lambda) = -\operatorname{sign}\gamma^s_{\lambda,\lambda'}\cos(\gamma-\gamma^s_{\lambda,\lambda'})$ and the previous inequality becomes

$$D\left|\operatorname{sign}\gamma^s_{\lambda,\lambda'}\tan\alpha\cos(\gamma-\gamma^s_{\lambda,\lambda'}) + \operatorname{sign}\gamma^s_{\lambda,\lambda'}\frac{\tan\beta}{\cos\alpha}\sin(\gamma-\gamma^s_{\lambda,\lambda'})\right| \leq v_{\max} \tag{4.67}$$

which gives the following conditions on the angles α and β:

- If $\gamma = \gamma^s_{\lambda,\lambda'}$, we have

  $$|\tan\alpha| \leq \frac{v_{\max}}{D} \tag{4.68}$$

  This constraint on α indirectly constrains the interval separating two source positions where DCCs can be applied because $|\alpha|$ increases with the angular distance $|\lambda' - \lambda|$ between two source positions. It is independent of β as is the intersection of the baseline $\mathcal{B}_{\lambda,\lambda'}$ with the detector at $\gamma^s_{\lambda,\lambda'}$.

- If $\gamma \neq \gamma^s_{\lambda,\lambda'}$, then isolating β from this inequality yields

  $$l_{\lambda,\lambda'}(\gamma) \leq \beta \leq u_{\lambda,\lambda'}(\gamma) \tag{4.69}$$

  where

  $$l_{\lambda,\lambda'}(\gamma) = \arctan\left(-\frac{\sin\alpha}{\tan(\gamma-\gamma^s_{\lambda,\lambda'})} - \frac{v_{\max}}{D}\left|\frac{\cos\alpha}{\sin(\gamma-\gamma^s_{\lambda,\lambda'})}\right|\right), \tag{4.70}$$

  and

  $$u_{\lambda,\lambda'}(\gamma) = \arctan\left(-\frac{\sin\alpha}{\tan(\gamma-\gamma^s_{\lambda,\lambda'})} + \frac{v_{\max}}{D}\left|\frac{\cos\alpha}{\sin(\gamma-\gamma^s_{\lambda,\lambda'})}\right|\right) \tag{4.71}$$

  are the equations of the smallest and highest angle β for which the curve $v_{\boldsymbol{\tau}}(\gamma)$ is not truncated for each detector column γ. Because $\gamma^s_{\lambda,\lambda'}$ is not the same for $\boldsymbol{s}_\lambda$ and $\boldsymbol{s}_{\lambda'}$, Equation 4.69 must be verified for the two source positions. However, it can be shown that $l_{\lambda',\lambda}(\gamma) = -u_{\lambda,\lambda'}(-\gamma)$ and $u_{\lambda',\lambda}(\gamma) = -l_{\lambda,\lambda'}(-\gamma)$ because a π rotation around the line defined by $(\boldsymbol{s}_\lambda + \boldsymbol{s}_{\lambda'})/2$ and $\boldsymbol{c}_{\lambda,\lambda'}$ swaps the two detectors. We therefore obtain the condition:

  $$|\beta| \leq \beta_{\max} = \min_{\gamma\in[-\gamma_{\max},\gamma_{\max}]} \min(u_{\lambda,\lambda'}(\gamma), -l_{\lambda,\lambda'}(-\gamma)). \tag{4.72}$$

  If $\beta_{\max} \leq 0$, the detector is too small to compute a DCC for this pair of source positions. Otherwise, we sample β in $B = \lfloor 2\beta_{\max}D/\Delta_v \rfloor$ planes.

4.3.5 Consistency metric

For a given pair of projections $(g_\lambda, g_{\lambda'})$, moments are computed over all the B planes and we define our pair-wise cone-beam consistency metric as

$$E^{Real}_{\lambda,\lambda'} = 2 \times \frac{1}{B} \sum_{b=1}^{B} \frac{\left| M_{\boldsymbol{\tau}_b} - M_{\boldsymbol{\tau}'_b} \right|}{M_{\boldsymbol{\tau}_b} + M_{\boldsymbol{\tau}'_b}} \tag{4.73}$$

where $M_{\boldsymbol{\tau}_b}, \boldsymbol{\tau}_b = (\lambda, \lambda', \beta_b)$ and $M_{\boldsymbol{\tau}'_b}, \boldsymbol{\tau}'_b = (\lambda', \lambda, \beta_b)$ are the moments on the b-th plane, making an angle β_b with the reference plane, of the projections g_λ and $g_{\lambda'}$. If the two projections g_λ and $g_{\lambda'}$ are consistent, then $E^{Real}_{\lambda,\lambda'} = 0$.

4.4 Numerical validation of DCCs

In this section, we detail the numerical validation of the derivation and implementation of both approaches to apply FBDCC to helical CT. They are validated with simulated and real data acquired on the Somatom go.SIM Siemens CT scanner, both of static phantoms.

4.4.1 Datasets

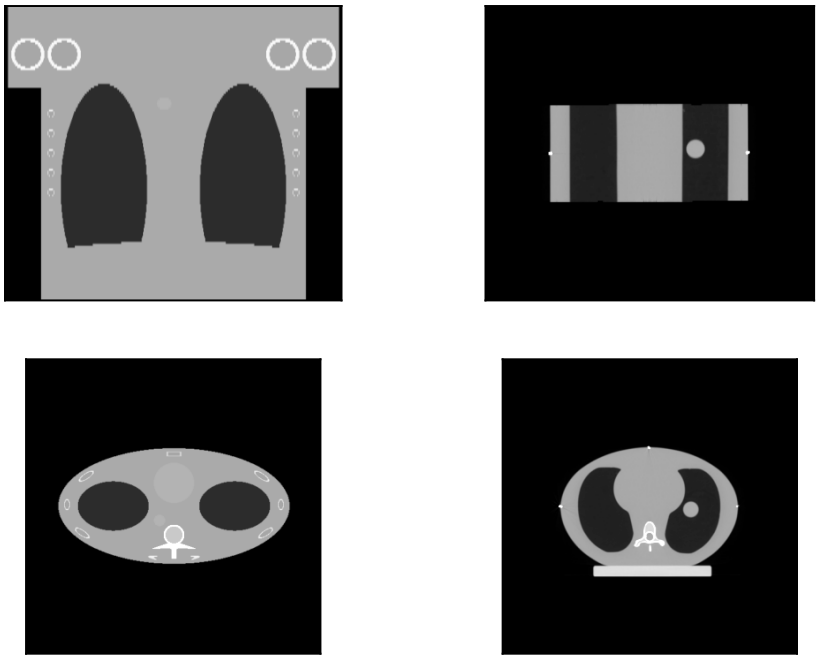

(a) Numerical phantom (b) Mechanical phantom

Figure 4.13: Presentation of the phantoms used for the validation of the DCC. Top row: coronal views. Bottom row: axial views.

4.4.1.1 Numerical phantom

Helical acquisitions of the thorax Forbild phantom, shown in Figure 4.13, were simulated with 360 projections per rotation and 10 rotations. The duration of a rotation was 0.35 s. The detector size was $[920, 32] \times [1.03, 1.09]$ mm. The helical pitch was $P = 0.07$, the radius of the helical trajectory was 610 mm and the detector-source distance was 1113 mm. The acquisitions were centered around $z = 0$ mm. Ideal projections and noisy projections

were generated. For noisy projections, Poisson noise was applied to the projections before taking the logarithm with 10^5 photons in air. Simulations were performed using the Reconstruction Toolkit (RTK, [Rit et al., 2013]). The numerical phantom was static.

4.4.1.2 Mechanical phantom

The CIRS Dynamic Thorax Motion Phantom model 008A containing a 3 cm diameter tumor in the left lung, shown in Figure 4.13, was scanned with the Somatom go.Sim Siemens CT scan according to a 4D protocol corresponding to a rotation time of 0.35 s and a pitch of 0.07. The tumor was static during the entire acquisition.

4.4.2 Experiment

The rebinning approach and the direct approach (computation of the DCC directly on the cylindrical detectors) were applied to various pairs of projections, from the simulations and the mechanical phantom acquisition, whose geometrical configuration varies.

For each pair, we computed

- The projections' moments on the virtual detector with Equation 4.17 for the rebinning approach,
- The projections' moments estimated with the first order approximation according to Section 4.3.3.1 for the direct approach,
- The projections' moments estimated with the Rectangular-windowed band-limited Hilbert kernel according to Equation 4.63 with the coefficients of Equation 4.64 and $\nu = 1$ for the direct approach,
- The projections' moments estimated with the Hann-windowed band-limited Hilbert kernel according to Equation 4.63 with the coefficients of Equation 4.65 and $\nu = 0.2$ for the direct approach.

4.4.3 Results

The consistency measurements for all the pairs obtained with both approaches are presented in Table 4.1.

Pair characteristics	Noiseless data	Noisy data.	Real data
Baseline away from the FOV	0.38	0.82	2.32
Baseline tangent to the FOV	0.18	0.01	7.38

(a) Rebinning approach.

Pair characteristics	Noiseless data	Noisy data.	Real data
No singularity	0.68/0.46/0.46	1.2/1.02/1.02	2.28/2.94/2.94
Singularity - flat gradient	1.48/0.64/0.64	87.02/3.62/101.1	-
Singularity - steep gradient	3.96/10.2/11.8	7.42/12.14/9.24	-
Singularity	-	-	213.24/6.72/1275.24

(b) Direct approach. Errors $E^{Real}_{\lambda,\lambda'}$ for the three integration methods are given as: rectangular-windowed kernel/Hann-windowed kernel/first order integration.

Table 4.1: Errors $E^{Virt}_{\lambda,\lambda'}$ (Table 4.1a) and $E^{Real}_{\lambda,\lambda'}$ (Table 4.1b) (stated as percentage) computed with the rebinning approach or the direct approach for various pairs of cone-beam projections from simulated and real data.

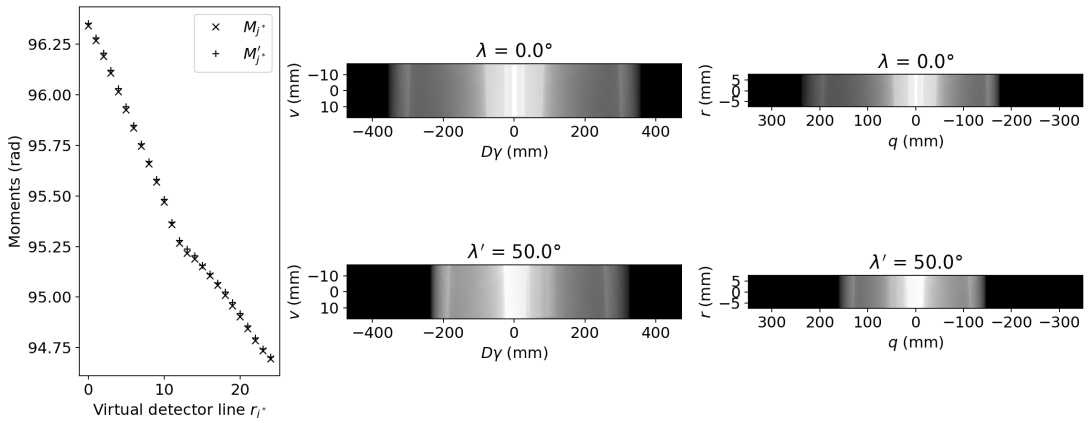

Figure 4.14: FBDCCs computed with the rebinning approach applied to a pair of projections largely satisfying the FOV condition. The first column shows the projections' moments computed with the implementation described in Section 4.2.3. The central column shows the two projections for which DCCs are computed. The last column shows the weighted backprojections of each projection. The aspect ratios (ratio of width to the height) of the projections and weighted backprojections are both equal to 4.5.

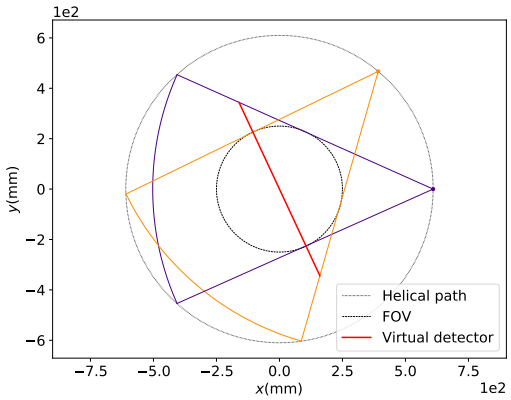

Figure 4.15: 2D view of a pair geometry that largely satisfies the FOV condition. The two fans are plotted in yellow and purple and the virtual detector is plotted in red.

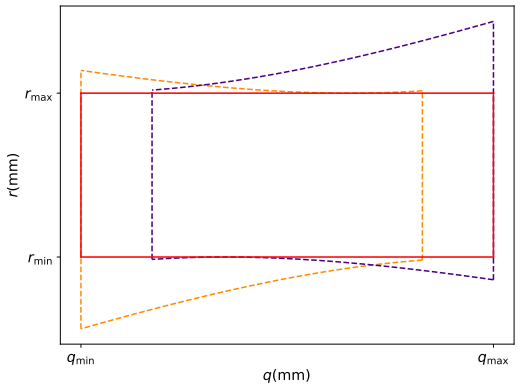

Figure 4.16: Illustration of the backprojection for a pair largely satisfying the FOV condition. The backprojections are the dotted colored lines and the virtual detector is the continuous red line.

4.4.3.1 Numerical phantom - noiseless simulation

FBDCCs computed with the rebinning approach are illustrated in Figure 4.14 for a pair of projections largely satisfying the FOV condition and in Figure 4.17 for a pair of projections whose baseline is tangent to the FOV. In both cases, the small value of the errors (see Table 4.1a, first column) validates the implementation described in Section 4.2.3. The distortion of the backprojections are illustrated in Figures 4.15 and 4.16 for the pair largely satisfying the FOV condition and in Figures 4.18 and 4.19 for the pair with a baseline tangent to the FOV. The distortion is more important for a pair whose baseline is tangent to the FOV than for a pair largely satisfying the FOV condition because the baseline is closer to the backprojection plane for the latter pair. Consequently, the magnification factor m_{BP} is higher for a pair whose baseline is tangent to the FOV resulting in a lower number of rows on the virtual detector (1 row in Figure 4.17) than for a pair largely satisfying the FOV condition (≈ 25 rows in Figure 4.14). However, the distortion impact on the FBDCC is limited as the errors are similar and close to zero (see Table 4.1a, first

column).

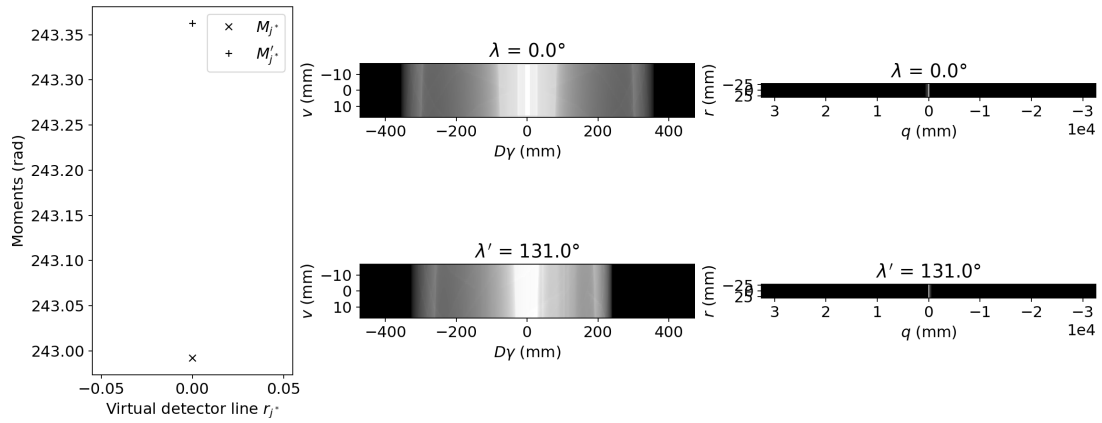

Figure 4.17: FBDCCs computed with the rebinning approach applied to a pair of projections whose baseline is tangent to the FOV. The first column shows the projections' moments computed with the implementation described in Section 4.2.3. The central column shows the two projections for which DCC are computed. The last column shows the weighted backprojection of each projection. The aspect ratio of the projections is 4.5 and the aspect ratio of the weighted backprojections is 45.

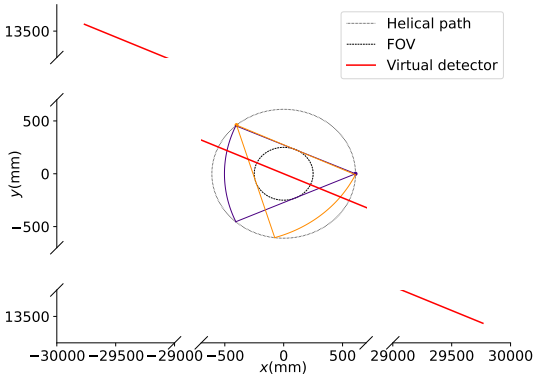

Figure 4.18: 2D view of a pair geometry whose baseline is tangent to the FOV. The two fans are plotted in yellow and purple and the virtual detector in red.

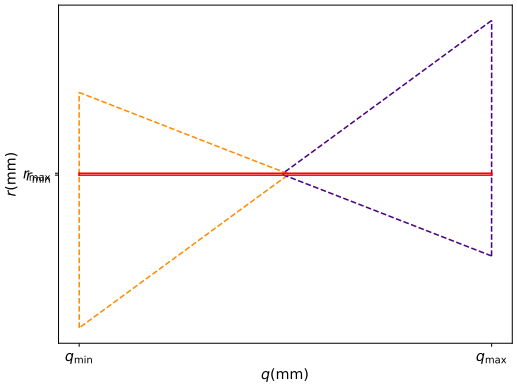

Figure 4.19: Illustration of the backprojection for a pair whose baseline is tangent to the FOV. The backprojections are the dotted colored lines and the virtual detector is the continuous red line.

FBDCCs computed with the direct approach are illustrated in Figure 4.20 for a pair whose baseline does not intersect the FOV and in Figures 4.21 and 4.22 for two pairs whose baselines intersect the FOV. When the baseline does not intersect the FOV, the errors (see Table 4.1b, first row, first column) are similar to the one obtained with the rebinning approach (see Table 4.1a, first row, first column) and close to zero, which validates the three integration methods in this case. When the baseline and the FOV intersect, the validation of the implementation is not straightforward as the errors (see Table 4.1b, second and third rows, first column) differ depending on the location of the *singular point* with coordinate $(\gamma^s_{\lambda,\lambda'}, v_{\boldsymbol{\tau}}(\gamma^s_{\lambda,\lambda'}))$ in the projection, but also on the integration method. If the singular point is located in spatially smooth regions in both cone-beam projections (Figure 4.21), the corresponding moments match as shown by the small values of the errors (see Table 4.1b, second row, first column) for the three integration methods. If the singular point is located

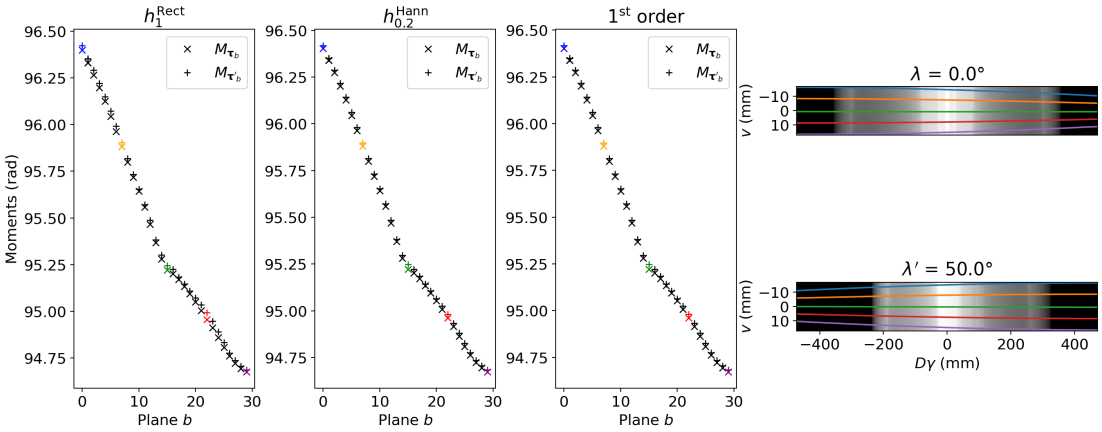

Figure 4.20: FBDCCs computed with the direct approach applied to a pair of simulated projections whose baseline does not intersect the FOV. There is no singularity in the computation of the moments. From left to right: integration with the Rectangular-windowed Hilbert kernel, integration with the Hann-windowed Hilbert kernel, integration with the first order approximation and the two projections for which FBDCCs are computed. Five planes are plotted: the first (in blue) and last (in purple) plane, the central plane (in green) and two intermediate planes (in red and orange).

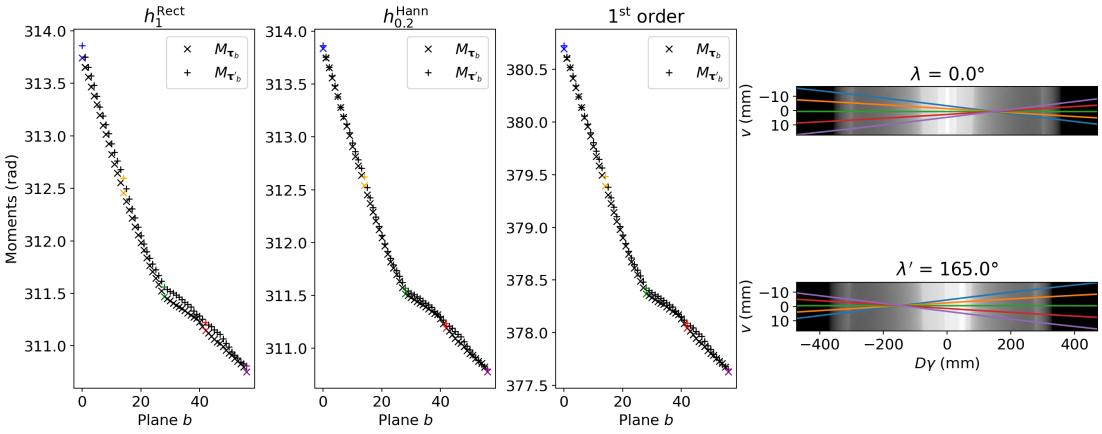

Figure 4.21: FBDCCs computed with the direct approach applied to a pair of simulated projections whose baseline intersects the FOV. The singular point is located in a spatially smooth region of the two cone-beam projections. From left to right: integration with the Rectangular-windowed Hilbert kernel, integration with the Hann-windowed Hilbert kernel, integration with the first order approximation and the two projections for which FBDCCs are computed. Five planes are plotted: the first (in blue) and last (in purple) plane, the central plane (in green) and two intermediate planes (in red and orange).

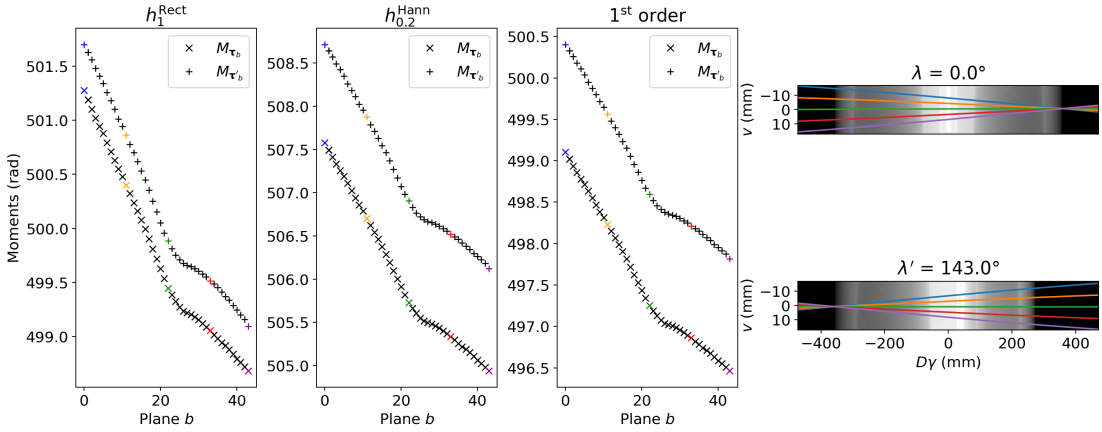

Figure 4.22: FBDCCs computed with the direct approach applied to a pair of simulated projections whose baseline intersects the FOV. The singular point is located close to steep spatial gradients of the two cone-beam projections. From left to right: integration with the Rectangular-windowed Hilbert kernel, integration with the Hann-windowed Hilbert kernel, integration with the first order approximation and the two projections for which FBDCCs are computed. Five planes are plotted: the first (in blue) and last (in purple) plane, the central plane (in green) and two intermediate planes (in red and orange).

close to steep spatial gradients of one of the two projections (Figure 4.22), an inconsistency is highlighted by the high values of the errors (see Table 4.1b, third row, first column), with a larger value using the Hann-windowed kernel or the first order approximation than the rectangular-windowed kernel.

4.4.3.2 Numerical phantom - noisy simulation

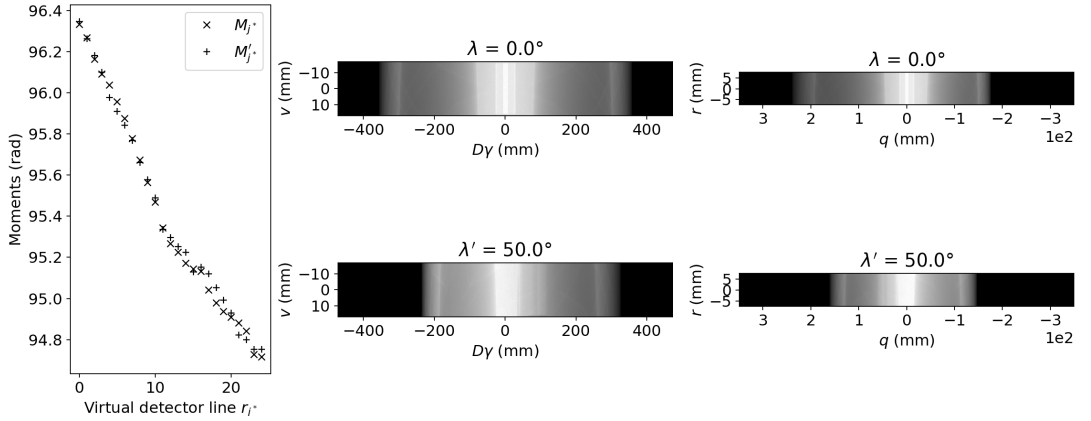

Figure 4.23: FBDCCs computed with the rebinning approach applied to a pair of noisy projections largely satisfying the FOV condition. The first column shows the projections' moments computed with the implementation described in Section 4.2.3. The central column shows the two projections for which DCCs are computed. The last column shows the weighted backprojection of each projection. The aspect ratios of the projections and weighted backprojections are both equal to 4.5.

The influence of noise on the FBDCCs computed with the rebinning approach is illustrated in Figure 4.23 for a pair of projections largely satisfying the FOV condition and in Figure 4.24 for a pair of projections whose baseline is tangent to the FOV. For both pairs, the errors slightly increase (see Table 4.1a, second column) compared to the ideal case.

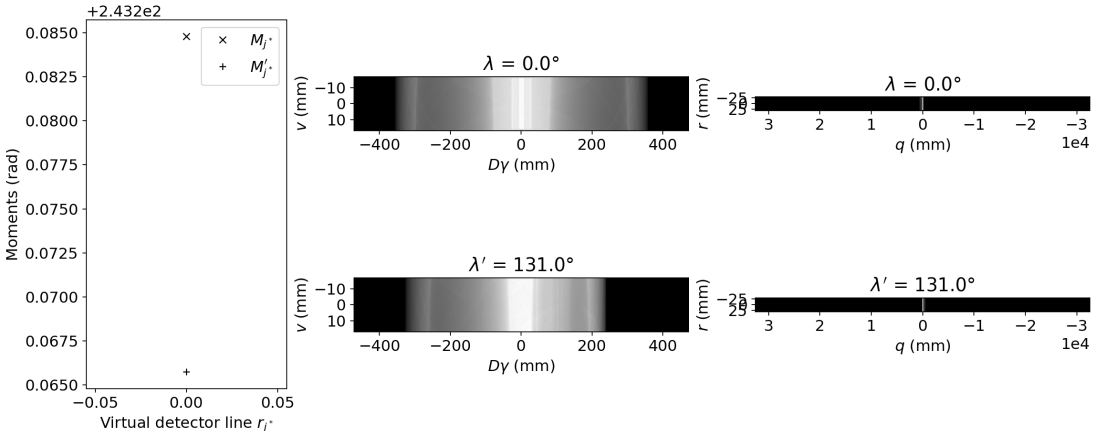

Figure 4.24: FBDCCs computed with the rebinning approach applied to a pair of noisy projections whose baseline is tangent to the FOV. The first column shows the projections' moments computed with the implementation described in Section 4.2.3. The central column shows the two projections for which DCCs are computed. The last column shows the weighted backprojection of each projection. The aspect ratio of the projections is 4.5 and the aspect ratio of the weighted backprojections is 45.

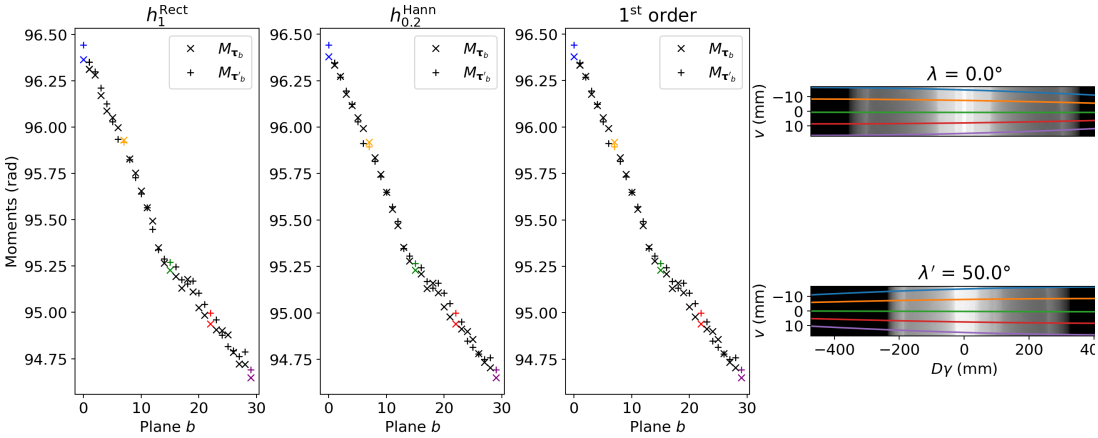

Figure 4.25: FBDCCs computed with the direct approach applied to a pair of noisy projections whose baseline does not intersect the FOV. There is no singularity in the computation of the moments. From left to right: integration with the Rectangular-windowed Hilbert kernel, integration with the Hann-windowed Hilbert kernel, integration with the first order approximation and the two projections for which FBDCCs are computed. Five planes are plotted: the first (in blue) and last (in purple) plane, the central plane (in green) and two intermediate planes (in red and orange).

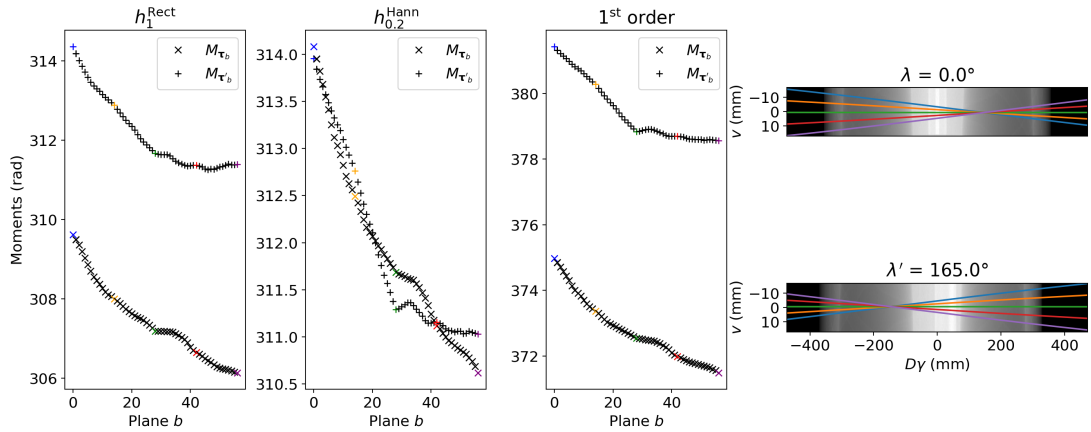

Figure 4.26: FBDCCs computed with the direct approach applied to a pair of noisy projections whose baseline intersects the FOV. The singular point is located in a spatially smooth region of the two cone-beam projections. From left to right: integration with the Rectangular-windowed Hilbert kernel, integration with the Hann-windowed Hilbert kernel, integration with the first order approximation and the two projections for which FBDCCs are computed. Five planes are plotted: the first (in blue) and last (in purple) plane, the central plane (in green) and two intermediate planes (in red and orange).

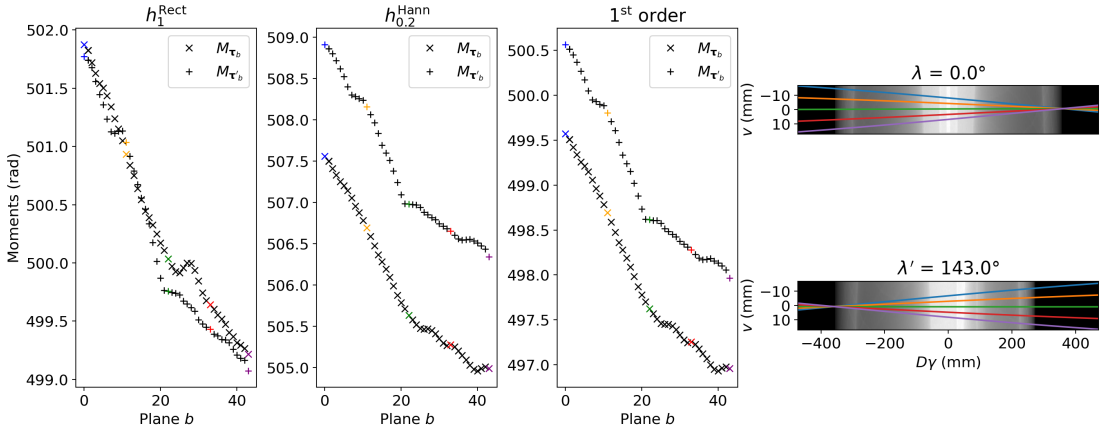

Figure 4.27: FBDCCs computed with the direct approach applied to a pair of noisy projections whose baseline intersects the FOV. The singular point is located close to steep spatial gradients of the two cone-beam projections. From left to right: integration with the Rectangular-windowed Hilbert kernel, integration with the Hann-windowed Hilbert kernel, integration with the first order approximation and the two projections for which FBDCCs are computed. Five planes are plotted: the first (in blue) and last (in purple) plane, the central plane (in green) and two intermediate planes (in red and orange).

The influence of noise on the FBDCCs computed in the cylindrical detector coordinates is illustrated in Figure 4.25 for a pair whose baseline does not intersect the FOV and in Figures 4.26 and 4.27 for two pairs whose baseline intersects the FOV. If the baseline and the FOV do not intersect, the errors (see Table 4.1b first row, second column) slightly increase compared to the ideal case with the three integration methods. If the baseline and the FOV intersect, the noise has great impact on the DCC, regardless of the location of the singular point in the projections, as shown by a large increase of the errors (see Table 4.1b second and third rows, second column).

4.4.3.3 Mechanical phantom

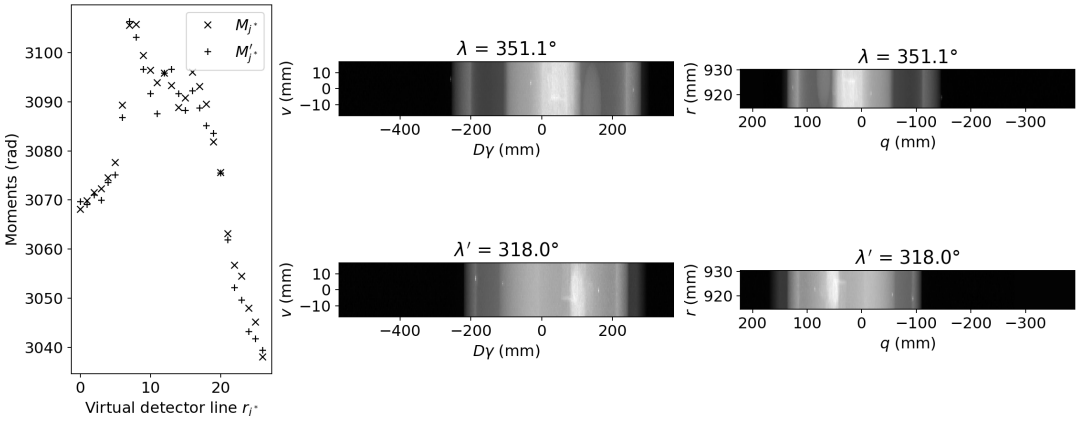

Figure 4.28: FBDCCs computed with the rebinning approach applied to a pair of projections of the mechanical phantom (real data) largely satisfying the FOV condition. The first column shows the projections' moments computed with the implementation described in Section 4.2.3. The central column shows the two projections for which DCCs are computed. The last column shows the weighted backprojection of each projection. The aspect ratios of the projections and weighted backprojections are both equal to 4.5.

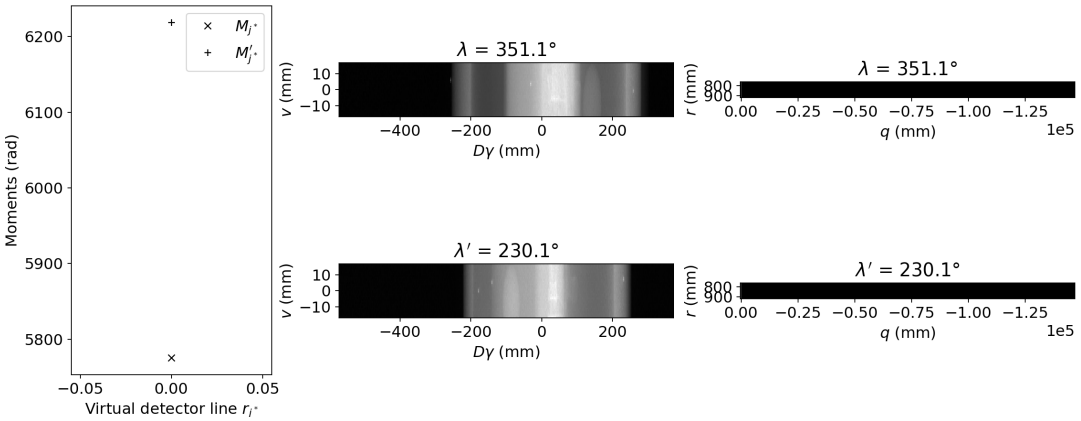

Figure 4.29: FBDCCs computed with the rebinning approach applied to a pair of projections of the mechanical phantom (real data) whose baseline is tangent to the FOV. The first column shows the projections' moments computed with the implementation described in Section 4.2.3. The central column shows the two projections for which DCCs are computed. The last column shows the weighted backprojection of each projection. The aspect ratio of the projections is 4.5 and the aspect ratio of the weighted backprojections is 45.

FBDCCs computed with the rebinning approach are illustrated in Figure 4.28 for a

pair of projections largely satisfying the FOV condition and in Figure 4.29 for a pair of projections whose baseline is tangent to the FOV. The noise increases the errors (see Table 4.1a third column) compared to the ideal case (see Table 4.1a first column). As the level of noise increases in real data compared to our simulations, the errors are higher than for the noisy simulations for the two pair-wise geometries (see Table 4.1a second column).

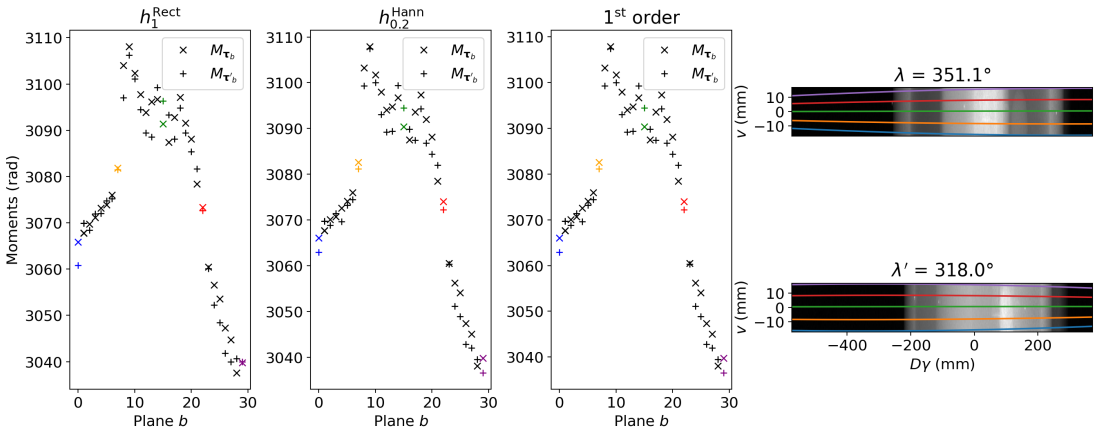

Figure 4.30: FBDCCs computed with the direct approach applied to a pair of projections of the mechanical phantom (real data) whose baseline does not intersect the FOV. There is no singularity in the computation of the moments. From left to right: integration with the Rectangular-windowed Hilbert kernel, integration with the Hann-windowed Hilbert kernel, integration with the first order approximation and the two projections for which FBDCCs are computed. Five planes are plotted: the first (in blue) and last (in purple) plane, the central plane (in green) and two intermediate planes (in red and orange).

FBDCCs computed with the direct approach are illustrated in Figure 4.30 for a pair whose baseline does not intersect the FOV and in Figure 4.31 for a pair whose baseline intersects the FOV. If the baseline does not intersect the FOV, the three integration methods give similar results to those obtained with the rebinning approach. The noise in real data leads to higher errors than for the noisy simulations (see Table 4.1b first row, last column). If the baseline and the FOV intersect, the errors strongly vary with the integration method (see Table 4.1b last row, last column). The integration with the first order approximation is highly unstable with a very high error. Regarding the integration methods with the Hilbert kernels, the errors are higher with a rectangular-windowed kernel than the Hann-windowed kernel that looks more stable in the presence of noise.

4.4.4 Discussion

4.4.4.1 Rebinning versus direct approach

The results show that for a pair whose baseline does not intersect the FOV, both approaches give similar results: same moment values (see Figures 4.14 and 4.20) and similar errors (see Table 4.1a first row, first column and Table 4.1b first row, first column). The direct approach offers more planes on which a FBDCC can be computed than rows on the virtual detector for the rebinning approach because of the sampling choice we made for both approaches. The number of planes for the direct approach would have been smaller if we had chosen an equi-spaced sampling along a certain axis rather than an equi-angular sampling. Both approaches are robust to noise and give similar results in terms of moment values (see Figures Figure 4.23 and 4.25, and Figures 4.28 and 4.30) and errors that are around 5% (see Table 4.1a first row, second and third columns, and Table 4.1b first row, second and third columns).

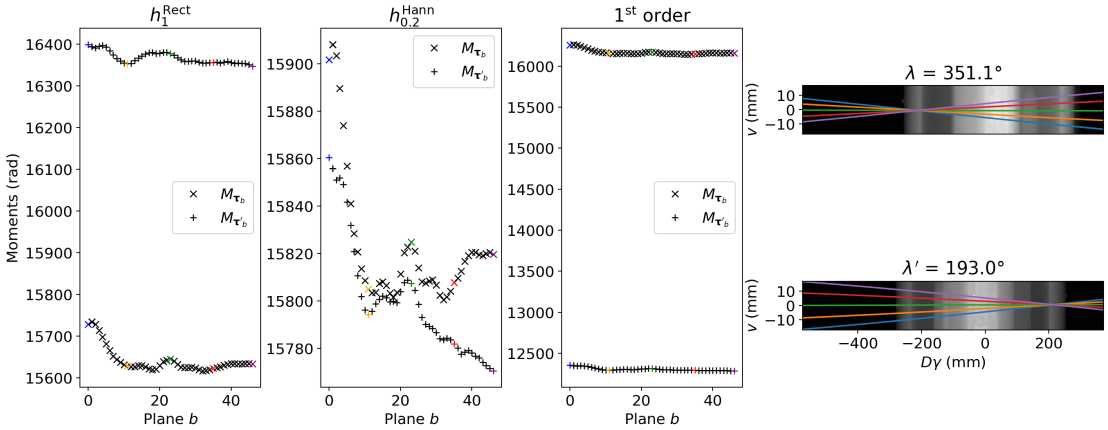

Figure 4.31: FBDCCs computed with the direct approach applied to a pair of projections of the mechanical phantom (real data) whose baseline intersects the FOV. There is a singularity in the computation of the moments. From left to right: integration with the Rectangular-windowed Hilbert kernel, integration with the Hann-windowed Hilbert kernel, integration with the first order approximation and the two projections for which FBDCCs are computed. Five planes are plotted: the first (in blue) and last (in purple) plane, the central plane (in green) and two intermediate planes (in red and orange).

The major advantage in computing the FBDCC in the cylindrical detector coordinates relates to the applicability of the DCC. Indeed, it enables to consider pairs whose baseline intersects the FOV unlike the rebinning approach to a virtual plane (Section 4.2, [Lesaint et al., 2017]). This is particularly useful, especially in helical CT where the number of pairs eligible for a DCC is limited because of the limited axial size of the detector.

4.4.4.2 Comparison of the integration methods for the FBDCC computed in the cylindrical detector coordinates

The three integration methods are equivalent for pairs of noiseless (see Figures 4.20 and Table 4.1b first row, first column) or noisy (see Figures 4.25 and 4.30 and Table 4.1b first row, second and third columns) projections whose baseline does not intersect the FOV. However, the numerical stability of the three integration methods strongly varies when the singular point is located in the projection, and when the projections are corrupted by noise.

In the context of noiseless data, two cases arise depending on the location of the singular point.

• If the singular point is located in a spatially smooth region of the two projections (see Figure 4.21 and Table 4.1b second row, first column), the three integration methods are validated by the small values of the errors. However, moment values differ from the integration with the Hilbert Kernel to the integration with the first order approximation because of the kernel values as shown in Figure 4.32. They are higher around the singular point for the first order approximation than the Hilbert kernels.

• If the singular point is located close to the steep spatial gradients of one of the two projections (see Figure 4.22 and Table 4.1b third row, first column), high errors are obtained with the three integration methods. In this situation, the sampling induces interpolation errors, emphasized by the integration kernels, making the projections inconsistent. With a ten times thinner sampling, interpolation errors are reduced, the moments are closer and the errors smaller for the three integration methods as illustrated in Figure 4.33.

In Figure 4.22, we observe that h_1^{Rect} is more stable than $h_{0.2}^{\text{Hann}}$ regarding the location of the singularity and that the moment values are higher with the Hann kernel than the

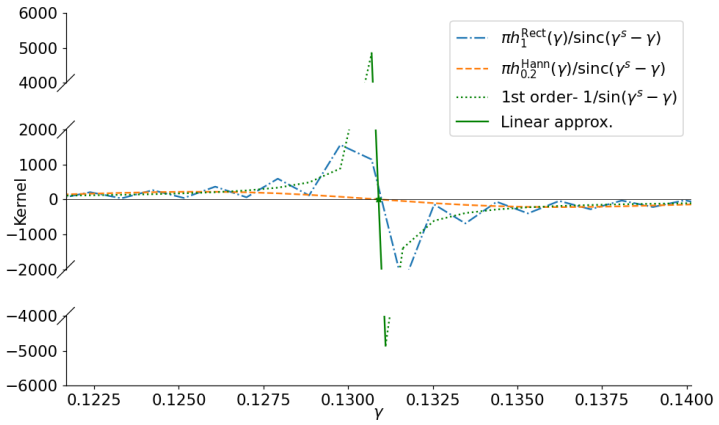

Figure 4.32: Plot of the three kernels used in the numerical integration of the FBDCC with the direct approach for the pair in Figure 4.21. The Rectangular-windowed Hilbert kernel is drawn in blue, the Hann-windowed Hilbert kernel is drawn in orange, and the first order integration elements are plotted in green.

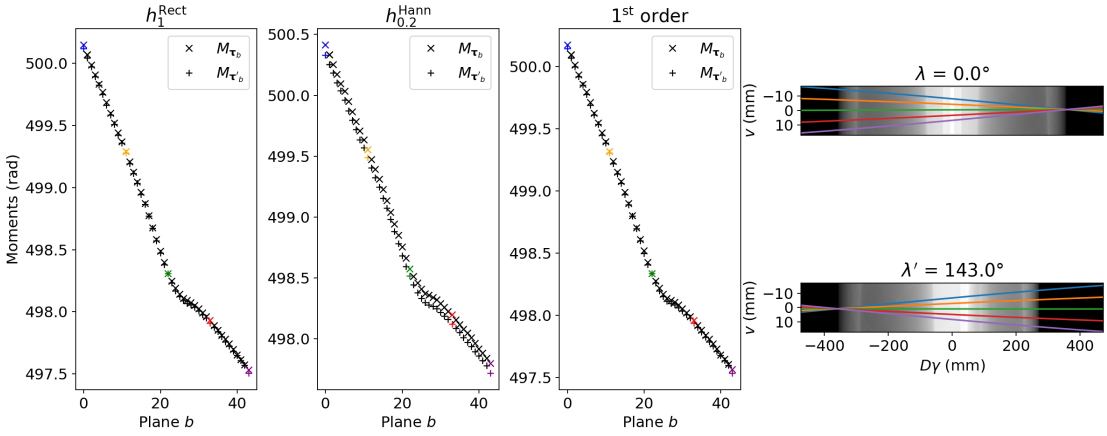

Figure 4.33: Computation of the FBDCC for a pair of simulated projection with a ten times thinner sampling than Figure 4.22. The singular point is close to the spatial gradients of both projections.

Rectangular kernel. Both are related to the width of the kernel. Indeed, computing the moments with the kernel $h_{0.2}^{\text{Rect}}$ gives similar moments values and a similar error ($E_{\lambda,\lambda'}^{Real} = 8.92\%$) as computing the moments with $h_{0.2}^{\text{Hann}}$ (see Figure 4.34). The projection values around the singularity are more smoothed with a parameter $\nu = 0.2$ than $\nu = 1$. Therefore, the interpolation errors around the steep gradient are accumulated which decreases the numerical stability of the integration method.

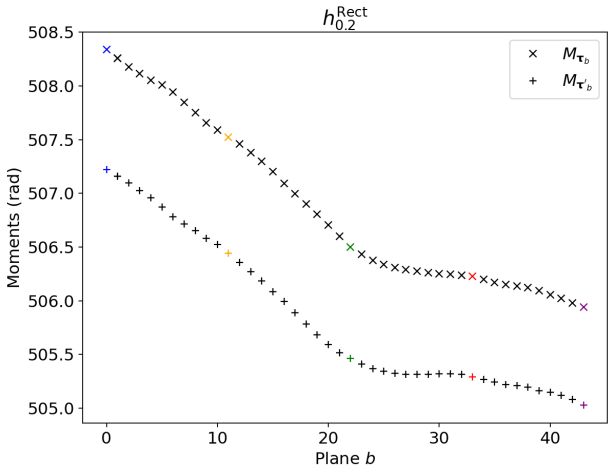

Figure 4.34: FBDCC of the pair Figure 4.22 computed with the direct approach and the Hilbert kernel $h_{0.2}^{\text{Rect}}$.

In the context of noisy data, FBDCCs are impacted by noise for the three integration methods regardless of the location of the singular point in the projections (see Figure 4.31 and Table 4.1b last row, last column). The integration with a first order approximation is the least stable as shown by the moments difference (Figure 4.31). This instability comes from the added sample that is badly interpolated in the presence of noise. The incorrect value is emphasized by the integration kernel and induces high inconsistencies. We investigated other implementations of the first order approximation such as adding a symmetrical sample with respect to the second nearest sample to the singularity (instead of the nearest sample) or evaluating the integral without the symmetrical contribution around the singularity. However, none of them gave satisfactory results. Regarding the Hilbert kernel integrations, the rectangular-windowed kernel is less stable than the Hann-windowed kernel. This variation in the numerical stability is explained by the shape of the Hann-windowed kernel that suppresses more high frequencies, i.e. noise, than the rectangular window, making the Hann-windowed integration more robust with respect to noise.

With those observations, a compromise must be made between numerical stability regarding the singular point location and robustness to noise. In Figures 4.26 and 4.31, we see that the noise has a greater impact on the DCC than the location of the singular point in the projections. As a result, the numerical integration of the moments will be performed with the Hann-windowed band-limited Hilbert kernel in the rest of the thesis.

4.4.4.3 FBDCC versus Grangeat-based DCCs

We mentioned in the introduction that the use of Grangeat-based DCCs could be an option, especially since the intermediate function involved in the Grangeat DCCs does not have a singularity. It was proven that if the projections verify the FBDCC (see Equation 4.29), they will also verify the Grangeat DCCs [Lesaint, 2018]. However, the reciprocal proposition is false as shown by [Lesaint et al., 2018]. The authors showed that truncated

projections may still verify Grangeat-based DCCs but not the FBDCC by adding a certain constant offset to the projection values. This explains our choice to work with the FBDCC. The robustness of the different pair-wise DCCs to discretization and noise might be different since the DCC used in this work has a singularity while the Grangeat DCCs require the computation of a derivative (which is also known to be sensitive to noise).

4.5 Conclusion

In this chapter, we developed and analyzed two approaches to apply the FBDCC to helical CT. The first approach rebins the cone-beam projections onto a virtual detector and applies the FBDCC along each row of the virtual detector. The rebinning approach is robust to noise, but only applies to pairs of projections whose baseline does not intersect with the FOV. The second approach computes the FBDCC directly in the cylindrical detector coordinates and enables the computation of the FBDCC for such pairs. The singularity in the computation of the moment is dealt with by using a first order approximation of the integrand or by bandlimiting the Hilbert kernel. The Hilbert integration with a Hann windowing is more robust than the first order approximation with respect to noise and sampling errors. If the pair's baseline and the FOV do not intersect, DCCs are as stable and robust as in the rebinning approach. When they do, even without noise, the Hilbert kernel h_ν strongly amplifies the discretization error, with both windowings, resulting in inconsistencies. This makes the FBDCC sensitive to noise.

Chapter 5

Local motion detection in helical CT using data consistency conditions

In conventional CT, the patient is assumed to remain static during the acquisition. In 4D CT, motion resulting from the breathing of the patient is assumed cyclic. In all cases, unexpected motion creates inconsistencies in the projections resulting in artifacts on the tomographic images.

In this chapter, we study the ability of the cone-beam pair-wise DCCs, presented in Chapter 4, to detect motion in a helical CT. In the previous chapter, we showed that the two approaches give almost identical results for pairs whose baseline does not intersect the FOV. Moreover, the computation of the FBDCC in the detector coordinates makes it possible to consider pairs whose baseline intersects the FOV. To maximize the number of possible pairs, we focus here on the approach that computes the FBDCC in the detector coordinates. However, we highlighted that the FBDCC is highly sensitive to noise and sampling errors for pairs whose baseline intersect the FOV. We therefore propose a noise-aware metric involving the zeroth order moments variance resulting from the noise in the projections.

The content of this chapter is based on two contributions: the submitted paper [Mouchet et al., 2022b] and the IEEE NSS/MIC conference 2022 proceeding [Mouchet et al., 2022a].

5.1 Cone-beam pair wise DCCs in helical CT

Cone-beam pair wise DCC are applied to any pair of cone-beam projections g_λ and $g_{\lambda'}$, whose baseline is not parallel to the helix axis, and verifying the applicability conditions from Section 4.3.4. We consider a plane $\Pi_{\boldsymbol{\tau}}$, defined in Section 4.3.1, that contains the two source positions $\boldsymbol{s}_\lambda$ and $\boldsymbol{s}_{\lambda'}$ and crosses the two lateral borders of both cone-beam projections. If the two fan-beam projections resulting from the intersection of $\Pi_{\boldsymbol{\tau}}$ with g_λ and $g_{\lambda'}$ are untruncated, the FBDCC states that

$$M_{\boldsymbol{\tau}} = M_{\boldsymbol{\tau}'} \tag{5.1}$$

where $M_{\boldsymbol{\tau}}$ and $M_{\boldsymbol{\tau}'}$ are the moments of the projections g_λ and $g_{\lambda'}$ in the plane $\Pi_{\boldsymbol{\tau}}$ with $\boldsymbol{\tau} = (\lambda, \lambda', \beta)$ and $\boldsymbol{\tau}' = (\lambda', \lambda, \beta)$. The mathematical expression of $M_{\boldsymbol{\tau}}$ is derived in Section 4.3.2 and given by Equation 4.62.

We sample B planes with the same baseline, as described in Section 4.3.4, and define $\overline{M_{\lambda,\lambda'}}$ as the mean moment of g_λ over the B planes

$$\overline{M_{\lambda,\lambda'}} = \frac{1}{B}\sum_{b=1}^{B} M_{\boldsymbol{\tau}_b}. \tag{5.2}$$

$M_{\boldsymbol{\tau}_b}$, $\boldsymbol{\tau}_b = (\lambda, \lambda', \beta_b)$ is the moment on the b-th plane, making an angle β_b with the reference plane, of the projection g_λ (see Section 4.3.1 for the definition of the reference plane).

5.2 Noise-aware consistency metric

We begin this section by describing the noise model of the projections. Then, the noise-aware consistency metric is presented, and derived in terms of the noise of the projections.

5.2.1 Noise model

We recall the line integral model that makes the link between x-ray attenuation and a projection $g_\lambda(\gamma, v)$:

$$g_\lambda(\gamma, v) = -\ln \frac{I(\lambda, \gamma, v)}{I_0(\lambda, \gamma, v)} \tag{5.3}$$

where $I_0(\lambda, \gamma, v)$ and $I(\lambda, \gamma, v)$ are the initial and final energy fluence of the beam emitted at angle λ in the direction of the pixel (γ, v).

According to [Kak and Slaney, 1988, chapter 5], we assume that the noise in a projection pixel comes from the variations of the energy fluence I that can be statistically described by a Poisson distribution with parameter $\bar{I}$, such that

$$\mathrm{P}\{I\} = \frac{\bar{I}^I}{I!}\boldsymbol{e}^{-\bar{I}}, \tag{5.4}$$

where $\mathrm{P}\{I\}$ is the probability that the energy fluence takes the value I. Following [Kak and Slaney, 1988, chapter 5], we assume that I_0 is a known constant and that the variations of the energy fluence I are much smaller than its average value $\bar{I}$. Hence, the variance of a projection pixel can be approximated with

$$\mathrm{Var}\left(g_\lambda(\gamma, v)\right) \approx \frac{1}{\bar{I}(\lambda, \gamma, v)}. \tag{5.5}$$

As we assume that the variations of the measured fluence I are small, we have $\bar{I}(\lambda, \gamma, v) \approx I(\lambda, \gamma, v)$ and the variance of the projections is finally written as

$$\mathrm{Var}\left(g_\lambda(\gamma, v)\right) \approx \frac{1}{I(\lambda, \gamma, v)} = \frac{1}{I_0(\lambda, \gamma, v)\exp\left(-g_\lambda(\gamma, v)\right)}. \tag{5.6}$$

The values of the initial energy fluence $I_0(\lambda, \gamma, v)$ are not the same for the simulated and real data and are given in the next two paragraphs.

5.2.1.1 Simulated data

For simulated data, the initial energy fluence is the same for all projections. Consequently, we have

$$I_0(\lambda, \gamma, v) = I_0 = 10^5 \tag{5.7}$$

and the expression of a pixel noise is given in Equation 5.6

5.2.1.2 Real data

For real data, the initial energy fluence $I_0(\lambda, \gamma, v)$ is determined with the relationship from Equation 1.1, that was modified to take into account the bow-tie attenuation. We have

$$I_0(\lambda, \gamma, v) = w_{BT}(\gamma) m_Z i(\lambda) U^2 \tag{5.8}$$

where $w_{BT}(\gamma)$ is the bow-tie filter attenuation value at fan angle γ, m_Z is a proportionality coefficient that includes the atomic number Z of the target and the probability of x-ray production, $i(\lambda)$ is the tube current at gantry angle λ and U is the tube voltage. The tube voltage U is fixed for the complete acquisition and can be retrieved from the DICOM files, the bow-tie filter attenuation values are provided by the manufacturer, and the values $i(\lambda)$ can be extracted from the raw data. As a result, to evaluate $I_0(\lambda, \gamma, v)$ for any projection pixel, we need to estimate the proportionality coefficient m_Z.

The estimation of m_Z is obtained by comparing the measured initial energy fluence in an air region of a projection and the theoretical initial energy fluence $w_{BT}(\gamma)i(\lambda)U^2$ given by Equation 5.8. In an air region, called g_{air}, the pixel values of the projections should be zero and the variance of the projection is the inverse of the initial energy fluence of the beam. Using Equation 5.6, we have

$$\text{Var}(g_{\text{air}}) = \frac{1}{I_0(\lambda, \gamma, v)} \tag{5.9}$$

$$I_0(\lambda, \gamma, v) = \frac{1}{\text{Var}(g_{\text{air}})} \tag{5.10}$$

Inserting Equation 5.10 in Equation 5.8, we obtain the following formula for the proportionality coefficient m_Z

$$m_Z = \frac{I_0(\lambda, \gamma, v)}{w_{BT}(\gamma)i(\lambda)U^2} = \frac{1}{\text{Var}(g_{\text{air}})} \frac{1}{w_{BT}(\gamma)i(\lambda)U^2}. \tag{5.11}$$

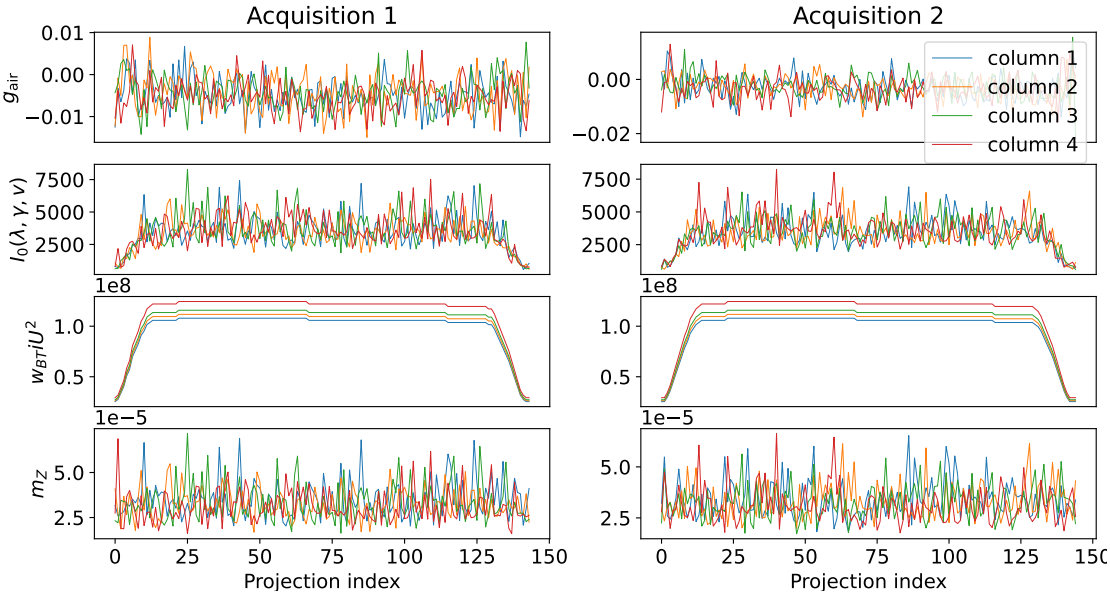

Figure 5.1: Computation of the different variables for the estimation of the proportionality coefficient m_Z. Top row: Pixel values for different air regions g_{air}. Second row: initial energy fluence $I_0(\lambda, \gamma, v)$ determined from the variance of the pixels. Third row: theoretical initial energy fluence $w_{BT}(\gamma)i(\lambda)U^2$. Bottom row: estimation of the coefficient m_Z for the four columns.

We applied this method to determine the proportionality coefficient of the Somatom go.Sim CT scan. In 289 projections taken from 2 different acquisitions (144 for acquisition 1 and 145 for acquisition 2) performed with the Somatom go.Sim Siemens CT scanner, we selected 4 columns of pixels (in total $4 \times N_{rows}$ pixels) of the projections without object. For each column, we measured the mean value of the pixels (top row Figure 5.1) and we

deduced the initial energy fluence $I_0(\lambda, \gamma, v)$ by measuring the variance of the pixels with Equation 5.10 (second row Figure 5.1).

The theoretical energy fluence $w_{BT}(\gamma)i(\lambda)U^2$ (third row Figure 5.1) was calculated for the same columns of pixels using the tube voltage value $U = 120$ kV (for the two acquisitions) found in the DICOM, and the bow-tie coefficient corresponding to this voltage and these columns provided by the manufacturer, and the extracted tube current $i(\lambda)$ from the raw data.

The coefficient m_Z obtained for each column was calculated using Equation 5.11 (bottom row Figure 5.1) and averaged over the $4 \times 289 = 1156$ measurements to obtain a final estimation of the coefficient $m_Z = (3.29 \pm 0.93) \times 10^{-5}$ $\mathrm{A}^{-1}\mathrm{V}^{-2}$.

5.2.2 The consistency metric

As mentioned in the introduction of this chapter, the noise impacts the FBDCC differently depending on the geometrical configuration of the pair. If the pair's baseline and the FOV do not intersect, the FBDCC is robust to noise (see Figure 4.25 and Figure 4.30). If the pair's baseline and the FOV intersect, the FBDCC is highly impacted by noise and sampling errors leading to the high variability of the zeroth order moments (see Figure 4.26, Figure 4.27 and Figure 4.31). Moreover, the level of noise is not the same for all projections, for example, between lateral and antero-posterior views of a patient. To account for the previous observations, we define the consistency metric between two cone-beam projections as

$$E_{\lambda,\lambda'} = \frac{B^{-1}\sum_{b=1}^{B}\left|M_{\boldsymbol{\tau}_b} - M_{\boldsymbol{\tau}'_b}\right|}{\sqrt{B}\sqrt{\mathrm{Var}(\overline{M_{\lambda,\lambda'}}) + \mathrm{Var}(\overline{M_{\lambda',\lambda}})}} \tag{5.12}$$

where the denominator is an approximation of the noise of the numerator coming from the projections pixels. The denominator is in fact the standard deviation of the mean moments difference, i.e. the numerator without the absolute value. Let $\overline{M_{\lambda,\lambda'}}$ and $\overline{M_{\lambda,\lambda'}}$ be two uncorrelated random variables, then we have

$$\sqrt{\mathrm{Var}\left(\overline{M_{\lambda,\lambda'}} - \overline{M_{\lambda',\lambda}}\right)} = \sqrt{\mathrm{Var}\left(\overline{M_{\lambda,\lambda'}}\right) + \mathrm{Var}\left(\overline{M_{\lambda',\lambda}}\right)}. \tag{5.13}$$

To explain the $\sqrt{B}$ weight in the denominator, we need to consider the mean moment of a projection $\overline{M_{\lambda,\lambda'}}$. The mean moment is taken over B random variables $M_{\boldsymbol{\tau}_b}$ that we suppose uncorrelated with the same standard deviation σ. Consequently, the standard deviation of $\overline{M_{\lambda,\lambda'}}$ is

$$\sqrt{\mathrm{Var}\left(\overline{M_{\lambda,\lambda'}}\right)} = \frac{\sigma}{\sqrt{B}}. \tag{5.14}$$

This equation shows that the variance of the mean moment depends on the number of planes B. However, we wish to define a consistency metric that does not depend on the number of plane, thus we normalize the metric with $\sqrt{B}$.

In fact, the hypothesis of uncorrelation between the B moments is not always valid. If a singularity is present in the computation of the moments, DCC planes intersect at the singular point, and the same projection pixels are used to interpolate the projection values along the planes, making the B moments correlated. If there is no singularity, the planes do not intersect and different pixels of the projection are used for the interpolation (assuming that the axial distance between two planes is wider than a pixel width).

Theoretical formula of the noise approximation The denominator of Equation 5.12 involves the variance $\mathrm{Var}(\overline{M_{\lambda,\lambda'}})$ of the mean moment of the projection g_λ. To express it in terms of the projection pixels' noise $\mathrm{Var}(g(\gamma_i, v_j))$ given in Section 5.2.1, we use a similar development as the one presented in [Wunderlich and Noo, 2008] for the derivation of the

noise for CT images reconstructed with fan-beam reconstruction algorithms. The first hypothesis made here is that two pixels are uncorrelated. However, two moments $M_{\boldsymbol{\tau}_k}$ and $M_{\boldsymbol{\tau}_l}$ may use the same pixels of the projection g_λ, and be correlated, because of the interpolation of $v_{\boldsymbol{\tau}}$. Thus, their co-variance should be accounted for. Starting by expending $\mathrm{Var}(\overline{M_{\lambda,\lambda'}})$, we have

$$\mathrm{Var}(\overline{M_{\lambda,\lambda'}}) = \frac{1}{B^2}\sum_{b=1}^{B}\mathrm{Var}\left(M_{\boldsymbol{\tau}_b}\right) + \frac{2}{B^2}\sum_{1\leq k<l\leq B}\mathrm{Cov}\left(M_{\boldsymbol{\tau}_k}, M_{\boldsymbol{\tau}_l}\right). \tag{5.15}$$

The moment $M_{\boldsymbol{\tau}}$ is discretized using the same sampling of the detector as presented in Section 4.3.3.2, i.e $i \in \{1, ..., N_{cols}\}$, $j \in \{1, ..., N_{rows}\}$. We recall the discretization of the moment $M_{\boldsymbol{\tau}}$

$$M_{\boldsymbol{\tau}} \simeq \Delta_\gamma \sum_{i=1}^{N_{\text{cols}}} \frac{D\,\mathrm{sign}\left(\gamma^s_{\lambda,\lambda'}\right)}{\sqrt{D^2 + v^2_{\boldsymbol{\tau}}(\gamma_i)}|\cos\alpha|}\frac{\pi h_\nu(\gamma^s_{\lambda,\lambda'} - \gamma_i)}{\mathrm{sinc}(\gamma^s_{\lambda,\lambda'} - \gamma_i)} g_\lambda(\gamma_i, v_{\boldsymbol{\tau}}(\gamma_i)) \tag{5.16}$$

where $g_\lambda(\gamma_i, v_{\boldsymbol{\tau}}(\gamma_i))$ is obtained with linear interpolation using Equation 4.57 and $h_\nu(\gamma^s_{\lambda,\lambda'} - \gamma)$ is a band-limited version of the Hilbert kernel as described in Section 4.3.3.2. In this chapter, we choose to work only with the Hann-windowed kernel given in Equation 4.65 as we observed that it was the most robust integration method with noisy projections. The bandwidth of the kernel is adapted to the amount of noise in the acquisition with the parameter ν. To ease the notation, we introduce

$$a_{\boldsymbol{\tau}}(\gamma) = \Delta_\gamma \frac{D\,\mathrm{sign}\left(\gamma^s_{\lambda,\lambda'}\right)}{\sqrt{D^2 + v^2_{\boldsymbol{\tau}}(\gamma_i)}|\cos\alpha|}\frac{\pi h_\nu(\gamma^s_{\lambda,\lambda'} - \gamma_i)}{\mathrm{sinc}(\gamma^s_{\lambda,\lambda'} - \gamma_i)} \tag{5.17}$$

and Equation 5.16 becomes

$$M_{\boldsymbol{\tau}} \simeq \sum_{i=1}^{N_{\text{cols}}} a_{\boldsymbol{\tau}}(\gamma) g_\lambda(\gamma_i, v_{\boldsymbol{\tau}}(\gamma_i)). \tag{5.18}$$

We now express each component of Equation 5.15 in terms of the noise of the projection pixel $\mathrm{Var}(g(\gamma_i, v_j))$. Using Equation 5.18, we develop $\mathrm{Var}\left(M_{\boldsymbol{\tau}_b}\right)$:

$$\begin{aligned}
\mathrm{Var}\left(M_{\boldsymbol{\tau}_b}\right) &= \mathrm{Var}\left(\sum_{i=1}^{N_{\text{cols}}} a_{\boldsymbol{\tau}}(\gamma_i) g_\lambda(\gamma_i, v_{\boldsymbol{\tau}_b}(\gamma_i))\right) && (5.19)\\
&= \mathrm{Var}\left(\sum_{i=1}^{N_{\text{cols}}} a_{\boldsymbol{\tau}}(\gamma_i)\left((1-w_{i,j})g_\lambda(\gamma_i, v_j) + w_{i,j} g_\lambda(\gamma_i, v_{j+1})\right)\right) && (5.20)\\
&= \sum_{i=1}^{N_{\text{cols}}} a^2_{\boldsymbol{\tau}}(\gamma_i)\mathrm{Var}\left((1-w_{i,j})g_\lambda(\gamma_i, v_j) + w_{i,j} g_\lambda(\gamma_i, v_{j+1})\right) && (5.21)
\end{aligned}$$

The two pixels $g_\lambda(\gamma_i, v_j)$ and $g_\lambda(\gamma_i, v_{j+1})$ are assumed uncorrelated, thus

$$\begin{aligned}
\mathrm{Var}\left((1-w_{i,j})g_\lambda(\gamma_i, v_j) + w_{i,j} g_\lambda(\gamma_i, v_{j+1})\right) = \\
(1-w_{i,j})^2\mathrm{Var}\left(g_\lambda(\gamma_i, v_j)\right) + w^2_{i,j}\mathrm{Var}\left(g_\lambda(\gamma_i, v_{j+1})\right)
\end{aligned} \tag{5.22}$$

which gives the final expression of $\mathrm{Var}\left(M_{\boldsymbol{\tau}_b}\right)$,

$$\mathrm{Var}\left(M_{\boldsymbol{\tau}_b}\right) = \sum_{i=1}^{N_{\text{cols}}} a^2_{\boldsymbol{\tau}_b}(\gamma_i)\left((1-w_{i,j})^2\mathrm{Var}\left(g_\lambda(\gamma_i, v_j)\right) + w^2_{i,j}\mathrm{Var}\left(g_\lambda(\gamma_i, v_{j+1})\right)\right). \tag{5.23}$$

Let us now express the co-variance between two moments $\mathrm{Cov}\left(M_{\boldsymbol{\tau}_k}, M_{\boldsymbol{\tau}_l}\right)$ in terms of the noise of the projection pixel. Using Equation 5.18, we develop $\mathrm{Cov}\left(M_{\boldsymbol{\tau}_k}, M_{\boldsymbol{\tau}_l}\right)$:

$$\mathrm{Cov}\left(M_{\boldsymbol{\tau}_k}, M_{\boldsymbol{\tau}_l}\right) = \quad \mathrm{Cov}\left(\sum_{i_k=1}^{N_{\mathrm{cols}}} a_{\boldsymbol{\tau}_k}(\gamma_{i_k}) g_\lambda(\gamma_{i_k}, v_{\boldsymbol{\tau}_k}(\gamma_{i_k})), \sum_{i_l=1}^{N_{\mathrm{cols}}} a_{\boldsymbol{\tau}_l}(\gamma_{i_l}) g_\lambda(\gamma_{i_l}, v_{\boldsymbol{\tau}_l}(\gamma_{i_l}))\right) \tag{5.24}$$

$$= \quad \sum_{i_k=1}^{N_{\mathrm{cols}}} \sum_{i_l=1}^{N_{\mathrm{cols}}} a_{\boldsymbol{\tau}_k}(\gamma_{i_k}) a_{\boldsymbol{\tau}_l}(\gamma_{i_l}) \mathrm{Cov}\left(g_\lambda(\gamma_{i_k}, v_{\boldsymbol{\tau}_k}(\gamma_{i_k})), g_\lambda(\gamma_{i_l}, v_{\boldsymbol{\tau}_l}(\gamma_{i_l}))\right). \tag{5.25}$$

Developing $\mathrm{Cov}\left(g_\lambda(\gamma_{i_k}, v_{\boldsymbol{\tau}_k}(\gamma_{i_k})), g_\lambda(\gamma_{i_l}, v_{\boldsymbol{\tau}_l}(\gamma_{i_l}))\right)$ with the interpolation formulas of $g_\lambda(\gamma_{i_k}, v_{\boldsymbol{\tau}_k}(\gamma_{i_k}))$ and $g_\lambda(\gamma_{i_l}, v_{\boldsymbol{\tau}_l}(\gamma_{i_l}))$ (see Equation 4.57) and using the bilinearity of the co-variance, we have

$$\begin{aligned}
\mathrm{Cov}\left(g_\lambda(\gamma_{i_k}, v_{\boldsymbol{\tau}_k}(\gamma_{i_k})), g_\lambda(\gamma_{i_l}, v_{\boldsymbol{\tau}_l}(\gamma_{i_l}))\right) = {} & (1 - w_{i_k,j_k})(1 - w_{i_l,j_l}) \mathrm{Cov}\left(g_\lambda(\gamma_{i_k}, v_{j_k}), g_\lambda(\gamma_{i_l}, v_{j_l})\right) \\
& + (1 - w_{i_k,j_k}) w_{i_l,j_l} \mathrm{Cov}\left(g_\lambda(\gamma_{i_k}, v_{j_k}), g_\lambda(\gamma_{i_l}, v_{j_l+1})\right) \\
& + w_{i_k,j_k}(1 - w_{i_l,j_l}) \mathrm{Cov}\left(g_\lambda(\gamma_{i_k}, v_{j_k+1}), g_\lambda(\gamma_{i_l}, v_{j_l})\right) \\
& + w_{i_k,j_k} w_{i_l,j_l} \mathrm{Cov}\left(g_\lambda(\gamma_{i_k}, v_{j_k+1}), g_\lambda(\gamma_{i_l}, v_{j_l+1})\right).
\end{aligned} \tag{5.26}$$

Pixels are assumed to be uncorrelated, so the co-variance of two pixels is not 0 only if they are the same pixel. Knowing that $\mathrm{Cov}(X, X) = \mathrm{Var}(X)$, we have the following expressions for the co-variances involved in Equation 5.26:

$$\mathrm{Cov}\left(g_\lambda(\gamma_{i_k}, v_{j_k}), g_\lambda(\gamma_{i_l}, v_{j_l})\right) = \delta_{i_k,i_l}\delta_{j_k,j_l} \mathrm{Var}(g_\lambda(\gamma_{i_k}, v_{j_k})) \tag{5.27}$$

$$\mathrm{Cov}\left(g_\lambda(\gamma_{i_k}, v_{j_k}), g_\lambda(\gamma_{i_l}, v_{j_l+1})\right) = \delta_{i_k,i_l}\delta_{j_k,j_l+1} \mathrm{Var}(g_\lambda(\gamma_{i_k}, v_{j_k})) \tag{5.28}$$

$$\mathrm{Cov}\left(g_\lambda(\gamma_{i_k}, v_{j_k+1}), g_\lambda(\gamma_{i_l}, v_{j_l})\right) = \delta_{i_k,i_l}\delta_{j_k+1,j_l} \mathrm{Var}(g_\lambda(\gamma_{i_k}, v_{j_k+1})) \tag{5.29}$$

$$\mathrm{Cov}\left(g_\lambda(\gamma_{i_k}, v_{j_k+1}), g_\lambda(\gamma_{i_l}, v_{j_l+1})\right) = \delta_{i_k,i_l}\delta_{j_k+1,j_l+1} \mathrm{Var}(g_\lambda(\gamma_{i_k}, v_{j_k+1})) \tag{5.30}$$

where the Kronecker delta $\delta_{i,i'}$ is 1 if $i = i'$ and 0 otherwise. Using Equation 5.27 to Equation 5.30 in Equation 5.26, inserting Equation 5.26 in Equation 5.25 and noticing that

$$\sum_{i_k=1}^{N_{\mathrm{cols}}} \sum_{i_l=1}^{N_{\mathrm{cols}}} \delta_{i_k,i_l} a_{\boldsymbol{\tau}_k}(\gamma_{i_k}) a_{\boldsymbol{\tau}_l}(\gamma_{i_l}) = \sum_{i=1}^{N_{\mathrm{cols}}} a_{\boldsymbol{\tau}_k}(\gamma_i) a_{\boldsymbol{\tau}_l}(\gamma_i), \tag{5.31}$$

we have

$$\begin{aligned}
&\mathrm{Cov}\left(M_{\boldsymbol{\tau}_k}, M_{\boldsymbol{\tau}_l}\right) = \\
&\sum_{i=1}^{N_{\mathrm{cols}}} a_{\boldsymbol{\tau}_k}(\gamma_i) a_{\boldsymbol{\tau}_l}(\gamma_i) \left((1 - w_{i,j_k})(1 - w_{i,j_l})\delta_{j_k,j_l} + (1 - w_{i,j_k}) w_{i,j_l}\delta_{j_k,j_l+1}\right) \mathrm{Var}(g_\lambda(\gamma_i, v_{j_k})) \\
&+ \sum_{i=1}^{N_{\mathrm{cols}}} a_{\boldsymbol{\tau}_k}(\gamma_i) a_{\boldsymbol{\tau}_l}(\gamma_i) \left(w_{i,j_k}(1 - w_{i,j_l})\delta_{j_k+1,j_l} + w_{i,j_k} w_{i,j_l+1}\delta_{j_k+1,j_l+1}\right) \mathrm{Var}(g_\lambda(\gamma_i, v_{j_k+1}))
\end{aligned} \tag{5.32}$$

resulting in

$$\mathrm{Cov}\left(M_{\boldsymbol{\tau}_k}, M_{\boldsymbol{\tau}_l}\right) = \sum_{i=1}^{N_{\mathrm{cols}}} a_{\boldsymbol{\tau}_k}(\gamma_i) a_{\boldsymbol{\tau}_l}(\gamma_i) \left(V_{i,j_k,j_l} \mathrm{Var}\left(g_\lambda(\gamma_i, v_{j_k})\right) + W_{i,j_k,j_l} \mathrm{Var}\left(g_\lambda(\gamma_i, v_{j_k+1})\right)\right) \tag{5.33}$$

with

$$V_{i,j_k,j_l} = (1 - w_{i,j_k})(1 - w_{i,j_l})\delta_{j_k,j_l} + (1 - w_{i,j_k}) w_{i,j_l}\delta_{j_k,j_l+1} \tag{5.34}$$

$$W_{i,j_k,j_l} = w_{i,j_k}(1 - w_{i,j_l})\delta_{j_k+1,j_l} + w_{i,j_k} w_{i,j_l}\delta_{j_k+1,j_l+1}. \tag{5.35}$$

5.3 Datasets

The metric from Equation 5.12 was applied to a motion detection problem in helical CT on simulated, mechanical phantom, and patient data.

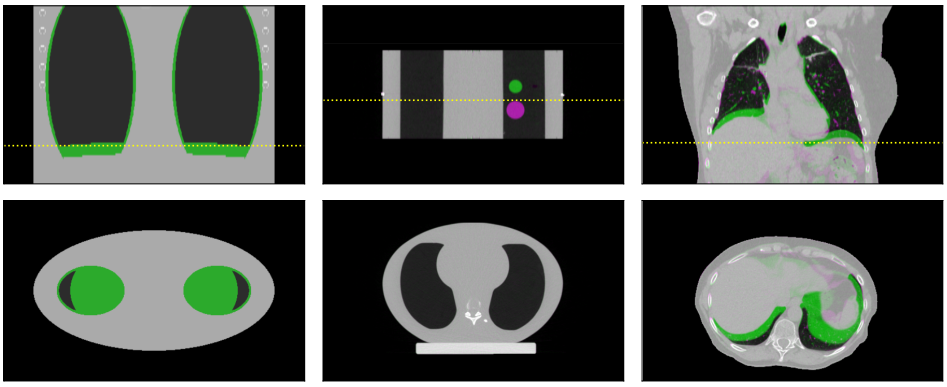

Figure 5.2: Coronal (top) and axial (bottom) slices of the three CT images reconstructed from the projections used in this study: Forbild phantom (simulated, left), CIRS phantom (real data, center) and clinical data (real data, right). The two extreme positions are superimposed in green (end-exhale) and purple (end-inhale).

5.3.1 Numerical phantom

The detection of motion with FBDCC in the detector coordinates was first tested on simulated acquisitions of the dynamic thorax Forbild phantom [Bergner and Kachelriess, 2009], displayed in Figure 5.2, left column. Helical acquisitions were simulated with 360 projections per rotation and four rotations. The duration of a rotation was 0.5 s. The detector size was 920×32 pixels of 1.03×1.09 mm. The helical pitch was $d = 15.36$ mm, the radius of the helical trajectory was 610 mm and the detector-source distance was 1113 mm. Ten rays were simulated and averaged per pixel. The acquisitions were centered around $z = -160$ mm. Noisy projections were generated using the Reconstruction Toolkit (RTK, [Rit et al., 2013]). For noisy projections, Poisson noise was added to the projections before taking their logarithm with 10^5 photons in air as described in Section 5.2.1.1. When breathing, the phantom's lungs followed the motion $c(t) = 1 - \cos(2\pi t/T_{\text{resp}})^2,\ t \in [0, 2]$, with a respiratory period of $T_{\text{resp}} = 2$ s, and the breathing started at the beginning of the acquisition. In total, two acquisitions were simulated: one acquisition of the static phantom and one acquisition of a moving phantom. The bandwidth parameter of the discretized Hilbert kernel h_ν was $\nu = 0.2$ and all moments $M_{\boldsymbol{\tau}}$ were computed with Equation 5.16.

5.3.2 Mechanical phantom

The CIRS Dynamic Thorax Motion Phantom model 008A with a 3 cm diameter tumor in the left lung was scanned with the Somatom go.Sim Siemens CT scan with a rotation time of 0.35 s and a pitch $P = 0.07$ (the corresponding table feed is $d = 1.34$ mm), which is one of the clinical protocol for 4D CT acquisitions recommended by the manufacturer (see Table 2.1). The tumor motion was a sinusoidal wave of $T_{\text{resp}} = 4$ s and the motion amplitudes were 20 mm and 5 mm in the SI and AP directions, respectively. The phantom was scanned twice, once with the tumor static and once with the tumor moving. The 3D

CT frames at the two extreme phases of the 4D CT image of the moving phantom are shown in Figure 5.2, central column.

5.3.3 Patient data

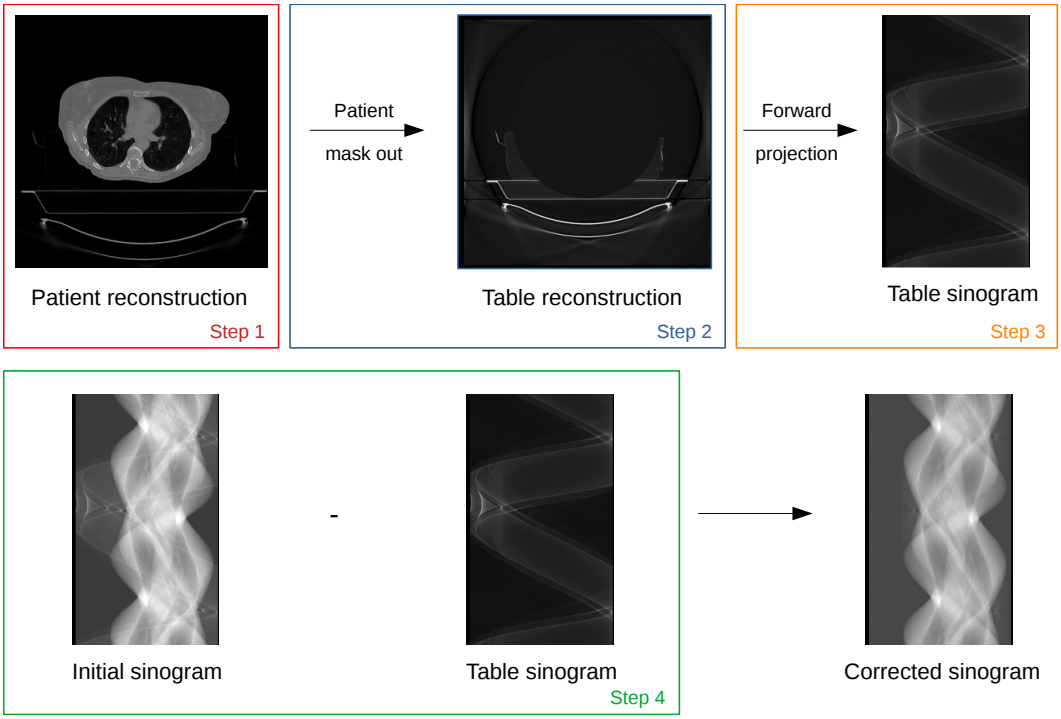

Figure 5.3: Workflow for the correction of truncated sinogram. The reconstruction were performed with the CG algorithm, with 100 iterations and a regularization parameter $\Gamma = 100$.

Patient 1. End-inhale and end-exhale CT images from the 4D acquisition of the first patient are shown in Figure 5.2, right column. The rotation time was the same as that of the CIRS phantom but the helical pitch was $P = 0.08$ (the corresponding table feed is $d = 1.54$ mm).

Patient 2. A second patient who suffered from severe irregular breathing was selected from our database of 4D CT acquisitions (see Figure 6.3). The rotation time was 0.5 s and the helical pitch was $P = 0.07$ (the corresponding table feed is $d = 1.34$ mm).

The particularity of patient data is that the projections are truncated because the FOV is not large enough to contain the patient table. Therefore, a pre-processing step consisting in the removal of the table from the projections was necessary to compute the DCCs which assume no lateral truncation. We followed the algorithm, illustrated in Figure 5.3, proposed in [Mory et al., 2016] which is four steps: firstly, a 3D reconstruction of the whole volume (body + table) is computed; secondly, the patient is masked out from the reconstructed image to keep the table part only; thirdly, the table part is forward-projected according to the acquisition geometry; fourthly, the resulting table projections are subtracted from the measured projections.

The main issue in verifying DCCs for patient data is that we have no ground truth or static acquisition that we can refer to. To verify that DCCs detect motion, a reference respiratory phase of the patient was visually measured by identifying end-exhale projections (phase 0%) from the visible displacement of the diaphragm in the projections.

The bandwidth parameter of the discretized Hilbert kernel h_ν was $\nu = 0.1$ to take into account the higher noise level in real data and all moments $M_{\boldsymbol{\tau}}$ were computed with Equation 5.16.

5.4 Results

5.4.1 Numerical phantom

We begin this section with the validation of the theoretical formula of the standard deviation derived in Equation 5.15 with a batch approach. Then, results regarding the detection of motion using DCCs are presented.

5.4.1.1 Validation of the noise approximation

The standard deviation formula of the mean moments difference was verified with a batch approach. 10 000 realizations of Poisson noise as described in Figure 5.6 are simulated. For each realization, the moments $\overline{M_{\lambda,\lambda'}}$ and $\overline{M_{\lambda',\lambda}}$ are computed for eligible pairs (λ, λ') (see Section 4.3.4), with λ a fixed reference projection. Then, the standard deviation of the mean moments difference and the standard deviation of the mean moments absolute difference for each pair are calculated over all realizations.

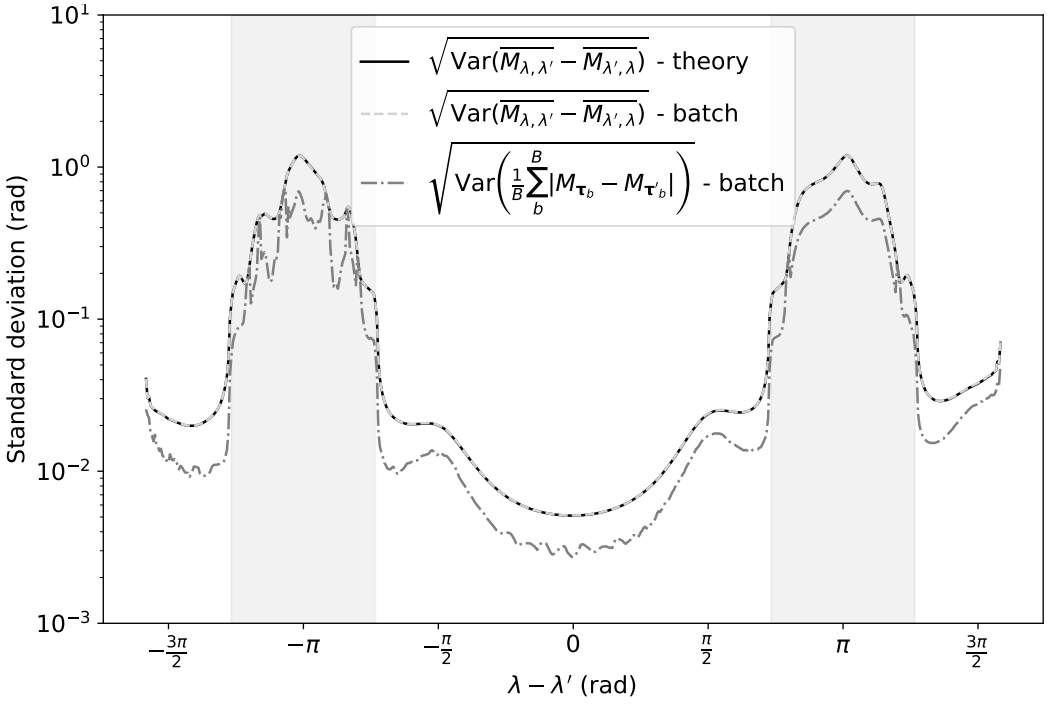

Figure 5.4: Validation of the noise approximation. Theoretical (black line) and experimental (dotted light-gray line) standard deviations of the mean moments difference, experimental standard deviation of the mean moments absolute difference (dash-dotted gray line) for all eligible pairs $(\boldsymbol{s}_\lambda, \boldsymbol{s}_{\lambda'})$ computed from the fixed reference projection $\lambda = 0$.

Figures 5.4 and 5.5 show the theoretical and batch standard deviations of the mean moments difference and the batch standard deviation of the mean moments absolute difference obtained with 10 000 realizations from two reference projections at $\lambda = 0°$ and $\lambda = 90°$. The batch approach validates the theoretical formula of the standard deviation derived in Equation 5.15 in both cases. In Figure 5.4, pairs with an absolute source angle difference close to $\pi/2$ and $3\pi/2$ suffer from higher noise and moments variance due to

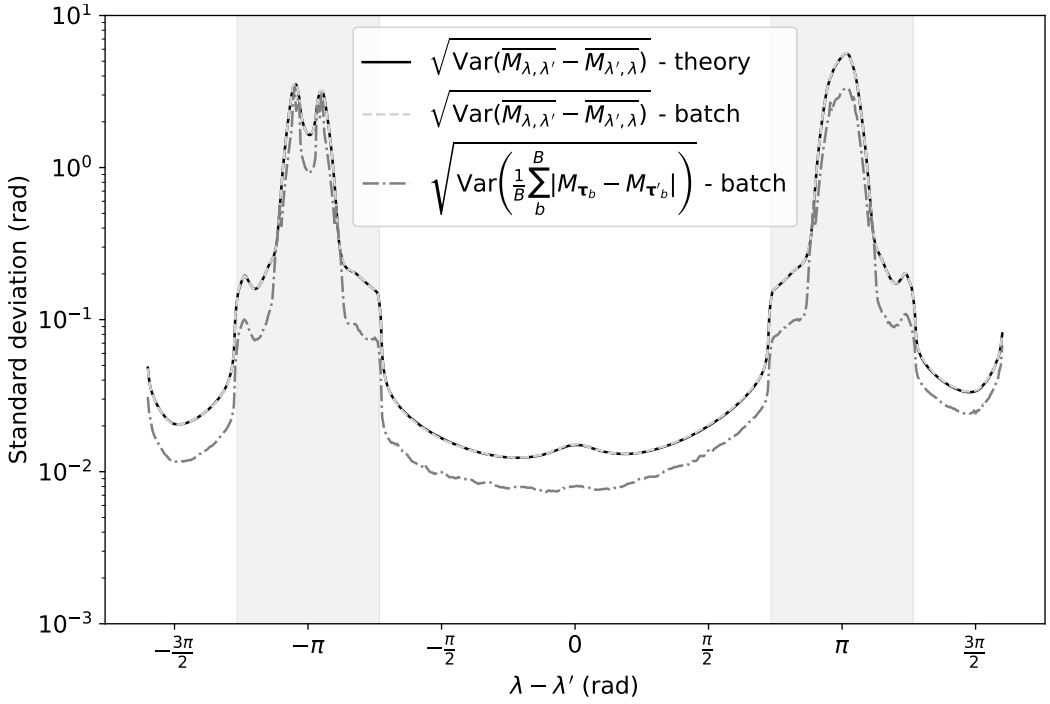

Figure 5.5: Validation of the noise approximation. Theoretical (black line) and batch (dotted light-gray line) standard deviations of the mean moments difference, batch standard deviation of the mean moments absolute difference (dash-dotted gray line) for all eligible pairs $(\boldsymbol{s}_\lambda, \boldsymbol{s}_{\lambda'})$ computed from the fixed reference projection $\lambda = 90°$.

the elliptical shape of the Forbild thorax phantom. This is corroborated by the standard deviations computed from a lateral source position (see Figure 5.5) where we observe the reversed case: the noise is higher around the reference projection (where the phantom is viewed laterally) than for absolute source angle difference close to $\pi/2$. The standard deviations are smaller around the reference from $\lambda = 0°$ than from $\lambda = 90°$ because of the elliptical shape of the phantom. The highest noise, independently of the reference projection, is for pairs with an absolute source angle difference close to π, i.e. pairs whose baseline intersects the FOV. Those highest values confirm the high sensitivity of the DCC with respect to noise for such pairs. The values are higher when the reference projection is taken at $\lambda = 90°$ (Figure 5.5) than $\lambda = 0°$ (Figure 5.4) because of the elliptical shape of the phantom. The increase of the standard deviation for pairs with an absolute source angle difference above $3\pi/2$ is caused by the decrease of DCC planes (as the displayed values, in Figures 5.5 and 5.4, are not normalized by $\sqrt{B}$).

In comparison to the standard deviation of the mean absolute difference of the moments, the noise is over-estimated for any source angle difference with a mean relative error of 42% for Figure 5.4 and 40% for Figure 5.5. However, the general shape of the variations is similar to the one of the mean difference standard deviation. Thus, we consider this estimation of the noise acceptable for our use.

5.4.1.2 Application to motion detection

Figure 5.6 shows the consistency metric $E_{\lambda,\lambda'}$ and its different parts for a fixed projection of reference at $\lambda = 0°$ at end-exhale and all other source positions λ' with which DCCs can be computed (see Section 4.3.4), for both static and dynamic simulations of the phantom.

When the baseline and the FOV do not intersect (white background), the consistency

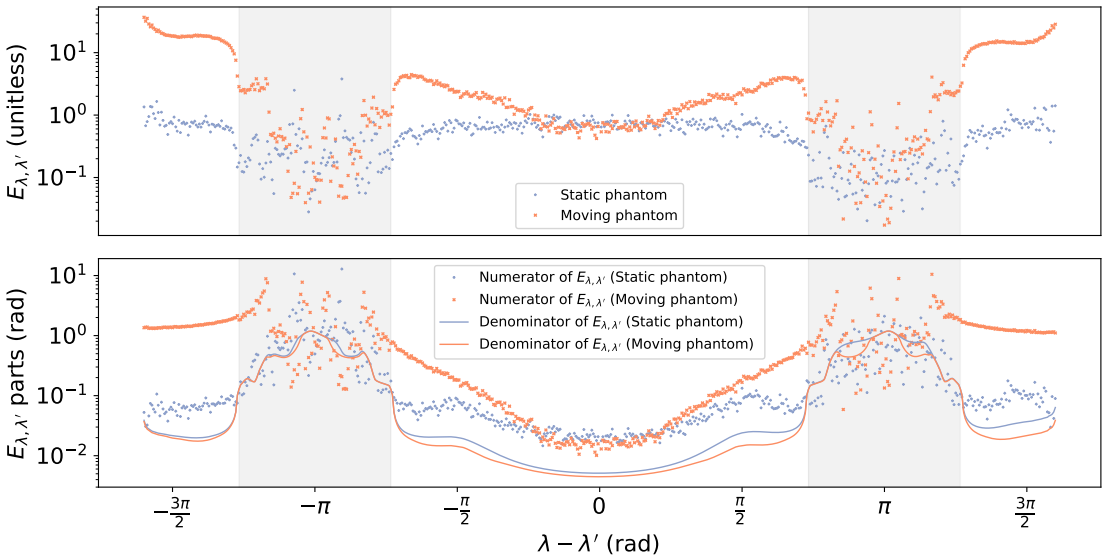

Figure 5.6: Consistency metric $E_{\lambda,\lambda'}$ (top row) and its parts (bottom row) for all pairs (λ, λ') with noisy projections. The blue line and dots correspond to the static acquisition and the orange line and dots correspond to the acquisition where the phantom moves. The gray rectangles mark the geometrical situation where the baseline intersects the FOV.

metric for the static acquisitions is rather constant and around 0.8. This is the expected value for uncorrelated samples of a normal distribution for which the mean absolute deviation (the numerator of $E_{\lambda,\lambda'}$) is $\sigma\sqrt{2\pi^{-1}} \simeq 0.8\sigma$ and the standard deviation (the denominator) is also σ. The values are centered around a lower value when the baseline and the FOV intersect (gray background) which may be due to stronger correlations between the B samples since the DCC planes all intersect each projection at the singular point.

When the phantom moves (orange curves with square symbols in Figure 5.6), the detection of motion is possible when the baseline does not intersect the FOV (white background) and the inconsistency increases with $|\lambda - \lambda'|$ as does the motion amplitude of the phantom's lungs. When the baseline and the FOV intersect (gray background), it is generally difficult to detect motion because the inconsistencies due to motion are dominated by those due to noise and interpolation errors. Motion seems to be detectable only on the side of the gray rectangles, i.e. when the baseline intersects the FOV but not the phantom, in which case the singular point is in an air region of the projection, which is locally constant and the least noisy.

5.4.2 Phantom data

The results of the consistency metric for the CIRS phantom are presented for all possible pairs with one fixed projection of reference $\lambda = 36 \times 360° + 0.14°$ in Figure 5.7 and $\lambda = 50 \times 360° + 169.83°$ in Figure 5.8. In Figure 5.7, the reference projection was acquired when the tumor was at an extreme position of its motion cycle. In Figure 5.8, the reference projection was acquired when the tumor was at an intermediate position of its motion cycle.

For a static tumor (top row in Figures 5.7 and 5.8), the consistency metric follows the pattern observed in Figure 5.6 in the previous section, i.e., rather constant for all pairs with noisier values when the baseline and the FOV intersect. For a moving tumor (middle row in Figures 5.7 and 5.8), the consistency metric seems to follow the tumor phase (bottom row of Figures 5.7 and 5.8): the values are close to the ones obtained for a static phantom for projections separated by about 4 s on Figure 5.7 and about 2 s on Figure 5.8, as expected since the phantom has the same position at mid-exhale and mid-inhale.

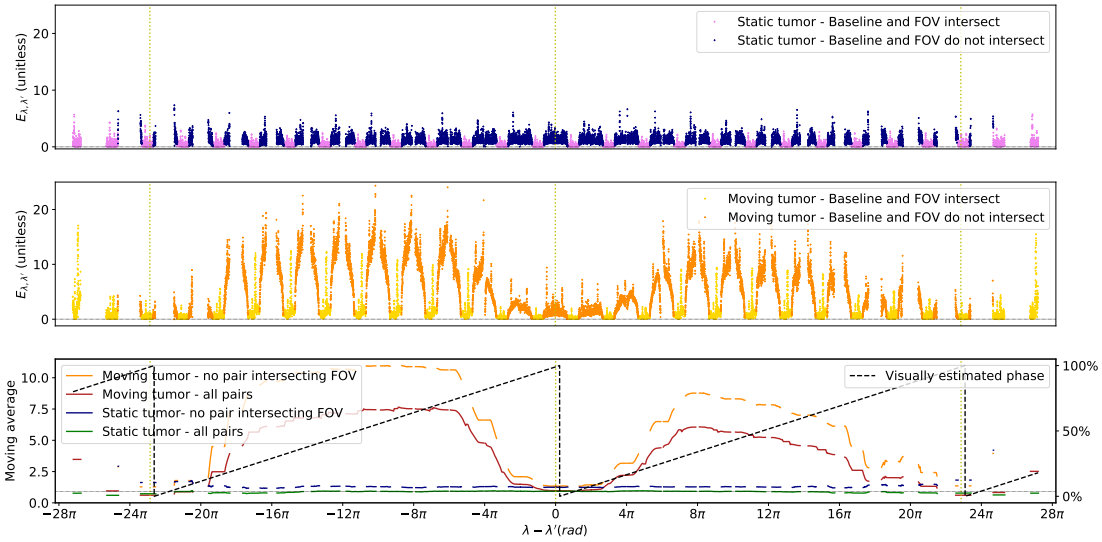

Figure 5.7: Consistency metric $E_{\lambda,\lambda'}$ computed from a reference projection at $\lambda = 36 \times 360° + 0.14°$ acquired when the tumor was at an extreme position of the breathing cycle. Top: static tumor. Center: moving tumor. Bottom: moving average over one gantry rotation of the above plots and tumor motion. The moving average is only computed when the center of the window has a DCC.

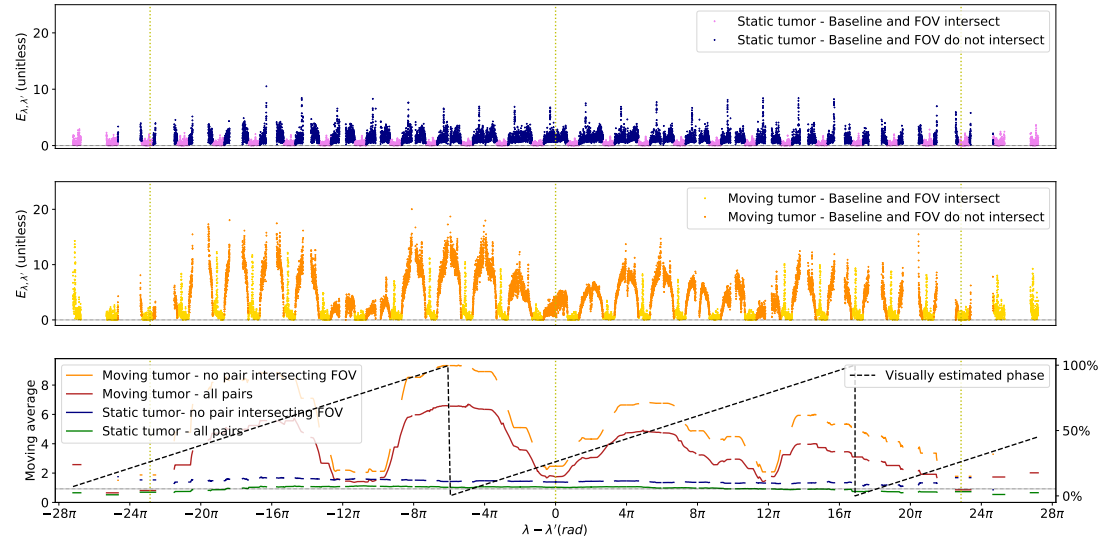

Figure 5.8: Consistency metric $E_{\lambda,\lambda'}$ computed from a reference projection at $\lambda = 51 \times 360° + 169.83°$ acquired when the tumor was at an intermediate position of the breathing cycle. Top: static tumor. Center: moving tumor. Bottom: moving average over one gantry rotation of the above plots and tumor motion. The moving average is only computed when the center of the window has a DCC.

Noise and interpolation effects are quite large in both the static and dynamic acquisitions. For pairs whose baseline intersects the FOV, the inconsistencies are mainly caused by the projection noise and those due to tumor motion are not visible. This is also the case for pairs whose baseline is close to the FOV without intersecting it. This noise can be reduced with a moving average with a 2π width, using all pairs or only those whose baseline does not intersect the FOV (bottom row in Figures 5.7 and 5.8). The moving average improves the detection of inconsistencies due to motion in both cases since the noise is averaged out. The values obtained from the static acquisition are constant which confirms the consistency of the projections with their respective reference, while those obtained from the moving acquisitions match the values of the static curves only when the phantom has the same phase as the phase of the reference projection, i.e. when the phantom is at the same position.

The benefit of computing DCCs when the baseline intersects the FOV is demonstrated by only computing the moving average at points for which the center of the 2π window has a DCC. Excluding pairs whose baseline does not intersect the FOV results in the dashed orange curve whereas the red curve is more continuous with nearly no gap for one period of motion around the reference value λ. There are also two more rotations, for $|\lambda - \lambda'| > 25\pi$, for which the only available DCCs correspond to pairs with a baseline intersecting the FOV (Figures 5.7 and 5.8).

5.4.3 Patient data

Patient 1. DCCs of the first patient data are similarly displayed for a reference projection at angle $\lambda = 154 \times 360° + 0.14°$ at end-inhale in Figure 5.9, at angle $\lambda = 159 \times 360° + 0.14°$ at end-exhale in Figure 5.10 and at angle $\lambda = 171 \times 360° + 180.14°$ at an intermediate position of the respiratory cycle in Figure 5.11. The respiratory period of the patient was about 3.7 s. The beginning of the phase is taken at the end of expiration. The behavior of the DCCs is similar to the phantom data. The moving average computed from the consistency metric indicates consistent and inconsistent projections that are in agreement with the estimated phase for the three reference projections.

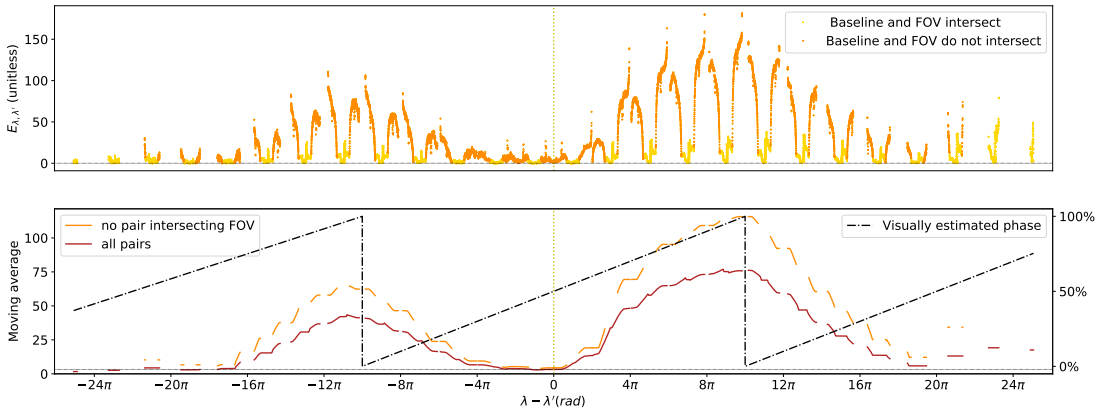

Figure 5.9: Consistency metric (top) and moving average (bottom) for patient 1 set of projections using a reference projection at $\lambda = 154 \times 360° + 0.14°$ at end-inhale.

Patient 2. For this patient, DCC were applied to projections acquired in the region of the artifacts. The results are similarly displayed for a reference projection at angle $\lambda = 132 \times 360° + 322.56°$ in Figure 5.12. The estimated respiratory period was about 5.2 s. It is difficult to identify the phase of the respiratory cycle at which the projection was acquired because the consistency measurements are constant around the projection

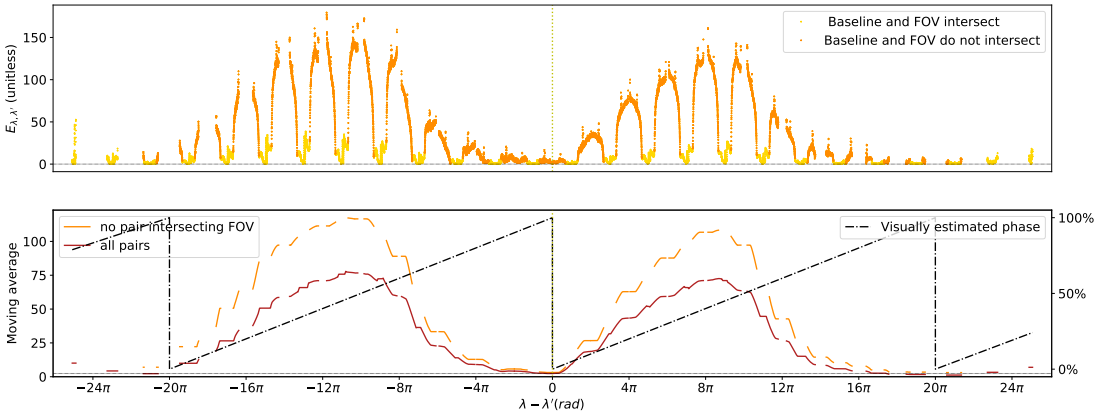

Figure 5.10: Consistency metric (top) and moving average (bottom) for patient 1 set of projections using a reference projection at $\lambda = 159 \times 360° + 0.14°$ at end-exhale.

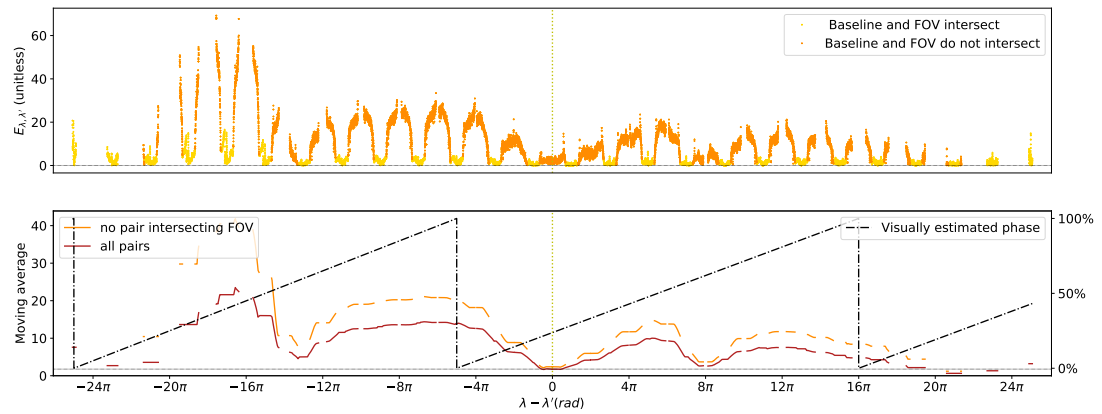

Figure 5.11: Consistency metric (top) and moving average (bottom) for patient 1 set of projections using a reference projection at $\lambda = 171 \times 360° + 180°$ at an intermediate position of the respiratory cycle.

of reference. The constant consistency measurements suggest that the patient was static during this part of the acquisition. This steadiness resulted in artifacts on the tomographic images (see Figure 6.3).

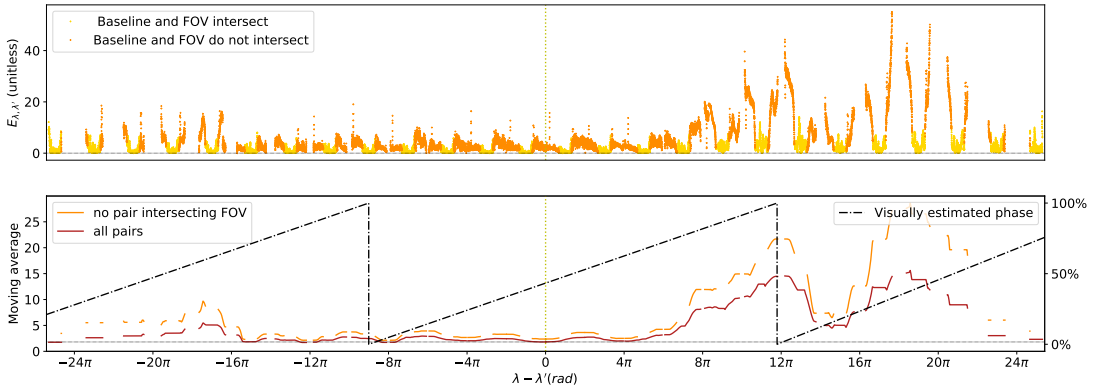

Figure 5.12: Consistency metric (top) and moving average (bottom) for patient 2 set of projections using a reference projection at $\lambda = 131 \times 360° + 322.56°$ at an intermediate position of the respiratory cycle.

5.5 Discussion

In the first part of this chapter, we proposed a theoretical formula to approximate the standard deviation of cone-beam pair-wise DCCs in helical CT and validated it with batch simulations. The resulting formula explains the observed variability of the DCCs depending on the angular distance between source positions.

In a second part, a noise-aware metric was defined with the standard deviation approximation and applied to a motion detection problem in helical CT. Our results on simulated and real data indicate that DCCs can identify breathing motion as well as irregular breathing on a clinical CT scanner. Motion is detected when the baseline does not intersect the FOV but sensitivity to noise might prevent it otherwise. For pairs whose baseline does not intersect the FOV, the inconsistency measured by the numerator of Equation 5.12 is mostly due to motion and the inconsistency due to noise may be assumed smaller. For pairs whose baseline intersects the FOV, the numerator of Equation 5.12 measures both inconsistencies, due to noise and motion, but the noise inconsistency may weigh more than the motion inconsistency. Therefore, normalizing by an estimate of the noise bring the value of the consistency metric of those pairs around 0.8, which is the expected value of the consistency metric for noisy static projections (see Section 5.4.1.2). If the motion inconsistency is large, the metric of such pairs should be above 0.8 (see Figure 5.8 around $|\lambda - \lambda'| = 28\pi$ for example). Sensitivity to noise can be reduced in such pairs and other pairs with a simple low-pass filter as a moving average (see Figures 5.7, 5.8, 5.9, 5.10, 5.11 and 5.12). The proposed metric normalizes the inconsistency by an estimate of the noise level to give more weight to pairs where the motion inconsistency dominates the noise inconsistency in the moving average. Considering all pairs, and not just those whose baseline does not intersect the FOV, increases the set of DCCs in an acquisition. This is particularly useful for the identification of local inconsistencies, as a blank projection in the sequence or rapid motion. Discarding pairs whose baseline intersects the FOV might prevent the detection of such issues.

An important contribution of this work is the consistency metric that includes the variations of the moments due to noise. The literature (see Section 3.4.2) regarding the impact of noise on the DCCs is scarce. When mentioned, the robustness with respect to

noise was because of the high quantity of redundant pairs to which DCCs are applied. However, in helical CT, the number of redundant pairs is limited because of the axial displacement of the table limiting the robustness of such metrics. The derivation of the moments variance offers a way to take into account the noise in helical CT and provides information regarding the impact of noise on the DCCs.

5.6 Conclusion

In this chapter, we have demonstrated the ability of the DCCs to detect motion directly (for pairs whose baseline does not intersect the FOV) or indirectly with the help of a low-pass filter (considering all the pairs) using a noise-aware consistency metric. This increases the number of DCCs available in a helical acquisition. However, the detection of motion presented in this chapter is only *local*, i.e. with respect to a fixed reference projection. Due to the axial truncation of the projections inherent to a helical acquisition, DCCs cannot be computed between all projections and it is necessary to connect the projections together to evaluate the presence of motion during an entire helical CT. This issue is addressed in the next chapter.

Chapter 6

Global motion detection in helical CT using data consistency conditions

The ability of the cone-beam pair-wise DCCs to detect motion was verified in Chapter 5. However, this detection was only local, i.e, between a fixed projection of reference and a limited number of other projections with which a DCC could be computed (see Section 4.3.4). To verify the consistency of a projection with the other projections of the acquisition, it is necessary to connect pairs of projections between which DCCs cannot be computed.

In this chapter, we present two methods to estimate motion during an entire CT acquisition. In the first method, we construct a graph that inter-connects all the projections and that provides a consistency measurement between any pair of projections in a helical acquisition. The second method extends the local detection method from the previous chapter to the entire acquisition in order to extract the respiratory signal from the projections.

6.1 Cone-beam pair-wise DCCs in helical CT

For two source positions $\boldsymbol{s}_\lambda$ and $\boldsymbol{s}_{\lambda'}$, whose baseline is not parallel to the helix axis, and for which there is at least one plane on which the FBDCC can be applied (Section 4.3.4), the FBDCC states that

$$M_{\boldsymbol{\tau}} = M_{\boldsymbol{\tau}'} \tag{6.1}$$

where $M_{\boldsymbol{\tau}}$ and $M_{\boldsymbol{\tau}'}$ are the moments of the projections g_λ and $g_{\lambda'}$ in the plane $\Pi_{\boldsymbol{\tau}}$ with $\boldsymbol{\tau} = (\lambda, \lambda', \beta)$ and $\boldsymbol{\tau}' = (\lambda', \lambda, \beta)$. A description of the geometry and the mathematical expression of $M_{\boldsymbol{\tau}}$ (Equation 4.62) are given in Section 4.3.

6.2 Motion detection in helical CT using a graph approach

The content of this section is based on a contribution presented at the 2020 IEEE Nuclear Science Symposium and Medical Imaging Conference (NSS/MIC) [Mouchet et al., 2020].

6.2.1 Theory

In Chapters 4 and 5, we observed that the FBDCC is unstable when the baseline of a pair intersects the FOV, i.e. when there is a singularity in the computation of the moment. In this part, we will not consider such pairs because of their instability. The only pairs considered here are those satisfying the FOV condition (see Section 4.2.4.1) and with at least one plane where the FBDCC can be computed as illustrated in Figure 6.1.

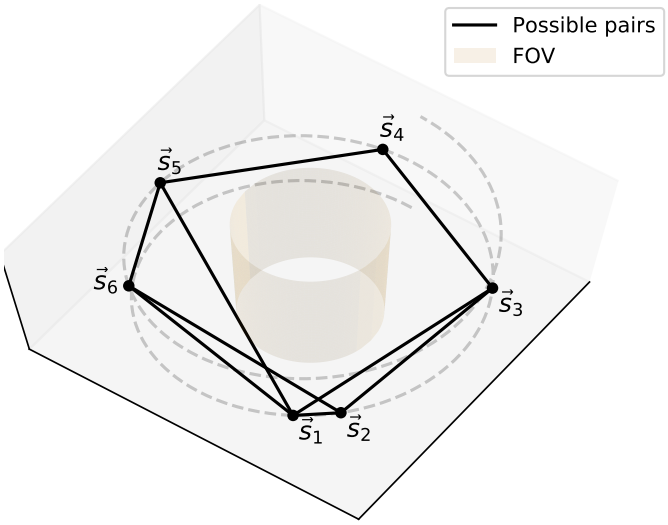

Figure 6.1: Pairs used in the graph approach computed for six source positions. The source positions are identified with their index instead of the angle λ. The black lines illustrate pairs of source positions whose baseline does not intersect the FOV. Here, one cannot compute a DCC between $\boldsymbol{s}_4$ and $\boldsymbol{s}_6$ but one can verify that $E_{4,5} + E_{5,6} = 0$.

Due to the axial displacement of the table, the number of pairs eligible for a DCC is limited. Moreover, the FOV condition and the need of common data (see Section 4.2.4.1 and Section 4.3.4) prevent the computation of DCCs between many pairs of projections. For example, in Figure 6.1, we see that the source positions $\boldsymbol{s}_4$ and $\boldsymbol{s}_6$ are not connected because their baseline would cross the FOV. However, they are both connected to $\boldsymbol{s}_5$. We call $\boldsymbol{s}_5$ an intermediate projection between $\boldsymbol{s}_4$ and $\boldsymbol{s}_6$. Consequently, even if DCCs can only be computed for a few pairs, it is still possible to connect two projections via intermediate projections.

To assess the consistency between any pair of cone-beam projections g_λ and $g_{\lambda'}$, we propose to construct a graph with the projections as vertices and connect two vertices if there is a DCC between the corresponding projections. Each edge is weighted by the consistency metric introduced in Chapter 5 in Equation 5.12

$$E_{\lambda,\lambda'} = \frac{1}{B}\sum_{b=1}^{B} \frac{\left|M_{\boldsymbol{\tau}_b} - M_{\boldsymbol{\tau}'_b}\right|}{\sqrt{B}\sqrt{\mathrm{Var}(\overline{M_{\lambda,\lambda'}}) + \mathrm{Var}(\overline{M_{\lambda',\lambda}})}} \tag{6.2}$$

where B is the number of DCC planes, sampled as described in Section 4.3.4, for the pair $(\boldsymbol{s}_\lambda, \boldsymbol{s}_{\lambda'})$. $M_{\boldsymbol{\tau}_b}$, $\boldsymbol{\tau}_b = (\lambda, \lambda', \beta_b)$ and $M_{\boldsymbol{\tau}'_b}$, $\boldsymbol{\tau}'_b = (\lambda', \lambda, \beta_b)$ are the moments on the b-th plane, making an angle β_b with the reference plane, of the projections g_λ and $g_{\lambda'}$ (see Section 4.3.1 for the definition of the reference plane). If the projections are consistent, then

$$E_{\lambda,\lambda'} = 0. \tag{6.3}$$

and $E_{\lambda,\lambda'} \geq 0$ otherwise. If two source positions $\boldsymbol{s}_\lambda$ and $\boldsymbol{s}_{\lambda'}$ are directly connected and consistent, then the weight $E_{\lambda,\lambda'}$ of the edge connecting those two vertices is 0, as given by Equation 6.3. Moreover, if all projections are consistent along a path, then the sum of the edge weights along that path is also zero. For example in Figure 6.1, if $\boldsymbol{s}_4$ is consistent with $\boldsymbol{s}_5$, then $E_{4,5}$ is 0 and if $\boldsymbol{s}_6$ is consistent with $\boldsymbol{s}_5$, then $E_{5,6}$ is also 0. We then have $E_{4,5} + E_{5,6} = 0$. Therefore, to identify consistent and inconsistent projections, we propose to use the shortest path between two vertices as a measurement of the consistency between the two corresponding projections. The shortest path between two vertices is the path

along which the sum of the DCCs was smaller than along any other possible path between the two vertices. It is calculated with Dijkstra's algorithm [Dijkstra, 1959]. If the shortest path is zero, then all projections along the path are consistent. If the shortest path is not zero, then there is no path between the two projections with all projections consistent along that path.

6.2.2 Datasets

6.2.2.1 Numerical phantom

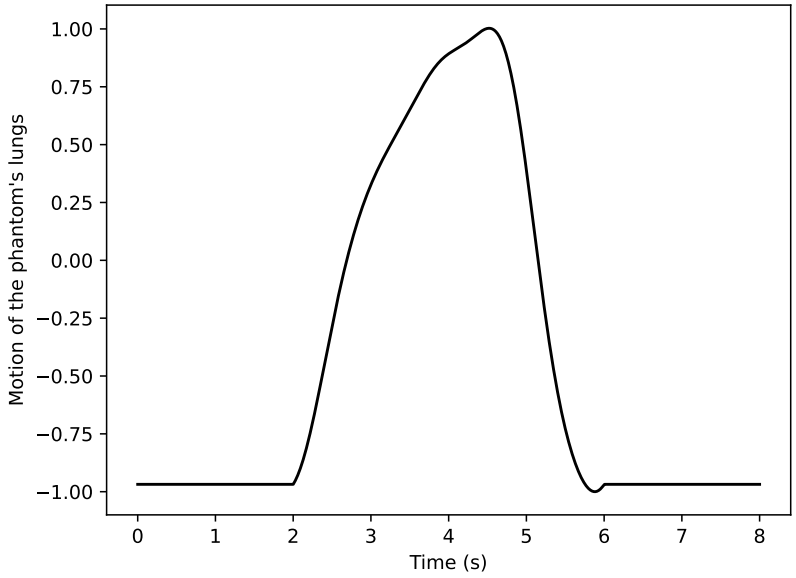

Figure 6.2: Motion of the phantom lungs during the acquisition. The motion model is taken from [Bergner and Kachelriess, 2009].

Using the Reconstruction Toolkit (RTK [Rit et al., 2013]), we simulated two acquisitions of the 4D Forbild thorax phantom [Bergner and Kachelriess, 2009] (see Figure 4.13, left column) with respiratory period $T_{resp} = 4$ s (see Figure 6.2). The simulated geometry is the same as the one used for the simulations of Chapters 4 and 5, we briefly recall it here. The detector size is $[920, 32] \times [1.03, 1.09]$ mm, the radius of the helical trajectory is 610 mm and the detector-source distance is 1113 mm. The acquisitions are centered around $z = 30$ mm. The first acquisition is a conventional CT ($T_{rot} = 0.5$ s, $P = 0.8$) and the second acquisition is a 4D CT with parameters corresponding to a breathing period $T_{resp} = 4$ s ($T_{rot} = 0.35$ s, $P = 0.07$). Projections are simulated at a rate of 200 Hz for the conventional CT and 100 Hz for the 4D CT. Poisson noise is applied to the projections before taking the logarithm with 10^5 photons in air. The acquisitions are divided in three parts: between $t_0 = 0.0$ s and $t_1 = 2$ s, the phantom is static at end-inhale; between t_1 and $t_3 = 6$ s, the phantom breathes for one respiratory cycle, reaching end-exhale at $t_2 = 4.5$ s; and it is back to its static position from end-inhale t_3 to $t_4 = 8.0$ s.

6.2.2.2 Patient data

We selected one patient from our database of 4D CT acquisitions. This patient was scanned twice according to a 4D protocol with a pitch of $P = 0.07$ (the corresponding table feed is $d = 1.34$ mm) and a rotation time of 0.5 s. For one acquisition, referred to

as acquisition 1, strong artifacts are visible around the tumor for an axial displacement around $z = -50$ mm (see Figure 6.3). For the other acquisition, referred to as acquisition 2, an artifact free image was obtained (see Figure 6.4). After removing the truncated part (patient's table) of the sinograms according to Figure 5.3, each sinogram is sub-sampled at a rate of 100 Hz (the initial sampling rate is 3000 Hz).

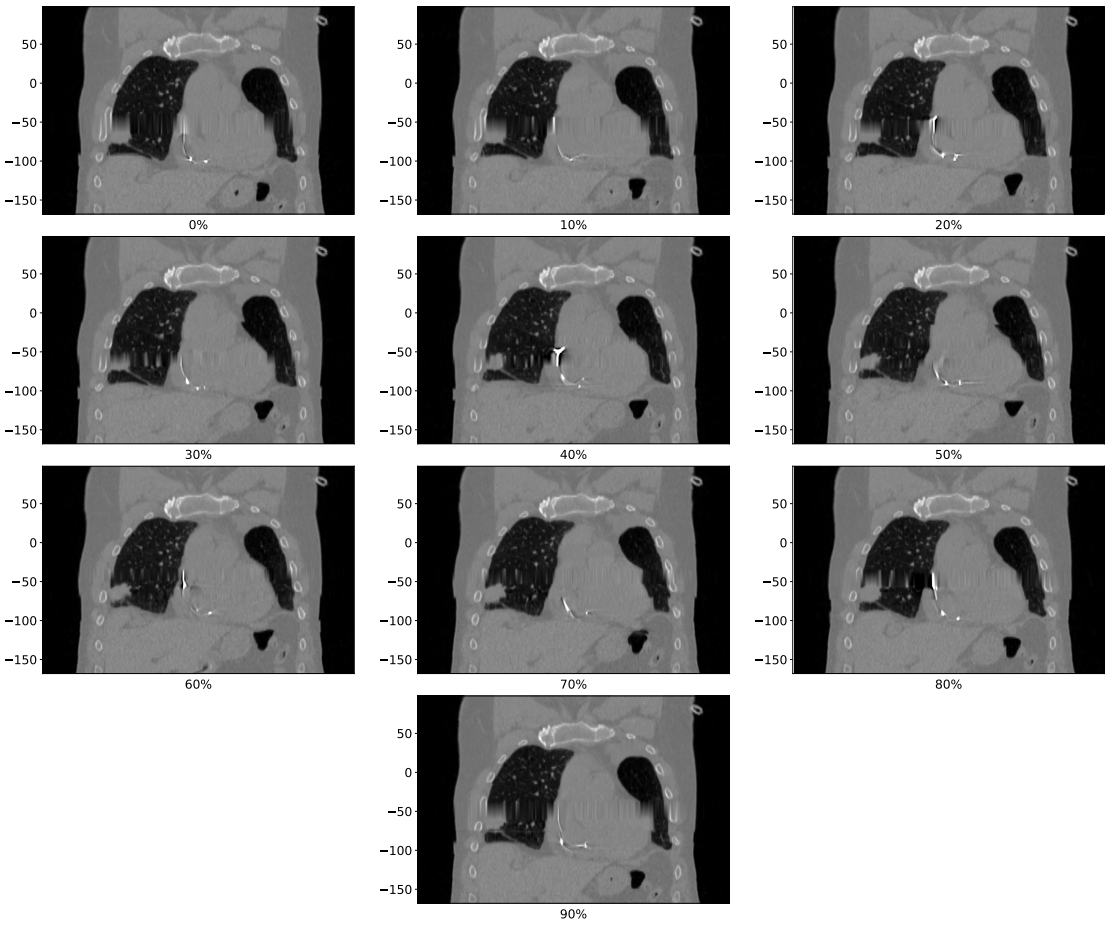

Figure 6.3: 3D frames of the 4D CT image of patient 2. The ten images (0% to 90%) correspond to the ten phases of the respiratory cycle. A tumor is located at the axial displacement $z = -75$ mm and a strong artifact is visible around $z = -50$ mm.

The moments are computed with the Hann-windowed band-limited Hilbert kernel with a band-width parameter $\nu = 0.2$ for simulated projections and $\nu = 0.1$ for real data (see Section 4.3.3.2)

6.2.3 Results

In the presentation of the results, we refer to shortest path between two vertices as the path along which the sum of the DCCs was smaller than along any other possible path between the two vertices. The sum of the DCCs along the shortest path between two vertices corresponds to the sum of the edge weights along the path to get from one vertex to the other. Finally, the length of the shortest path between two vertices corresponds to the number of edges crossed to get from one vertex to the other.

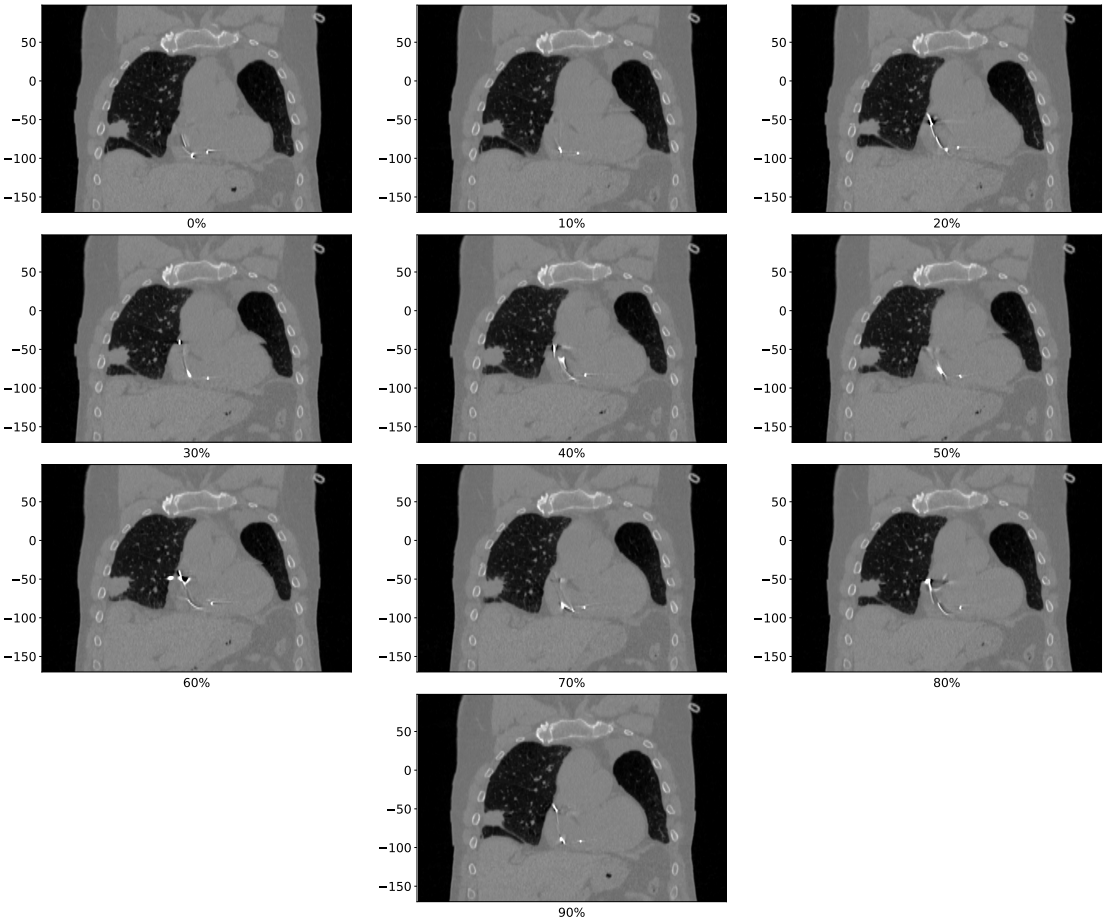

Figure 6.4: 3D frames of the 4D CT image of patient 2. The ten images (0% to 90%) correspond to the ten phases of the respiratory cycle. A tumor is located at the axial displacement $z = -75$ mm and a no artifact is visible around $z = -50$ mm.

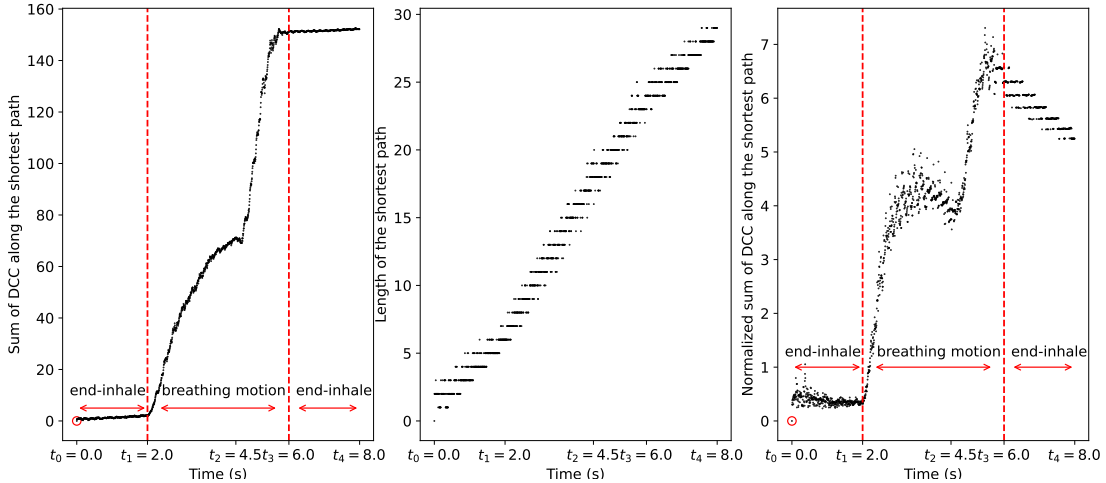

Figure 6.5: Graph approach applied to a simulated conventional CT. From left to right: sum of the DCCs along the shortest path from the projection at $t_0 = 0$ s (red circle); length of the shortest path; sum of the DCC along the shortest path normalized by the shortest path length.

6.2.3.1 Numerical phantom

Figure 6.5, left, shows the sum of the DCCs along the shortest path computed from the reference projection at $t_0 = 0$ s for the simulated conventional CT. It is immediately possible to identify where motion occurs, i.e. between t_1 and t_3 where the sum of DCCs along the shortest path strongly increases. Between t_0 and t_1, the sum of the DCCs is constant and equal to zero: all projections acquired in this interval of time are consistent with the reference. Between t_3 and t_4, the sum of DCCs is also constant indicating the stillness of the phantom. To assess the consistency of the projections acquired in the interval $[t_3, t_4]$, another graph can be computed from the projection at t_4 as shown in Figure 6.6, left. However, on both graphs, we cannot identify that the phantom is at the same position (end-inhale) in the intervals $[t_0, t_1]$ and $[t_3, t_4]$ because all paths between t_1 and t_3 contain inconsistent intermediate projections. The presence of noise prevents the metric $E_{\lambda,\lambda'}$ to be exactly zero. Consequently, a small drift appears due to the sum of the positive weights along the shortest path. To compensate for it, the sum of DCCs is normalized by the length of the shortest path (see Figure 6.5 and Figure 6.6, center). On the normalized plots (see Figure 6.5 and Figure 6.6, right), the drift is corrected. Projections acquired until t_1 are consistent with the reference projection acquired at t_0 because the measurements are close to zero in Figure 6.5, and same for t_3 to t_4 in Figure 6.6. No other assumptions can be made, as the measurements are no longer constant between t_3 and t_4 in Figure 6.5 and between t_0 and t_1 in Figure 6.6.

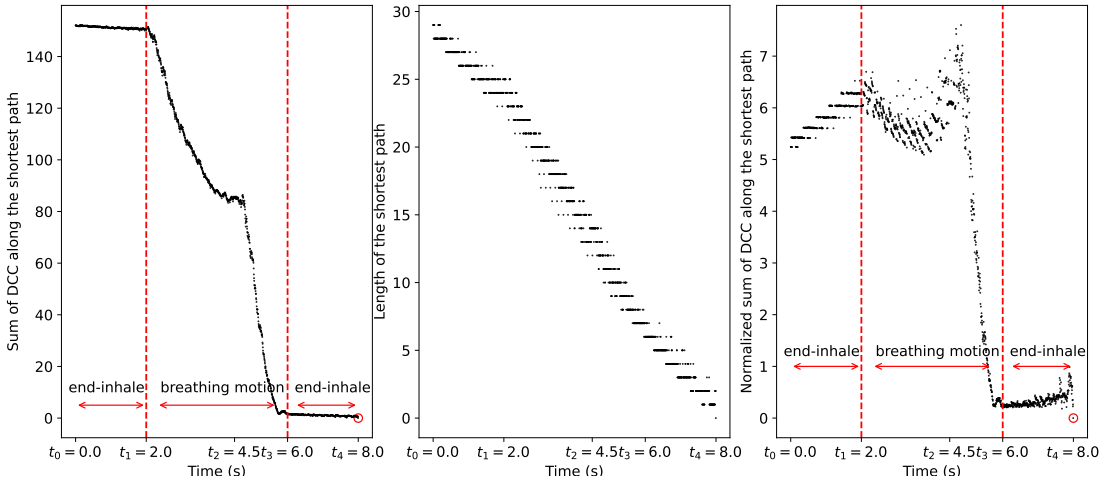

Figure 6.6: Graph approach applied to a simulated conventional CT. From left to right: sum of the DCCs along the shortest path from the projection at $t_4 = 8$ s (red circle); length of the shortest path; sum of the DCC along the shortest path normalized by the shortest path length.

Figure 6.7, left, shows the sum of the DCCs along the shortest path computed from the reference projection at $t_0 = 0$ s for the simulated 4D CT. It is also possible to clearly identify when motion occurs (between t_1 and t_3). Thanks to the 4D CT acquisition parameters, there exists a DCC between the projections at t_1 and t_3. This enables us to qualify the projections acquired between t_3 and t_4 as consistent (sum of the DCCs along the shortest path close to zero) with the reference projection at t_0 even though they are not directly connected. The drift is corrected by normalizing the sum of the DCCs with the length of the shortest path (see Figure 6.7, center) as previously. On the normalized plot, the periods of stillness and the period of motion are clearly identified. However, the normalization deteriorates the respiratory trace visible on the non normalized plot.

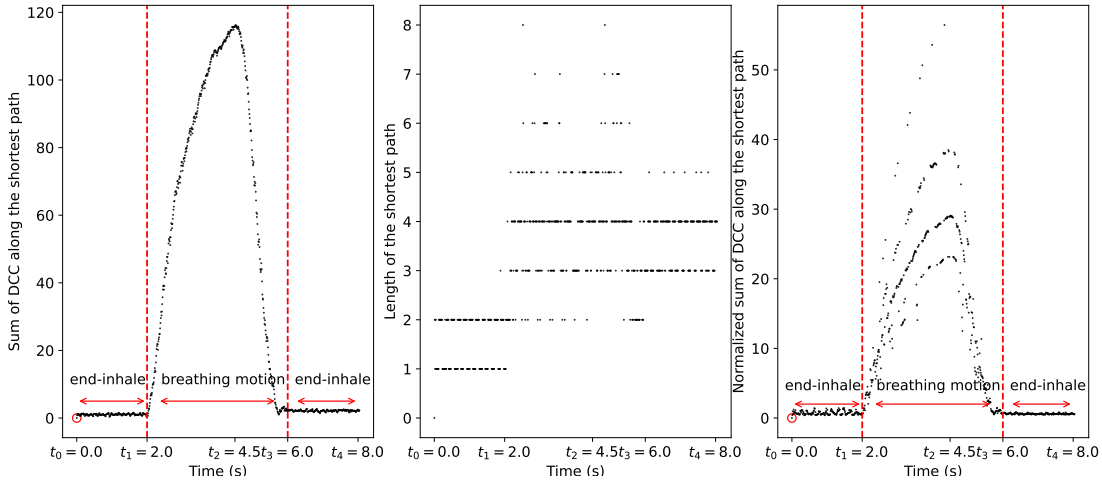

Figure 6.7: Graph approach applied to a simulated 4D CT. From left to right: sum of the DCC along the shortest path from the projection at $t_0 = 0$ s (red circle); length of the shortest path; sum of the DCC along the shortest path normalized by the path length.

6.2.3.2 Patient data

The results for the patient acquisitions are presented in Figures 6.8, 6.9 and 6.10. The sum of the DCCs along the shortest path and the length of the shortest path are plotted as a function of the axial displacement of the source z to compare the results with the quality of the CT images.

The sum of the DCCs along the shortest path gives an estimate of the motion during acquisition 1 (Figure 6.3) in Figure 6.8 and during acquisition 2 (Figure 6.4) in Figures 6.9 and 6.10. The reference projection is taken at $z = -100$ mm in Figures 6.8 and 6.9, and at $z = 50$ mm in Figure 6.10. For $z \in [-10, 100]$ mm, the measurements indicate that there is no motion as a linear evolution of the sum of the DCC along the shortest path is visible in Figures 6.8, 6.9, and 6.10 (similarly to the stationary phase from the simulations results). For this range of axial displacements, the upper body is scanned, so it is expected to have a linear drift of the shortest path due to the increase of the path length and the accumulation of inconsistencies due to the projection noise. Between $z = -140$ mm and $z = -10$ mm in Figures 6.9, and 6.10 and between $z = -10$ mm and $z = -25$ mm and $z = -75$ mm and $z = -150$ mm in Figure 6.8, oscillations are present that may correspond to a respiratory trace. In Figure 6.4, $z \in [-140, -10]$ matches with the extent of the lungs indicating that the oscillations correspond to the breathing motion of the patient. In Figure 6.3, $z \in [-25, -10]$ and $z \in [-140, -75]$ matches with the beginning of the lungs and the upper abdominal organs, also indicating that the oscillations correspond to the breathing motion. Around $z = -50$ mm, the measurements in Figure 6.8 are constant which indicates a stationary phase. This range of axial displacement corresponds to the location of the artifact on the 4D CT image (Figure 6.3). The patient did not breath during a certain period of time. Around $z = -100$ mm the amplitude of the oscillations strongly increases in Figures 6.8 and 6.9. This axial displacement matches with the location of the diaphragm on the 4D CT images (Figures 6.3 and 6.4): the motion amplitude is stronger around the diaphragm. However, in Figure 6.10, the respiratory trace is less visible. For axial displacement smaller than $z = -140$ mm in Figures 6.9, and 6.10 and $z = -150$ mm in Figure 6.8, almost no motion is detected.

Furthermore, the graph approach highlights consistent projections with the reference projection at $z = -100$ mm in Figures 6.8 and 6.9 as the measurements are close to zero for the projection at $z = -110$ mm. No other consistent projections are identified. In

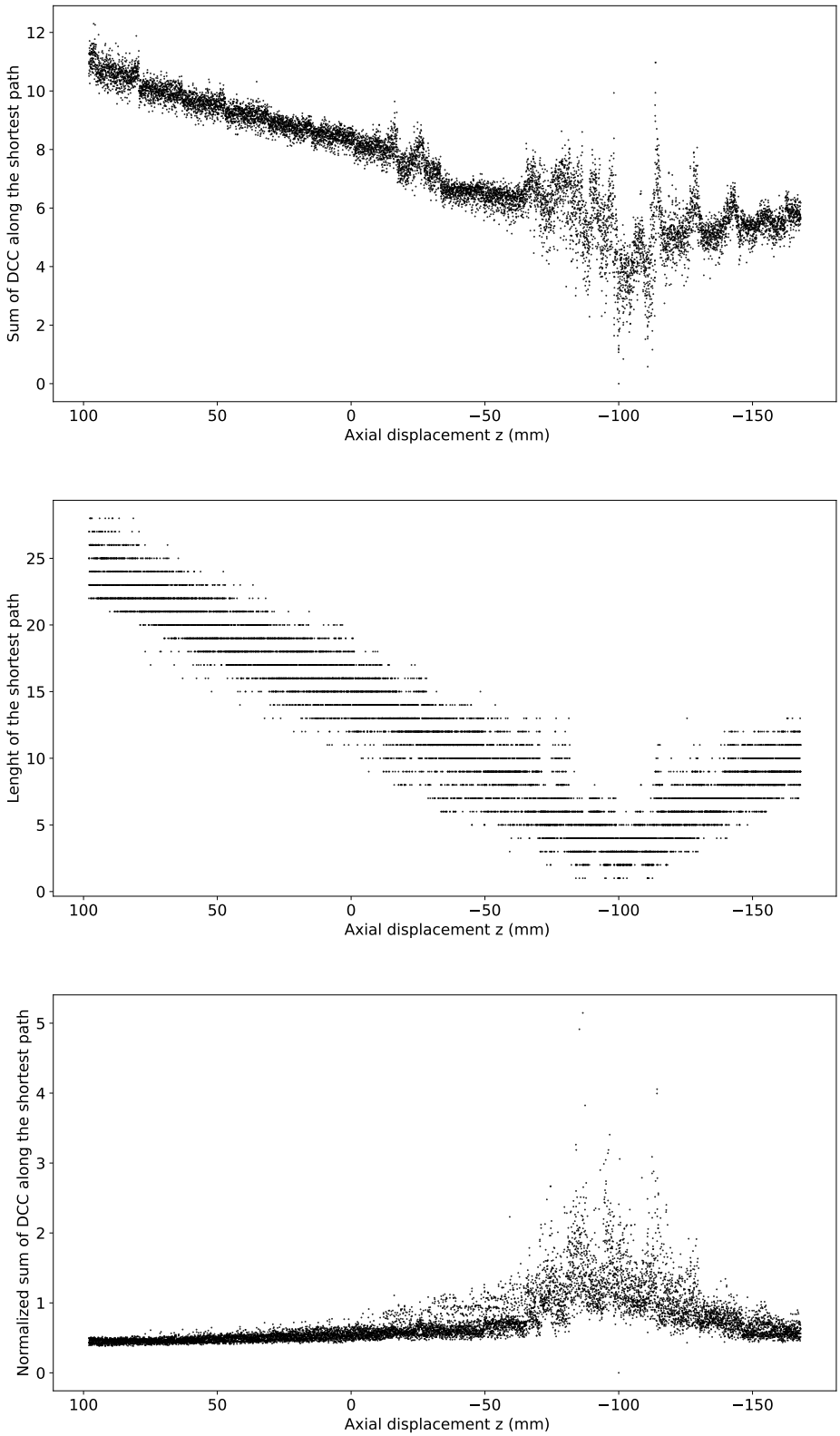

Figure 6.8: Graph approach applied to the first 4D CT acquisition of patient 2 from the reference projections at $z = -100$ mm. From top to bottom: sum of the DCCs along the shortest path from the projection at $z = -100$ mm; length of the shortest path; sum of the DCC along the shortest path normalized by the path length.

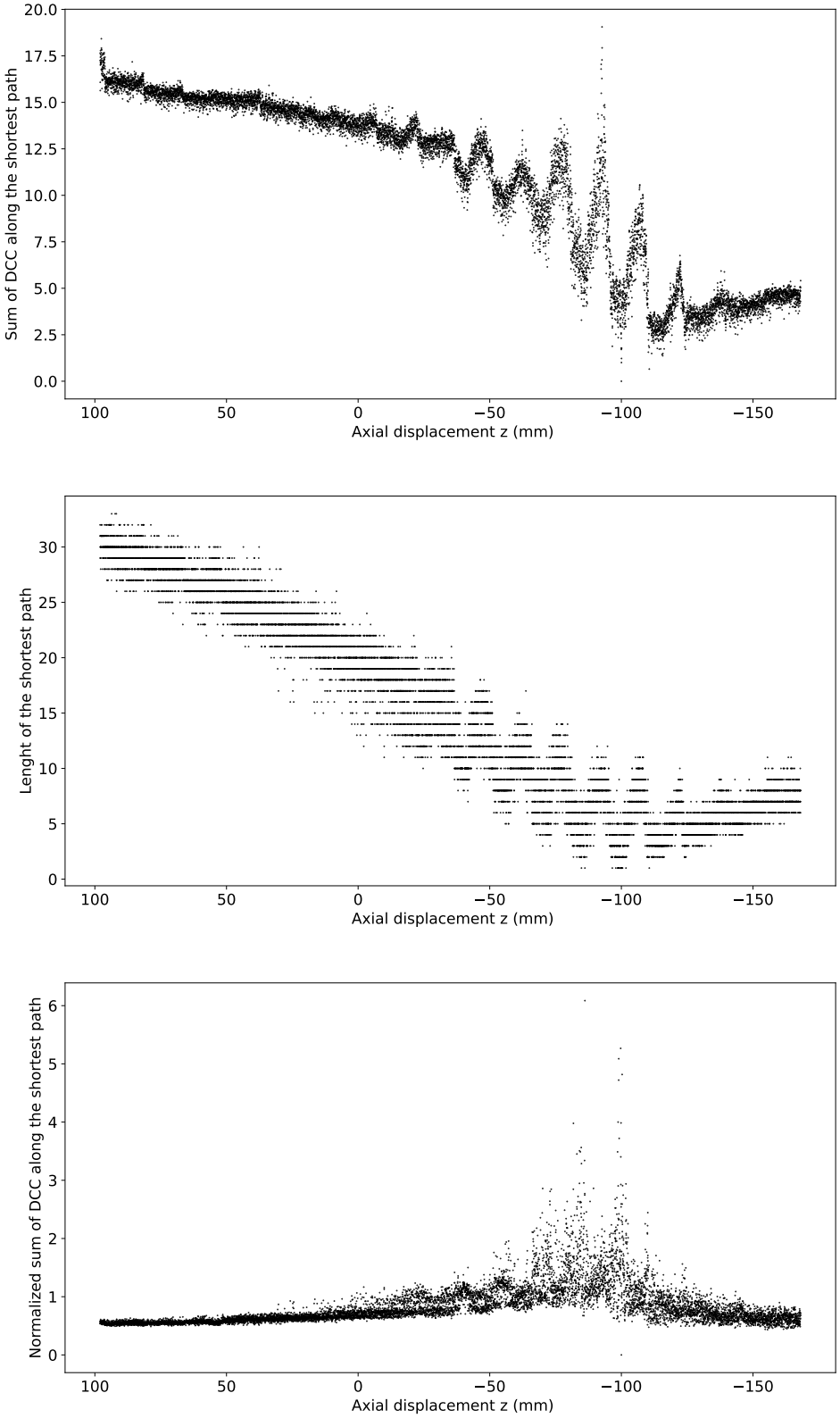

Figure 6.9: Graph approach applied to the second 4D CT acquisition of patient 2 from the reference projections at z=−100 mm. From top to bottom: sum of the DCCs along the shortest path from the projection at z=−100 mm; length of the shortest path; sum of the DCC along the shortest path normalized by the path length.

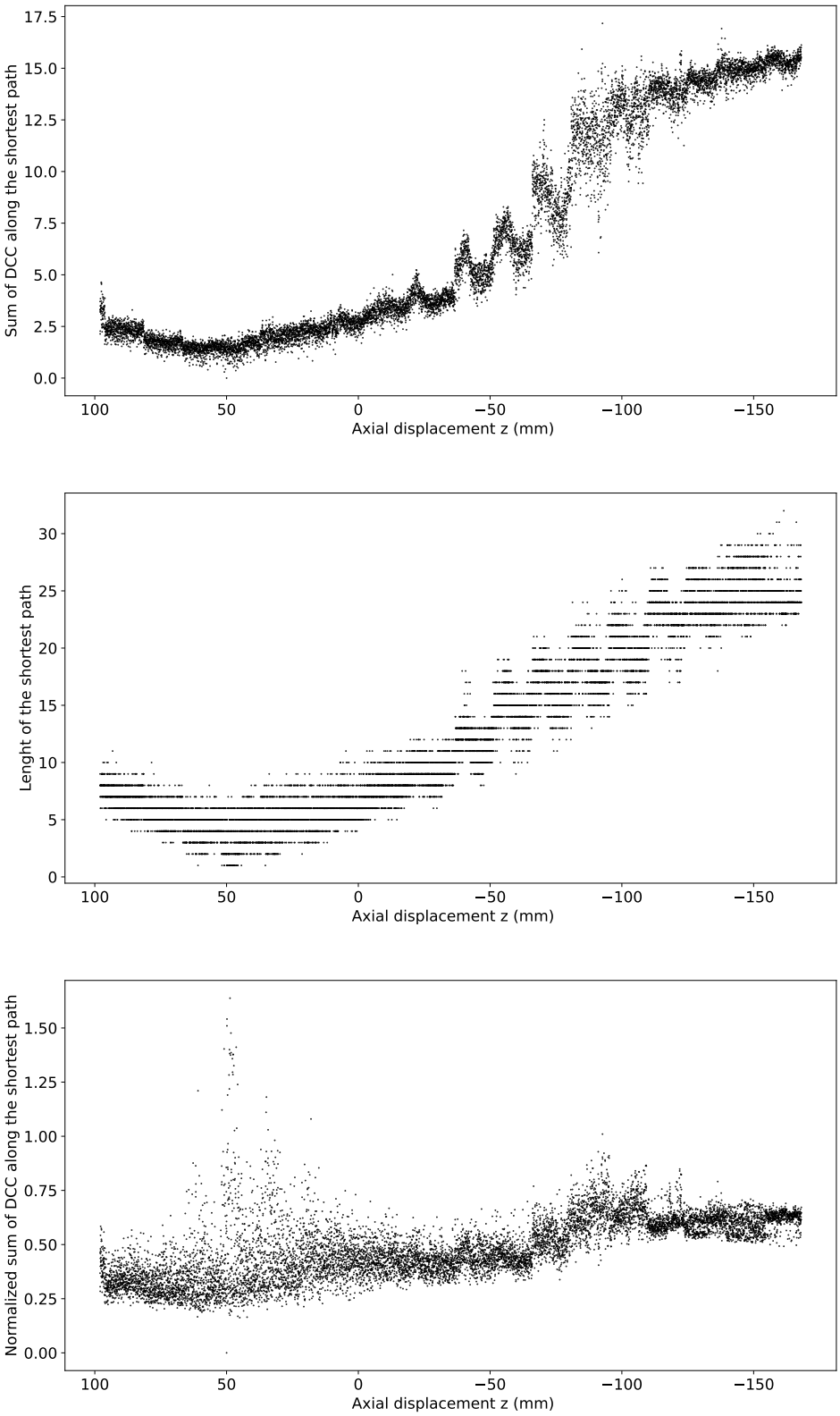

Figure 6.10: Graph approach applied to the first 4D CT acquisition of patient 2 from the reference projections at $z = 50$ mm. From top to bottom: sum of the DCCs along the shortest path from the projection at $z = 50$ mm; length of the shortest path; sum of the DCC along the shortest path normalized by the path length.

Figure 6.10, many projections around the reference projection at $z = 50$ mm are consistent with the reference. However, the drift prevents us to establish an interval of consistency.

To compensate for the drift, the sum of the DCCs is normalized by the length of the shortest path (middle plot in Figures 6.8, 6.9, and 6.10) and the normalized measurements are shown in the bottom plot of each figure. The drift is corrected as the measurements are now centered around 0.5 for all graphs. Setting a threshold measurement at 0.5, an interval of consistency for the projection of reference at $z = 50$ mm in Figure 6.10 is visible. However, the variations of the motion are lost in the three cases. We can only assume that motion is detected for $z \in [-150, -75]$ mm as the measurements are all over 0.5.

6.2.4 Discussion

We proposed a graph approach that inter-connects projections in a helical acquisition and provides an consistency measurement between a projection of reference and the other projections of the acquisition.

The graph approach was applied to conventional and 4D helical acquisitions where it allowed the identification of consistent projections with any reference projection in simulated and real data for which the sum of the DCCs should be zero (Figures 6.5, 6.6, and 6.7), or smaller than the mean lower values of the other measurements (Figures 6.8 and 6.9 bottom plots).

It also gives an estimate of the motion during an entire CT: regular breathing patterns (see Figures 6.9 and 6.10) as well as irregular breathing (see Figure 6.8) were highlighted on the 4D CT acquisitions.

Computing the shortest path directly and summing the DCCs along them allowed for the identification of consistent projections with a chosen reference. However, it induces a drift as the length of the shortest paths increases, preventing the identification of consistent projections that are not directly connecting to the reference. This drift is caused by the projection noise that is accumulated as more nodes are appended to the shortest path. To compensate for the drift, we normalize the sum of the DCCs by the length of the shortest path. This normalization corrects the drift, but may deteriorate the shape of the respiratory trace (Figures 6.7, 6.8, 6.9 and 6.10) or even the consistency results (see Figures 6.8, 6.9).

The lower value of the normalized measurements, around 0.5 (Figures 6.5, 6.6, 6.7, 6.8, 6.9 and 6.10), differs from 0.8 which was the expected value of the consistency metric (see Section 5.4.1.2) for noisy data. Projections directly connected and consistent with the reference have measurements around this expected value (see Figures 6.5, 6.6). Dijkstra algorithm's compute the shortest path by minimizing the sum of the DCCs along the edges crossed. Thus, it will select edges with a weight that may be smaller than 0.8. In Figure 5.6, the smallest value of the errors (for pairs whose baseline does not intersect the FOV) correspond to 0.5, which is the value we observe here.

The graph approach is limited by the applicability of the FBDCC. If the DCC range of applicability is not large enough to reach the next consistent projection, the shortest path cannot avoid intermediate inconsistent projections and it is not possible to identify consistent projections (see Figures 6.5). To increase the number of DCCs, a solution would be to consider pairs whose baseline intersects the FOV. However, using those pairs directly may not be of high interest because their consistency metric is close to zero (due to the strong influence of noise) and they would just increase the length of the shortest path. To benefit from those pairs, applying the graph approach to the metric filtered by the moving average may be a solution (see Chapter 5), but would require further investigations. As the moving average applies to a set of pairs from one reference, the filtered metrics may differ for the pair (λ, λ') if we consider the one computed from λ or the one computed from λ' as the values of other pairs influence the moving average.

6.3 Extraction of the respiratory signal using DCCs

In this section, we present a preliminary work on how the local motion detection method presented in Chapter 5 can be extended to the entire acquisition to extract the respiratory signal.

6.3.1 Experimental observations

In the previous chapter, we selected one projection of reference and computed the DCCs for eligible pairs. For each pair, the noise-aware consistency metric (see Equation 5.12) was computed and a moving average filter around one rotation was applied to each point with a DCC to remove the noise component from the consistency metric. The aim was to obtain consistency measurements between projections, whatever their position in the respiratory cycle, hence our choice to work with a positive metric. In this part, we wish to recover information regarding the respiratory phase at which projections were acquired. Consequently, we will observe the influence of the respiratory phase on a signed version of the consistency metric. The signed metric is defined as

$$\tilde{E}_{\lambda,\lambda'} = \frac{B^{-1}\sum_{b=1}^{B} M_{\boldsymbol{\tau}_b} - M_{\boldsymbol{\tau}'_b}}{\sqrt{B}\sqrt{\mathrm{Var}(\overline{M_{\lambda,\lambda'}}) + \mathrm{Var}(\overline{M_{\lambda',\lambda}})}}. \tag{6.4}$$

where $\sqrt{\mathrm{Var}(\overline{M_{\lambda,\lambda'}}) + \mathrm{Var}(\overline{M_{\lambda',\lambda}})}$ is the standard deviation of the numerator. The standard deviation is given in Equation 5.15 as a function of the noise of projection pixels.

We show in Figures 6.11, 6.12 and 6.13 , the signed consistency metric and the moving average computed for the three reference projections from the acquisition of patient 1 presented in Section 5.3.3.

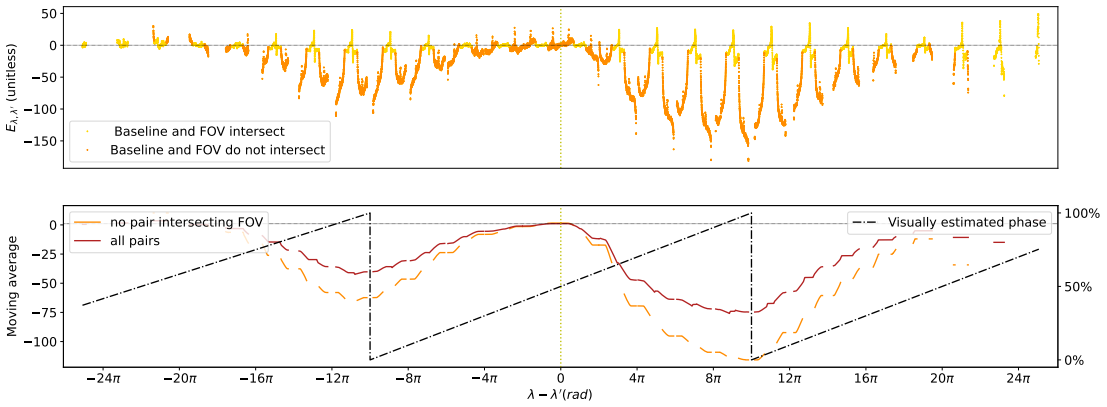

Figure 6.11: Signed consistency metric (top) and its moving average (bottom) the projections of patient 1 using a reference projection $\lambda = 154 \times 360° + 0.14°$ at end-inhale. On the bottom plot, the orange curve is the moving average computed with pairs whose baseline does not intersect the FOV (orange points on the top plot) and the red curve is the moving average computed with all the pairs (yellow and orange points on the top plot).

Similarly to the positive metric, the signed metric highlights consistent and inconsistent projections in agreement with the estimated phase (dashed-dotted black line on the plots). More than the consistency information, we observe a link between the sign of the consistency measurements mean and the position of the reference in the respiratory cycle. When the projection of reference is acquired at the end of the inspiration (Figure 6.11), the mean of the consistency measurements is negative. When the projection of reference is acquired at the end of the expiration (Figure 6.12), the mean of the consistency measurements is

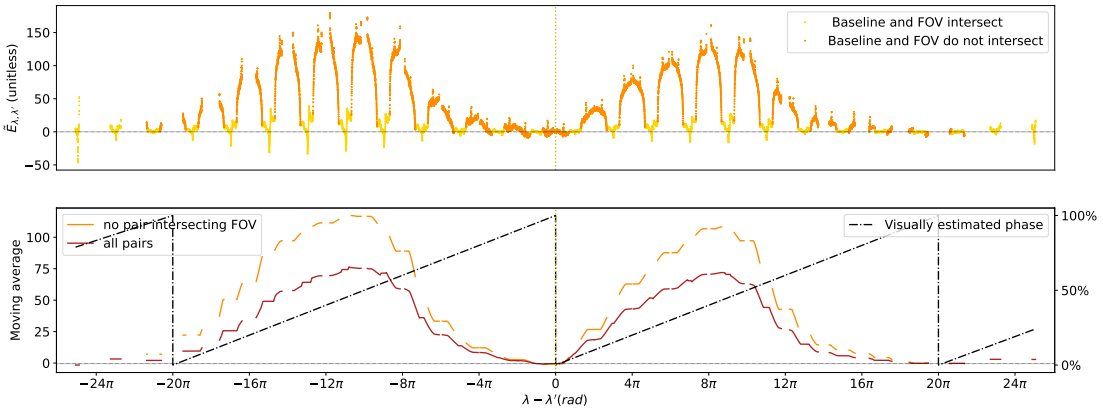

Figure 6.12: Signed consistency metric (top) and its moving average (bottom) for the projections of patient 1 using a reference projection $\lambda = 159 \times 360° + 360° + 0.14°$ at end-exhale. On the bottom plot, the orange curve is the moving average computed with pairs whose baseline does not intersect the FOV (orange points on the top plot) and the red curve is the moving average computed with all the pairs (yellow and orange points on the top plot).

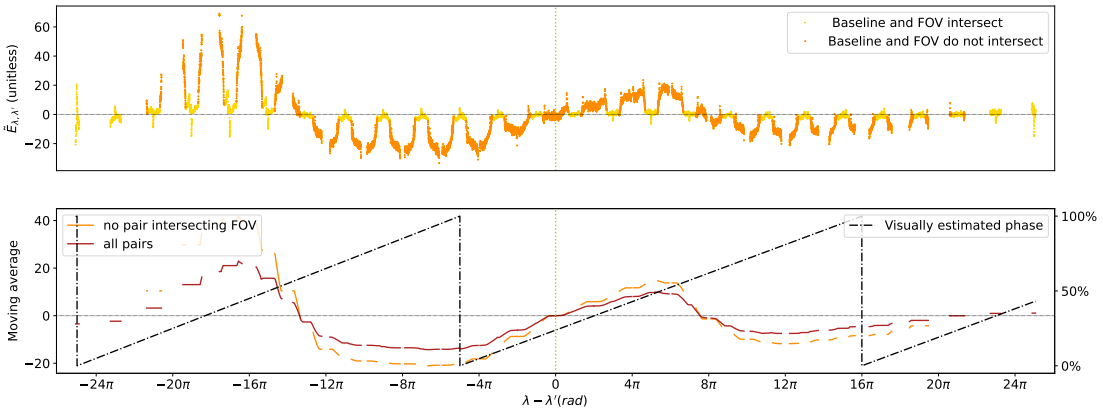

Figure 6.13: Signed consistency metric (top) and its moving average (bottom) for patient 1's set of projections using a reference projection $\lambda = 171 \times 360° + 180.14°$ at an intermediate position of the respiratory cycle. On the bottom plot, the orange curve is the moving average computed with pairs whose baseline does not intersect the FOV (orange points on the top plot) and the red curve is the moving average computed with all the pairs (yellow and orange points on the top plot).

positive. When the projection of reference is acquired at an intermediate position of the respiratory cycle (Figure 6.11), the mean of the consistency measurements is around zero.

Moreover, centering the moving average curve around 0, i.e. subtracting the mean and applying the moving average on the centered measurements, the three curves are overlaid on each other and a respiratory trace is recovered as shown in Figure 6.14. After the adjustment, the projections acquired around end-inhale have a positive metric, the projections acquired around end-exhale have a negative metric, and the projections acquired at an intermediate projections have a metric around zero.

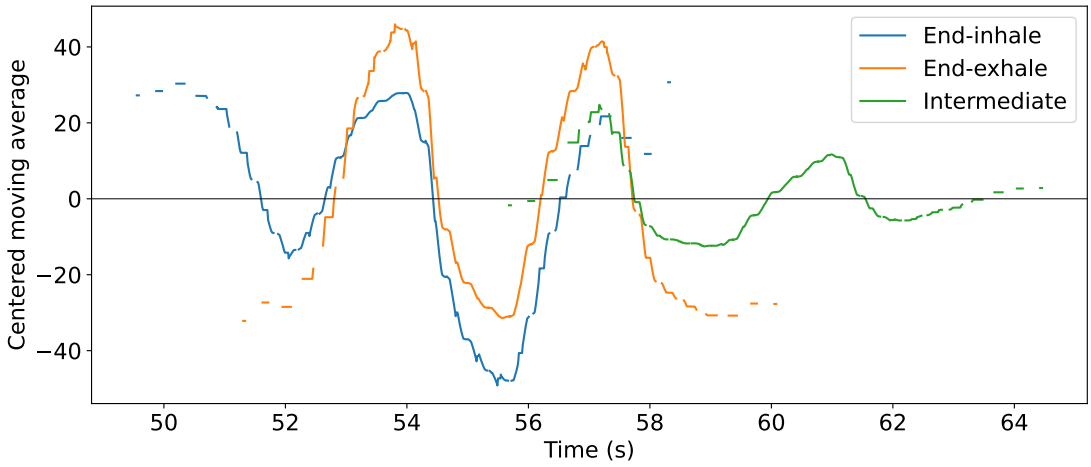

Figure 6.14: Adjustment of the three moving average from the Figures 6.11 (blue line), 6.12 (orange line), and 6.11 (green line) computed with all pairs.

From those observations, we can either extract the respiratory signal from the mean of the consistency measurements or from the superimposition of centered moving averages.

6.3.2 Extraction of the respiratory signal

The steps to extract the respiratory signal from a helical acquisition are described in Algorithm 1. We call Λ the stack of all projections and $\mathcal{P}_\lambda$ the set of all possible pairs (λ, λ') with a DCC computed from the reference projection λ. One projection of reference is selected every 1 s during the acquisition. The set of reference projections is noted Λ_{ref}.

Algorithm 1 Algorithm for the extraction of a respiratory signal from a helical acquisition.

Input: Stack of projections Λ, Λ_{ref}
Output: Set of mean metrics and of centered moving averages for every $\lambda \in \Lambda_{\text{ref}}$
  for every projection of reference $\lambda \in \Lambda_{\text{ref}}$ **do**
    Generate all pairs $(\lambda, \lambda') \in \mathcal{P}_\lambda$ according to Section 4.3.4
    Compute the signed metrics $\tilde{E}_{\lambda,\lambda'}$
    Compute the mean of the metrics $M_\lambda = \sum_{\lambda' \in \mathcal{P}_\lambda} \tilde{E}_{\lambda,\lambda'} / \text{Card}(\mathcal{P}_\lambda)$
    Apply a 2π moving average filter to the centered metrics $\tilde{E}_{\lambda,\lambda'} - M_\lambda$
  end for

6.3.3 Results

This algorithm was applied to both acquisitions (Figures 6.3 and 6.4) of the patient presented in Section 6.2.3.2. The extracted signals with the two methods are plotted Figures 6.15 to 6.18 for both acquisitions. The results are shown as a function of the axial

displacements z of the source (for comparison with the quality of the images) and the acquisition time.

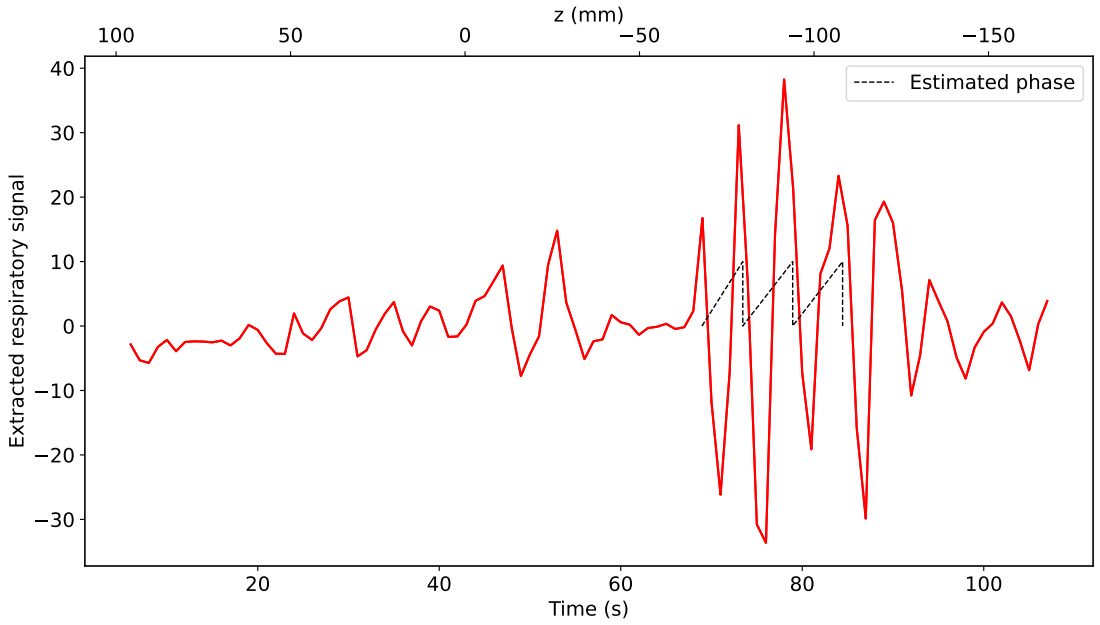

Figure 6.15: Extraction of the respiratory signal from acquisition 1 of the patient with algorithm 1 using the mean M_λ of the metrics (continuous red line). The visually estimated phase corresponds to the dashed black line.

Figures 6.15 and 6.16 show the extracted respiratory signal from acquisition 1 (Figure 6.3) and acquisition 2 (Figure 6.4) of the patient with the mean metrics. The respiratory period of the patient was estimated around 5.2 s for acquisition 1 and around 6.2 s for acquisition 2 (see Section 5.3.3 for the estimation of the respiratory phase). The obtained motion estimate is similar to the one obtained with the graph approach in Figure 6.8 for acquisition 1 and in Figure 6.9 for acquisition 2. However, motion is detected much earlier with this approach: at $z = 50$ mm (at the beginning of the lung) instead of $z = -10$ mm (in the upper lobes) for the graph approach. In Figure 6.15, the period of stillness corresponding to the location of the artifacts in the image is between $z = -40$ mm and $z = -65$ mm in Figure 6.15. A respiratory trace is visible on the two signals for $z \in [-40, 50]$ mm and $z \in [-168, -65]$ mm in Figure 6.15 and for $z \in [-168, 50]$ mm in Figure 6.16. However, some irregularities are present around $z = -150$ mm in the latter figure that were not visible with the graph approach. Around the diaphragm ($z = -100$ mm) the respiratory signal is in agreement with the estimated phase for both acquisitions.

Figures 6.17 and 6.18 show the extracted respiratory signal from acquisition 1 (Figure 6.3) and acquisition 2 (Figure 6.4) of the patient using the centered moving averages. The beginning of the detection of motion (around $z = 50$ mm) is more visible on the moving averages. In Figure 6.17, the artifact area ($z \in [-65, -40]$), is better emphasized with the moving averages. In the upper-abdominal region (around $z = -145$ mm), the curves superimpose but the breathing appears to be irregular, which was not visible in Figure 6.15. In Figure 6.18, a respiratory trace is clearly visible with the superimposition of the moving averages. However, around $z = -150$ mm, the curves do not superimpose correctly and are in opposition.

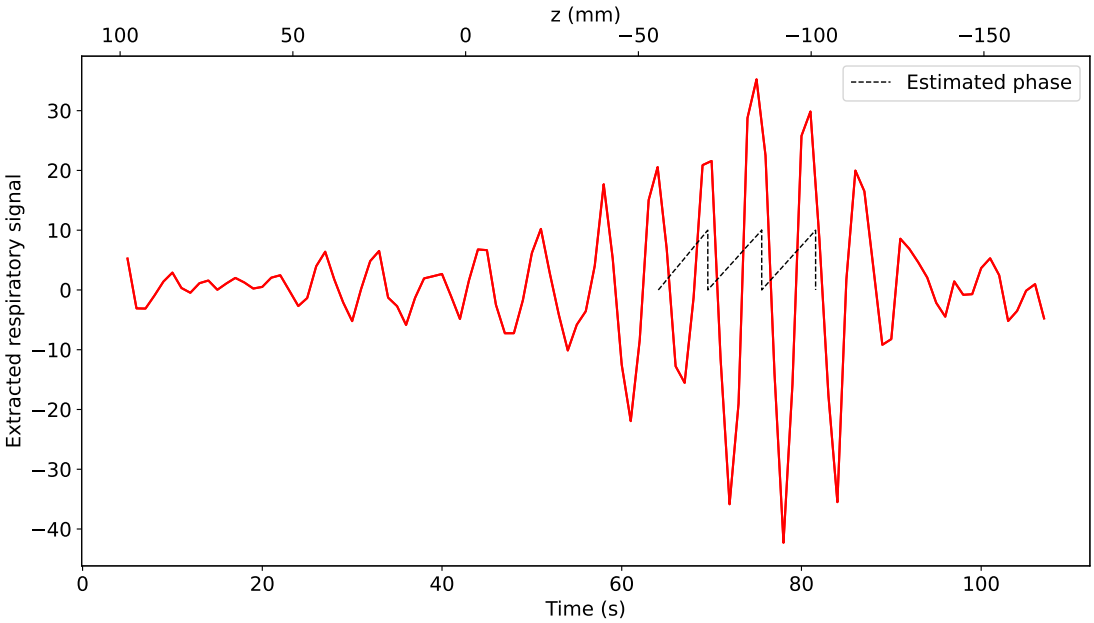

Figure 6.16: Extraction of the respiratory signal from acquisition 2 of the patient with algorithm 1 using the mean M_λ of the metrics (continuous red line). The visually estimated phase corresponds to the dashed black line.

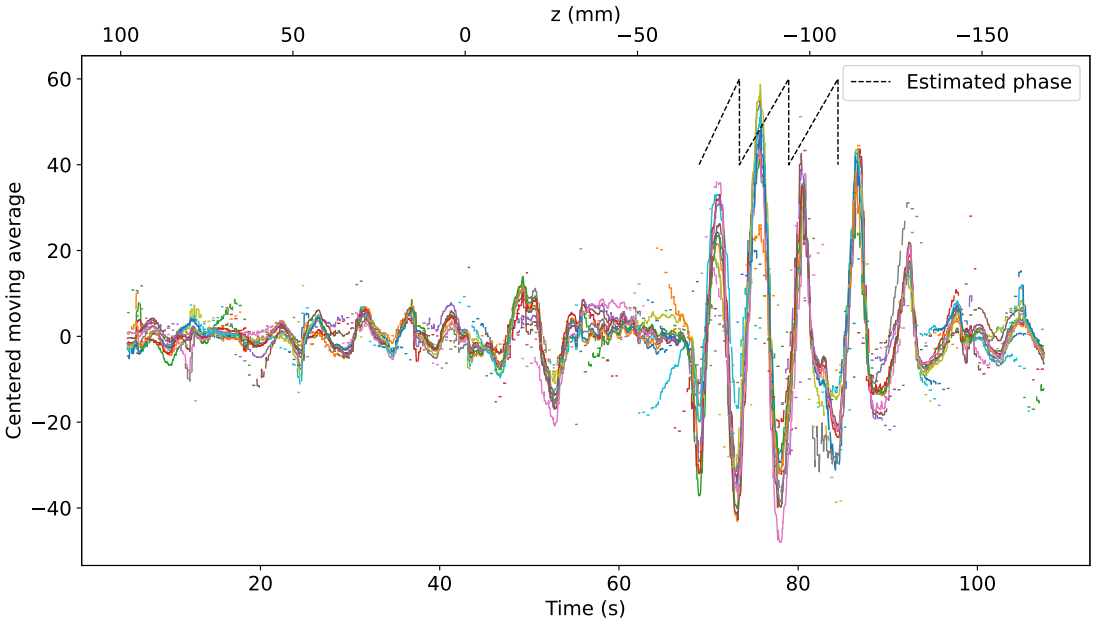

Figure 6.17: Extraction of the respiratory signal from acquisition 1 of the patient with algorithm 1 using the centered moving average. The visually estimated phase corresponds to the dashed black line.

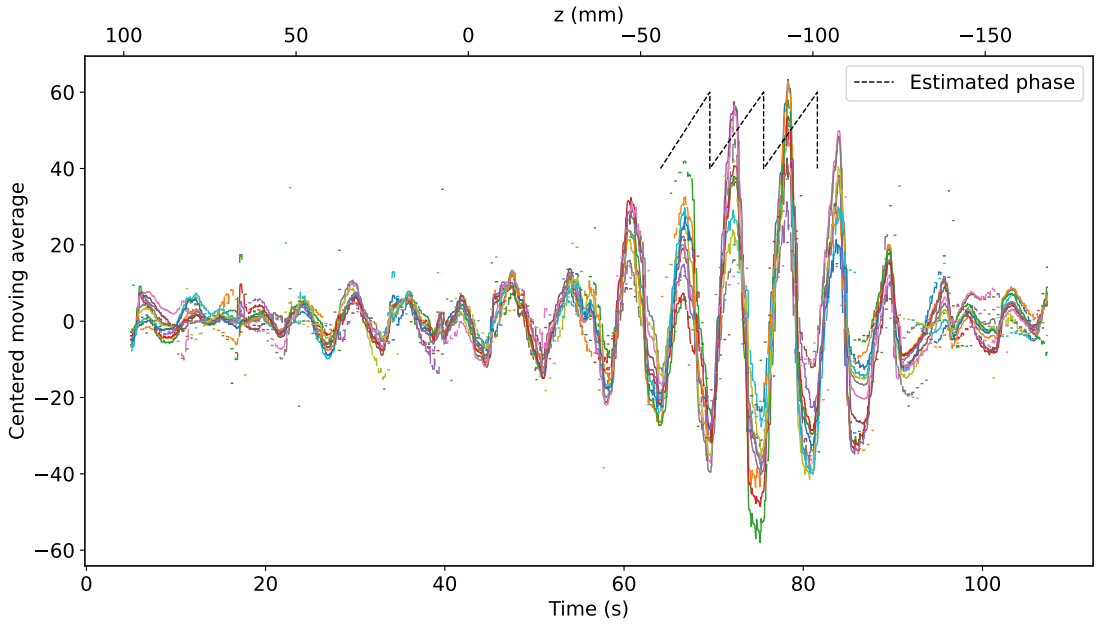

Figure 6.18: Extraction of the respiratory signal from acquisition 2 of the patient with algorithm 1 using the centered moving average. The visually estimated phase corresponds to the dashed black line.

6.3.4 Discussion

The presented methods to extract a respiratory signal from projections acquired during a helical CT rely on the sign of the consistency measurements that varies according to the position of the reference projection in the respiratory cycle. During inhalation, the lungs fill with air. During expiration, the lungs are emptied of air, the projection are more dense at end-exhale than end-inhale, and thus the projection values increases between the two positions. As a result, the moments of the projections acquired at end-inhale are smaller than those of the projections acquired during expiration and the consistency metric is negative (see Figure 6.11). A similar reasoning can be applied for a projection of reference acquired at end-exhale or at an intermediate position of the respiratory cycle. Consequently, it is possible to extract the respiratory signal using the mean of the metrics, or by adjusting the moving average curves around zero (see Figures 6.15, 6.17, 6.16 and 6.18). However, this reasoning is clearly not perfect, it does not apply to the abdomen, and is just a hypothesis to explain the variations of the signed metric, as some instabilities are to be noted (see Figure 6.18, end of acquisition).

When the mean values or the moving averages are around zero over a certain interval (see Figures 6.15 and 6.17), they only indicate a period during which the patient is static. The notion of consistency between two projections is lost regardless of the method.

The plot of the moving averages (Figures 6.17 and 6.18) provides more information than the mean metrics curve (Figures 6.15 and 6.16). The mean metrics only provide information for the reference projections (every one second of the acquisition in our case). However, the moving averages provide information for each projection with at least one DCC and the variations of the consistency metrics are continuously visible.

Finally, this section aimed at describing experimental observations and is only preliminary work. More investigations are needed to develop a robust algorithm that rigorously extracts the respiratory signal directly from the projections and use it to recover the phase of the breathing. Particularly, the interpretation of the curves was based on the quality of the CT image, i.e. on prior knowledge regarding the acquired object, which limits the use of the actual algorithms.

6.4 Conclusion

In the first part of this chapter, a motion detection method based on a graph approach that uses DCCs and connects all projections in a helical CT was presented. This interconnection provides consistency measurements between one projection of reference with all other projections in the acquisition. It was tested on simulated and real CT acquisitions with 3D and 4D protocols. It highlighted consistent and inconsistent projections with the chosen reference and provided an estimate of the breathing motion during the acquisition.

In the second part of this chapter, a preliminary algorithm that extracts the respiratory signal from a stack of projections was presented. Applied to real 4D acquisitions, the extracted respiratory signals were in agreement with the 4D CT images and provided an estimation of the breathing motion and its regularity during the acquisition.

Conclusions and prospects

The objective of this thesis was to detect motion in helical CT using consistency conditions. The main application of the developed algorithms was the detection of irregular or unexpected motion from 4D CT acquisitions used for the radiotherapy planning of thoracic and upper-abdominal cancers. Irregular breathing induces artifacts on 4D CT images whose quality directly impacts the quality of the radiotherapy.

Contributions

The first step of this thesis was to adapt existing DCCs to helical CT. DCCs have mainly been developed for planar trajectory (linear or circular trajectory) with a flat panel detector. In helical CT, the trajectory is 3D and the detector is cylindrical. This specificity constrained us to apply DCCs to pairs of cone-beam projections. The FBDCC states that for two source positions on a linear trajectory, the moments of the projections, i.e. the integral of the cosine-weighted fan-beam projections, must be equal if the projections are consistent. By considering a virtual linear trajectory between two source positions, the FBDCC was adapted to the helical trajectory using two approaches.

The first approach rebins the two projections on a virtual detector whose rows are parallel to the virtual linear trajectory. Each row of the virtual detector corresponds to a fan-beam within the cone-beam projection and the FBDCC is applied along each row of the virtual detector. To perform the rebinning approach, the intersection between the two cone-beams and the backprojection plane parallel to the baseline must be computed to define the virtual detector. For pairs whose baseline intersects the FOV, the direction of the ray matching the direction of the baseline is parallel to the backprojection plane and never intersects it. The backprojection of this ray is not defined which prevents the computation of the virtual detector as we defined it. Hence, such pairs are not eligible for the rebinning approach.

The second approach computes the FBDCC directly in the cylindrical detector coordinates on a set of planes containing both source positions and intersecting the two lateral borders of both cone-beam projections. Indeed, as the computation of the FBDCC requires the evaluation of two integrals along the angular coordinate of the detector, fan-beam projections resulting from the intersection of a plane and the cone-beam projections must not be laterally truncated. The difference between the two approaches relates to their applicability conditions. The rebinning approach only applies to pairs of projections with a sufficient overlap and whose baseline does not intersect the FOV. The direct approach alleviates the FOV condition by dealing numerically with a singularity that arises in the moment computation and thus only necessitates a sufficient overlap between the two projections. By computing the FBDCC directly in the cylindrical detector coordinates, the moment corresponds in this case to the scalar product between a weighted fan-beam projection and a Hilbert kernel. The numerical integration is performed by band-limiting the Hilbert kernel with a Hann window to deal with the singularity. The two approaches were tested and validated on simulated and real acquisitions of static phantoms. For pairs whose baseline does not intersect the FOV, the two approaches gave similar results and

were robust to noise. For pairs whose baseline intersects the FOV, only the direct approach could be applied, and it was shown that the DCCs were subject to sampling errors and thus very sensitive to noise.

The second step of this work was to verify that the FBDCC adapted to the helical trajectory could detect motion. The direct approach was chosen to maximize the number of pairs eligible for a DCC. A consistency metric was defined between two projections as the mean absolute difference of the moments over the uncertainty of the mean difference of the moments. The advantage of this metric is that it takes into account the variations of the moments due to the noise in the projections as we showed that the impact of noise strongly varies with the geometrical configuration of a given pair. The moments uncertainty was estimated as a function of the noise of the projection pixels with a similar approach as the one used for the derivation of noise in CT images reconstructed with fan-beam reconstruction algorithms [Wunderlich and Noo, 2008], and verified with a batch approach. The consistency metric was applied to simulated, mechanical phantom and patient data acquired on a diagnostic helical CT. The consistency of all eligible pairs computed from one projection of reference was assessed with the consistency metric. The detection of motion was directly possible by considering only pairs whose baseline does not intersect the FOV but not for pairs whose baseline intersects the FOV because the impact of noise was too important for such pairs. For the three datasets, the measurements increased with the amplitude of the motion. The use of a moving average to reduce the sensitivity to noise for pairs whose baseline intersects the FOV allowed the identification of consistent and inconsistent projections that were in agreement with the estimated phases for the mechanical phantom and patient data. The method was applied to the acquisition of a patient for which artifacts were present in the 4D reconstruction and DCC highlighted that the patient was not breathing when the region of the artifacts was acquired.

Finally, we proposed two methods to estimate motion during an entire helical CT. The first method assesses the consistency of one projection of reference with the other projections of a helical acquisition even if a DCC cannot be directly computed. Firstly, all pairs eligible for a FBDCC were computed and the consistency metric, previously defined, calculated for each pair. Secondly, a graph was constructed with the projections as vertices and an edge between two vertices if a DCC can be computed between the corresponding pair of projections. The edge is then weighted by the consistency metric of the corresponding pair. The consistency between a projection of reference and other projections was measured by computing the shortest path from the reference vertex and the other vertices. On simulated and real data, the graph approach allowed the identification of consistent projections with the chosen projection of reference and gave an estimation of the motion during the acquisition. The consistency measurements were normalized by the number of vertices along the path to compensate for the drift caused by the accumulated inconsistency due to noise. On simulated and real data, the normalized measurements deteriorated the estimation of the motion. Moreover, the consistency information was lost for some real data. The second method introduces a preliminary algorithm allowing the extraction of the breathing signal from the projections using a signed version of the consistency metric. A link between the sign of the metric and the end-inhale/end-exhale positions at which the projection of reference is acquired was observed. The respiratory signal was extracted by measuring the mean of the consistency measurements for a set of reference projections regularly selected along the acquisition or by re-adjusting their moving average curves. Both methods were applied to real 4D CT acquisitions. They allowed to globally assess the presence of motion during an entire helical CT and highlighted irregular motion that was in agreement with the observed artifacts on the reconstructed 4D CT images.

Remaining challenges

Other DCC in helical CT

The FBDCC used in this thesis is not the only one that can be applied pair-wise to arbitrary x-ray source trajectories. Exploring the use of Grangeat-based DCCs [Debbeler et al., 2013, Aichert et al., 2015, Lesaint, 2018] in helical CT could be beneficial in terms of robustness to discretization errors. The intermediate function involved in the computation of Grangeat DCCs does not involve a singularity suggesting that they would be more adapted for pairs whose baseline intersects the FOV than the FBDCC. However, they contain a differentiation step that may be sensitive to noise too. They were formulated in the detector coordinates for pairs of projections with a flat panel detector [Aichert et al., 2015, Lesaint, 2018]. Their extension to a cylindrical detector could similarly be established. An alternative would be to rebin the cylindrical projections to corresponding planar projections and apply the pair-wise Grangeat-DCC [Lesaint, 2018] to those rebinned projections.

In our work, pairs with equal gantry angles but on successive rotations cannot be considered because of the axial truncation of the projections. A way to consider those pairs would be the development of a consistency condition for sources on a line that could handle truncated projections in the direction of the trajectory. Such DCCs were established for truncated fan-beam projections with sources on a circular trajectory in [Clackdoyle and Desbat, 2015]. However, the development of such DCCs in 3D would be even more complex and would probably require prior knowledge of the extent of the object, which limits the use of the DCCs. The benefit of considering those pairs would be to apply higher order DCCs (higher than the zeroth order) by considering more than two projections and increasing the robustness of the inconsistency detection.

Phase retrieval from the extracted respiratory signal

The extracted signal from Chapter 6 could be used to recover the phase of the breathing signal and to sort the projections with a phase-based algorithm. The use of this signal in an amplitude-based sorting algorithm may be more difficult as the value of the measurements varies with the amplitude of the motion, which is quite important around the diaphragm, but decreases away from it. The accurate extraction of the respiratory signal from the projections would be beneficial to the patient as the breathing signal recording device would no longer be required.

Sorting of projections with DCCs

DCCs offer an alternative way to cope with irregular breathing. The main drawback with the current methods is that they assume a cyclic breathing motion. However, it is never accurately cyclic and the respiratory period varies from one respiratory cycle to another.

A first possibility would be to use DCCs to assess the consistency of pre-formed subsets of projections with the phase-based or amplitude-based sorting methods and remove the projections that do not verify the consistency conditions.

Another possibility would be to sort the projections directly with the consistency conditions and the graph approach. The same graph could be constructed with projections as vertices and an edge between vertices when a DCC can be computed between the two projections. Each vertex (or projection) could be labeled as belonging to a phase of the respiratory cycle. Using an appropriate weighting inversely proportional to the consistency measurements, a maximum flow-minimum cut algorithm [Boykov et al., 2001] may be applied to the graph to form subsets of projections corresponding to the ten phases of the respiratory cycle. This algorithm aims at minimizing the total energy of a graph by forming subsets of vertices with the same label by cutting edges with the lowest cost. Moreover, it would allow the use of all projections in the part of the acquisition where there is no

motion (when the upper-body is acquired for example) as the projections would be sorted according to their consistency and not the respiratory phase.

Only necessary DCC

All the detection methods we developed are based on a consistency condition which is necessary only: the FBDCC. It means that if our consistency measurement is not zero, then the projections are inconsistent. On the other hand, it is possible that the consistency measurement equals zero, even in the presence of noise or motion. This is the case in 2D with the FBDCC if the object motion is parallel to the trajectory [Clackdoyle et al., 2014]. In helical CT, the FBDCC can apply to any pair of cone-beam projections whose baseline is not parallel to the helix axis. Thus, there is a high number of virtual linear trajectories, with various directions. In our application, the detection of breathing motion, we made no hypothesis regarding the direction of the motion, except that the motion is non rigid. Thus, from one reference projection, there should always be one pair for which motion is detectable. In fact, if we assume that the strongest component of motion is in the superior-inferior direction, then all pairs should detect motion if the scanned object is not constant in this direction, except those with a baseline parallel to the helix axis, that would detect the antero-posterior and the lateral components of the motion. Therefore, the parameters that may influence consistency assessment based on only necessary DCCs should be analyzed to develop robust DCC-based artifact detection and reduction methods.

Résumé étendu

Le cancer du poumon est l'un des cancers les plus répandus dans le monde et était le cancer faisant le plus grand nombre de mort en 2020 avec 1,8 million de décès [World Health Organization, 2022]. Le premier choix de traitement est la chirurgie, au cours de laquelle les cellules cancéreuses sont retirées de l'organisme, mais cela n'est pas toujours possible. Alternativement, la radiothérapie peut être utilisée pour tuer les cellules cancéreuses en les irradiant avec des rayons X à haute énergie. Une difficulté majeure de la radiothérapie des cancers du poumon est la respiration des patients. Elle induit des mouvements pulmonaires et tumoraux qui ne sont pas pris en compte en radiothérapie conventionnelle. La radiothérapie quadridimensionnelle (4D) est apparue pour estimer le mouvement de la tumeur et le gérer pendant l'administration des radiations. La radiothérapie 4D est principalement basée sur des images de tomodensitométrie (TDM) 4D.

Les projections de rayons X correspondent aux images d'atténuation des rayons X par le corps. Lors d'un scanner TDM, plusieurs projections du patient sont acquises sous différents angles. Les projections sont traitées pour obtenir une image TDM du patient, appelée reconstruction tomographique. Lors d'une acquisition, le patient est supposé immobile. Si le patient respire librement, cela crée des artéfacts sur les images TDM car le mouvement respiratoire n'est pas pris en compte dans les algorithmes de reconstruction conventionnels. La TDM 4D tient compte du mouvement respiratoire en synchronisant les projections avec un signal respiratoire acquis simultanément. Le signal respiratoire est divisé en phases et des sous-ensembles de projections sont formés en conséquence. Chaque sous-ensemble, correspondant à une phase du cycle respiratoire, est reconstruit séparément avec des algorithmes de reconstruction classiques, et les images TDM 3D correspondantes sont regroupées pour obtenir une image TDM 4D du patient aux différentes phases du cycle respiratoire. Cet algorithme, appelé TDM corrélée à la respiration (RCCT, de l'anglais *respiratory correlated computed tomography*), suppose que le mouvement respiratoire est cyclique, ce qui n'est pas toujours le cas, notamment pour les patients souffrant de maladies respiratoires. Par conséquent, les artéfacts de mouvement peuvent dégrader la qualité des images TDM 4D. De plus, le signal respiratoire acquis fait référence au mouvement externe du patient et peut différer du mouvement interne de la tumeur, conduisant à une reconstruction incorrecte de la tumeur.

Il est nécessaire d'identifier clairement si deux ou plusieurs projections appartiennent à la même phase respiratoire pour limiter les artéfacts sur les images TDM, c'est-à-dire d'évaluer la cohérence entre deux projections. Les conditions de cohérence des données (CCD) sont un outil mathématique qui caractérise la redondance dans les projections de rayons X et évalue la cohérence entre deux projections. Des CCD ont été proposées pour diverses géometries d'acquisition, mais pas pour les scanners TDM à géometrie hélicoïdale qui est la géométrie de la plupart des scanners TDM 4D.

L'objectif de cette thèse est de détecter le mouvement en TDM hélicoïdale à l'aide des CCD avec une application à la détection de mouvement irrégulier dans les images TDM 4D utilisées pour la planification de la radiothérapie des cancers du poumon. Dans le premier chapitre, les bases de la physique des rayons X et de la TDM à rayons X sont introduites avec un focus particulier sur la TDM hélicoïdale. Dans le deuxième chapitre, l'impact du

mouvement respiratoire sur la radiothérapie et la TDM conventionnelle est développé et les bases de la TDM 4D ainsi que ses limites actuelles sont présentées. Dans le troisième chapitre, les CCD sont d'abord illustrées par un exemple en géométrie parallèle avant d'être introduites pour différentes géométries d'acquisition. Une présentation approfondie des applications des CCD est effectuée en mettant l'accent sur les applications pour la détection et la correction de mouvement.

Les contributions de cette thèse sont présentées dans les chapitres 4 à 6. Dans le chapitre 4, nous proposons deux approches pour appliquer les CCD à la TDM hélicoïdale et énonçons les conditions d'applicabilité de ces CCD. Dans le chapitre 5, une méthode de détection de mouvement locale basée sur les conditions de cohérence, prenant en compte l'impact du bruit sur les CCD, est présentée. Dans le chapitre 6, deux méthodes globales de détection de mouvement sont introduites : la première évalue la cohérence d'une projection avec les autres projections de l'acquisition ; la deuxième méthode extrait le signal respiratoire directement des projections. Les implémentations de CCD et les méthodes de détection de mouvement sont toutes deux évaluées sur des données simulées et réelles acquises sur le scanner TDM du service de radiothérapie du centre anti-cancer Léon Bérard à Lyon.

I Tomodensitométrie

I.1 Physique des rayons X

Les rayons X sont des ondes électromagnétiques découvertes en 1895 par le physicien allemand Whilhem Röntgen (1845-1923). Leurs caractéristiques et propriétés sont expliquées par la dualité onde-particule. En tant qu'ondes, ils sont caractérisés par leur longueur d'onde (entre 10^{-8} m et 10^{-12} m). En tant que particules, appelées photons, ils sont caractérisés par leur énergie (en keV).

Les rayons X sont produits dans un tube à rayons X : des électrons, contenus dans un filament (cathode, souvent en tungsten), sont accélérés en direction d'une cible (anode, souvent en tungsten) en appliquant une très haute différence de potentiel (entre 40 kV et 150 kV en imagerie de diagnostique) entre la cathode et l'anode. Lors de l'impact avec la cible, les éléctrons vont interagir avec les atomes de la cible, et de ces interactions, deux types de rayonnements peuvent se produire :

- les électrons peuvent être décélérés et de cette décélération émerge un rayonnement de Bremsstrahlung (voir Figure 1.1a),
- ils peuvent éjecter un électron de la couche électronique des atomes de la cible, générant un réarrangement électronique et l'émission de rayonnement caractéristique (voir Figure 1.1b).

Tous les électrons ne sont pas décélérés de la même manière et les photons à la sortie du tube n'ont pas tous la même énergie. En conséquence, la distribution énergétique d'un faisceau de rayon X est polyénergétique. Elle se compose d'une composante continue résultant des rayonnements de Bremsstrahlung et de composantes discrètes résultants des rayonnements caractéristiques (voir Figure 1.2).

Le nombre de photons produit I_0 dans un tube à rayon X dépend de la différence de potentiel U appliquée entre la cathode et l'anode, de l'ampérage du tube i et du matériau de la cible (voir Equation 1.1). A la sortie du tube, le faisceau de rayon X est généralement filtré de manière à supprimer les photons de basse énergie. Un filtre bien connu est le filtre en *papillon*. Son utilisation permet de réduire l'intensité du flux de photons émis vers les bords du détecteur car ces photons sont généralement moins atténués par le patient qui est moins épais qu'au centre du détecteur. Il permet donc d'homogénéiser la distribution

de dose (quantité de radiation reçue) dans le patient. En pratique, la tension et le filtre sont choisis par les fabricants et cliniciens pour être conformes aux normes médicales. L'ampérage du tube peut être modulé en fonction de la position du tube de rayon X par rapport au patient. Par exemple, un patient large nécessite un flux plus important afin de compenser l'augmentation de l'atténuation.

Traversant un objet, les rayons X peuvent interagir avec la matière. Les quatres interactions principales des rayons X sont l'absorption photoélectrique, la diffusion Compton, la diffusion de Rayleigh et la production d'une paire électron-positron. Ces quatre interactions sont illustrées Figure 1.4. En imagerie à transmission, les photons sont principalement absorbés (effet photoélectrique) ou diffusés (diffusion Compton ou Rayleigh) lorsqu'ils interagissent avec les atomes du corps humain.

L'atténuation peut être définie comme le rapport du nombre de photons émis n'ayant pas interragi avec un matériau sur le nombre de photons émis. Le pouvoir d'atténuation d'un matériau est donné par son coefficient d'atténuation exprimé en cm^{-1}. Le corps humain est composé de différents matériaux (eau, os, muscle...), chacun caractérisé par son coefficient d'atténuation. Pour des photons monoénergétiques, la loi de *Beer-Lambert*, Equation 1.2, fait le lien entre le nombre de photons initial I_0 et le nombre de photons final I pour un faisceau se déplaçant le long de la ligne $\mathcal{L}$ et traversant un patient caractérisé par son coefficient d'atténuation f en tout point $\boldsymbol{x}$ de l'espace. Dans la suite du manuscrit, nous supposons que les faisceaux de rayon X sont monoénergétiques.

Le nombre de photons final est mesuré à l'aide d'un détecteur à rayons X qui mesure l'énergie totale reçue dans chaque pixel du détecteur. La mesure de l'énergie peut se faire de deux manières : l'énergie reçue est directement convertie en une charge électrique résultant de l'ionisation des atomes du détecteur par les rayons X, ou bien indirectement à l'aide d'un scintillateur qui convertit l'énergie reçue en lumière visible. La distribution de la lumière visible est ensuite mesurée à l'aide d'un photodétecteur pour obtenir une image. Dans la suite du manuscrit, nous supposons que les détecteurs sont parfaits, c'est-à-dire qu'il n'y a ni bruit électronique ni courant d'obscurité.

I.2 Tomodensitométrie hélicoïdale

L'objectif de la TDM est de retrouver les coefficients d'atténuation $f(\boldsymbol{x})$ à partir des intensités détectées. Pour ce faire, l'Equation 1.2 peut se réécrire comme l'Equation 1.3. Le côté droit de cette équation est appelée intégrale de ligne et est le point de départ de la TDM.

Cette thèse se concentre sur un scanner TDM à géométrie hélicoïdale : le SOMATOM go.Sim, commercialisé par Siemens Healthcare et utilisé quotidiennement au centre Léon Bérard. Un scanner hélicoïdal est composé d'un système rotatif, composé d'une source et d'un détecteur, et d'une table, sur laquelle le patient se positionne. La table se déplace axialement à l'intérieur du système rotatif pendant que celui-ci tourne.

Tout au long de cette thèse, nous considérons les coordonnées patient 3D (x, y, z) définies dans la base ortho-normale $(\boldsymbol{e}_x, \boldsymbol{e}_y, \boldsymbol{e}_z)$. La source ponctuelle $\boldsymbol{s}_\lambda$ se déplace le long de l'hélice $(R\cos\lambda, R\sin\lambda, \frac{d\lambda}{2\pi})$, où R est le rayon de l'hélice , $\lambda \in n_{rot} \times [0, 2\pi)$ est l'angle du système rotatif, pris entre $\boldsymbol{e}_x$ et la projection de $\boldsymbol{s}_\lambda$ sur le plan $(\boldsymbol{e}_x, \boldsymbol{e}_y)$ (mesuré positivement dans le sens des aiguilles d'une montre lorsqu'il est vu dans la direction $\boldsymbol{e}_z$), n_{rot} le nombre de rotations, et d est le pas de la table par rotation, c'est-à-dire la distance parcourue par la source le long de l'axe z en une rotation. Le détecteur est un détecteur courbe correspondant à une portion de cylindre de rayon D dont l'axe est défini par la source $\boldsymbol{s}_\lambda$ et l'axe de rotation $\boldsymbol{e}_z$. À une position de source donnée $\boldsymbol{s}_\lambda$, les coordonnées (γ, v) d'un point du détecteur $\boldsymbol{p}_\lambda(\gamma, v)$ sont fournies Equation 1.7. L'angle γ est pris entre les rayons $\boldsymbol{p}_\lambda(0, 0)$ et $\boldsymbol{p}_\lambda(\gamma, 0)$, et est mesuré positivement dans le sens antihoraire lorsqu'il est vu dans la direction $\boldsymbol{e}_z$. Les limites du détecteur sont $\gamma \in [-\gamma_{\max}, \gamma_{\max}]$ et

$v \in [-v_{\max}, v_{\max}]$. La direction $\boldsymbol{\theta}$ du rayon sortant de $\boldsymbol{s}_\lambda$ et frappant le détecteur courbe de rayon D au point $\boldsymbol{p}_\lambda(\gamma, v)$ après avoir traversé un objet avec la fonction d'atténuation f est donnée Equation 1.8. En géometrie hélicoïdale, l'intégrale de ligne est définie Equation 1.9. Pour simplifier les notations, notons $g_\lambda(\gamma, v) = g(\lambda, \gamma, v)$ et g_λ est la projection à faisceau conique depuis la position de source $\boldsymbol{s}_\lambda$.

Tout au long de la thèse, nous faisons l'hypothèse suivante : le patient est entièrement contenu dans la région appelée champ de vue (FOV, de l'anglais *Field-of-view*). Le FOV est la région définie par $\sqrt{x^2 + y^2} \leq R_{\text{FOV}}$, avec $R > R_{\text{FOV}} \overset{\text{def}}{=} R \sin \gamma_{\max}$. Par conséquent, f est nul en dehors du FOV et les intégrales de ligne définies ci-dessus ne sont pas tronquées dans la direction de γ. Cependant, du fait de la hauteur limitée du détecteur qui ne couvre pas entièrement le patient, les projections sont le plus souvent tronquées axialement en TDM hélicoïdale. Ce problème est connu sous le nom de problème d'objet long.

II Tomodensitométrie et mouvement respiratoire

II.1 Planification de la radiothérapie et mouvement respiratoire

Le mouvement respiratoire peut être caractérisé par deux variables : sa fréquence ainsi que l'amplitude et la direction du mouvement des organes qui en résulte. Le nombre de cycles respiratoires pour un adulte varie entre 12 et 20 par minute [George et al., 2005]. Lors de la respiration, la contraction du diaphragme entraîne la déformation des poumons et le mouvement des organes abdominaux supérieurs. La direction et l'amplitude du mouvement des tumeurs pulmonaires dépendent de leur proximité avec le diaphragme : plus la tumeur est proche du diaphragme, plus l'amplitude de son mouvement est grande (de 10 à 30 mm) et plus le mouvement est présent dans la direction tête-pied. L'amplitude du mouvement des tumeurs situées dans les lobes supérieurs et médians est plus faible que pour celles situées dans les lobes inférieurs [Keall et al., 2006]. Cependant, pour certains patients, la direction du mouvement la plus importante est la direction antéro-postérieure. De plus, la trajectoire du mouvement peut ne pas être la même pendant l'inspiration et l'expiration.

En TDM conventionnelle, le patient est supposé immobile pendant toute l'acquisition. Les algorithmes de reconstruction ne prennent pas en compte le mouvement respiratoire du patient provoquant des artéfacts sur les images reconstruites tels que du flou et/ou la déformation de structures (voir Figure 2.1). La reconstruction incorrecte des volumes va diminuer la qualité de la planification de traitement et donc la qualité de la radiothérapie.

Afin de prendre en compte le mouvement respiratoire durant la planification et la délivrance du traitement, la radiothérapie 4D est utilisée. Pour ce faire, la composante temps est ajoutée aux techniques conventionnelles. L'objectif de la planification 4D est de caractériser le plus précisément possible le mouvement de la tumeur au cours d'un cycle respiratoire. Il existe différentes techniques de TDM permettant de retranscrire le mouvement respiratoire :

- une acquisition TDM lente (la durée totale d'une rotation pour le système rotatif passe de 0.5 s à 4 s), durant laquelle le patient respire librement, permet d'obtenir une image sur laquelle toute l'étendue du mouvement de la tumeur est visible [Dieterich et al., 2016];
- la réalisation de plusieurs acquisitions conventionnelles (deux acquisitions pour lesquelles le patient retient sa respiration à la fin de l'inspiration et à la fin de l'expiration, et une durant laquelle il respire librement) permet d'identifier le volume de la tumeur aux deux phases extrêmes de la respiration et offre une idée de l'étendue du mouvement de la tumeur [Shih et al., 2004];
- la TDM 4D permet d'obtenir une image TDM 3D à chaque phase du cycle respiratoire et donc retranscrit le mouvement de la tumeur au court d'un cycle respiratoire entier

[Ford et al., 2003]. Il existe deux modes d'acquisition pour obtenir une image TDM 4D. Le premier, appelé TDM 4D-Ciné, durant lequel la table du patient est fixe et une position axiale est acquise pendant un cycle respiratoire. Une fois la position axiale acquise, la table se déplace afin de faire l'acquisition de la position axiale suivante pendant un cycle respiratoire, et ainsi de suite. Le deuxième, appelé TDM 4D hélicoïdale, consiste à acquérir de manière continue le volume souhaité, c'est à dire que la table du patient se déplace continuellement pendant l'acquisition. Pour ce faire, le pas de l'hélice durant une rotation est largement diminué comparé à celui d'une acquisition conventionnelle. La thèse se concentre sur ce deuxième mode d'acquisition.

II.2 TDM 4D hélicoïdale

La TDM 4D hélicoïdale nécessite que chaque point du volume scanné soit acquis pour chaque phase du cycle respiratoire et qu'il y ait suffisamment de projections pour reconstruire chaque point à chacune des phases [Pan, 2005].

Pendant une acquisition 4D hélicoïdale, le signal respiratoire est enregistré en même temps que les projections sont acquises. Le signal respiratoire est divisé en différentes phases et les projections sont triées en conséquence, comme illustré Figure 2.3. Chaque sous-ensemble de projections est ensuite utilisé pour reconstruire une image TDM 3D du patient à la phase du cycle respiratoire correspondante. Le regroupement des images TDM 3D reconstruites pour les différentes phases du signal respiratoire permet d'obtenir une image TDM 4D [Ford et al., 2003]. Le signal respiratoire externe peut être enregistré de différentes manières (voir Figure 2.4). Au centre Léon Bérard, le mouvement respiratoire est enregistré à l'aide d'un capteur de pression intégré dans une ceinture placée autour de la poitrine (au niveau du diaphragme) du patient. La respiration fait varier la pression exercée sur le capteur, résultant en un signal respiratoire. Les projections peuvent ensuite être triées selon la phase dans laquelle le patient était lors de leur acquisition [Ford et al., 2003] ou bien selon l'amplitude du cycle respiratoire au moment de leur acquisition [Lu et al., 2006, Li et al., 2012].

Bien qu'elle prenne en compte le mouvement respiratoire durant l'acquisition d'images pour la planification du traitement, la TDM 4D a d'importantes limites. La plupart des méthodes de tri reposent sur l'hypothèse que le mouvement respiratoire des patients est régulier, ce qui n'est pas toujours le cas, particulièrement pour les patients souffrant de difficultés respiratoires. La respiration irrégulière provoque des artéfacts de structures et de sous-échantillonnage (lorsqu'il n'y a pas assez de projections pour reconstruire une position axiale), détériorant la qualité des images TDM 4D (voir Figure 2.6). De plus, le signal enregistré se réfère au mouvement externe du corps et est souvent différent du mouvement interne des organes et de la tumeur.

Il existe déjà certaines méthodes pour améliorer la gestion des mouvements respiratoires irréguliers. Les patients peuvent être amenés à suivre des instructions sur le rythme et la profondeur de leur respiration pendant une acquisition [George et al., 2006, Neicu et al., 2006, Venkat et al., 2008]. Une plaque de compression peut être utilisée afin de contraindre la direction du mouvement dans la direction tête-pied [Negoro et al., 2001]. On peut également corriger les artéfacts sur les images reconstruites [Ehrhardt et al., 2007, Schreibmann et al., 2006, Zhang et al., 2013] ou bien optimiser le tri des projections [Werner et al., 2017]. Toutes ces alternatives améliorent la qualité des images TDM 4D pour la planification de traitement, mais cela n'est pas suffisant et il est nécessaire de proposer de nouvelles méthodes pour mieux gérer la respiration irrégulière et améliorer encore plus la qualité des images TDM 4D.

III Conditions de cohérence des données

D'un point de vue mathématique, les *Conditions de cohérence des données* (CCD), ou *conditions de rang*, sont des équations mathématiques caractérisant l'image d'un opérateur linéaire. Cela signifie que tous les éléments appartenant à l'image de cet opérateur doivent satisfaire les CCD. En TDM, l'acquisition est modélisée par un opérateur linéaire, comme la transformée de Radon pour la géométrie parallèle 2D et la transformée de faisceau divergent pour les géométries divergentes, d'un espace objet vers un espace de projection. Par conséquent, les CCD doivent être vérifiées par les projections. En d'autres termes, les CCD caractérisent les redondances dans les projections de rayons X. Tout effet externe non pris en compte dans le modèle entraînera probablement des incohérences dans les projections qui ne vérifieront plus les CCD. Parmi ceux-ci, on peut trouver le mouvement, le bruit, le durcissement de faisceau, le rayonnement diffusé, etc... Les CCD s'appliquent directement aux projections, avant toute reconstruction. Cela en fait un outil très intéressant et pratique pour corriger ou utiliser les informations dans les projections et reconstruire des images TDM sans artefacts.

III.1 Conditions de cohérence existantes

Les CCD dépendent de la géométrie du scanner TDM car elles dépendent des projections données par le modèle d'intégrale de ligne qui est spécifique au système d'acquisition des rayons X.

Les projections parallèles d'une fonction 2D doivent vérifier la condition de cohérence suivante : la somme de toutes les intégrales de ligne mesurées pour chaque projection est constante pour toutes les projections de la trajectoire. Cette CCD est connue comme l'ordre zéro des CCD de Helgason-Ludwig. Cette condition est seulement nécessaire mais fait partie d'un ensemble de conditions complètes (c'est-à-dire nécessaires et suffisantes). Elles indiquent que les moments d'ordre n des projections parallèles d'une fonction 2D doivent être un polynome homogène d'ordre n en les coordonnées de la source. Si elles sont vérifiées, les projections sont bien la transformée de Radon d'une certaine fonction d'atténuation et les projections sont dites cohérentes [Ludwig, 1966, Helgason, 1965].

Des CCD complètes pour des projections à faisceau en éventail d'une fonction 2D acquises sur une trajectoire linéaire ont également été proposées [Clackdoyle, 2013] et ont la même forme que les conditions de Helgason-Ludwig. Dans cette thèse, nous nous intéressons particulièrement à l'ordre zéro de ces conditions pour faisceau en éventail qui indique que le moment d'ordre zéro de chaque projection est constant le long de la trajectoire [Chen and Leng, 2005, Wei et al., 2006, Levine et al., 2010, Tang et al., 2012, Clackdoyle, 2013]. Le moment d'ordre zéro correspond à la somme de toutes les intégrales de ligne mesurées dans une projection pondérées par l'angle des rayons correspondants. Dans la suite de la thèse, nous appelons cette CCD la FBDCC.

La dérivation de CCD pour les projections à faisceau conique d'une fonction 3D est plus complexe. La première possibilité pour appliquer des CCD à des projections à faisceau conique est d'appliquer les CCD pour faisceau en éventail sur chaque ligne des détecteurs 2D [Leng et al., 2007, Berger et al., 2017]. Cette méthode a surtout été utilisée pour une trajectoire circulaire de la source à rayons X avec un détecteur plan. La seconde possibilité est d'appliquer la FBDCC à une paire de projections à faisceau conique en rééchantillonnant les deux projections sur un détecteur virtuel dont les lignes sont parallèles à la ligne connectant les deux positions de sources et d'appliquer la FBDCC le long de chaque ligne du détecteur virtuel [Levine et al., 2010, Lesaint et al., 2017]. Cette méthode à l'avantage de pouvoir gérer la troncature axiale des projections coniques car elle permet de sélectionner seulement une partie des projections coniques pour appliquer la FBDCC. Troisièmement, les CCD dérivées depuis l'équation de Grangeat [Grangeat, 1991], qui

lie la transformée de Radon d'une fonction 3D à ses projections coniques, peuvent être appliquées à n'importe quelle trajectoire en considérant également des paires de projections [Debbeler et al., 2013, Aichert et al., 2015, Lesaint et al., 2018]. Elles indiquent qu'une certaine fonction intermédiaire, définie à partir des projections, doit être constante pour la paire de projections considérée. Ces CCD peuvent également gérer les troncatures axiales des projections, cependant, comme la FBDCC, elles ne sont que des conditions nécessaires. Enfin, il existe des CCD pour des trajectoires planes de la source de rayons X qui intersectent [Clackdoyle et al., 2016, Nguyen, 2021] ou n'intersectent pas [Clackdoyle and Desbat, 2013] le plan du détecteur, mais elles ne peuvent pas gérer la troncature axiale des projections et ne sont donc pas intéressantes pour la trajectoire hélicoïdale.

III.2 Application des conditions de cohérence des données

En TDM, de nombreux algorithmes de correction d'artéfacts basés sur les CCD ont été proposés. Généralement, tous les algorithmes de réduction d'artéfacts basés sur les CCD sont construits sur la minimisation d'une fonction de coût dérivée des CCD. Cette fonction de coût prend généralement la forme d'une différence des moindres carrés moyennée sur toutes les CCD possibles dans l'acquisition.

Les CCD ont été utilisées afin de corriger les artéfacts liés au durcissement de faisceau [Tang et al., 2011, Mou et al., 2008, Abdurahman et al., 2016, Wurfl et al., 2017, Abdurahman et al., 2018], pour calibrer des scanners TDM de manière automatique [Debbeler et al., 2013, Aichert et al., 2015, Lesaint et al., 2017], pour corriger les artéfacts de diffusion [Kim et al., 2015, Debbeler et al., 2013, Hoffmann et al., 2018] et pour compléter des projections à données manquantes [Kudo and Saito, 1991a, Huang, 2020, Chen and Leng, 2005, Tang et al., 2012].

Une des applications principales des CCD est la correction de mouvement rigide ou non-rigide. De nombreux papiers ont été publiés afin de compenser les mouvements rigides [Wei et al., 2006, Yu et al., 2006, Yu and Wang, 2007, Clackdoyle et al., 2014, Frysch and Rose, 2015, Bier et al., 2017, Preuhs et al., 2019] en utilisant les CCD. Les applications pour la correction et la détection de mouvements non-rigides se concentrent surtout sur les mouvements cardiaques et respiratoires [Leng et al., 2007, Unberath et al., 2017, Berger et al., 2017, Luo and Luo, 2018, Lian et al., 2020]. Dans ces papiers, les CCD sont appliquées à une trajectoire circulaire avec des projections à faisceau conique acquises sur un détecteur plan.

Ce bilan sur les CCD montre que peu de CCD ont été appliquées à une trajectoire hélicoïdale de la source et encore moins à des projections coniques acquises sur un détecteur cylindrique. Les prochaines parties de cette thèse se portent donc sur l'adaptation de CCD existantes à la géométrie hélicoïdale avec détecteur cylindrique afin de détecter le mouvement respiratoire en TDM hélicoïdale, en se concentrant principalement sur les acquisitions réalisées pour la planification de traitement des tumeurs pulmonaires et abdominales supérieures.

IV Conditions de cohérence des données en tomodensitométrie hélicoïdale

Le chapitre précédent a présenté les CCD existantes ainsi que leurs applications. La plupart des CCD s'appliquaient aux trajectoires linéaires ou circulaires des sources de rayons X, mais aucune directement à une trajectoire hélicoïdale.

L'objectif de ce chapitre est de développer des méthodes pour appliquer les CCD en TDM hélicoïdale. Les CCD de faisceau conique pour les sources sur un plan ne peuvent pas être appliquées à la géométrie hélicoïdale car elles nécessitent des projections non tronquées. En TDM hélicoïdale, les projections sont généralement tronquées axialement

en raison de la taille limitée du détecteur qui ne couvre pas la totalité de l'objet. En raison de cette particularité de la TDM hélicoïdale, connue sous le nom de problème d'objet long, nous ne pouvons utiliser que des CCD capables de gérer la troncature axiale. La FBDCC et les CCD basées sur l'équation de Grangeat peuvent s'appliquer aux projections tronquées axialement car elles ne nécessitent qu'une partie des projections à faisceau conique. Dans cette thèse, nous choisissons de travailler avec la FBDCC car il a été démontré qu'elle est plus robuste que les CCD basées sur l'équation de Grangeat en ce qui concerne la détection d'incohérences [Lesaint et al., 2018]. Ce choix est discuté à la fin de ce chapitre.

Nous proposons ici deux approches pour appliquer la FBDCC à la TDM hélicoïdale. Nous commençons par introduire la géométrie par paire de projections à faisceau conique en TDM hélicoïdale. Ensuite, nous détaillons les deux méthodes d'application de la FBDCC à une trajectoire hélicoïdale. Premièrement, nous appliquons la FBDCC en utilisant un rééchantillonnage. Deuxièmement, la FBDCC est directement exprimée dans les coordonnées du détecteur cylindrique. Les détails de mise en œuvre sont donnés et les deux méthodes sont validées par des simulations numériques et des données de fantômes mécaniques acquises sur un scanner clinique TDM.

IV.1 Géométrie par paire en TDM hélicoïdale

Le système de coordonnées de l'objet est noté $(\boldsymbol{e}_x, \boldsymbol{e}_y, \boldsymbol{e}_z)$. Considérons deux positions de source $\boldsymbol{s}_\lambda$ et $\boldsymbol{s}_{\lambda'}$ sur une trajectoire hélicoïdale et leurs projections à faisceau conique correspondantes g_λ et $g_{\lambda'}$. L'expression des projections à faisceau conique est donnée Section 1.3.2. La ligne reliant les deux positions de source, notée $\mathcal{B}_{\lambda,\lambda'}$, est appelée la *baseline*. Cette configuration est illustrée Figure 4.1. Cette géométrie par paire est le point de départ de l'application de la FBDCC en TDM hélicoïdale.

IV.2 CCD par paire de faisceaux coniques par rééchantillonnage

Cette méthode a été décrite dans [Levine et al., 2010] et appliquée à une trajectoire circulaire avec un détecteur plan dans [Lesaint et al., 2017]. Nous l'avons adaptée à la trajectoire hélicoïdale avec un détecteur cylindrique. Cette méthode consiste à rééchantillonner une paire de projections à faisceau conique sur un détecteur plan virtuel dont les lignes sont parallèles à la baseline. Le long de chacune des lignes du détecteur virtuel, une FBDCC peut être calculée en supposant que les projections ne sont pas tronquées le long des lignes du détecteur virtuel. Pour cela, nous considérons des paires de projections dont la baseline n'est pas parallèle à l'axe de l'hélice. Les projections pouvant être tronquées axialement, le rééchantillonnage des projections pour une paire dont la baseline est parallèle à l'axe de l'hélice engendrera des projections tronquées latéralement sur le détecteur virtuel. De ce fait, la méthode de rééchantillonnage ne peut s'appliquer à ces paires.

Pour appliquer cette méthode, nous considérons donc une paire de projections comme décrite Section 4.1 et nous supposons que la baseline et le FOV ne s'intersectent pas. Le rééchantillonnage des projections sur le détecteur virtuel se fait en trois étapes :

1. définir l'orientation du détecteur virtuel. Celle-ci est donnée par le repère virtuel $(\boldsymbol{q}_{\lambda,\lambda'}, \boldsymbol{r}_{\lambda,\lambda'}, \boldsymbol{l}_{\lambda,\lambda'})$ dont la matrice de rotation pour passer de ce repère au repère monde est donnée Equation 4.1. Ce repère est illustré Figure 4.2. Le détecteur virtuel est ensuite défini dans un plan de rétroprojection, noté Π_{BP}, donné par les axes $(\boldsymbol{q}_{\lambda,\lambda'}, \boldsymbol{r}_{\lambda,\lambda'})$, orthogonal à $\boldsymbol{l}_{\lambda,\lambda'}$ et passant par l'origine du repère monde $\boldsymbol{o} = (0, 0, 0)$.

2. définir les limites du détecteur virtuel. Pour cela, l'intersection de chaque faisceau conique avec le plan de rétroprojection est calculée avec l'Equation 4.2 dans le repère monde puis avec l'Equation 4.3 dans le repère virtuel, comme illustré Figure 4.4. Afin d'éviter toute troncature latérale des projections rééchantillonnées, les limites

du détecteur virtuel sont définies comme l'intervalle le plus large contenant les deux rétroprojections dans la direction de $\boldsymbol{q}_{\lambda,\lambda'}$ et l'intervalle le plus petit dans la direction de $\boldsymbol{r}_{\lambda,\lambda'}$. Ces deux intervalles sont donnés par les Equations 4.6 et 4.8. Le détecteur peut être enfin défini par les coordonnées de deux coins opposés dans le repère virtuel $(q_{\min}, r_{\min}, 0)$ et $(q_{\max}, r_{\max}, 0)$ comme illustré Figure 4.4.
Si nous autorisions les paires dont la baseline intersecte le FOV, les deux rayons correspondant à la direction de la baseline (l'un provenant de $\boldsymbol{s}_\lambda$ et l'autre de $\boldsymbol{s}_{\lambda'}$) seraient parallèles au plan de rétroprojection et ne se couperaient jamais. Pour de tels rayons, nous aurions $(\boldsymbol{s}_\lambda - \boldsymbol{p}_\lambda(\gamma, v)) \cdot \boldsymbol{l}_{\lambda,\lambda'} = 0$. Equation 4.2 n'étant pas défini, par conséquent, Equation 4.3 et le détecteur virtuel ne sont pas définis.

3. rétroprojeter les deux projections g_λ et $g_{\lambda'}$ sur le détecteur virtuel. Cela est fait en utilisant la cartographie inverse donnée Equation 4.11. Les projections rééchantillonnées sur le détecteur virtuel sont notées g^*_λ et $g^*_{\lambda'}$.

Le moment d'ordre zero calculé sur le détecteur est donné Equation 4.13 et sa discrétisation est donnée Equation 4.17. La mesure de cohérence d'une paire de projection est donnée Equation 4.20.

Comme indiqué dans les paragraphes précédents, la FBDCC ne peut pas s'appliquer à n'importe quelle paire de projections. La première condition est que la baseline et le FOV ne s'intersectent pas, sinon le détecteur ne peut être défini. Pour s'assurer qu'une paire de projections remplisse cette condition, il faut que la différence de l'angle qui caractérise leur position le long de la trajectoire satisfasse l'Equation 4.18 comme illustré Figure 4.7. La seconde condition est qu'il y ait suffisamment de recouvrement entre les deux projections autour du plan de rétroprojection. Pour cela, les limites selon l'axe $\boldsymbol{r}_{\lambda,\lambda'}$ du détecteur virtuel doivent satisfaire l'Equation 4.19 comme illustré Figure 4.4. Si cela n'est pas le cas, comme sur la Figure 4.8, le détecteur virtuel ne peut être défini.

IV.3 CCD par paire de faisceaux coniques sur détecteur cylindrique

Dans cette partie, les CCD sont appliquées à la trajectoire hélicoïdale en calculant les moments d'ordre zéro directement dans les coordonnées du détecteur cylindrique. Ce faisant, nous évitons le calcul du détecteur virtuel, ce qui permet le calcul de FBDCCs pour les paires dont la baseline intersecte le FOV, et augmentons le nombre de paires avec au moins une CCD en TDM hélicoïdale.

Nous considérons une paire de positions de source $(\boldsymbol{s}_\lambda, \boldsymbol{s}_{\lambda'})$ comme dans la Section 4.1. La FBDCC peut être calculée sur tout plan contenant les deux positions de la source. Comme la FBDCC s'applique à des projections non tronquées latéralement, le plan doit également couper les deux bords latéraux des deux projections pour éviter la troncature latérale (les projections à faisceau conique ne sont initialement pas tronquées dans la direction de γ). Ces plans contiennent tous la baseline de vecteur directeur $\boldsymbol{b}_{\lambda,\lambda'}$ et sont définis par un angle β qu'ils forment avec le plan de reference $\Pi_{\lambda,\lambda'}$. Pour chaque plan, on peut définir un nouveau repère $(\boldsymbol{c}_{\boldsymbol{\tau}}, \boldsymbol{b}_{\lambda,\lambda'}, \boldsymbol{n}_{\boldsymbol{\tau}})$, où $\boldsymbol{\tau} = (\lambda, \lambda', \beta)$ caractérise un plan. Comme précédemment, nous considérons uniquement les paires pour lesquelles la baseline n'est pas parallèle à l'axe de l'hélice afin d'éviter d'avoir des projections tronquées le long de l'intersection entre les différents plans et les deux projections à faisceau conique. En effet, l'intersection d'un plan $\Pi_{\boldsymbol{\tau}}$ avec les deux projections définit deux projections à faisceau en éventail pour lesquelles une FBDCC peut être calculée (voir Figure 4.10). L'intersection d'un plan $\Pi_{\boldsymbol{\tau}}$ et de la projection g_λ est notée $v_{\boldsymbol{\tau}}$ et est donnée par l'Equation 4.31. Après un changement de variable de la coordonnée 1D ϕ de la projection à faisceau en éventail (définie Figure 4.11) aux coordonnées 2D $(\gamma, v_{\boldsymbol{\tau}}(\gamma))$ de la projection à faisceau conique, l'expression du moment dans les coordonnées du détecteur cylindrique $(\gamma, v_{\boldsymbol{\tau}}(\gamma))$ est donnée Equation 4.53.

La variable $\gamma^s_{\lambda,\lambda'}$ est une singularité et correspond géométriquement à la coordonnée angulaire à laquelle la baseline peut intersecter le détecteur. Si la baseline et le FOV ne s'intersectent pas, la singularité est en dehors des bornes d'intégration. Ainsi, la discrétisation du moment peut se faire avec la règle des trapèzes donnée Equation 4.56. Si la baseline et le FOV s'intersectent, la singularité est dans l'intervalle d'intégration et il faut la gérer. Pour gérer cette singularité lors du calcul numérique des moments d'ordre zéro, nous utilisons deux méthodes:

1. la première consiste à estimer l'intégrale autour de la singularité en utilisant une approximation du premier ordre dans un intervalle symétrique autour de la singularité, comme montré par [King, 2009, chapitre 14] et illustré Figure 4.12. La valeur de l'intégrale sur cette intervalle est donnée Equation 4.58. L'estimation de l'intégrale sur les intervalles restants se fait avec la règle des trapèzes comme ils ne contiennent pas de singularité.

2. la seconde consiste à reformuler le moment en utilisant un noyau de Hilbert (voir Equation 4.62). La discrétisation du moment est alors assez simple (voir Equation 4.63) et la singularité est gérée grâce à la discrétisation d'une version limitée en bande du noyau de Hilbert : une obtenue par un fenêtrage rectangulaire Equation 4.64, l'autre par un fenêtrage de Hann Equation 4.65.

En traitant la singularité, le calcul de la FBDCC dans le détecteur physique supprime la condition de FOV de la méthode de rééchantillonnage. Le principal avantage de cette approche directe est de considérer les paires dont la baseline peut couper le FOV. Par conséquent, la validité de la FBDCC ne dépend que de la présence de projections à faisceau en éventail non tronquées. Comme les projections peuvent être tronquées dans la direction axiale, les CCD ne sont applicables que pour certaines paires de positions de source (c'est-à-dire certains $\lambda - \lambda'$) et certains plans (c'est-à-dire certains β) pour lesquels les courbes du détecteur $\mathcal{C}_{\boldsymbol{\tau}}$ et $\mathcal{C}_{\boldsymbol{\tau}'}$ (Figure 4.10) sont comprises entre les limites inférieure et supérieure du détecteur. On peut donc en déduire des conditions sur la distance angulaire séparant deux positions de sources si la singularité est dans l'intervalle d'intégration (Equation 4.68) et sur β si la singularité est en dehors de l'intervalle d'intégration (Equation 4.69).

Pour une paire de projections à faisceau conique, supposant que la condition sur l'angle β donnée Equation 4.72 est vérifiée pour les deux positions de source, on peut définir $B = \lfloor 2\beta_{\max} D/\Delta_v \rfloor$ plans sur lesquels une FBDCC peut être calculée. La mesure de cohérence pour la paire correspondante est donnée Equation 4.73.

IV.4 Validation numérique

Afin de valider les CCD proposées, nous avons calculé les moments et les mesures de cohérence pour différentes paires de projections issues de simulations numériques (non bruitées et bruitées) de l'acquisition du fantôme de thorax avec la géométrie du Somatom go.Sim et de l'acquisition réelle d'un fantôme mécanique réalisé avec le scanner Somatom go.Sim (voir Figure 4.13). Pour la simulation et l'acquisition, les fantômes étaient statiques. La simulation a été réalisée avec le logiciel RTK [Rit et al., 2013].

Les moments ont été calculés avec la méthode de rééchantillonnage et la méthode directe, en utilisant les trois méthodes d'intégration présentées.

Les résultats montrent que pour une paire dont la baseline ne coupe pas le FOV, les deux approches donnent des résultats similaires : mêmes valeurs de moments (voir Figures 4.14 et 4.20) et erreurs similaires (voir Table 4.1a première ligne, première colonne et Table 4.1b première ligne, première colonne). L'approche directe offre plus de plans sur lesquels une FBDCC peut être calculée que de lignes sur le détecteur virtuel pour l'approche de rééchantillonnage en raison du choix d'échantillonnage que nous avons fait

pour les deux approches. Le nombre de plans pour l'approche directe aurait été plus petit si nous avions choisi un échantillonnage équi-espacé le long d'un certain axe plutôt qu'un échantillonnage équi-angulaire. Les deux approches sont robustes au bruit et donnent des résultats similaires en termes de valeurs de moments (voir les Figures 4.23 et 4.25, et Figures 4.28 et 4.30) et des erreurs de l'ordre de 5% (voir Table 4.1a première ligne, deuxième et troisième colonnes, et Table 4.1b première ligne, deuxième et troisième colonnes).

L'avantage majeur du calcul de la FBDCC dans les coordonnées cylindriques du détecteur concerne l'applicabilité de la CCD. En effet, il permet de considérer les paires dont la baseline intersecte le FOV contrairement à l'approche de rééchantillonnage sur un plan virtuel (Section 4.2, [Lesaint et al., 2017]). Ceci est particulièrement utile, notamment en TDM hélicoïdale où le nombre de paires éligibles à une CCD est limité en raison de la taille axiale restreinte du détecteur.

Pour l'approche directe, les trois méthodes d'intégration sont équivalentes pour les paires dont la baseline ne coupe pas le FOV et qui sont issues d'acquisitions sans bruit (voir les figures 4.20 et Table 4.1b première ligne, première colonne) et avec bruit (voir figures 4.25 et 4.30 et Table 4.1b première ligne, deuxième et troisième colonnes). Cependant, la stabilité numérique des trois méthodes d'intégration varie fortement lorsque le point de singularité est situé dans la projection, et lorsque les projections sont corrompues par du bruit.

Dans le cas de données non bruitées, deux cas se présentent en fonction de l'emplacement du point de singularité.

• Si le point de singularité est situé dans une région spatialement lisse des deux projections (voir Figure 4.21 et Table 4.1b deuxième ligne, première colonne), les trois méthodes d'intégration sont validées par les faibles valeurs des erreurs. Cependant, les valeurs des moments diffèrent entre l'intégration avec le noyau de Hilbert et l'intégration avec l'approximation du premier ordre en raison des valeurs des noyaux comme le montre la Figure 4.32. Elles sont plus élevées autour du point de singularité pour l'approximation du premier ordre que pour les noyaux de Hilbert.

• Si le point de singularité est situé à proximité de gradients spatiaux abrupts de l'une des deux projections (voir Figure 4.22 et Table 4.1b troisième ligne, première colonne), des erreurs élevées sont obtenues avec les trois méthodes d'intégration. Dans cette situation, l'échantillonnage induit des erreurs d'interpolation, accentuées par les noyaux d'intégration, rendant les projections incohérentes. Avec un échantillonnage dix fois plus fin, les erreurs d'interpolation sont réduites, les moments sont plus proches et les erreurs plus petites pour les trois méthodes d'intégration comme l'illustre la Figure 4.33.

Dans la Figure 4.22, nous observons que h_1^{Rect} est plus stable que $h_{0.2}^{\text{Hann}}$ en ce qui concerne l'emplacement de la singularité et que les valeurs des moments sont plus élevées avec le noyau de Hann qu'avec le noyau rectangulaire. Les deux sont liés à la largeur du noyau. En effet, le calcul des moments avec le noyau $h_{0.2}^{\text{Rect}}$ donne des valeurs de moments similaires et une erreur similaire ($E_{\lambda,\lambda'}^{Real} = 8.92\%$) à celles données par le calcul des moments avec $h_{0.2}^{\text{Hann}}$ (voir Figure 4.34). Les valeurs de projection autour de la singularité sont plus lissées avec un paramètre $\nu = 0.2$ que $\nu = 1$. Par conséquent, les erreurs d'interpolation autour du gradient abrupt sont accumulées, ce qui diminue la stabilité numérique de la méthode d'intégration.

Dans le cas de données bruitées, les FBDCCs sont impactées par le bruit pour les trois méthodes d'intégration, quel que soit l'emplacement du point de singularité dans les projections (voir Figure 4.31 et Table 4.1b dernière ligne, dernière colonne). L'intégration avec une approximation du premier ordre est la moins stable (voir Figure 4.31 figure de droite). Cette instabilité provient de l'échantillon ajouté qui est mal interpolé en présence de bruit. La valeur incorrecte est accentuée par le noyau d'intégration et induit de fortes incohérences. Nous avons étudié d'autres implémentations de l'approximation du premier

ordre comme l'ajout d'un échantillon symétrique par rapport au deuxième échantillon le plus proche de la singularité (au lieu de l'échantillon le plus proche) ou l'évaluation de l'intégrale sans la contribution symétrique autour de la singularité. Cependant, aucune de ces méthodes n'a donné de résultats satisfaisants. En ce qui concerne les intégrations du noyau de Hilbert, le noyau à fenêtre rectangulaire est moins stable que le noyau à fenêtre de Hann. Cette variation de la stabilité numérique s'explique par la forme du noyau à fenêtre de Hann qui supprime plus de hautes fréquences, c'est-à-dire de bruit, que la fenêtre rectangulaire, ce qui rend l'intégration à fenêtre de Hann plus robuste vis-à-vis du bruit.

Avec ces observations, un compromis doit être fait entre la stabilité numérique concernant la localisation du point de singularité et la robustesse au bruit. Sur les figures 4.26 et 4.31, on constate que le bruit a un impact plus important sur les CCD que l'emplacement du point de singularité dans les projections. En conséquence, l'intégration numérique des moments sera effectuée avec le noyau de Hilbert à bande limitée par une fenêtre de Hann dans la suite de la thèse.

Nous avons mentionné dans l'introduction que l'utilisation des CCD basées sur l'équation de Grangeat pourrait être une option, d'autant plus que la fonction intermédiaire impliquée dans ces CCD n'a pas de singularité. Il a été prouvé que si les projections vérifient la FBDCC (voir Equation 4.29), elles vérifieront également les CCD basées sur l'équation de Grangeat [Lesaint, 2018]. Cependant, la proposition réciproque est fausse comme le montre [Lesaint et al., 2018]. Les auteurs ont montré que des projections tronquées peuvent vérifier les CCD basées sur l'équation de Grangeat mais pas la FBDCC en ajoutant un certain décalage constant aux valeurs de projection. Cela explique notre choix de travailler avec la FBDCC. La robustesse des différentes CCD par paire à la discrétisation et au bruit pourrait être différente puisque la FBDCC utilisée dans ce travail a une singularité alors que les CCD de Grangeat nécessitent le calcul d'une dérivée (qui est également connue pour être sensible au bruit).

IV.5 Conclusion

Dans ce chapitre, nous avons développé et analysé deux approches pour appliquer la FBDCC à la TDM hélicoïdale. La première approche consiste à rééchantillonner les projections à faisceau conique sur un détecteur virtuel et à appliquer la FBDCC le long de chaque ligne du détecteur virtuel. Cette approche est robuste au bruit, mais ne s'applique qu'aux paires de projections dont la baseline ne croise pas le FOV. La deuxième approche calcule la FBDCC directement dans les coordonnées cylindriques du détecteur et permet de calculer la FBDCC pour ces paires. La singularité dans le calcul du moment est traitée en utilisant une approximation du premier ordre de l'intégrande ou en limitant en bande le noyau de Hilbert. L'intégration de Hilbert avec un fenêtrage de Hann est plus robuste que l'approximation de premier ordre en ce qui concerne le bruit et les erreurs d'échantillonnage. Si la baseline de la paire et les FOV ne se croisent pas, les CCD sont aussi stables et robustes que dans l'approche de rééchantillonnage. Lorsqu'ils le font, même sans bruit, le noyau de Hilbert h_ν amplifie fortement l'erreur de discrétisation, avec les deux fenêtrages, ce qui entraîne des incohérences. Cela rend la FBDCC sensible au bruit.

V Détection de mouvement locale en tomodensitométrie hélicoïdale par l'utilisation des conditions de cohérence des données

En TDM conventionnelle, le patient est supposé statique pendant l'acquisition. Dans le cas de la TDM 4D, le mouvement résultant de la respiration du patient est supposé cyclique. Dans les deux cas, un mouvement irrégulier crée des incohérences dans les projections, ce qui entraîne des artéfacts sur les images tomographiques.

Dans ce chapitre, nous étudions la capacité des CCD par paire de faisceaux coniques, présentées au chapitre 4, à détecter le mouvement en TDM hélicoïdale. Dans le chapitre précédent, nous avons montré que les deux approches donnent des résultats presque identiques pour les paires dont la baseline n'intersecte pas le FOV. De plus, le calcul de la FBDCC dans les coordonnées du détecteur permet de considérer les paires dont la baseline intersecte le FOV. Pour maximiser le nombre de paires possibles, nous nous concentrons ici sur l'approche qui calcule la FBDCC dans les coordonnées du détecteur. Nous avons mis en évidence que la FBDCC est très sensible au bruit et aux erreurs d'échantillonnage pour les paires dont la baseline intersecte le FOV. Nous proposons donc une mesure prenant en compte le bruit et impliquant la variance des moments d'ordre zéro résultant du bruit dans les projections.

V.1 Matériels et méthodes

Le bruit des projections provient des fluctuations du nombre de photons mesuré. Ces variations peuvent être décrites statistiquement par une loi de Poisson [Kak and Slaney, 1988, chapter 5]. En supposant que ces variations sont plus faibles que le nombre moyen de photons attendu, il est possible d'obtenir une estimation des variations de la valeur des pixels des projections en fonction du nombre moyen de photons mesuré dans ce pixel (Equation 5.6).

Comme précédemment, les CCD sont appliquées à des paires de projections à faisceaux coniques tant qu'elles vérifient les conditions d'applicabilité présentées Section 4.3.4. Pour mesurer la cohérence de deux projections, nous définissons à l'Equation 5.12 l'erreur correspondant à la moyenne de la différence absolue des moments d'ordre zéro calculés sur les plans possibles de la paire, normalisée par une approximation de la variance correspondante (donc par une approximation du bruit). La variance de la moyenne de la différence absolue des moments est approximée par celle de la moyenne de la différence des moments. La variance de la moyenne de la différence des moments correspond à la somme des variances des moments moyens pour chaque projection et nous l'avons exprimée en fonction de la variance des pixels des projections Equation 5.15. L'expression théorique de cette variance a été vérifiée à l'aide d'une approche statistique (Section 5.4.1.1) sur données simulées.

Nous avons ensuite utilisé notre mesure de cohérence pour détecter le mouvement, sur données simulées avec le logiciel RTK, et réelles acquises avec le scanner Somatom go.Sim en sélectionnant une projection de référence calculant toutes les paires possibles avec cette référence et la mesure de cohérence correspondante pour chacune des paires.

V.2 Résultats et discussion

Dans la première partie de ce chapitre, nous avons proposé une formule théorique permettant d'approximer l'écart-type des CCD par paires de faisceaux coniques en TDM hélicoïdale et l'avons validée par des simulations et une approche statistique. La formule résultante explique la variabilité observée des CCD en fonction de la distance angulaire entre les positions de source : les paires séparées de 90° sont plus impactées par le bruit à cause de la forme elliptique du fantôme qui atténue beaucoup les photons pour les projec-

tions visualisant le fantôme latéralement ; les paires séparées de 180° sont celles les plus impactées par le bruit à cause de l'intersection entre le FOV et la baseline.

Dans une deuxième partie, une mesure prenant en compte le bruit a été définie avec l'approximation de l'écart-type et appliquée à un problème de détection de mouvement en TDM hélicoïdale. Nos résultats sur données simulées et réelles indiquent que les CCD peuvent identifier le mouvement respiratoire ainsi que la respiration irrégulière sur un scanner TDM clinique. Le mouvement est détecté lorsque la baseline n'intersecte pas le FOV mais la sensibilité au bruit peut l'en empêcher dans le cas contraire. Pour les paires dont la baseline ne coupe pas le FOV, l'incohérence mesurée par le numérateur de l'Equation 5.12 est principalement due au mouvement et l'incohérence due au bruit peut être considérée comme plus petite. Pour les paires dont la baseline intersecte le FOV, le numérateur de l'Equation 5.12 mesure les deux incohérences, dues au bruit et au mouvement, mais l'incohérence due au bruit peut peser plus lourd que l'incohérence due au mouvement. La normalisation par une estimation du bruit amène la valeur de la mesure de cohérence de ces paires autour de 0.8, qui est la valeur attendue de la mesure de cohérence pour les projections bruitées d'un objet statique (voir Section 5.4.1.2). Si l'incohérence du mouvement est importante, la mesure de cohérence de ces paires devrait être supérieure à 0.8 (voir Figure 5.8 autour de $|\lambda - \lambda'| = 28\pi$ par exemple). La sensibilité au bruit peut être réduite pour ces paires avec un simple filtre passe-bas comme une moyenne glissante (voir les figures 5.7, 5.8, 5.9, 5.10, 5.11 et 5.12). La mesure de cohérence proposée normalise l'incohérence par une estimation du niveau de bruit pour donner plus de poids dans la moyenne glissante aux paires où l'incohérence du mouvement domine l'incohérence du bruit. La prise en compte de toutes les paires, et pas seulement de celles dont la baseline ne coupe pas le FOV, augmente l'ensemble des CCD dans une acquisition hélicoïdale. Ceci est particulièrement utile pour l'identification d'incohérences locales, comme une projection vide dans la séquence ou un mouvement rapide. L'élimination des paires dont la baseline intersecte le FOV pourrait empêcher la détection de tels problèmes.

Une contribution importante de ce travail est la mesure de cohérence qui inclut les variations des moments dues au bruit. La littérature (voir Section 3.4.2) concernant l'impact du bruit sur les CCD est rare. Lorsque cela a été mentionné, la robustesse par rapport au bruit était obtenue par la grande quantité de paires redondantes auxquelles les CCD sont appliquées. Cependant, en TDM hélicoïdale, le nombre de paires redondantes est limité en raison du déplacement axial de la table, ce qui limite la robustesse de ces mesures. La dérivation de la variance des moments offre un moyen de prendre en compte le bruit en TDM hélicoïdale et fournit des informations concernant l'impact du bruit sur les CCD.

V.3 Conclusion

Dans ce chapitre, nous avons démontré la capacité des CCD à détecter le mouvement directement (pour les paires dont la baseline ne coupe pas le FOV) ou indirectement à l'aide d'un filtre passe-bas (en considérant toutes les paires) en utilisant une mesure de cohérence prenant en compte le bruit. Cela augmente le nombre de CCD disponibles dans une acquisition hélicoïdale. Cependant, la détection de mouvement présentée dans ce chapitre n'est que *locale*, c'est-à-dire par rapport à une projection de référence fixe. En raison de la troncature axiale des projections inhérente à une acquisition hélicoïdale, les CCD ne peuvent pas être calculées entre toutes les projections et il est nécessaire de connecter les projections entre elles pour évaluer la présence de mouvement pendant toute une acquisition hélicoïdale.

VI Détection de mouvement globale en tomodensitométrie hélicoïdale par l'utilisation des conditions de cohérence des données

La capacité des CCD par paires de faisceaux coniques à détecter le mouvement a été vérifiée au chapitre 5. Cependant, cette détection n'était que locale, c'est-à-dire entre une projection de référence fixe et un nombre limité d'autres projections avec lesquelles une CCD pouvait être calculée (voir Section 4.3.4). Pour vérifier la cohérence d'une projection avec les autres projections de l'acquisition, il est nécessaire de connecter les paires de projections entre celles pour lesquelles aucune FBDCC ne peut être calculée.

Dans ce chapitre, nous présentons deux méthodes pour estimer le mouvement en TDM hélicoïdale. Pour la première méthode, nous construisons un graphe qui interconnecte toutes les projections et qui fournit une mesure de cohérence entre toute paire de projections dans une acquisition hélicoïdale. La seconde méthode étend la méthode de détection locale du chapitre précédent à l'ensemble de l'acquisition afin d'extraire le signal respiratoire des projections.

VI.1 Détection de mouvement en TDM hélicoïdale par une approche de graphe

Dans cette partie, nous considérons uniquement les paires pour lesquelles la baseline et le FOV ne se coupent pas et pour lesquelles il est possible de calculer au moins une FBDCC (voir Figure 6.1). Les paires pour lesquelles la baseline et le FOV se coupent sont trop sensibles au bruit pour être utilisées ici.

En raison du déplacement axial de la table, le nombre de paires éligibles pour au moins une FBDCC est limité. De plus, la condition de FOV et le besoin de données communes (voir Section 4.2.4.1 et Section 4.3.4) empêchent le calcul des CCD entre de nombreuses paires de projections. Il est donc nécessaire d'interconnecter les projections afin de mesurer leur cohérence.

L'approche de graphe consiste à construire un graphe où les sommets sont les projections et où deux sommets sont connectés s'il existe au moins une FBDCC entre les projections correspondantes. Chaque arête du graphe est pondérée par la mesure de cohérence (Equation 5.12) resultant du calcul des CCD entre les deux sommets correspondants. Si deux projections sont directement connectées et cohérentes, alors la valeur du poids sur l'arête les connectant est supposée être autour de zéro. Si deux projections ne sont pas directement connectées, mais qu'il est possible de partir de l'une et de rejoindre l'autre par l'intermédiaire d'une autre projection, c'est-à-dire en passant par un autre sommet, et que chacune des projections est cohérente avec la projection intérmédiaire, alors la somme des poids le long des arêtes traversées doit également être autour de zéro. Ainsi, pour identifier les projections cohérentes et incohérentes, nous proposons d'utiliser le chemin le plus court entre deux sommets comme mesure de la cohérence entre les deux projections correspondantes. Le chemin le plus court entre deux sommets est le chemin le long duquel la somme des CCD est plus petite que le long de tout autre chemin possible entre les deux sommets. Il est calculé avec l'algorithme de Dijkstra [Dijkstra, 1959]. Si le chemin le plus court est nul, alors toutes les projections le long du chemin sont cohérentes. Si le chemin le plus court n'est pas égal à zéro, alors il n'existe pas de chemin entre les deux projections avec toutes les projections cohérentes le long de ce chemin.

L'approche de graphe interconnecte les projections dans une acquisition hélicoïdale et fournit une mesure de cohérence entre une projection de référence et toutes les autres projections de l'acquisition.

Nous avons testé cette approche sur des acquisitions conventionnelles et 4D hélicoïdales

où elle a permis l'identification de projections cohérentes avec n'importe quelle projection de référence dans des données simulées et réelles pour lesquelles la somme des CCD devrait être nulle (Figures 6.5, 6.6, et 6.7), ou plus petite que les valeurs inférieures moyennes des autres mesures (figures 6.8 et 6.9, tracés du bas).

Elle donne également une estimation du mouvement pendant une acquisition entière : des mouvements respiratoires réguliers (voir figures 6.9 et 6.10) ou irréguliers (voir Figure 6.8) ont été mis en évidence sur les TDM 4D.

Le calcul direct du chemin le plus court et la sommation des CCD le long de celui-ci a permis l'identification de projections cohérentes avec une référence choisie. Cependant, cela induit une dérive au fur et à mesure que la longueur du chemin le plus court augmente, empêchant l'identification des projections cohérentes qui ne sont pas directement connectées à la référence. Cette dérive est causée par le bruit dans les projections qui s'accumule au fur et à mesure que des sommets sont ajoutés au chemin le plus court. Pour compenser la dérive, nous normalisons la somme des CCD par la longueur du chemin le plus court. Cette normalisation corrige la dérive, mais peut détériorer la forme de la trace respiratoire (Figures 6.7, 6.8, 6.9 et 6.10) ou même les résultats de cohérence (voir Figures 6.8, 6.9).

La valeur minimale des mesures normalisées, environ 0.5 (Figures 6.5, 6.6, 6.7, 6.8, 6.9 et 6.10), diffère de 0.8 qui était la valeur attendue de la mesure de cohérence (voir Section 5.4.1.2) pour des données bruitées acquises pour un objet statique. Les projections directement connectées et cohérentes avec la référence ont des mesures autour de cette valeur attendue (voir Figures 6.5, 6.6). L'algorithme de Dijkstra calcule le chemin le plus court en minimisant la somme des CCD le long des arêtes traversées. Ainsi, il sélectionnera les arêtes dont le poids peut être inférieur à 0.8. Dans la Figure 5.6, la plus petite valeur des erreurs (pour les paires dont la baseline n'intersecte pas le FOV) correspond à 0.5, ce qui est la valeur que nous observons ici.

L'approche par graphe est limitée par l'applicabilité de la FBDCC. Si la plage d'applicabilité des CCD n'est pas assez grande pour atteindre la projection cohérente suivante, le chemin le plus court ne peut pas éviter les projections incohérentes intermédiaires et il n'est pas possible d'identifier les projections cohérentes (voir figures 6.5). Pour augmenter le nombre de CCD, une solution serait de considérer les paires dont la baseline intersecte le FOV. Cependant, l'utilisation directe de ces paires peut ne pas présenter un grand intérêt car leur mesure de cohérence est proche de zéro (en raison de la forte influence du bruit) et elles ne feraient qu'augmenter la longueur du chemin le plus court. Pour tirer parti de ces paires, l'inclusion de la mesure de cohérence filtrée par la moyenne glissante à l'approche de graphe peut être une solution (voir le chapitre 5), mais elle nécessiterait des recherches supplémentaires. Comme la moyenne glissante s'applique à un ensemble de paires provenant d'une référence, les mesures filtrées peuvent différer pour la paire (λ, λ') si l'on considère celles calculées à partir de λ ou celles calculées à partir de λ' car les valeurs des autres paires influencent la moyenne glissante.

VI.2 Extraction du signal respiratoire par l'utilisation des conditions de cohérence des données

Dans le chapitre précédent, nous avons sélectionné une projection de référence et calculé les CCD pour toutes les paires possibles. Pour chaque paire, la mesure de cohérence tenant compte du bruit (voir Equation 5.12) a été calculée et une moyenne glissante autour d'une rotation a été appliquée à chaque point avec une CCD pour supprimer la composante de bruit de la métrique de cohérence. L'objectif était d'obtenir des mesures de cohérence entre les projections, quelle que soit leur position dans le cycle respiratoire, d'où notre choix de travailler avec une mesure positive. Dans cette partie, nous souhaitons récupérer des informations concernant la phase respiratoire à laquelle les projections ont été acquises. Par conséquent, nous observons l'influence de la phase respiratoire sur une version signée

de la mesure de cohérence donnée Equation 6.4.

Pour analyser l'influence de la phase respiratoire sur la mesure de cohérence signée, nous sélectionnons trois projections de réference acquises quand le patient 1, présenté Section 5.3.3, était en fin d'inspiration, en fin d'expiration, et à une position intermédiaire du cycle respiratoire.

De même que la mesure positive, la mesure signée met en évidence les projections cohérentes et incohérentes en accord avec la phase estimée du signal respiratoire (ligne noire en pointillés sur les graphiques). En plus de l'information de cohérence, nous observons un lien entre le signe de la moyenne des mesures de cohérence et la position de la référence dans le cycle respiratoire. Lorsque la projection de référence est acquise à la fin de l'inspiration (Figure 6.11), la moyenne des mesures de cohérence est négative. Lorsque la projection de référence est acquise à la fin de l'expiration (Figure 6.12), la moyenne des mesures de cohérence est positive. Lorsque la projection de référence est acquise à une position intermédiaire du cycle respiratoire (Figure 6.11), la moyenne des mesures de cohérence est voisine de zéro.

De plus, en centrant la courbe de moyenne glissante autour de 0, c'est-à-dire en soustrayant la moyenne et en appliquant la moyenne glissante sur les mesures centrées, les trois courbes se superposent les unes sur les autres et une trace respiratoire est récupérée comme montré dans Figure 6.14. Après l'ajustement, les projections acquises autour de la fin de la respiration ont une valeur positive, les projections acquises autour de la fin de la respiration ont une valeur négative, et les projections acquises à une phase intermédiaire ont une valeur proche de zéro.

À partir de ces observations, nous pouvons extraire le signal respiratoire soit de la moyenne des mesures de cohérence, soit de la superposition des moyennes glissantes centrées selon l'Algorithme 1.

Les méthodes présentées pour extraire un signal respiratoire à partir de projections acquises lors d'une TDM hélicoïdale reposent sur le signe des mesures de cohérence qui varie en fonction de la position de la projection de référence dans le cycle respiratoire. Pendant l'inspiration, les poumons se remplissent d'air. Pendant l'expiration, les poumons se vident d'air. La projection est plus dense en fin d'expiration qu'en fin d'expiration, et donc les valeurs des projection augmentent entre les deux positions. En conséquence, les moments des projections acquises en fin d'inspiration sont plus petits que ceux des projections acquises pendant l'expiration et la mesure de cohérence est négative (voir Figure 6.11). Un raisonnement similaire peut être appliqué pour une projection de référence acquise en fin d'expiration ou à une position intermédiaire du cycle respiratoire. Par conséquent, il est possible d'extraire le signal respiratoire en utilisant la moyenne des métriques, ou en ajustant les courbes de moyenne glissante autour de zéro (voir figures 6.15, 6.17, 6.16 et 6.18). Cependant, ce raisonnement n'est évidemment pas parfait, il ne s'applique pas à l'abdomen, et n'est qu'une hypothèse pour expliquer les variations de la mesure signée, car certaines instabilités sont à noter (voir Figure 6.18, fin de l'acquisition).

Lorsque les valeurs moyennes ou les moyennes glissantes sont proches de zéro sur un certain intervalle (voir figures 6.15 et 6.17), elles indiquent seulement une période pendant laquelle le patient est statique. La notion de cohérence entre deux projections est perdue quelle que soit la méthode.

Le tracé des moyennes glissantes (figures 6.17 et 6.18) fournit plus d'informations que la courbe des mesures moyennes (figures 6.15 et 6.16). La mesure moyenne ne fournit des informations que pour les projections de référence (toutes les secondes de l'acquisition dans notre cas). En revanche, les moyennes glissantes fournissent des informations pour chaque projection ayant au moins une CCD et les variations des mesures de cohérence sont visibles en continu.

Enfin, cette section visait à décrire des observations expérimentales et ne constitue qu'un travail préliminaire. Des investigations supplémentaires sont nécessaires pour développer un algorithme robuste qui extrait rigoureusement le signal respiratoire directement des projections et l'utilise pour récupérer la phase de la respiration. En particulier, l'interprétation des courbes est basée sur la qualité des images TDM 4D, c'est-à-dire sur des connaissances préalables concernant l'objet acquis, ce qui limite l'utilisation des algorithmes actuels.

VI.3 Conclusion

Dans la première partie de ce chapitre, une méthode de détection de mouvement basée sur une approche de graphe qui utilise des CCD et connecte toutes les projections d'une trajectoire hélicoïdale a été présentée. Cette interconnexion fournit des mesures de cohérence entre une projection de référence et toutes les autres projections de l'acquisition. Elle a été testée sur des acquisitions TDM simulées et réelles avec des protocoles 3D et 4D. Elle a mis en évidence les projections cohérentes et incohérentes avec la référence choisie et a fourni une estimation du mouvement respiratoire pendant l'acquisition.

Dans la deuxième partie de ce chapitre, un algorithme préliminaire permettant d'extraire le signal respiratoire des projections a été présenté. Appliqué à des acquisitions 4D réelles, les signaux respiratoires extraits étaient en accord avec les images TDM 4D et ont fourni une estimation du mouvement respiratoire et de sa régularité pendant l'acquisition.

VII Conclusion

L'objectif de cette thèse était de détecter le mouvement en TDM hélicoïdale en utilisant des conditions de cohérence des données. L'application principale des algorithmes développés était la détection de mouvements irréguliers à partir d'acquisitions TDM 4D réalisées dans le cadre de la planification de la radiothérapie des cancers thoraciques et abdominaux supérieurs. Une respiration irrégulière induit des artéfacts sur les images TDM 4D dont la qualité impacte directement la qualité de la radiothérapie.

La première étape de cette thèse a été d'adapter des CCD existantes à la TDM hélicoïdale. Les CCD ont été principalement développées pour une trajectoire plane (trajectoire linéaire ou circulaire) avec un détecteur plan. En TDM hélicoïdale, la trajectoire est 3D et le détecteur est cylindrique. Cette spécificité nous a contraint à appliquer les CCD à des paires de projections à faisceau conique. La FBDCC stipule que pour deux positions de source sur une trajectoire linéaire, les moments des projections, c'est-à-dire l'intégrale des projections de faisceau en éventail pondérées par un cosinus, doivent être égaux si les projections sont cohérentes. En considérant une trajectoire linéaire virtuelle entre deux positions de sources, la FBDCC a été adaptée à la trajectoire hélicoïdale en utilisant deux approches.

La première approche rééchantillonne deux projections sur un détecteur virtuel dont les lignes sont parallèles à la trajectoire linéaire virtuelle. Chaque rangée du détecteur virtuel correspond à un faisceau en éventail dans la projection à faisceau conique et la FBDCC est appliquée le long de chaque ligne du détecteur virtuel. Pour effectuer l'approche de rééchantillonnage, l'intersection entre les deux faisceaux coniques et le plan de rétroprojection parallèle à la baseline doit être calculée pour définir le détecteur virtuel. Pour les paires dont la baseline coupe le FOV, la direction du rayon correspondant à la direction de la baseline est parallèle au plan de rétroprojection et ne le coupe jamais. La rétroprojection de ce rayon n'est pas définie ce qui empêche le calcul du détecteur virtuel tel que nous l'avons défini. Par conséquent, ces paires ne sont pas éligibles à l'approche de rééchantillonnage.

La deuxième approche calcule la FBDCC directement dans les coordonnées cylindriques du détecteur sur un ensemble de plans contenant les deux positions de source et coupant les deux bords latéraux des deux projections à faisceau conique. En effet, comme le calcul de la FBDCC nécessite l'évaluation de deux intégrales le long de la coordonnée angulaire du détecteur, les projections en éventail résultant de l'intersection d'un plan et les projections à faisceau conique ne doivent pas être tronquées latéralement. La différence entre les deux approches concerne leurs conditions d'applicabilité. L'approche de rééchantillonnage ne s'applique qu'aux paires de projections avec un recouvrement suffisant et dont la baseline ne coupe pas le FOV. L'approche directe supprime la condition du FOV en traitant numériquement une singularité qui survient au moment du calcul et ne nécessite donc qu'un recouvrement suffisant entre les deux projections. En calculant la FBDCC directement dans les coordonnées cylindriques du détecteur, le moment correspond dans ce cas au produit scalaire entre une projection en éventail pondérée et un noyau de Hilbert. L'intégration numérique est effectuée en limitant en bande le noyau de Hilbert avec une fenêtre de Hann pour traiter la singularité. Les deux approches ont été testées et validées sur des acquisitions simulées et réelles de fantômes statiques. Pour les paires dont la baseline ne coupe pas le FOV, les deux approches ont donné des résultats similaires et étaient robustes au bruit. Pour les paires dont la baseline coupe le FOV, seule l'approche directe pouvait être appliquée, et il a été montré que les CCD étaient sujettes à des erreurs d'échantillonnage et très sensibles au bruit.

La deuxième étape de ce travail a été de vérifier que la FBDCC adaptée à la trajectoire hélicoïdale pouvait détecter le mouvement. L'approche directe a été choisie pour maximiser le nombre de paires éligibles à une CCD. Une mesure de cohérence a été définie entre deux projections comme la moyenne des différences absolues des moments sur l'incertitude de la moyenne des différences des moments. L'avantage de cette mesure est qu'elle prend en compte les variations des moments dues au bruit dans les projections car nous avons montré que l'impact du bruit varie fortement avec la configuration géométrique d'une paire. L'incertitude des moments a été estimée en fonction du bruit des pixels de projection avec une approche similaire à celle utilisée pour la dérivation du bruit dans les images TDM reconstruites avec des algorithmes de reconstruction pour faisceau en éventail [Wunderlich and Noo, 2008], et vérifiées avec une approche statistique. La mesure de cohérence a été appliquée à des données simulées, des données du fantôme mécanique et de données patients acquises sur un scanner de diagnostic. La cohérence de toutes les paires éligibles calculées à partir d'une projection de référence a été évaluée avec la mesure de cohérence. La détection de mouvement était directement possible en ne considérant que les paires dont la baseline ne coupe pas le FOV mais pas les paires dont la baseline coupe le FOV car l'impact du bruit était trop important pour de telles paires. Pour les trois jeux de données, les mesures ont augmenté avec l'amplitude du mouvement. L'utilisation d'une moyenne glissante pour réduire la sensibilité au bruit pour les paires dont la baseline croise le FOV a permis d'identifier des projections cohérentes et incohérentes qui étaient en accord avec les phases du signal respiratoire pour le fantôme mécanique et les données du patient. La méthode a été appliquée à l'acquisition d'un patient pour lequel des artéfacts étaient présents dans la reconstruction 4D et les CCD ont mis en évidence que le patient ne respirait pas lorsque la région des artéfacts a été acquise.

Enfin, nous avons proposé deux méthodes pour estimer le mouvement pendant toute une acquisition hélicoïdale. La première méthode évalue la cohérence d'une projection de référence avec les autres projections d'une acquisition hélicoïdale même si aucune CCD ne peut être calculée directement. Tout d'abord, toutes les paires éligibles à une FBDCC ont été calculées et la mesure de cohérence, précédemment définie, calculée pour chaque paire. Deuxièmement, un graphe a été construit avec les projections comme sommets et une arête

entre deux sommets si une CCD peut être calculée entre la paire de projections correspondante. L'arête est ensuite pondérée par la mesure de cohérence de la paire correspondante. La cohérence entre une projection de référence et d'autres projections a été mesurée en calculant le chemin le plus court entre le sommet de référence et les autres sommets. Sur des données simulées et réelles, l'approche graphique a permis d'identifier des projections cohérentes avec la projection de référence choisie et a donné une estimation du mouvement lors de l'acquisition. Les mesures de cohérence ont été normalisées par le nombre de sommets le long du chemin pour compenser la dérive causée par l'incohérence accumulée due au bruit. Sur données simulées et réelles, les mesures normalisées ont détérioré l'estimation du mouvement. De plus, les informations de cohérence ont été perdues pour certaines données réelles. La deuxième méthode introduit un algorithme préliminaire permettant d'extraire le signal respiratoire des projections en utilisant une version signée de la mesure de cohérence. Un lien entre le signe de la mesure et les positions de fin d'inspiration/fin d'expiration auxquelles la projection de référence est acquise a été observé. Le signal respiratoire a été extrait en mesurant la moyenne des mesures de cohérence pour un ensemble de projections de référence régulièrement sélectionnées au cours de l'acquisition ou en réajustant leurs courbes de moyennes glissantes. Les deux méthodes ont été appliquées à des acquisitions TDM 4D réelles. Elles ont permis d'évaluer globalement la présence de mouvement pendant toute une TDM hélicoïdale et ont mis en évidence un mouvement irrégulier en accord avec les artéfacts observés sur les images TDM 4D reconstruites.

Appendix A: Scientific contributions

Conference papers

Mouchet, M., Rit, S., and Létang, J. (2020). Motion detection in helical CT using data consistency conditions. In *2020 IEEE Nucl. Sci. Symp. Med. Imag. Conf. (NSS/MIC)*, pages 1-3.

Mouchet, M., Rit, S., Lesaint, J., and Létang, J. (2022a). Variance of cone-beam pair-wise consistency conditions in helical CT. *To appear in 2022 IEEE Nucl. Sci. Symp. Med. Imag. Conf. (NSS/MIC)*.

Submitted article

Mouchet, M., Rit, S., Lesaint, J., and Létang, J. (2022). Cone-beam pair-wise data consistency conditions in helical CT. *Submitted paper*.

Bibliography

[Abdelnour et al., 2007] Abdelnour, A. F., Nehmeh, S. A., Pan, T., Humm, J. L., Vernon, P., Schöder, H., Rosenzweig, K. E., Mageras, G. S., Yorke, E., Larson, S. M., and Erdi, Y. E. (2007). Phase and amplitude binning for 4D-CT imaging. *Physics in Medicine and Biology*, 52(12):3515–3529.

[Abdurahman et al., 2016] Abdurahman, S., Frysch, R., Bismark, R., Friebe, M., and Rose, G. (2016). Calibration free beam hardening correction using grangeat-based consistency measure. In *2016 IEEE Nuclear Science Symposium and Medical Imaging Conference (NSS/MIC)*, pages 1–3.

[Abdurahman et al., 2018] Abdurahman, S., Frysch, R., Bismark, R., Melnik, S., Beuing, O., and Rose, G. (2018). Beam hardening correction using cone beam consistency conditions. *IEEE Transactions on Medical Imaging*, 37(10):2266–2277.

[Aichert et al., 2015] Aichert, A., Berger, M., Wang, J., Maass, N., Doerfler, A., and Maier, A. K. (2015). Epipolar consistency in transmission imaging. *IEEE Transactions on Medical Imaging*, 34(11):2205–2219.

[Berger et al., 2017] Berger, M., Xia, Y., Aichinger, W., Mentl, K., Unberath, M., Aichert, A., Riess, C., Hornegger, J., Fahrig, R., and Maier, A. (2017). Motion compensation for cone-beam CT using fourier consistency conditions. *Physics in Medicine & Biology*, 62(17):7181–7215.

[Bergner and Kachelriess, 2009] Bergner, F. and Kachelriess, M. (2009). 4D generalized thorax phantom. Technical report, Institute of Medical Physics (IMP), Friedrich-Alexander-University of Erlangen-Nürnberg. Available: http://www.imp.uni-erlangen.de/phantoms/thorax/4D_Thorax_Description.pdf.

[Beutel et al., 2000] Beutel, J., Kundel, H. L., and Van Metter, R. L., editors (2000). *Handbook of medical imaging: Volume 1. Physics and Psychophysics*.

[Bier et al., 2017] Bier, B., Aichert, A., Felsner, L., Unberath, M., Levenston, M., Gold, G., Fahrig, R., and Maier, A. (2017). Epipolar consistency conditions for motion correction in weight-bearing imaging. In Maier-Hein, geb. Fritzsche, K. H., Deserno, geb. Lehmann, T. M., Handels, H., and Tolxdorff, T., editors, *Bildverarbeitung für die Medizin 2017*, pages 209–214. Springer Berlin Heidelberg.

[Boykov et al., 2001] Boykov, Y., Veksler, O., and Zabih, R. (2001). Fast approximate energy minimization via graph cuts. *IEEE Transactions on Pattern Analysis and Machine Intelligence*, 23(11):1222–1239.

[Bushberg et al., 2011] Bushberg, J. T., Seibert, J. A., Leidholdt, E. M., and Boone, J. M. (2011). *The essential Physics of Medical Imaging, third tdition*. Lippincott Williams and Wilkins.

[Chen and Leng, 2005] Chen, G.-H. and Leng, S. (2005). A new data consistency condition for fan-beam projection data. *Medical Physics*, 32(4):961–967.

[Clackdoyle, 2013] Clackdoyle, R. (2013). Necessary and sufficient consistency conditions for fanbeam projections along a line. *IEEE Transactions on Nuclear Science*, 60(3):1560–1569.

[Clackdoyle and Desbat, 2013] Clackdoyle, R. and Desbat, L. (2013). Full data consistency conditions for cone-beam projections with sources on a plane. *Physics in Medicine and Biology*, 58(23):8437–8456.

[Clackdoyle and Desbat, 2015] Clackdoyle, R. and Desbat, L. (2015). Data consistency conditions for truncated fanbeam and parallel projections. *Medical Physics*, 42(2):831–845.

[Clackdoyle et al., 2016] Clackdoyle, R., Desbat, L., Lesaint, J., and Rit, S. (2016). Data consistency conditions for cone-beam projections on a circular trajectory. *IEEE Signal Processing Letters*, 23(12):1746–1750.

[Clackdoyle et al., 2014] Clackdoyle, R., Rit, S., Hoskovec, J., and Desbat, L. (2014). Fan-beam data consistency conditions for applications to motion detection. In *The third international conference on image formation in X-ray computed tomography*.

[Clements et al., 2013] Clements, N., Kron, T., Franich, R., Dunn, L., Roxby, P., Aarons, Y., Chesson, B., Siva, S., Duplan, D., and Ball, D. (2013). The effect of irregular breathing patterns on internal target volumes in four-dimensional CT and cone-beam ct images in the context of stereotactic lung radiotherapy. *Medical Physics*, 40(2):021904.

[Debbeler et al., 2013] Debbeler, C., Maass, N., Elter, M., Dennerlein, F., and Buzug, T. M. (2013). A new CT rawdata redundancy measure applied to automated misalignement correction. In *The 12th International Meeting on Fully Three-Dimensional Image Reconstruction in Radiology and Nuclear Medicine*, pages 264–267.

[Debbeler et al., 2019] Debbeler, C., Maass, N., Elter, M., Dennerlein, F., and Buzug, T. M. (2019). Scatter correction using pair-wise fan beam consistency conditions. In *The 15th International Meeting on Fully Three-Dimensional Image Reconstruction in Radiology and Nuclear Medicine*, pages 1–5.

[Dieterich et al., 2016] Dieterich, S., Ford, E., Pavord, D., and Zeng, J. (2016). *Practical Radiation Oncology Physics*, pages 252–263.

[Dijkstra, 1959] Dijkstra, E. (1959). A note on two problems in connexion with graphs. *Numerische Mathematik*, 1:269–271.

[Ehrhardt and Lorenz, 2013] Ehrhardt, J. and Lorenz, C., editors (2013). *4D modeling and estimation of respiratory motion for radiation therapy*. Spring.

[Ehrhardt et al., 2007] Ehrhardt, J., Werner, R., Säring, D., Frenzel, T., Lu, W., Low, D., and Handels, H. (2007). An optical flow based method for improved reconstruction of 4D CT data sets acquired during free breathing. *Medical physics*, 34:711–721.

[Feldkamp et al., 1984] Feldkamp, L. A., Davis, L. C., and Kress, J. W. (1984). Practical cone-beam algorithm. *Journal of the Optical Society of America A*, 1(6):612–619.

[Fitzpatrick et al., 2006] Fitzpatrick, M. J., Starkschall, G., Antolak, J. A., Fu, J., Shukla, H., Keall, P. J., Klahr, P., and Mohan, R. (2006). Displacement-based binning of time-dependent computed tomography image data sets. *Medical Physics*, 33(1):235–246.

[Ford et al., 2003] Ford, E., Mageras, G., Yorke, E., and Ling, C. (2003). Respiration-correlated spiral CT: A method of measuring respiratory-induced anatomic motion for radiation treatment planning. *Medical physics*, 30:88–97.

[Frysch and Rose, 2015] Frysch, R. and Rose, G. (2015). Rigid motion compensation in interventional c-arm ct using consistency measure on projection data. In Navab, N., Hornegger, J., Wells, W. M., and Frangi, A., editors, *Medical Image Computing and Computer-Assisted Intervention – MICCAI 2015*, pages 298–306. Springer International Publishing.

[George et al., 2006] George, R., Chung, T. D., Vedam, S. S., Ramakrishnan, V., Mohan, R., Weiss, E., and Keall, P. J. (2006). Audio-visual biofeedback for respiratory-gated radiotherapy: Impact of audio instruction and audio-visual biofeedback on respiratory-gated radiotherapy. *International Journal of Radiation Oncology*Biology*Physics*, 65(3):924–933.

[George et al., 2005] George, R., Vedam, S. S., Chung, T. D., Ramakrishnan, V., and Keall, P. J. (2005). The application of the sinusoidal model to lung cancer patient respiratory motion. *Medical Physics*, 32(9):2850–2861.

[Glide-Hurst et al., 2013] Glide-Hurst, C. K., Smith, M. S., Ajlouni, M., and Chetty, I. J. (2013). Evaluation of two synchronized external surrogates for 4D CT sorting. *Journal of Applied Clinical Medical Physics*, 14(6):117–132.

[Grangeat, 1991] Grangeat, P. (1991). *Mathematical framework of cone beam 3D reconstruction via the first derivative of the radon transform*, pages 66–97. Springer Berlin Heidelberg.

[Grangeat, 2002] Grangeat, P. (2002). *La tomographie*. Hermes Science.

[Han et al., 2011] Han, D., Bayouth, J., Bhatia, S., Sonka, M., and Wu, X. (2011). Characterization and identification of spatial artifacts during 4D-CT imaging. *Medical Physics*, 38(4):2074–2087.

[Helgason, 1965] Helgason, S. (1965). *The Radon transform on Euclidean spaces, compact two-point homogeneous spaces and Grassmann manifolds*. The Institute for Advanced Study, Princeton, N. J., USA.

[Hoffmann et al., 2018] Hoffmann, M., Würfl, T., Maass, N., Dennerlein, F., Aichert, A., and Maier, A. K. (2018). Empirical scatter correction using the epipolar consistency condition. In *Mathematics*.

[Huang, 2020] Huang, Y. (2020). *Consistency Conditions, Compressed Sensing and Machine Learning for Limited Angle Tomography*. PhD thesis, Friedrich-Alexander-University of Erlangen-Nürnberg.

[Hunjan et al., 2008] Hunjan, S., Starkschall, G., Rosen, I., Prado, K., Tolani, N., and Balter, P. (2008). Comparison of breath-hold and free-breathing positions of an external fiducial by analysis of respiratory traces. *Journal of Applied Clinical Medical Physics*, 9(3):34–42.

[Kachelrieß et al., 2004] Kachelrieß, M., Knaup, M., and Kalender, W. (2004). Extended parallel backprojection for standard three-dimensional and phase-correlated four-dimensional axial and spiral cone-beam CT with arbitrary pitch, arbitrary cone-angle, and 100 *Medical physics*, 31:1623–1641.

[Kak and Slaney, 1988] Kak, A. C. and Slaney, M. (1988). *Principles of Computerized Tomographic Imaging*. Society for Industrial and Applied Mathematics.

[Kalender, 1994] Kalender, W. A. (1994). Principles and applications of spiral CT. *Nuclear Medicine and Biology*, 21(5):693–699.

[Kalender et al., 1990a] Kalender, W. A., Seissler, W., Klotz, E., and Vock, P. (1990a). Spiral volumetric CT with single-breath-hold technique, continuous transport, and continuous scanner rotation. *Radiology*, 176(1):181–183.

[Kalender et al., 1990b] Kalender, W. A., Seissler, W., and Vock, P. (1990b). Single-breath-hold spiral volumetric CT by continuous patient translation and scanner rotation. *Radiology*, 176(1):181–183.

[Kallender, 2011] Kallender, W. A. (2011). *Computed Tomography: Fundamentals, System Technology, Image Quality, Applications, 3rd Edition*. Publicis.

[Katsevich, 2002] Katsevich, A. (2002). Analysis of an exact inversion algorithm for spiral cone-beam CT. *Physics in Medicine and Biology*, 47(15):2583–2597.

[Katsevich, 2004] Katsevich, A. (2004). An improved exact filtered backprojection algorithm for spiral computed tomography. *Advances in Applied Mathematics*, 32(4):681–697.

[Keall et al., 2006] Keall, P. J., Mageras, G. S., Balter, J. M., Emery, R. S., Forster, K. M., Jiang, S. B., Kapatoes, J. M., Low, D. A., Murphy, M. J., Murray, B. R., Ramsey, C. R., Van Herk, M. B., Vedam, S. S., Wong, J. W., and Yorke, E. (2006). The management of respiratory motion in radiation oncology report of AAPM Task Group 76. *Medical physics*, 33(10):3874—3900.

[Kim et al., 2015] Kim, C., Park, M., Sung, Y., Lee, J., Choi, J., and Cho, S. (2015). Data consistency-driven scatter kernel optimization for x-ray cone-beam CT. *Physics in medicine and biology*, 60(15):5971–5994.

[King, 2009] King, F. W. (2009). *Hilbert Transforms*, volume 1 of *Encyclopedia of Mathematics and its Applications*. Cambridge University Press.

[Kudo et al., 1998] Kudo, H., Noo, F., and Defrise, M. (1998). Cone-beam filtered-backprojection algorithm for truncated helical data. *Physics in Medicine and Biology*, 43(10):2885–2909.

[Kudo et al., 2004] Kudo, H., Rodet, T., Noo, F., and Defrise, M. (2004). Exact and approximate algorithms for helical cone-beam CT. *Physics in Medicine and Biology*, 49(13):2913–2931.

[Kudo and Saito, 1991a] Kudo, H. and Saito, T. (1991a). Helical-scan computed tomography using cone-beam projections. In *1991 IEEE Nuclear Science Symposium and Medical Imaging Conference*, volume 3, pages 1958–1962.

[Kudo and Saito, 1991b] Kudo, H. and Saito, T. (1991b). Sinogram recovery with the method of convex projections for limited-data reconstruction in computed tomography. *Journal of The Optical Society of America A-optics Image Science and Vision*, 8(7):1148–1160.

[Leng et al., 2007] Leng, S., Nett, B., Speidel, M., and Chen, G.-H. (2007). Motion artifact reduction in fan-beam and cone-beam computed tomography via the fan-beam data consistency condition (FDCC). In Hsieh, J. and Flynn, M. J., editors, *Medical Imaging*

2007: Physics of Medical Imaging, volume 6510, page 65101W. International Society for Optics and Photonics, SPIE.

[Lesaint, 2018] Lesaint, J. (2018). *Data consistency conditions in X-ray transmission imaging and their application to the self-calibration problem.* PhD thesis, Université Grenoble Alpes.

[Lesaint et al., 2017] Lesaint, J., Rit, S., Clackdoyle, R., and Desbat, L. (2017). Calibration for circular cone-beam CT based on consistency conditions. *IEEE Transactions on Radiation and Plasma Medical Sciences*, 1(6):517–526.

[Lesaint et al., 2018] Lesaint, J., Rit, S., Clackdoyle, R., and Desbat, L. (2018). GCC and FBCC for linear tomosynthesis. *Fifth international conference on image formation in X-ray computed tomography*, pages 114–118.

[Levine et al., 2010] Levine, M. S., Sidky, E. Y., and Pan, X. (2010). Consistency conditions for cone-beam CT data acquired with a straight-line source trajectory. *Tsinghua Science & Technology*, 15(1):56–61.

[Li et al., 2012] Li, H., Noel, C., Garcia-Ramirez, J., Low, D., Bradley, J., Robinson, C., Mutic, S., and Parikh, P. (2012). Clinical evaluations of an amplitude-based binning algorithm for 4DCT reconstruction in radiation therapy. *Medical Physics*, 39(2):922–932.

[Li et al., 2006] Li, X. A., Stepaniak, C., and Gore, E. (2006). Technical and dosimetric aspects of respiratory gating using a pressure-sensor motion monitoring system. *Medical Physics*, 33(1):145–154.

[Lian et al., 2020] Lian, M. L., Li, Y., Gu, X., and Luo, S. (2020). A retrospective respiratory gating system based on epipolar consistency conditions. *Molecular & Cellular Biomechanics*, 17(1):48–49.

[Lu et al., 2006] Lu, W., Parikh, P., Hubenschmidt, J., Bradley, J., and Low, D. (2006). A comparison between amplitude sorting and phase-angle sorting using external respiratory measurement for 4D CT. *Medical physics*, 33:2964–2974.

[Ludwig, 1966] Ludwig, D. (1966). The Radon transform on Euclidean space. *Communications on pure and applied mathematics*, 19:49–81.

[Luo and Luo, 2018] Luo, S. and Luo, S. (2018). An epipolar based algorithm for respiratory signal extraction of small animal CT. *Sensing and Imaging*, 19(4).

[Mory et al., 2016] Mory, C., Janssens, G., and Rit, S. (2016). Motion-aware temporal regularization for improved 4D cone-beam computed tomography. *Physicis in Medicine and Biology*, 61(18):6856–6877.

[Mou et al., 2008] Mou, X., Tang, S., Luo, T., Zhang, Y., and Yu, H. (2008). Beam hardening correction based on HL consistency in polychromatic transmission tomography. In Hsieh, J. and Samei, E., editors, *Medical Imaging 2008: Physics of Medical Imaging*, volume 6913, page 691333. International Society for Optics and Photonics, SPIE.

[Mouchet et al., 2022a] Mouchet, M., Létang, J., Lesaint, J., and Rit, S. (2022a). Variance of cone-beam pair-wise DCC. In *To appear in 2022 IEEE Nuclear Science Symposium and Medical Imaging Conference (NSS/MIC)*.

[Mouchet et al., 2022b] Mouchet, M., Létang, J., Lesaint, J., and S., R. (2022b). Cone-beam pair-wise DCC in helical CT. *Submitted paper*.

[Mouchet et al., 2020] Mouchet, M., Rit, S., and Létang, J. (2020). Motion detection in helical CT using data consistency conditions. In *2020 IEEE Nuclear Science Symposium and Medical Imaging Conference (NSS/MIC)*, pages 1–3.

[Negoro et al., 2001] Negoro, Y., Nagata, Y., Aoki, T., Mizowaki, T., Araki, N., Takayama, K., Kokubo, M., Yano, S., Koga, S., Sasai, K., Shibamoto, Y., and Hiraoka, M. (2001). The effectiveness of an immobilization device in conformal radiotherapy for lung tumor: reduction of respiratory tumor movement and evaluation of the daily setup accuracy. *International Journal of Radiation Oncology,Biology, Physics*, 50(4):889–898.

[Neicu et al., 2006] Neicu, T., Berbeco, R., Wolfgang, J., and Jiang, S. B. (2006). Synchronized moving aperture radiation therapy (SMART): improvement of breathing pattern reproducibility using respiratory coaching. *Physics in Medicine and Biology*, 51(3):617–636.

[Nguyen, 2021] Nguyen, M. H. (2021). *Data Consistency Conditions in 3D Tomography and Scanner Calibration using Analytic Approaches.* PhD thesis, Université Grenoble Alpes.

[Noo et al., 1999] Noo, F., Defrise, M., and Clackdoyle, R. (1999). Single-slice rebinning method for helical cone-beam CT. *Physics in Medicine and Biology*, 44(2):561–570.

[Noo et al., 2004] Noo, F., Pack, J., and Heuscher, D. (2004). Exact helical reconstruction using native cone-beam geometries. *Physics in Medicine and Biology*, 48(23):3787–818.

[Pan, 2005] Pan, T. (2005). Comparison of helical and cine acquisitions for 4D-CT imaging with multislice CT. *Medical physics*, 32:627–634.

[Preuhs et al., 2019] Preuhs, A., Manhart, M. T., Hoppe, E., Kowarschik, M., and Maier, A. K. (2019). Motion gradients for epipolar consistency. *15th International Meeting on Fully Three-Dimensional Image Reconstruction in Radiology and Nuclear Medicine.*

[Rietzel and Chen, 2006] Rietzel, E. and Chen, G. T. Y. (2006). Improving retrospective sorting of 4D computed tomography data. *Medical Physics*, 33(2):377–379.

[Rit et al., 2013] Rit, S., Vila Oliva, M., Brousmiche, S., Labarbe, R., Sarrut, D., and Sharp, G. (2013). The Reconstruction Toolkit (RTK), an open-source cone-beam CT reconstruction toolkit based on the Insight Toolkit (ITK). In *International Conference on the Use of Computers in Radiation Therapy (ICCR) 2013*, volume 489, page 012079.

[Schaller et al., 2000] Schaller, S., Noo, F., Sauer, F., Tam, K., Lauritsch, G., and Flohr, T. (2000). Exact radon rebinning algorithm for the long object problem in helical cone-beam CT. *IEEE Transactions on Medical Imaging*, 19(5):361–375.

[Schaller et al., 2001] Schaller, S., Stierstorfer, K., Bruder, H., Kachelrieß, M., and Flohr, T. (2001). Novel approximate approach for high-quality image reconstruction in helical cone-beam CT at arbitrary pitch. In Sonka, M. and Hanson, K. M., editors, *Medical Imaging 2001: Image Processing*, volume 4322, pages 113–127. International Society for Optics and Photonics, SPIE.

[Schreibmann et al., 2006] Schreibmann, E., Chen, G. T., and Xing, L. (2006). Image interpolation in 4D CT using a bspline deformable registration model. *International Journal of Radiation Oncology, Biology, Physics*, 64(5):1537–1550.

[Shih et al., 2004] Shih, H., Jiang, S., Aljarrah, K., Doppke, K., and Choi, N. (2004). Internal target volume determined with expansion margins beyond composite gross tumor volume in three-dimensional conformal radiotherapy for lung cancer. *International journal of radiation oncology, biology, physics*, 60(2):613–622.

[Stierstorfer et al., 2002] Stierstorfer, K., Flohr, T., and Bruder, H. (2002). Segmented multiple plane reconstruction: A novel approximate reconstruction scheme for multi-slice spiral CT. *Physics in Medicine and Biology*, 47(15):2571–2581.

[Stierstorfer et al., 2004] Stierstorfer, K., Rauscher, A., Boese, J., Bruder, H., Schaller, S., and Flohr, T. (2004). Weighted FBP - A simple approximated 3D FBP algorithm for multislice spiral CT with good dose usage for arbitrary pitch. *Physics in Medicine and Biology*, 49(11):2209–2218.

[Tam, 2000] Tam, K. C. (2000). Exact local regions-of-interest reconstruction in spiral cone-beam filtered-backprojection CT: theory. In Hanson, K. M., editor, *Medical Imaging 2000: Image Processing*, volume 3979, pages 506–519. International Society for Optics and Photonics, SPIE.

[Tam et al., 1998] Tam, K. C., Samarasekera, S., and Sauer, F. (1998). Exact cone beam CT with a spiral scan. *Physics in Medicine and Biology*, 43(4):1015–1024.

[Tang et al., 2011] Tang, S., Mou, X., Xu, Q., Zhang, Y., Bennett, J., and Yu, H. (2011). Data consistency condition-based beam-hardening correction. *Optical Engineering*, 50(7):076501.

[Tang et al., 2012] Tang, S., Xu, Q., Mou, X., and Tang, X. (2012). The mathematical equivalence of consistency conditions in the divergent-beam computed tomography. *Journal of X-ray science and technology*, 20(1):45–68.

[Tang et al., 2006] Tang, X., Hsieh, J., Nilsen, R., Dutta, S., Samsonov, D., and Hagiwara, A. (2006). A three-dimensional-weighted cone beam filtered backprojection (CB-FBP) algorithm for image reconstruction in volumetric CT - Helical scanning. *Physics in medicine and biology*, 51:855–74.

[Thomas et al., 2014] Thomas, D., Lamb, J., White, B., Jani, S., Gaudio, S., Lee, P., Ruan, D., McNitt-Gray, M., and Low, D. (2014). A novel fast helical 4D-CT acquisition technique to generate low-noise sorting artifact–free images at user-selected breathing phases. *International Journal of Radiation Oncology,Biology, Physics*, 89(1):191–198.

[Tikhonov, 1963] Tikhonov, A. N. (1963). Regularization of incorrectly posed problems. *Soviet Mathematics Doklady*, 4(6):1624–1627.

[Turbell and Danielsson, 1999] Turbell, H. and Danielsson, P. (1999). An improved PI-method for reconstruction from helical cone-beam projections. In *1999 IEEE Nuclear Science Symposium and Medical Imaging Conference*, volume 2, pages 865–868.

[Unberath et al., 2017] Unberath, M., Aichert, A., Achenbach, S., and Maier, A. (2017). Consistency-based respiratory motion estimation in rotational angiography. *Medical Physics*, 44(9):e113–e124.

[Van Gompel et al., 2006] Van Gompel, G., Defrise, M., and Dyck, D. (2006). Elliptical extrapolation of truncated 2D CT projections using Helgason-Ludwig consistency conditions. In Flynn, M. J. and Hsieh, J., editors, *Medical Imaging 2006: Physics of Medical Imaging*, volume 6142, page 61424B. International Society for Optics and Photonics, SPIE.

[Venkat et al., 2008] Venkat, R. B., Sawant, A., Suh, Y., George, R., and Keall, P. J. (2008). Development and preliminary evaluation of a prototype audiovisual biofeedback device incorporating a patient-specific guiding waveform. *Physics in Medicine and Biology*, 53(11):197–208.

[Vock et al., 1989] Vock, P., Jung, H., and Kalender, W. A. (1989). Single-breathhold spiral volumetric CT of the lung. In *75th anniversary scientific assembly and annual meeting of the Radiological Society of North America*.

[Vock et al., 1990] Vock, P., Soucek, M., Daepp, M., and Kalender, W. A. (1990). Lung: spiral volumetric CT with single-breath-hold technique. *Radiology*, 176(3):864–867.

[Wei et al., 2006] Wei, Y., Yu, H., and Wang, G. (2006). Integral invariants for computed tomography. *IEEE Signal Processing Letters*, 13(9):549–552.

[Welch et al., 1998] Welch, A., Campbell, C., Clackdoyle, R., Natterer, F., Hudson, M., Bromiley, A., Mikecz, P., Chillcot, F., Dodd, M., Hopwood, P., Craib, S., Gullberg, G., and Sharp, P. (1998). Attenuation correction in PET using consistency information. *IEEE Transactions on Nuclear Science*, 45(6):3134–3141.

[Werner et al., 2017] Werner, R., Hofmann, C., Muecke, E., and Gauer, T. (2017). Reduction of breathing irregularity-related motion artifacts in low-pitch spiral 4D CT by optimized projection binning. *Radiation Oncology*, 12(100):1–8.

[World Health Organization, 2022] World Health Organization (2022). Cancer. `https://www.who.int/news-room/fact-sheets/detail/cancer`. [Online; accessed 24-September-2022].

[Wunderlich and Noo, 2008] Wunderlich, A. and Noo, F. (2008). Image covariance and lesion detectability in direct fan-beam x-ray computed tomography. *Physicis in Medicine and Biology*, 53(10):2471–2493.

[Wurfl et al., 2017] Wurfl, T., Maass, N., Dennerlein, F., Huang, X., and Maier, A. (2017). Epipolar consistency guided beam hardening reduction-ECC^2. In *The 14th International Meeting on Fully Three-Dimensional Image Reconstruction in Radiology and Nuclear Medicine*.

[Yamamoto et al., 2008] Yamamoto, T., Langner, U., Loo, B., Shen, J., and Keall, P. (2008). Retrospective analysis of artifacts in four-dimensional CT images of 50 abdominal and thoracic radiotherapy patients. *International Journal of Radiation Oncology, Biology, Physics*, 72(4):1250–1258.

[Yan and Leahy, 1992] Yan, X. and Leahy, R. M. (1992). Cone beam tomography with circular, elliptical and spiral orbits. *Physics in Medicine and Biology*, 37(3):493–506.

[Yu and Wang, 2007] Yu, H. and Wang, G. (2007). Data consistency based rigid motion artifact reduction in fan-beam CT. *IEEE transactions on medical imaging*, 26(2):249–260.

[Yu et al., 2006] Yu, H., Wei, Y., Hsieh, J., and Wang, G. (2006). Data consistency based translational motion artifact reduction in fan-beam CT. *IEEE Transactions on Medical Imaging*, 25(6):792–803.

[Zhang et al., 2020] Zhang, X., Tang, J., Sharp, G. C., Xiao, L., Xu, S., and Lu, H.-M. (2020). A new respiratory monitor system for four-dimensional computed tomography by measuring the pressure change on the back of body. *The British Journal of Radiology*, 93(1108):20190303.

[Zhang et al., 2013] Zhang, Y., Yang, J., Zhang, L., Court, L. E., Balter, P. A., and Dong, L. (2013). Modeling respiratory motion for reducing motion artifacts in 4D CT images. *Medical Physics*, 40(4):041716.

FOLIO ADMINISTRATIF

THESE DE L'INSA LYON, MEMBRE DE L'UNIVERSITE DE LYON

NOM : MOUCHET DATE de SOUTENANCE : 06/12/2022

Prénoms : Mélanie

TITRE : Détection de mouvement respiratoire en tomodensitométrie par l'utilisation des conditions de cohérence des données

NATURE : Doctorat Numéro d'ordre : 2022ISAL0108

Ecole doctorale : Electronique, Electrotechnique, Automatique

Spécialité :Traitement du Signal et de l'Image

RESUME :
Les images de tomodensitométrie (TDM) quadridimensionnelles (4D) sont utilisées pour la planification de la radiothérapie des tumeurs thoraciques et abdominales supérieures afin de tenir compte des mouvements respiratoires. Cette modalité repose sur l'hypothèse que le cycle respiratoire est périodique, ce qui n'est pas toujours le cas, en particulier pour les patients souffrant de maladies respiratoires, entraînant des artefacts sur les images tomographiques qui peuvent avoir un impact sur la radiothérapie. Le but de cette thèse est de détecter le mouvement en TDM hélicoïdale en utilisant des conditions de cohérence des données (CCD). Les CCD sont des équations mathématiques caractérisant la redondance dans les données de projections. Elles ont été développées pour plusieurs configurations de source et de détecteur, mais la littérature est rare sur la TDM hélicoïdale avec un détecteur cylindrique qui est la géométrie la plus utilisée en TDM 4D. La première contribution de cette thèse propose deux approches pour appliquer les CCD à des paires de projections à faisceau conique. La première approche rééchantillonne deux projections sur un détecteur virtuel dont les lignes sont parallèles à la ligne reliant les positions de source pour appliquer des CCD de faisceau en éventail le long de chaque ligne. La seconde approche calcule les CCD dans les coordonnées du détecteur cylindrique pour augmenter le nombre de CCD dans une acquisition hélicoïdale. La deuxième contribution étudie la capacité des CCD à détecter localement le mouvement. Une mesure de cohérence est introduite pour tenir compte du bruit d'acquisition dans les CCD en calculant la variance des CCD. Enfin, deux méthodes sont proposées pour détecter le mouvement lors d'une acquisition. La première construit un graphe dans lequel les sommets sont les projections et deux sommets sont connectés s'il existe des CCD entre les projections. La seconde extrait le signal respiratoire des projections en utilisant la mesure de cohérence. Toutes les contributions sont évaluées à l'aide de données simulées et réelles. Les CCD permettent la détection de mouvement pour la plupart des paires, mais pas directement pour celles dont les CCD sont fortement impactées par le bruit et pour lesquelles un filtre passe-bas a été appliqué afin de rendre la détection possible.

MOTS-CLÉS : tomodensitométrie hélicoïdale, condition de cohérence des données, détection de mouvement respiratoire

Laboratoire (s) de recherche : CREATIS

Directeur de thèse: Jean Létang

Président de jury : Laurent Desbat

Composition du jury : DEFRISE, Michel (Rapporteur), MAIER, Andreas (Rapporteur), ETXEBESTE, Ane (Examinatrice), DESBAT, Laurent (Examinateur), LETANG, Jean (Directeur de thèse), RIT, Simon (Co-directeur de thèse), LESAINT, Jérôme (invité), LEPETIT COIFFE, Matthieu (invité).